A CONSISTENT NONLINEAR FREQUENCY DOMAIN MODEL FOR FINITE DEPTH OCEAN WAVE PROPAGATION

A Dissertation

by

INCHUL KIM

Submitted to the Office of Graduate and Professional Studies of
Texas A&M University
in partial fulfillment of the requirements for the degree of

DOCTOR OF PHILOSOPHY

Chair of Committee,	James M. Kaihatu
Committee Members,	Hamn-Ching Chen
	Kuang-An Chang
	Orencio Duran Vinent
Head of Department,	Zachary Grasley

May 2022

Major Subject: Civil Engineering

ABSTRACT

A new nonlinear second-order frequency-domain model based on the mild-slope equation is outlined. The model is an enhancement over previous work in that a closer correspondence between scaling of nonlinearity and horizontal variation of bathymetry is made relative to earlier models. This results in additional terms in the nonlinear summation terms of the model, as amplitude gradient terms are required in order to formulate a completely consistent model at second order. From the resulting elliptic model equation, a parabolic approximation is developed in order to efficiently model the equations for most applications. Comparisons between the present model, previously-formulated models, and experimental data show that the present model does evidence improvement in performance over previous, less-consistent models. It is also found that the "phase mismatch," which arises from the dispersive nature of the resulting equations, can adversely impact performance; this is a potential problem with all models of this sort.

Using a scheme developed for stochastic formulations of these phase-resolved models, a hybrid consistent nonlinear mild-slope equation in frequency-domain is developed. Using this scheme, a newly simplified version of the present model retains quasi-cubic terms having a form of cubic term but originating from triad wave interaction terms is developed. Because of the quasi-cubic nonlinear summation having zero-mismatch, the hybrid model replicates the triad wave-wave interactions more accurately compared to the previous deterministic models.

A higher-order parabolic evolution equation is derived for high accuracy at large wave approach angles. As an alternative, a consistent nonlinear mild-slope equation based on the angular spectrum model is also developed. These two newly developed models are tested for accuracy in describing wave pattern by a refractive focal lens, elliptic shoal, and circular shoal with the several incidence angles. The newly developed models are further examined with field data in order to ensure the models' capability in simulating two-dimensional irregular wave processes. Lastly, a source term for triad interactions is derived from the present model for implementation into operational phase-averaged wave models.

DEDICATION

This dissertation is dedicated,

with love and respect,

to my parents, wife, brother, and parents-in-law.

ACKNOWLEDGEMENTS

I would like to express my sincere gratitude and appreciation to my committee chair, Dr. James M. Kaihatu, who provided guidance and encouragement during my doctoral study. His generous discussions and advice always have given critical moment to my dissertation work. It has been a great honor and privilege to have worked with him. Also, I would like to thank my committee members, Dr. Hamn-Ching Chen, Dr. Kuang-An Chang, and Dr. Orencio Duran Vinent, for their valuable comments and suggestions on my dissertation.

I would like to express my thanks and gratitude to my parents, brother, and parents-in-law for their love, support, and trust. Finally, my great and special thanks to my wife for encouragement, patience, and unconditional love throughout the course of my study.

CONTRIBUTORS AND FUNDING SOURCES

Contributors

This work was supervised by a dissertation committee consisting of Dr. James M. Kaihatu (chair), Dr. Hamn-Ching Chen, and Dr. Kuang-An Chang of the Department of Civil & Environmental Engineering, and Dr. Orencio Duran Vinent of the Department of Ocean Engineering.

Funding Sources

Graduate study was supported by a Doctoral Fellowship from the Zachry Department of Civil & Environmental Engineering at Texas A&M University. The work was also partly supported by grant P42 ES027704 from the National Institute of Environmental Health Sciences.

TABLE OF CONTENTS

Page

LIST OF FIGURES

Page

LIST OF TABLES

Page

CHAPTER I

INTRODUCTION[*]

1.1 Introduction

As surface waves on the ocean propagate from deep ocean towards the shore, they are increasingly transformed as they react to changes in the ocean bottom. Analytic expressions for the kinematics and dynamics of ocean waves do not generally work in these situations, so ocean wave propagation models are required. They are thus a cornerstone of coastal and ocean engineering research and practice. The prediction of the transformation of waves in coastal zone has been studied during the past several decades as bathymetry significantly affects the wavefield in shallow water, which leads to refraction, shoaling, diffraction, breaking, and bottom friction. The wavefield is also affected by the domain of propagation from tidal or other ambient currents. An appropriate prediction of wave transformation might ensure better estimation of sediment transport, sandbar, and longshore bar process as well as more reasonable management of shipping and offshore and coastal construction.

Most work regarding wave transformation until the early 1980s had considered the problems of refraction and diffraction separately. (e.g., Penney et al. (1952) for diffraction of water waves around a semi-infinite breakwater; Keller (1958) for refraction approximation by employing WKB approximations of the governing equation;

[*] Part of this chapter is reprinted with permission from Kim, I. C. and Kaihatu, J. M., 2021. A consistent nonlinear mild-slope equation model. Coastal Engineering, 170: 104006. Copyright [2021] by Elsevier. DOI: https://doi.org/10.1016/j.coastaleng.2021.104006.

and Memos (1980) for the diffraction of waves passing between two breakwaters.) The ray method, first developed to study refraction by O'Brien and Mason (1942), was widely used as an analytical tool for wave transformation. Since the ray method does not take into account diffraction effects caused by arbitrarily varying water depth, ray crossings behind bottom shoals would lead to infinite wave heights. This is one of the main disadvantages in the ray method. Additionally, another drawback of the ray model is the heavy computational requirement resulting from inconsistently varying grid of wave heights and directions in the nearshore region.

To address combined refraction and diffraction effects, the so-called mild-slope equation was first proposed by Berkhoff (1973). Smith and Sprinks (1975) and Booij (1981) also developed variations of the mild-slope equation by applying Green's identities and a variational principle of Luke (1967), respectively. While an accurate depiction of combined refraction and diffraction effects, the mild-slope equation is elliptic, requiring all boundaries to be pre-specified. However, the wave breaking location for open ocean problems cannot be specified in advance, the parabolic approximation (e.g., Radder, 1979) was developed to help address the problems associated with elliptic equations. By means of the parabolic approximation, models for monochromatic linear waves can be developed. The approximation can be developed in different ways; for example, Radder (1979) used a matrix splitting method, and Lozano and Liu (1980) utilized a multi scale-perturbation method. Extensions to the mild-slope equation (and / or the associated parabolic approximation) have been introduced to

account for the other effects. (e.g., Dalrymple et al. (1984) for frictional dissipation effects and Booij (1981), Liu (1983), and Kirby (1984) for wave-current interaction.)

By using the Wentzel-Kramers-Brullion (or WKB) expansions for wave potential and free surface elevation (thereby splitting them into a fast scale associated with the waveform, and a slow scale associated with other features such as bathymetric variation), Yue and Mei (1980), using Stokes-wave steepness parameter for the slow scale, developed similar equations to the parabolic mild-slope equation including nonlinear terms, which is extension of the parabolic method to the case of second-order Stokes waves in constant depth. Kirby and Dalrymple (1983) and Liu and Tsay (1984) extended the method to include the effect of slowly varying depth.

One difficulty with the parabolic approximation is the inherent assumption that a wave propagates at small angles to the *x*-axis (cross-shore axis) of the grid. Considerable effort has been expended in attempts to obtain better accuracy for waves propagating at larger angle: examples include Booij (1981) utilizing a matrix splitting method; Kirby (1986a) applying the Padé approximant of the square root term; Kirby (1986b) using minimax approximation, and Dalrymple and Kirby (1988), Dalrymple et al. (1989), and Suh et al. (1990) using a linear angular spectrum model, which assumes that the wavefield is periodic in the alongshore (*y*) direction.

Models which use the mild-slope equation (or its parabolic form) are part of a class of models referred to as “phase-resolved” models. These models simulate the dynamics of the actual free surface of the wave. This is to be distinguished from “phase averaged” models, which simulate the dynamics of a statistical representation of the

wave field (e.g., the directional spectrum) and, as such, the phase is not retained. Generally, phase-resolved wave models are used in local areas of the nearshore, while phase-averaged models are used for larger scale (global, regional) domains, and usually outside the nearshore area. Furthermore, phase-resolved models are divided into time-domain models (in which the dependent variable is modeled as an arbitrary function of space and time) and frequency-domain models (in which the dependent variables are *apriori* assumed to periodic functions of space and/or time, with complex amplitudes which are slowly-varying functions of space and/or time). Since the amplitudes of frequency domain models are complex, they retain phase information.

The formulations can describe adequately the wavefield for deep water, where the Ursell number ($Ur = \frac{a}{k^2 h^3}$, where a is the amplitude, k is the wave number, and h is the water depth) is less than one. However, for cases where the Ursell number is greater than one, Stokes wave theory becomes invalid (e.g., Dean and Dalrymple, 1991). This would include scenarios in shallow water (small kh) and/or high waves (large a).

As ocean waves are significantly affected by the bathymetry in shallow water, in addition to the transformation effects such as refraction, shoaling, and diffraction, nonlinear effects become more evident in the nearshore region. Since Peregrine (1967) introduced Boussinesq-type equations for shallow water wave propagation over mildly varying bottoms, models based on the Boussinesq equations have been used to simulate phase-resolved wave transformation processes in coastal regions. These Boussinesq equations are cast in the form of depth-averaged mass-and-momentum-conserving equations, and the dispersion relation associated with these equations is “weakly

dispersive" (i.e., the phase speeds of the waves are only weakly dependent on wave frequency). In addition, it can be shown that the shoaling relationship governing the wave amplification is Green's Law, which is suited for long waves in shallow water and which is essentially a monotonic increase in wave amplitude. Initial models for nonlinear wave propagation in shallow water were proposed using the Boussinesq equations of Peregrine (1967); examples include Rygg (1988) in time domain, and Freilich and Guza (1984), Liu et al. (1985), and Kirby (1991) in frequency domain. These models show good agreement to data in cases where the waves are in shallow water (i.e., where the relative water depth kh (where k is the wave number and h the water depth) is small). However, in intermediate or deep water, the weak dispersion and Green's Law shoaling characteristics tend to lead to significant error.

In an attempt to increase the dispersive range of Boussinesq models, a number of authors have generally proposed adding dispersive effects (creating so-called "extended Boussinesq models") in time-domain. This is usually done by retaining the weakly-nonlinear formulation of the classical Boussinesq equation while altering the dispersive characteristics of the model to be more representative of linear dispersion in deep water. Efforts include: Witting (1984) using a Taylor series expansion of the velocity about the bottom; Madsen et al. (1991) using additional convective terms in momentum equation; and Nwogu (1993) using the Taylor expansion for the horizontal velocity vector at an arbitrary location in the water column, the position of which is optimized by performing a best fit of the dispersion relation to linear theory. Since Madsen and Sørensen (1993) formulated the extended Boussinesq-type model in frequency-domain, several

subsequent studies successfully modeled frequency-domain equations based on the extended Boussinesq-type models (e.g., Chen and Liu, 1995; Kaihatu and Kirby, 1998). Recently, some of developments suggested extensions to include higher order terms in the equations (e.g., Wei et al., 1995; Wei and Kirby, 1995; Madsen and Schäffer, 1998; Gobbi et al., 2000). Further, other models treated the depth dependence of the solution via various Taylor series expansions and operators with velocities at still water level (e.g., Agnon et al., 1999; Madsen et al., 2003; Fuhrman and Madsen, 2009), or multi-layer models (e.g., Lynett and Liu, 2004; Liu and Fang, 2016; Liu et al., 2018) to help increase the linear characteristics of these models to better resemble that of fully-dispersive linear theory.

Another approach to circumvent the limitations of shallow water approximation, while still accounting for nonlinearity, is the extension of the fully-dispersive mild-slope equation (Berkhoff, 1973) to involve weakly nonlinear terms. Bryant (1973, 1974) formulated space-domain evolution equations on constant depth from the boundary value problem. To develop the formulation, spatial periodicity and near periodicity in time were assumed. Unfortunately, the spatially-periodic formulation made extension to variable bathymetry difficult. Agnon et al (1993) proposed a one-dimensional fully dispersive evolution equation by substituting potential functions satisfying Laplace equation and bottom boundary condition into the free surface boundary condition (truncated at second order) and accounting for resonant interactions between wave frequencies. Following Smith and Sprinks (1975), Kaihatu and Kirby (1995) developed two-dimensional fully dispersive parabolic model for a small angle of incidence by

means of Green's identities, using the same resonant interaction concepts as Agnon et al. (1993). Tang and Ouellet (1997) took into consideration additional nonlinear terms including nonlinear diffraction terms to the model of Kaihatu and Kirby (1995). Moreover, Kaihatu (2001) and Eldeberky and Madsen (1999) improved the models by introducing the second-order relationship between amplitudes of wave potential and those of free surface elevation in the dynamic free surface boundary condition. Several recent models in this regard have been derived: taking into account both triad and quartet wave-wave interaction (e.g., Janssen et al., 2006), treating oblique incident waves (e.g., Toledo, 2013), using the solution in terms of truncated Taylor series expansions and the dispersion operator (e.g., Bredmose et al., 2005; Vrecica and Toledo, 2016), and using multiple scale analysis for the spatial phase function in the equations (e.g., Ardani and Kaihatu, 2019).

1.2 Objectives and research overview

A primary aim of the present study is to derive a new nonlinear mild-slope equation model in frequency-domain for the propagating surface gravity waves within both offshore and nearshore wavefields, with a specific goal to include nonlinearity via a scaling relationship between the spatial modulation scales of the amplitude and those of the depth variations which is more consistent than in previous models (e.g., Kaihatu and Kirby, 1995). The consistent nonlinear mild-slope formulation is then analyzed further and compared to data. In Chapter 2, a nonlinear mild-slope equation is newly developed by using Green’s second identity from boundary value problem, and then the parabolic

approximation is used to reduce the boundary value problem to an initial value problem. The present model is compared not only with the existing parabolic nonlinear mild-slope equation models, but also with the Stokes third-order theory and stream function theory (Dean, 1965). Some numerical simulations for the cases of the finite number of waves, including Chapalain et al. (1992), Whalin (1971), and Berkhoff et al. (1982), are detailed to verify the ability of the present model in Chapter 3. In Chapter 4, starting from the formulations derived in Chapter 2, a simplified version of the present equations is proposed for the random waves represented as a sum of numerous waves. Chapter 5 details the modeling results of the simplified equation and demonstrates how the model performs for irregular waves propagating over a mildly sloping bottom. In Chapter 6, we extend the parabolic equation model to include wide-angle wave propagation over an irregular bathymetry and compares model simulations to laboratory observations. To verify the capability of the present models on the scale of the extended coastal zone, the numerical simulations of directional wave spectrum are presented in several cases of field data in Chapter 7. Summary and suggestions for further research are discussed in Chapter 8.

CHAPTER II

CONSISTENT NONLINEAR MILD-SLOPE EQUATION MODEL*

2.1 Introduction and scale consistency

Nonlinear mild-slope equations in the frequency domain are generally developed in the form of a parabolic equation, which allows for more straightforward modeling of open coastal regions. The parabolic form can be developed with a judicious choice of modulation scales, which quantify the variation of a given variable and helps determine the order of the derivatives to be retained. Kaihatu and Kirby (1995) followed the scaling approach of Yue and Mei (1980), where scales for amplitude of free surface elevation and the modulation scale δ (where A_n is function of δx and $\delta^{1/2} y$) were chosen as follows (using the small ordering parameter $\varepsilon = ka$, or wave steepness):

$$A_n \sim O(\varepsilon),\ O(\delta) \sim O(\varepsilon^2) \tag{2.1}$$

$$\frac{\partial A_n}{\partial x} = O(\varepsilon\delta) \sim O(\varepsilon^3),\ \frac{\partial A_n}{\partial y} = O(\varepsilon\delta^{1/2}) \sim O(\varepsilon^2) \tag{2.2}$$

where A_n is the complex amplitude of free surface elevation of nth frequency component. They also chose a scale for depth change $\nabla_h h$ (where ∇_h is a gradient operator in horizontal coordinates) as $O(\varepsilon^2)$ to retain terms of bottom boundary condition to second order in ε (following Kirby and Dalymple, 1983). Horizontal derivatives of depth-dependent wave

* This chapter is reprinted with permission from Kim, I. C. and Kaihatu, J. M., 2021. A consistent nonlinear mild-slope equation model. Coastal Engineering, 170: 104006. Copyright [2021] by Elsevier. DOI: https://doi.org/10.1016/j.coastaleng.2021.104006.

characteristics (e.g., wave number k, wave celerity C, the group velocity C_g) would then be restricted to $O(\varepsilon^2)$:

$$\frac{\partial h}{\partial x} = O\left(\varepsilon^2\right), \ \frac{\partial h}{\partial y} = O\left(\varepsilon^2\right) \tag{2.3}$$

$$\frac{\partial \left(kCC_g\right)}{\partial x} = O\left(\varepsilon^2\right), \ \frac{\partial \left(kCC_g\right)}{\partial y} = O\left(\varepsilon^2\right) \tag{2.4}$$

These choices of scales should allow the terms neglected in parabolic approximation to appear as a term at fifth order in ε:

$$\left[\left(CC_g\right)_n A_{nx}\right]_x = O\left(\varepsilon^3\delta, \varepsilon\delta^2\right) \sim O\left(\varepsilon^5\right) \tag{2.5}$$

The nonlinear terms in the model of Kaihatu and Kirby (1995) (those proportional to the square of the wave amplitude) are only at second order in ε, but additional terms can be included in the parabolic equation because they are at lower order than the first neglected term. The consequence for the model of Kaihatu and Kirby (1995), therefore, is that the nonlinear terms are incomplete, and should also include derivatives of amplitudes as well in order to be completely consistent with the ordering. The addition of these consistently-ordered terms was implicitly addressed by Tang and Ouellet (1997); however, they did not fully consider terms up to fourth order in ε. It is anticipated that models which are consistent with the ordering would be expected to more fully describe nonlinear wave propagation effects in situations where amplitudes vary considerably (e.g., instances of wave diffraction), thus more completely simulating triad wave-wave interaction between frequency components.

2.2 Derivation of equations

2.2.1 Boundary value problem

A Cartesian coordinate system (x, y, z) is selected, with z taken positive vertically upwards from the still water level. We consider a surface gravity wavefield over a varying bottom in a horizontal direction, and the varying water depth is $h(x, y)$. For inviscid, incompressible and irrotational fluid, the dimensional water wave boundary problem that the wave potential $\phi(x, y, z, t)$ (where t is time) and the free surface elevation $\eta(x, y, t)$ satisfies is given as:

$$\nabla_h^2\phi + \phi_{zz} = 0 \; ; \; -h \le z \le \eta \tag{2.6}$$

$$\phi_z = -\nabla_h h \cdot \nabla_h \phi \; ; \; z = -h \tag{2.7}$$

$$g\eta + \phi_t + \frac{1}{2}\left(\nabla_h\phi\right)^2 + \frac{1}{2}\phi_z^{\,2} = 0 \; ; \; z = \eta \tag{2.8}$$

$$\eta_t - \phi_z + \nabla_h\eta \cdot \nabla_h\phi = 0 \; ; \; z = \eta \tag{2.9}$$

where $\nabla_h = \left(\frac{\partial}{\partial x}, \frac{\partial}{\partial y}\right)$ is a gradient operator in horizontal coordinates, g is the gravitational acceleration, and subscripts indicate partial derivatives.

Following the method of Bryant (1973), we retain dimensional quantities while noting that the leading order nonlinearity is $O(\varepsilon^2)$. Using Taylor series about still water level, $z = 0$, the truncated boundary value problem is formulated as:

$$\nabla_h^2\phi + \phi_{zz} = 0 \; ; \; -h \le z \le 0 \tag{2.10}$$

$$\phi_z = -\nabla_h h \cdot \nabla_h \phi \; ; \; z = -h \tag{2.11}$$

$$g\eta = -\left[\phi_t + \frac{1}{2}\left(\nabla_h\phi\right)^2 + \frac{1}{2}{\phi_z}^2\right] - \eta\phi_{tz} + O\left(\varepsilon^3\right)\ ;\ z = 0 \tag{2.12}$$

$$\eta_t = \left[\phi_z - \nabla_h\eta\cdot\nabla_h\phi\right] + \eta\phi_{zz} + O\left(\varepsilon^3\right)\ ;\ z = 0 \tag{2.13}$$

Using the method of Smith and Sprinks (1975), Kaihatu and Kirby (1995) assumed a superposition of solutions for wave potential with depth dependence function from fully dispersive linear theory:

$$\phi\left(x,y,z,t\right) = \sum_{n=1}^{N} f_n\left(h,z\right)\tilde{\phi}_n\left(x,y,t\right) \tag{2.14}$$

and

$$f_n\left(h,z\right) = \frac{\cosh k_n\left(h+z\right)}{\cosh k_n h} \tag{2.15}$$

where f_n is depth dependence function, k_n is the wave number, and ω_n is the wave angular frequency. Subscript n indicates the nth frequency component. The wave number k_n is determined by the linear dispersion relation:

$${\omega_n}^2 = gk_n \tanh k_n h \tag{2.16}$$

After combining Equations (2.12) and (2.13) to eliminate η, combined free surface boundary condition for ϕ only is given:

$$\phi_z = -\frac{1}{g}\left[\phi_{tt} + \left(\nabla_h\phi\right)^2_t + \frac{1}{2}\left(\phi_z\right)^2_t - \frac{1}{2g}\left(\phi_t\right)^2_{zt} - \phi_t\phi_{zz}\right]\ ;\ z = 0 \tag{2.17}$$

Depth dependence function f_n satisfies the following set of equations:

$$f_{nzz} - {k_n}^2 f = 0\ ;\ -h \le z \le 0 \tag{2.18}$$

$$f_{nz} = 0\ ;\ z = -h \tag{2.19}$$

$$f_{nz} = \frac{\omega_n^{\,2}}{g} \;;\; z = 0 \tag{2.20}$$

2.2.2 Green's second identity

Applying Green's second identity for ϕ and f, we have:

$$\int_{-h}^{0} \left(f_n \phi_{nzz} - \phi_n f_{nzz} \right) dz = \left[f_n \phi_{nz} - \phi_n f_{nz} \right]_{z=0} - \left[f_n \phi_{nz} - \phi_n f_{nz} \right]_{z=-h} \tag{2.21}$$

Using Equations (2.10), (2.11), and (2.17) – (2.20), (2.21) becomes:

$$\begin{aligned} &-\int_{-h}^{0} \left(f_n \nabla_h^{\,2} \phi_n + k_n^{\,2} \phi_n f_n \right) dz \\ &= \left(N.L. \right) - \left[\frac{1}{g} \phi_{ntt} f_n + \frac{\omega_n^{\,2}}{g} \phi_n f_n \right]_{z=0} + \left[f_n \nabla_h h \cdot \nabla_h \phi_n \right]_{z=-h} \end{aligned} \tag{2.22}$$

where the nonlinear term is:

$$\left(N.L. \right) = \left[-\frac{f_n}{g} \left\{ \left(\nabla_h \phi_n \right)^2_{\,t} + \frac{1}{2} \left(\phi_{nz} \right)^2_{\,t} - \frac{1}{2g} \left(\phi_{nt} \right)^2_{\,zt} - \phi_{nt} \phi_{nzz} \right\} \right]_{z=0} \tag{2.23}$$

The horizontal derivatives of potential function ϕ are written in terms of $\tilde{\phi}$ and f:

$$\nabla_h \phi = \nabla_h \left(\tilde{\phi} f \right) = \left(\nabla_h \tilde{\phi} \right) f + \tilde{\phi} \frac{\partial f}{\partial h} \nabla_h h \tag{2.24}$$

$$\nabla_h^{\,2} \phi = \left(\nabla_h^{\,2} \tilde{\phi} \right) f + 2 \nabla_h \tilde{\phi} \frac{\partial f}{\partial h} \nabla_h h + \tilde{\phi} \frac{\partial^2 f}{\partial h^2} \left(\nabla_h h \right)^2 + \tilde{\phi} \frac{\partial f}{\partial h} \nabla_h^{\,2} h \tag{2.25}$$

Substituting Equations (2.24) and (2.25) into Equation (2.22):

$$\begin{aligned} &-\int_{-h}^{0} \left(\nabla_h \left[\left(\nabla_h \tilde{\phi}_n \right) f_n^{\,2} \right] + \tilde{\phi}_n f_n \frac{\partial^2 f_n}{\partial h^2} \left(\nabla_h h \right)^2 + \tilde{\phi} f_n \frac{\partial f_n}{\partial h} \nabla_h^{\,2} h + k_n^{\,2} \tilde{\phi}_n f_n^{\,2} \right) dz \\ &= \left(N.L. \right) - \left[\frac{1}{g} \tilde{\phi}_{ntt} f_n^{\,2} + \frac{\omega_n^{\,2}}{g} \tilde{\phi}_n f_n^{\,2} \right]_{z=0} + \left[\nabla_h \tilde{\phi}_n \cdot \nabla_h h \left(f_n^{\,2} \right) + \tilde{\phi}_n f_n \frac{\partial f_n}{\partial h} \left(\nabla_h h \right)^2 \right]_{z=-h} \end{aligned} \tag{2.26}$$

Using Leibnitz' rule, Equation (2.26) becomes:

$$-\nabla_h\left(\left[\int_{-h}^{0} f_n{}^2 dz\right]\nabla_h\tilde{\phi}_n\right)-k_n{}^2\left(\int_{-h}^{0} f_n{}^2 dz\right)\tilde{\phi}_n-\int_{-h}^{0}\left(f\frac{\partial^2 f}{\partial h^2}\tilde{\phi}\left(\nabla_h h\right)^2+f\frac{\partial f}{\partial h}\tilde{\phi}\nabla_h{}^2 h\right)dz$$
$$=(N.L.)-\left[\frac{1}{g}f_n{}^2\tilde{\phi}_{ntt}+\frac{\omega_n{}^2}{g}f_n{}^2\tilde{\phi}_n\right]_{z=0}+\left[f\frac{\partial f}{\partial h}\tilde{\phi}\left(\nabla_h h\right)^2\right]_{z=-h} \tag{2.27}$$

The water depth varies gradually (i.e., $|\nabla h| \sim O(\alpha) << 1$, where α is a parameter characterizing the bottom slope). Following Kirby and Dalrymple (1983), we assume $O(\alpha) \sim O(\varepsilon^2)$ in order to eliminate bottom boundary term of $O(\varepsilon^3)$ (i.e., $-\nabla_h h \cdot \nabla_h \phi$ in Equation 2.11) in the bottom boundary condition, similar to the manner in which the cubic nonlinear terms in the free surface boundary conditions are discarded. Additionally, the left-hand side of Equation (2.11) is zero by virtue of Equation (2.19) (i.e., $\phi_z|_{z=-h} = 0$ or $f_{nz}\tilde{\phi}_n\big|_{z=-h} = 0$), thus satisfying the bottom boundary condition. Then, Equation (2.27) is simplified by discarding the terms of $O(\varepsilon\alpha^2) \sim O(\varepsilon^5)$ which is at higher order than the leading order nonlinearity $O(\varepsilon^2)$:

$$-\nabla_h\left(\left[\int_{-h}^{0} f_n{}^2 dz\right]\nabla_h\tilde{\phi}_n\right)-k_n{}^2\left(\int_{-h}^{0} f_n{}^2 dz\right)\tilde{\phi}_n=(N.L)-\left[\frac{1}{g}f_n{}^2\tilde{\phi}_{ntt}+\frac{\omega_n{}^2}{g}f_n{}^2\tilde{\phi}_n\right]_{z=0} \tag{2.28}$$

Neglecting terms of $O(\varepsilon\alpha^2) \sim O(\varepsilon^5)$, the nonlinear terms can be also expressed in terms of $\tilde{\phi}$ and f:

$$(N.L.) = -\frac{1}{g}\left[\begin{array}{l} \left\{\sum_l\sum_m \left[\begin{array}{l} f_l f_m \left(\nabla_h \tilde{\phi}_l\right)\cdot\left(\nabla_h \tilde{\phi}_m\right) \\ + f_m \dfrac{\partial f_l}{\partial h}\tilde{\phi}_l \left(\nabla_h \tilde{\phi}_m\right)\cdot\nabla_h h + f_l \dfrac{\partial f_m}{\partial h}\tilde{\phi}_m \left(\nabla_h \tilde{\phi}_l\right)\cdot\nabla_h h \end{array}\right]\right\}_t \\ + \dfrac{1}{2}\left\{\sum_l\sum_m f_{lz} f_{mz}\tilde{\phi}_l\tilde{\phi}_m\right\}_t - \dfrac{1}{2g}\left\{\sum_l\sum_m \left(f_{lz} f_m + f_l f_{mz}\right)\tilde{\phi}_{lt}\tilde{\phi}_{mt}\right\}_t \\ - \dfrac{1}{2}\left\{\sum_l\sum_m f_l f_{mzz}\tilde{\phi}_{lt}\tilde{\phi}_m + f_{lzz} f_m\tilde{\phi}_l\tilde{\phi}_{mt}\right\} \\ \\ \end{array}\right]_{z=0} \tag{2.29}$$

where two arbitrary frequency modes, *l* and *m*, influence the *n*th frequency mode via triad wave-wave interaction between frequency components.

Expressions with depth dependence function are calculated as follows:

$$f_n(0) = 1 \tag{2.30}$$

$$f_{nz}(0) = \frac{\omega_n^{\,2}}{g} \tag{2.31}$$

$$f_{nzz}(0) = k_n^{\,2} \tag{2.32}$$

$$\int_{-h}^{0} f_n^{\,2} dz = \frac{\left(CC_g\right)_n}{g} \tag{2.33}$$

$$\int_{-h}^{0} \left(f_{nz}\right)^2 dz = \frac{\omega_n^{\,2}}{g}\left(1 - \frac{C_{gn}}{C_n}\right) \tag{2.34}$$

$$\frac{\partial f_n}{\partial h}(0) = \left[\frac{k_n \sinh k_n z}{\cosh^2 k_n h}\right]_{z=0} = 0 \tag{2.35}$$

The time dependency will be factored out by assuming periodicity in time:

$$\tilde{\phi}_n(x, y, t) = \frac{\hat{\phi}_n}{2} e^{-i\omega_n t} + \frac{\hat{\phi}_n^{\,*}}{2} e^{i\omega_n t} \tag{2.36}$$

Applying Equations (2.30) through (2.36) into Equations (2.28) and (2.29), elliptic form of nonlinear mild-slope equation is obtained:

$$\begin{aligned}
&\nabla_h \cdot \left[\left(CC_g \right)_n \nabla_h \hat{\phi}_n \right] + k_n{}^2 \left(CC_g \right)_n \hat{\phi}_n \\
&= -\frac{i}{4} \sum_{l=1}^{n-1} \left[\begin{array}{l} 2\omega_n \nabla_h \hat{\phi}_l \cdot \nabla_h \hat{\phi}_{n-l} - \left(\omega_l k_{n-l}{}^2 + \omega_{n-l} k_l{}^2 \right) \hat{\phi}_l \hat{\phi}_{n-l} \\ + \left\{ \dfrac{\omega_l \omega_{n-l} \omega_n}{g^2} \left(\omega_l{}^2 + \omega_{n-l}{}^2 + \omega_l \omega_{n-l} \right) \hat{\phi}_l \hat{\phi}_{n-l} \right\} \end{array} \right] \\
&- \frac{i}{2} \sum_{l=1}^{N-n} \left[\begin{array}{l} 2\omega_n \nabla_h \hat{\phi}_l^* \cdot \nabla_h \hat{\phi}_{n+l} - \left(\omega_{n+l} k_l{}^2 - \omega_l k_l{}^2 \right) \hat{\phi}_l^* \hat{\phi}_{n+l} \\ - \left\{ \dfrac{\omega_l \omega_{n+l} \omega_n}{g^2} \left(\omega_l{}^2 + \omega_{n+l}{}^2 - \omega_l \omega_{n+l} \right) \hat{\phi}_l^* \hat{\phi}_{n+l} \right\} \end{array} \right]
\end{aligned} \tag{2.37}$$

Compared to the elliptic equation of Kaihatu and Kirby (1995), Equation (2.37) is almost identical except that the nonlinear terms have a form of $-\omega k^2 \hat{\phi}\hat{\phi}$, rather than $\omega\hat{\phi}\nabla_h^2\hat{\phi}$ as seen in Equation 22 in Kaihatu and Kirby (1995). This term arises from using $-\phi_t\phi_{zz}$ in the combined free surface boundary condition (Equation 2.17), rather than $\phi_t\nabla_h{}^2\phi$ as used by Kaihatu and Kirby (1995). We explain how these different nonlinear terms in the elliptic equations have a significant effect on the parabolic equations in Section 2.3.

2.2.3 Parabolic approximation

While the model equation (2.37) is a comprehensive form of the nonlinear mild-slope equation, its elliptic formulation makes it difficult to implement for open coastal problems, though a form of the equation was implemented by Sharma et al. (2014). As mentioned earlier, elliptic equation requires pre-specification of all boundaries, which makes it difficult for open coast problems in which the location of breaking is unknown

apriori. In addition, the dependent variables in the equations oscillate at the scale of the individual waves, requiring high spatial resolution. To overcome these obstacles, we make use of the parabolic approximation (Radder, 1979; Lozano and Liu, 1980) to develop the model.

Incorporation of the parabolic approximation begins by imposing the following form for the velocity potential:

$$\hat{\phi}_n(x,y) = -\frac{ig}{\omega_n} A_n(x,y) e^{i\int k_n(x,y)dx} \tag{2.38}$$

where A_n is complex amplitude having the small spatial change (i.e., horizontal derivatives), and representing waves that propagate primarily in the $+x$ (axis normal to shore) direction.

Following the scaling approach of Yue and Mei (1980), orders of A_n and its horizontal derivatives are chosen, with derivatives of depth-dependent characteristics (e.g., wave number k, wave celerity C, the group velocity C_g) restricted to $O(\delta) \sim O(\varepsilon^2)$ due to the assumption of the bottom slope, $O(\alpha) \sim O(\varepsilon^2)$:

$$A_n \sim O(\varepsilon) \tag{2.39}$$

$$\frac{\partial A_n}{\partial x} = O(\varepsilon\delta) \sim O(\varepsilon^3), \ \frac{\partial A_n}{\partial y} = O(\varepsilon\delta^{1/2}) \sim O(\varepsilon^2) \tag{2.40}$$

$$\frac{\partial h}{\partial x} = O(\alpha) \sim O(\varepsilon^2), \ \frac{\partial h}{\partial y} = O(\alpha) \sim O(\varepsilon^2) \tag{2.41}$$

$$\frac{\partial\left[\left(kCC_g\right)_n\right]}{\partial x} = O(\alpha) \sim O(\varepsilon^2), \ \frac{\partial\left[\left(kCC_g\right)_n\right]}{\partial y} = O(\alpha) \sim O(\varepsilon^2) \tag{2.42}$$

Linear terms of Equation (2.37) are written with complex amplitude:

$$\left[\left(CC_g\right)_n A_{nx}\right]_x + 2i\left(kCC_g\right)_n A_{nx} + i\left(kCC_g\right)_{nx} A_n + \left[\left(CC_g\right)_n A_{ny}\right]_y \tag{2.43}$$

but which have the following ordering:

$$\left[\left(CC_g\right)_n A_{nx}\right]_x = \left(CC_g\right)_{nx} A_{nx} + \left(CC_g\right)_n A_{nxx} = O\left(\varepsilon\alpha\delta, \varepsilon\delta^2\right) \sim O\left(\varepsilon^5\right) \tag{2.44}$$

$$\left[2i\left(kCC_g\right)_n A_{nx}\right],\ \left[i\left(kCC_g\right)_{nx} A_n\right] = O\left(\varepsilon\delta, \varepsilon\alpha\right) \sim O\left(\varepsilon^3\right) \tag{2.45}$$

$$\left(CC_g\right)_{ny} A_{ny} = O\left(\varepsilon\alpha\delta^{1/2}\right) \sim O\left(\varepsilon^4\right) \tag{2.46}$$

$$\left(CC_g\right)_n A_{nyy} = O\left(\varepsilon\delta\right) \sim O\left(\varepsilon^3\right) \tag{2.47}$$

and we note that the orders of terms here are entirely equivalent to that of Kirby and Dalrymple (1983), including the smaller term (2.46) in the third order solvability condition.

At this stage it would be opportune to discuss the ordering in detail, in particular as it relates to the balance between nonlinearity ε, bottom slope α, and wave modulation scale δ. In the prior section we mentioned that only quadratic nonlinearity will be included, thus establishing the leading order nonlinearity as $O(\varepsilon^2)$. To be aligned with the parabolic equation ordering established above (as well as in prior studies), terms up to $O(\varepsilon^4)$ and equivalent (e.g., $O(\varepsilon\alpha\delta^{1/2})$ in Equation 2.46) can be retained. Since we are *apriori* limiting the nonlinearity to the leading order of $O(\varepsilon^2)$, the established ordering allows the retention of not only products of amplitude A_n to represent this order of nonlinearity, but also associated derivatives with respect to x and y. This is possible due to the ordering of $O(\delta) \sim O(\alpha) \sim O(\varepsilon^2)$ established in accord with Yue and Mei (1980)

and thus is a consistent incorporation of quadratic nonlinearity within the framework of a parabolic mild-slope equation model.

As an additional note, it is also worth comparison to the development of the linear parabolic mild-slope equation (Lozano and Liu 1980; Tsay and Liu, 1982; Liu 1986). In these linear models, the leading order is $O(\varepsilon)$, which scales the amplitude A_n as above (Equation 2.39). By assuming $O(\delta) \sim O(\alpha) \sim O(\varepsilon)$, these linear models retain the associated parabolic terms up to $O(\varepsilon^{2.5})$, determined by substituting ε for α and δ in $O(\varepsilon\alpha\delta^{1/2})$.

With this ordering established, we eliminate terms of $O(\varepsilon\delta\alpha, \varepsilon\delta^2) \sim O(\varepsilon^5)$ or higher in Equation (2.44):

$$\begin{aligned} &2i\left(kCC_g\right)_n A_{nx} + i\left(kCC_g\right)_{nx} A_n + \left[\left(CC_g\right)_n \left(A_n\right)_y\right]_y \\ &= \frac{1}{4}\sum_{l=1}^{n-1}\left[R_1 A_l A_{n-l} + R_2 A_{lx} A_{n-l} + R_3 A_l A_{n-lx} + R_4 A_{ly} A_{n-ly}\right] e^{i\int (k_l + k_{n-l} - k_n)dx} \\ &+ \frac{1}{2}\sum_{l=1}^{N-n}\left[S_1 A_l^* A_{n+l} + S_2 A_{lx}^* A_{n+l} + S_3 A_l^* A_{n+lx} + S_4 A_{ly}^* A_{n+ly}\right] e^{i\int (k_{n+l} - k_l - k_n)dx} \end{aligned} \tag{2.48}$$

where the interaction coefficients are:

$$\begin{aligned} R_1 = &\frac{g}{\omega_l \omega_{n-l}}\left[\omega_n^{\,2} k_l k_{n-l} + \left(k_l + k_{n-l}\right)\left(\omega_{n-l} k_l + \omega_l k_{n-l}\right)\omega_n\right] \\ &- \frac{\omega_n^{\,2}}{g}\left(\omega_l^{\,2} + \omega_l \omega_{n-l} + \omega_{n-l}^{\,2}\right) \end{aligned} \tag{2.49}$$

$$R_2 = -2i\frac{g\omega_n^{\,2} k_{n-l}}{\omega_l \omega_{n-l}} \tag{2.50}$$

$$R_3 = -2i\frac{g\omega_n^{\,2} k_l}{\omega_l \omega_{n-l}} \tag{2.51}$$

$$R_4 = -2\frac{g\omega_n^{\,2}}{\omega_l \omega_{n-l}} \tag{2.52}$$

and

$$S_1 = \frac{g}{\omega_l \omega_{n+l}}\left[\omega_n^{\,2} k_l k_{n+l} + \left(k_{n+l} - k_l\right)\left(\omega_{n+l} k_l + \omega_l k_{n+l}\right)\omega_n\right] - \frac{\omega_n^{\,2}}{g}\left(\omega_l^{\,2} - \omega_l \omega_{n+l} + \omega_{n+l}^{\,2}\right) \tag{2.53}$$

$$S_2 = 2i\frac{g\omega_n^{\,2} k_{n+l}}{\omega_l \omega_{n+l}} \tag{2.54}$$

$$S_3 = -2i\frac{g\omega_n^{\,2} k_l}{\omega_l \omega_{n+l}} \tag{2.55}$$

$$S_4 = 2\frac{g\omega_n^{\,2}}{\omega_l \omega_{n+l}} \tag{2.56}$$

The wave numbers k_n in the phase functions (the complex exponential terms in Equation 2.38) are functions of both x and y; however, the integration in the phase functions is performed only in the x direction in keeping with the parabolic approximation. Kaihatu and Kirby (1995) selected the method of Lozano and Liu (1980) to factor out the y-dependence from phase function by using the y-averaged wave number $\bar{k}_n(x)$ as a reference wave number:

$$\hat{\phi}_n\left(x,y\right) = -\frac{ig}{\omega_n} a_n\left(x,y\right) e^{i\int \bar{k}_n(x,y)dx} \tag{2.57}$$

where the amplitude functions are related:

$$A_n\left(x,y\right) = a_n\left(x,y\right)\exp\left[i\int \bar{k}_n\left(x\right) - k_n\left(x,y\right)dx\right] \tag{2.58}$$

Substituting Equation (2.58) into Equation (2.48) yields:

$$
\begin{aligned}
&2i\left(kCC_g\right)_n a_{nx} - 2\left(kCC_g\right)_n \left(\bar{k}_n - k_n\right) a_n + i\left(kCC_g\right)_{nx} a_n + \left[\left(CC_g\right)_n \left(a_n\right)_y\right]_y \\
&= \frac{1}{4}\sum_{l=1}^{n-1}\left[\begin{array}{l} R_1 a_l a_{n-l} + R_2\left(i\left\{\bar{k}_l - k_l\right\} a_l a_{n-l} + a_{lx} a_{n-l}\right) \\ +R_3\left(i\left\{\bar{k}_{n-l} - k_{n-l}\right\} a_l a_{n-l} + a_l a_{n-lx}\right) + R_4 a_{ly} a_{n-ly}\end{array}\right] e^{i\int\left(\bar{k}_l + \bar{k}_{n-l} - \bar{k}_n\right)dx} \\
&+ \frac{1}{2}\sum_{l=1}^{N-n}\left[\begin{array}{l} S_1 a_l^{\,*} a_{n+l} + S_2\left(-i\left\{\bar{k}_l - k_l\right\} a_l^{\,*} a_{n+l} + a_{lx}^{\,*} a_{n+l}\right) \\ +S_3\left(i\left\{\bar{k}_{n+l} - k_{n+l}\right\} a_l^{\,*} a_{n+l} + a_l^{\,*} a_{n+lx}\right) + S_4 a_{ly}^{\,*} a_{n+ly}\end{array}\right] e^{i\int\left(\bar{k}_{n+l} - \bar{k}_l - \bar{k}_n\right)dx}
\end{aligned}
\tag{2.59}
$$

We also reduce Equation (2.48) to one dimension for comparisons with unidirectional laboratory experiments:

$$
\begin{aligned}
&A_{nx} + \frac{\left(kCC_g\right)_{nx}}{2\left(kCC_g\right)_n} A_n \\
&= -\frac{i}{8\left(kCC_g\right)_n}\left[\begin{array}{l} \sum_{l=1}^{n-1}\left[R_1 A_l A_{n-l} + R_2 A_{lx} A_{n-l} + R_3 A_l A_{n-lx}\right] e^{i\int\left(k_l + k_{n-l} - k_n\right)dx} \\ +2\sum_{l=1}^{N-n}\left[S_1 A_l^{\,*} A_{n+l} + S_2 A_{lx}^{\,*} A_{n+l} + S_3 A_l^{\,*} A_{n+lx}\right] e^{i\int\left(k_{n+l} - k_l - k_n\right)dx}\end{array}\right]
\end{aligned}
\tag{2.60}
$$

2.3 Comparisons with other models

Two features are apparent in the present model. First, most models (Freilich and Guza, 1984; Liu et al., 1985; Agnon et al., 1993; Tang and Ouellet, 1997; Eldeberky and Madsen, 1999 among many others) were developed under the assumption that the order of amplitude A_n is the same as that of the spatial gradient of depth (or $O(\varepsilon)$) as well as modulation scale δ (where A_n is function of δx and $\delta^{1/2} y$). Because of this assumption, the neglected terms in parabolic approximation have the same order as the x-derivatives of amplitude in the nonlinear term $A_x A$. The calculation of scale under the assumption that

$A \sim O(\varepsilon)$, $A_x \sim O(\varepsilon^2)$, $(CC_g)_x \sim \nabla_h h \sim O(\varepsilon)$ was taken in the previous models (e.g., Kaihatu and Kirby, 1995):

$$A_{lx}A_{n-l} \sim \left[\left(CC_g\right)_n A_{nx}\right]_x \sim O\left(\varepsilon^3\right) \tag{2.61}$$

However, we can include the x-derivative nonlinear term A_xA in the parabolic equation, since it was assumed that amplitude is of lower order than depth change (or $O(\varepsilon^2)$) and modulation scale δ. For the present study, Equation (2.62) shows the comparison of order between the neglected terms in parabolic approximation and the nonlinear term A_xA which is one of the additional terms:

$$\left[\left(CC_g\right)_n A_{nx}\right]_x \sim O\left(\varepsilon^5\right) < A_{lx}A_{n-l} \sim O\left(\varepsilon^4\right) \tag{2.62}$$

2.3.1 Kaihatu and Kirby (1995)

The parabolic model of Kaihatu and Kirby (1995) is:

$$\begin{aligned} &2i\left(kCC_g\right)_n A_{nx} + i\left(kCC_g\right)_{nx} A_n + \left[\left(CC_g\right)_n \left(A_n\right)_y\right]_y \\ &= \frac{1}{4}\sum_{l=1}^{n-1} R_1 A_l A_{n-l} e^{i\int (k_l + k_{n-l} - k_n)dx} + \frac{1}{2}\sum_{l=1}^{N-n} S_1 A_l^* A_{n+l} e^{i\int (k_{n+l} - k_l - k_n)dx} \end{aligned} \tag{2.63}$$

where R_1 and S_1 are the same as Equation (2.48).

To examine the effect of x-derivative nonlinear term A_xA, Equations (2.48) and (2.63), respectively, were simplified into one-dimensional equations for constant depth. The model of Kaihatu and Kirby (1995) (Equation 2.63) is simplified into Equation (2.64):

$$A_{nx} = -\frac{i}{8\left(kCC_g\right)_n}\left[\sum_{l=1}^{n-1}\left[R_1 A_l A_{n-l}\right]e^{i\theta} + 2\sum_{l=1}^{N-n}\left[S_1 A_l^* A_{n+l}\right]e^{i\psi}\right] \tag{2.64}$$

and the present model (Equation 2.48) is simplified into Equation (2.65):

$$A_{nx} = -\frac{i}{8\left(kCC_g\right)_n}\left[\begin{array}{l}\sum_{l=1}^{n-1}\left[R_1 A_l A_{n-l} + R_2 A_{lx} A_{n-l} + R_3 A_l A_{n-lx}\right]e^{i\theta} \\ +2\sum_{l=1}^{N-n}\left[S_1 A_l^{*} A_{n+l} + S_2 A_{lx}^{*} A_{n+l} + S_3 A_l^{*} A_{n+lx}\right]e^{i\psi}\end{array}\right] \tag{2.65}$$

where interaction coefficients are the same as Equation (2.48), and:

$$\theta = \int k_l + k_{n-l} - k_n dx \tag{2.66}$$

$$\psi = \int k_{n+l} - k_l - k_n dx \tag{2.67}$$

are denoted as phase mismatches. These mismatches serve to mitigate the interaction between triads of frequencies by detuning the interactions. The interactions between wave number (e.g., $k_l + k_{n-l} - k_n$) have the same order of magnitude as weak dispersion μ^2 (where $\mu = kh$). In deep water, Kaihatu and Kirby (1997) argued that the phase mismatch can become large, which may violate the assumption of slow horizontal variation of amplitude.

To focus on the influence of x-derivative nonlinear term $A_x A$ on phase mismatch in the numerical model, we created an artificial case where all the values of wave characteristics (e.g., A, h, ω, k), at the wave maker station ($x = 0$) are given, and then calculate the amplitudes at the next grid point with forward difference method. To isolate the impact of μ^2, phase mismatches θ and ψ are expressed as $\mu^2 \kappa \Delta x$ (where κ is non-dispersive wave number and Δx is the step size of the model grid). The use of κ ensures dimensional homogeneity with the phase mismatches, while the size of μ determines the relative depth. In this artificial case, A_x is the only unknown, and the

other variables including A can be represented with constants K_1 and K_2 since these values are specified. Equation (2.68) is derived from Equation (2.64), which is the simplified version of the model of Kaihatu and Kirby (1995):

$$A_x = K_1 \exp\left(i\mu^2\kappa\Delta x\right) \tag{2.68}$$

For the present model (Equation 2.65, which is the simplified version of Equation 2.48), we obtain:

$$A_x = K_1 \exp\left(i\mu^2\kappa\Delta x\right) + K_2 A_x \exp\left(i\mu^2\kappa\Delta x\right) \tag{2.69}$$

Solving Equation (2.69) of the present model for A_x results in:

$$A_x = \frac{K_1 \exp\left(i\mu^2\kappa\Delta x\right)}{1 - K_2 \exp\left(i\mu^2\kappa\Delta x\right)} \tag{2.70}$$

While K_1 involves the square of the amplitude (i.e., AA or AA^*), K_2 involves only a single amplitude. Therefore, it is reasonable to assume K_2 to be greater than K_1, in accordance with the ordering. Assigning values of $K_1 = 1$ and $K_2 = 3$ or 5, the real part of A_x for each model is represented as:

$$\mathrm{Re}\left(A_x\right) = \begin{cases} \cos\left(\mu^2\kappa\Delta x\right) & \text{; Kaihatu and Kirby (1995)} \\ \dfrac{\cos\left(\mu^2\kappa\Delta x\right) - 3}{-6\cos\left(\mu^2\kappa\Delta x\right) + 10} & \text{; Present model with } K_2 = 3 \\ \dfrac{\cos\left(\mu^2\kappa\Delta x\right) - 5}{-10\cos\left(\mu^2\kappa\Delta x\right) + 26} & \text{; Present model with } K_2 = 5 \end{cases} \tag{2.71}$$

Figure 1 shows the real part of amplitude change depending on dimensionless grid size $\kappa\Delta x$ in shallow water ($\mu = 0.5$) and deep water ($\mu = 3$).

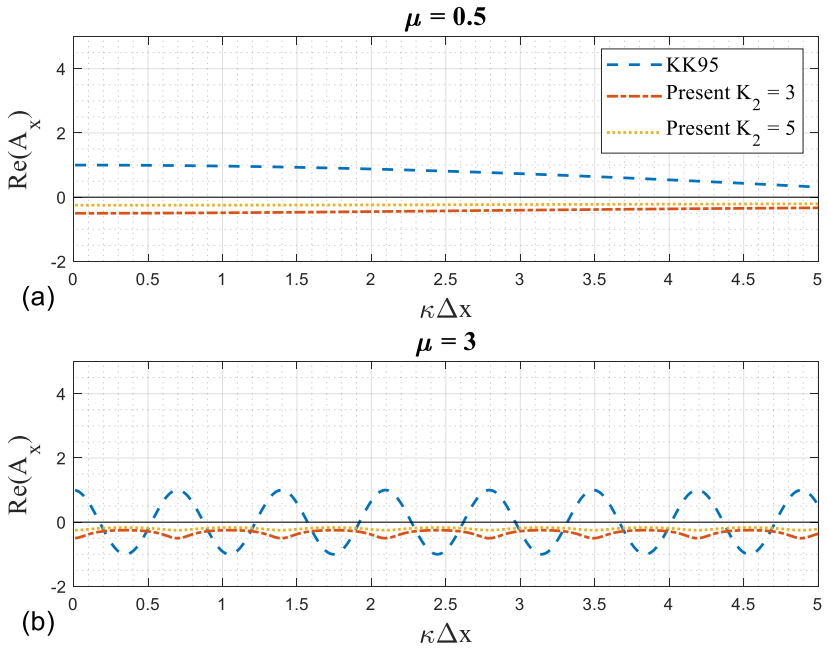

Figure 1 Comparison of Re(A_x) between model of Kaihatu and Kirby (1995) and the present model: (a) μ = 0.5; (b) μ = 3; (Dashed: model of Kaihatu and Kirby (1995); Dotted: present model with K_2 = 3; Dash-dot: present model with K_2 = 5).

It is desirable for the real part of the amplitude gradient A_x to demonstrate a low degree of sensitivity to the dimensionless step size $\kappa\Delta x$. From Figure 1, it is clear that the model of Kaihatu and Kirby (1995) shows a high degree of oscillation in deep water (μ = 3) as a function of $\kappa\Delta x$. However, also from Figure 1, we can see that the amplitude of the mismatch might not violate the assumption of slow varying amplitude in deep water, because the real part of $\exp[i\mu^2\kappa\Delta x]$ will only oscillate between – 1 and 1 even with large μ^2.

In contrast, mismatches in the present model (with x-derivative nonlinear term A_xA) shows a greatly reduced sensitivity to the dimensionless grid size. Because $\exp[i\mu^2\kappa\Delta x]$ is multiplied by A_x on the right-hand side of Equation (2.69) and serves as an oscillating coefficient of A_x, A_x might oscillate to a lesser degree (or remain almost constant similar to the case of zero-mismatch) even in deep water (μ = 3). In the interest of generalization, the simplest example for N = 2 is provided in Appendix A.

Another source of difference between the present model and that of Kaihatu and Kirby (1995) concerns the combined free surface boundary condition (Equation 2.17). We note that the last nonlinear term in the combined free surface boundary condition (2.17) is the vertical derivative $-\phi_t\phi_{zz}$. In previous studies (Agnon et al., 1993; Kaihatu and Kirby, 1995; Tang and Ouellet, 1997; Eldeberky and Madsen, 1999 among many others), the Laplace equation was used to trade the vertical derivative for horizontal derivatives, leading to the nonlinear term $\phi_t\nabla_h^2\phi$. It was generally further combined with $\nabla_h\phi_t\cdot\nabla_h\phi$, yielding $\nabla_h(\phi_t\nabla_h\phi)$ in the combined free surface boundary condition, affecting the resulting form of the model (e.g., Equation 2.23). To compare representation of

vertical derivatives with that of horizontal derivatives, we develop two equations with complex amplitude A_n solely based on these derivatives:

$$\begin{aligned}\nabla_h{}^2\phi\big|_{z=0} &= \nabla_h{}^2\left\{Af\,\exp\left[i\left(-\omega t+\int kdx\right)\right]\right\}_{z=0} \\ &= \left\{-k^2A+A_{xx}+2ikA_x+ik_xA+A_{yy}+A\left[\frac{\partial^2 f}{\partial h^2}\right]_{z=0}\left(\nabla_h h\right)^2\right\}e^{i\left[-\omega t+\int kdx\right]}\end{aligned} \tag{2.72}$$

$$\begin{aligned}-\phi_{zz}\big|_{z=0} &= \left\{-Af_{zz}e^{i\left[-\omega t+\int kdx\right]}\right\}_{z=0} \\ &= -k^2A\exp\left[i\left(-\omega t+\int kdx\right)\right]\end{aligned} \tag{2.73}$$

Since water depth h and complex amplitude A_n vary gradually in the horizontal direction, higher order terms arise from horizontal derivative of wave potential ϕ. As a result, when we represent the nonlinear term with the horizontal derivative (i.e., $\phi_t\nabla_h{}^2\phi$), we discard some of terms higher order than $O(\varepsilon^4)$, for example, the terms proportional to A_{xx} or $(\nabla_h h)^2$, while the representing with vertical derivative (i.e., $-\phi_t\phi_{zz}$) allows the parabolic equation to include the term without any discarded term. This allows the entirety of the nonlinear term $-\phi_t\phi_{zz}$ (or $\phi_t\nabla_h{}^2\phi$) to be retained. In addition, including fewer horizontal derivative terms, such as double derivative of complex amplitude with respect to y, can enhance model stability and reduce iterations required for numerical convergence.

2.3.2 Tang and Ouellet (1997)

The first model of Tang and Ouellet (1997) in dimensional form is:

$$\begin{aligned} & 2i\left(kCC_g\right)_n A_{nx} + i\left(kCC_g\right)_{nx} A_n + \left[\left(CC_g\right)_n \left(A_n\right)_y\right]_y \\ & = \frac{1}{4}\sum_{l=1}^{n-1}\left[\begin{array}{l}\left(R_1 + R_{11} + R_{12}\right) A_l A_{n-l} \\ + R_4 A_{ly} A_{n-ly} + R_5 A_l A_{n-lyy} + R_6 A_{lyy} A_{n-l}\end{array}\right] e^{i\int (k_l + k_{n-l} - k_n)dx} \\ & + \frac{1}{2}\sum_{l=1}^{N-n}\left[\begin{array}{l}\left(S_1 + S_{11} + S_{12}\right) A_l^* A_{n+l} \\ + S_4 A_{ly}^* A_{n+ly} + S_5 A_l^* A_{n+lyy} + S_6 A_{lyy}^* A_{n+l}\end{array}\right] e^{i\int (k_{n+l} - k_l - k_n)dx} \end{aligned} \tag{2.74}$$

where R_1, R_4, and S_1, S_4 are the same as Equation (2.48), and:

$$R_{11} = -i\frac{g\omega_n\omega_l}{\omega_l\omega_{n-l}}k_{n-lx} \tag{2.75}$$

$$R_{12} = -i\frac{g\omega_n\omega_{n-l}}{\omega_l\omega_{n-l}}k_{lx} \tag{2.76}$$

$$R_5 = -\frac{g\omega_n}{\omega_{n-l}} \tag{2.77}$$

$$R_6 = -\frac{g\omega_n}{\omega_l} \tag{2.78}$$

and

$$S_{11} = -i\frac{g\omega_n\omega_{n+l}}{\omega_l\omega_{n+l}}k_{lx} \tag{2.79}$$

$$S_{12} = -i\frac{g\omega_n\omega_l}{\omega_l\omega_{n+l}}k_{n+lx} \tag{2.80}$$

$$S_5 = -\frac{g\omega_n}{\omega_{n+l}} \tag{2.81}$$

$$S_6 = \frac{g\omega_n}{\omega_l} \tag{2.82}$$

Tang and Ouellet (1997) did not include the *x*-derivative nonlinear term, of which coefficients are R_2, R_3, S_2, and S_3 as well. In addition, the model of Tang and Ouellet (1997) has a greater number of terms (e.g., terms with R_{11}, R_{12}, R_5, and R_6) than the present model. These additional terms resulted from the double horizontal derivative nonlinear term $\phi_t \nabla_h^2 \phi$ discussed above, after neglecting higher order terms. In addition, the Laplace equation (2.10) dictates that Equation (2.72) should be identical to Equation (2.73), thus the sum of terms except for $-k^2 A$ in Equation (2.72) must cancel. As a result, neglecting some of the higher order terms in $\phi_t \nabla_h^2 \phi$ might lead to incomplete consideration of $\phi_t \nabla_h^2 \phi$ (or $-\phi_t \phi_{zz}$). Paradoxically, the present equation does not include the terms present in Tang and Ouellet (1997), but the final term in the combined free surface boundary condition (i.e., $-\phi_t \phi_{zz}$) insures full consideration of this boundary condition to the specified order.

2.3.3 Permanent form solutions

Kirby (1991) and Kaihatu (2001) derived a permanent form solution for the purpose of validating model behavior in deep and shallow water by comparison to analytic and numerical wave theories. For similar purposes, we also developed a numerical permanent form solution of the present model, and compared the results of this solution to those of Stokes third-order theory (e.g., Mei, 1983) and stream function theory (Dean, 1965). In addition, Kaihatu (2001) and Eldeberky and Madsen (1999) improved the models by introducing the second-order relationship between amplitudes of wave potential and those of free surface elevation in the dynamic free surface

boundary condition. To investigate the effect of second-order correction, the relationship between amplitudes of ϕ and η was used (Kaihatu, 2001):

$$\eta = \sum_{n=1}^{N} \frac{B_n}{2} e^{i\left[\int k_n(x,y)dx - \omega_n t\right]} + \text{C.C.} \tag{2.83}$$

where B_n denotes amplitude of η, and C.C. denotes conjugate complex.

$$B_n = A_n + \frac{1}{4g}\left[\sum_{l=1}^{n-1} IA_l A_{n-l} e^{i\int (\bar{k}_l + \bar{k}_{n-l} - \bar{k}_n)dx} + 2\sum_{l=1}^{N-n} JA_l^* A_{n+l} e^{i\int (\bar{k}_{n+l} - \bar{k}_l - \bar{k}_n)dx}\right] \tag{2.84}$$

where

$$I = \omega_l^{\,2} + \omega_l \omega_{n-l} + \omega_{n-l}^{\,2} - g^2 \frac{k_l k_{n-l}}{\omega_l \omega_{n-l}} \tag{2.85}$$

$$J = \omega_l^{\,2} - \omega_l \omega_{n+l} + \omega_{n+l}^{\,2} - g^2 \frac{k_l k_{n+l}}{\omega_l \omega_{n+l}} \tag{2.86}$$

Following Kaihatu (2001), a redefined velocity potential and free-surface elevation are used:

$$\phi = \sum_{n=1}^{N} \frac{-ig}{2\omega_n} \tilde{a}_n f_n(z) e^{i\left[\int n(k_1 + \tilde{k})dx - \omega_n t\right]} + \text{C.C.} \tag{2.87}$$

$$\eta = \sum_{n=1}^{N} \frac{\tilde{b}_n}{2} e^{i\left[\int n(k_1 + \tilde{k})dx - \omega_n t\right]} + \text{C.C.} \tag{2.88}$$

where k_1 is wave number of the first frequency mode, and $\tilde{k}$ is the difference between the linear wave number and non-dispersive wave number. Full details of the method can be found in Kaihatu (2001).

Assuming no change in energy flux, one-dimensional permanent form solutions for model of Kaihatu and Kirby (1995) were proposed (Kaihatu, 2001):

$$\left[n\left(k_1+\tilde{k}\right)-k_n \right]\tilde{a}_n+\frac{1}{8\left(\omega C_g\right)_n}\left[\sum_{l=1}^{n-1} R_1\tilde{a}_l\tilde{a}_{n-l}+2\sum_{l=1}^{N-n} S_1\tilde{a}_l\tilde{a}_{n+l} \right]=0 \tag{2.89}$$

For the present model, we obtain one-dimensional equations for permanent solution:

$$\begin{aligned}&\left[n\left(k_1+\tilde{k}\right)-k_n \right]\tilde{a}_n+\frac{1}{8\left(\omega C_g\right)_n}\\ &\cdot\left[\begin{aligned}&\sum_{l=1}^{n-1}\left\{ R_1+R_2\left(i\left[l\left(k_1+\tilde{k}\right)-k_l \right] \right)+R_3\left(i\left[\left(n-l\right)\left(k_1+\tilde{k}\right)-k_{n-l} \right] \right) \right\}\tilde{a}_l\tilde{a}_{n-l}\\ &+2\sum_{l=1}^{N-n}\left\{ S_1+S_2\left(-i\left[l\left(k_1+\tilde{k}\right)-k_l \right] \right)+S_3\left(i\left[\left(n+l\right)\left(k_1+\tilde{k}\right)-k_{n+l} \right] \right) \right\}\tilde{a}_l\tilde{a}_{n+l}\end{aligned} \right]=0\end{aligned} \tag{2.90}$$

The specified wave height H provides an additional equation:

$$H=2\sum_{n=1,3,5}^{N}\tilde{b}_n=2\sum_{n=1,3,5}^{N}\left[\tilde{a}_n+\frac{1}{4g}\left(\sum_{l=1}^{n-1} I\tilde{a}_l\tilde{a}_{n-l}+2\sum_{l=1}^{N-n} J\tilde{a}_l\tilde{a}_{n+l} \right) \right] \tag{2.91}$$

We compare the phase speeds and free surface profiles from the permanent form solutions of Kaihatu (2001) and present model with those from the Stokes third-order theory and 15th-order stream function theory. Table 1 shows the condition used in comparison. In Figures 2-5, we see that, while both permanent form solutions perform well, the present model has a better performance than model of Kaihatu and Kirby (1995). In particular, the present model outperforms that of Kaihatu and Kirby (1995) when both are compared to phase speed estimates from Stokes third-order theory for the condition of h = 9 m and H = 3 m. There seems to be little effect of second-order correction on the phase speed and free surface profile. The better fit appears at the smaller wave height. In the regimes of deep water, and shallow water, permanent form

solutions of the present model agree favorably with those from the Stokes third-order theory, and 15th-order stream function theory, respectively.

Table 1 Conditions for permanent form solution.

Theory	Comparison	T (s)	N	h (m)	H (m)
Stokes third-order	Phase speed	5	10	20-9	0.5, 1.0, 2.0, 3.0
	Free surface	5	10	20, 9	3
Stream function	Phase speed	10	15	10-1	0.1
	Free surface	10	15	10,1	0.1

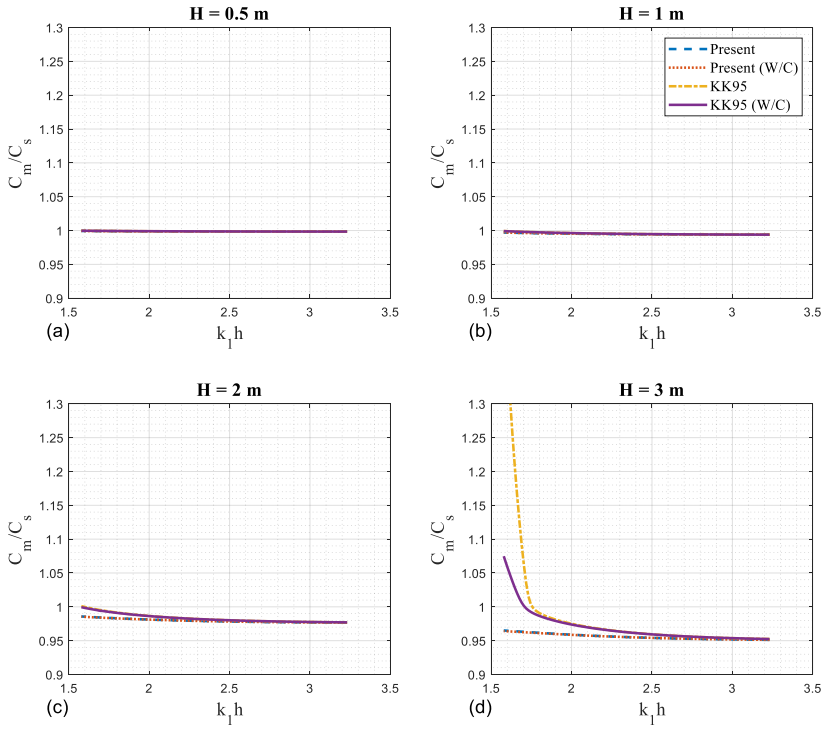

Figure 2 Comparison of phase speed between permanent-form solutions and third-order Stokes theory: (a) *H* = 0.5 m; (b) *H* = 1 m; (c) *H* = 2 m; (d) *H* = 3 m (Dashed: present model; Dotted: present model with second-order correction; Dash-dot: model of Kaihatu and Kirby (1995); Solid: model of Kaihatu and Kirby (1995) with second-order correction).

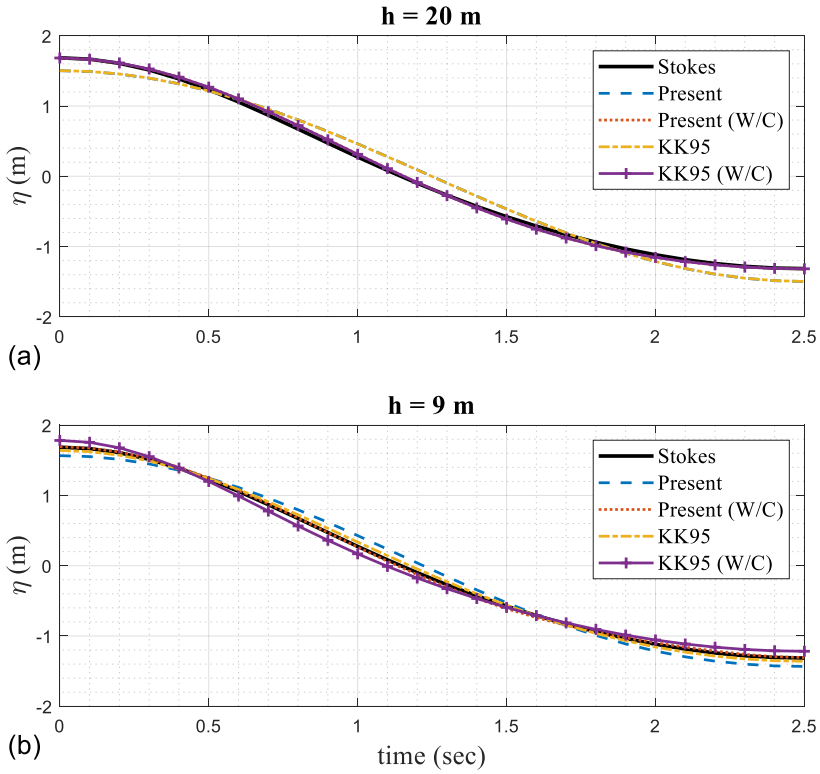

Figure 3 Comparison of free surface profiles between permanent-form solutions and third-order Stokes theory: (a) *h* = 20 m; (b) *h* = 9 m (Solid: third-order Stokes theory; Dashed: present model; Dotted: present model with second-order correction; Dash-dot: model of Kaihatu and Kirby (1995); Dash-cross: model of Kaihatu and Kirby (1995) with second-order correction).

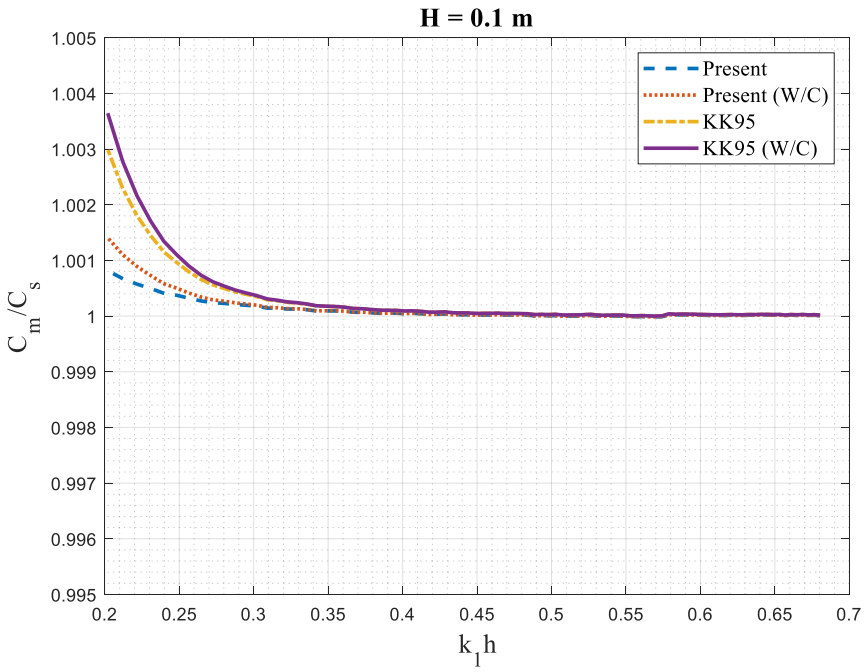

Figure 4 Comparison of phase speed between permanent-form solutions and 15th-order stream function theory (Dashed: present model without second-order correction; Dotted: present model; Dash-dot: model of Kaihatu and Kirby (1995); Solid: model of Kaihatu and Kirby (1995) with second-order correction).

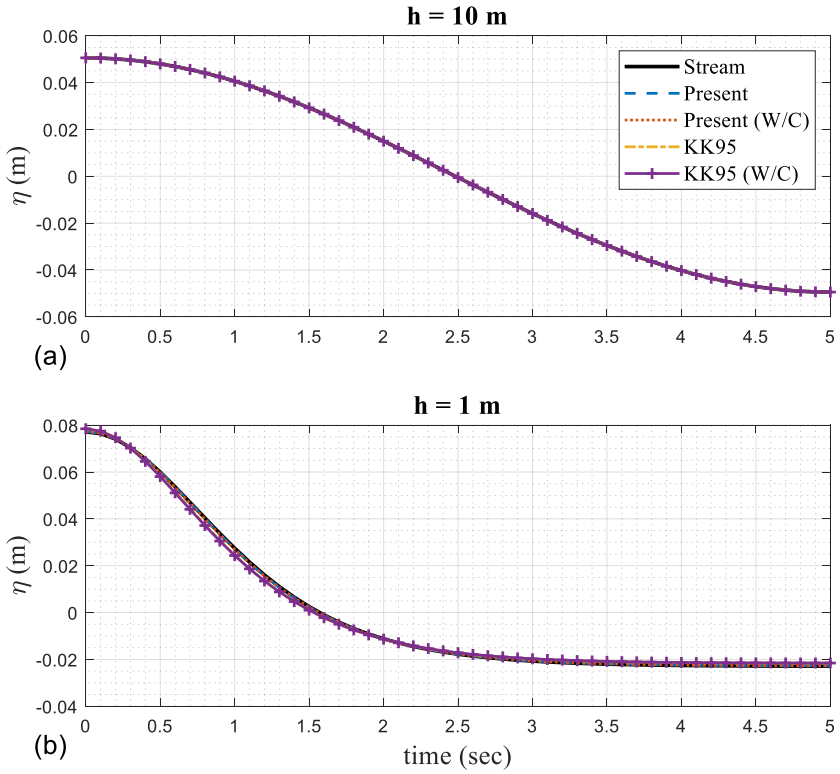

Figure 5 Comparison of free surface profiles between permanent-form solutions and 15th-order stream function theory: (a) *h* = 10 m; (b) *h* = 1 m (Solid: stream function theory; Dashed: present model; Dotted: present model with second-order correction; Dash-dot: model of Kaihatu and Kirby (1995); Dash-cross: model of Kaihatu and Kirby (1995) with second-order correction).

CHAPTER III

COMPARISON TO DATA: FINITE NUMBER OF WAVES*

3.1 Introduction

We compare numerical results from the present model to both experimental data and previous models. The Crank-Nicolson method (Crank and Nicholson, 1947) was adopted to model the two-dimensional parabolic Equation (2.59). The implementation of the method is similar to that of Liu et al. (1985). We use the notation that $[a_{n,j}^{i}]^{k}$ represents the nth harmonic function at x (= $i\Delta x$, i = 1 to N_x) and y (= $j\,\Delta y$, j = 1 to N_y). Because the nonlinear terms need to be centered between i and $i+1$, iteration is required. This was performed as follows:

$$\left[a_{l,j}^{i+1}a_{n-l.j}^{i+1}\right]^{k+1}=\begin{cases}a_{l,j}^{i}a_{n-l.j}^{i} & ;k=0\\ \left[a_{l,j}^{i+1}\right]^{k}\left[a_{n-l.j}^{i+1}\right]^{k} & ;k\geq 1\end{cases} \tag{3.1}$$

where the superscripts $k+1$ and k are the current and previous iterations, respectively. The initial guess (i.e., $k = 0$) are obtained from the previous x-level solutions. The iteration procedure is stopped and converged solutions are calculated when the relative error between two successive iteration solutions is less than 10^{-3}:

$$\frac{\left|\left(a_{n,j}^{i+1}\right)^{k+1}-\left(a_{n,j}^{i+1}\right)^{k}\right|}{\left|\left(a_{n,j}^{i+1}\right)^{k}\right|}<10^{-3} \tag{3.2}$$

* This chapter is reprinted with permission from Kim, I. C. and Kaihatu, J. M., 2021. A consistent nonlinear mild-slope equation model. Coastal Engineering, 170: 104006. Copyright [2021] by Elsevier. DOI: https://doi.org/10.1016/j.coastaleng.2021.104006.

For cases where a sine wave was specified at the offshore boundary, the amplitude for the first harmonic was prescribed with the recorded input values at the wave maker station for each experiment, and the initial conditions for higher harmonic waves are set to zero.

A grid convergence procedure was followed, in which the grid size is continually reduced until further reduction does not make any difference in results. Table 2 shows grid sizes and the number of grids used for computation of each experiment in this study.

Table 2 Grid sizes and the total number of grids for computation of each experiment.

Data	Chaplain et al. (1992)	Whalin (1971)	Berkhoff et al. (1982)
Δx (m)	0.094	0.24	0.083
Δy (m)	-	0.085	0.083
Grids	250	100×74	261×243

To quantitatively examine the performance of the models, we used the IOA (Index of Agreement) representing the ratio of mean square error and the potential error (Willmott, 1982). The IOA ranges from 0 to 1, with 1 corresponding to the ideal model:

$$I_a = 1 - \frac{\sum_{j=1}^{N_y}\sum_{i=1}^{N_x}\left(a_{n,j}^{i} - a_{n.j,obs}^{i}\right)^2}{\sum_{j=1}^{N_y}\sum_{i=1}^{N_x}\left[\left|a_{n,j}^{i} - \bar{a}_{n.j,obs}^{i}\right| + \left|a_{n,j,obs}^{i} - \bar{a}_{n.j,obs}^{i}\right|\right]^2} \tag{3.3}$$

where $a^i_{n,j}$ is the computed *n*th harmonic function from models at x (= $i\Delta x$, $i = 1 - N_x$) and y (= $j\Delta y$, $j = 1 - N_x$), and $a^i_{n,j,obs}$ is the observed *n*th harmonic function from experimental data at x (= $i\Delta x$) and y (= $j\Delta y$), and over bar indicates an average.

3.2 Chapalain et al. (1992)

Chapalain et al. (1992) conducted a laboratory experiment to model the transformation of long, small-amplitude waves in constant depth. The primary goal of this experiment was to investigate the energy transfer between a small number of harmonic components due to nonlinear interactions. The experiment was conducted in a wave flume that was 33.54 meters long and 1.3 meters deep. A wavemaker at the end of the flume generated monochromatic sinusoidal waves, which were allowed to evolve over the flat bottom. Regularly spaced wave gauges in the tank were used to record time series of the free surface elevation, and the resulting records were analyzed to determine the amplitudes of each harmonic. The experiment captured the phenomenon of recurrence, in which energy flowing from low frequencies to higher ones reversed this transfer to recapture the initial state. This phenomenon was first seen in water waves in the experiments of Boczar-Karakiewicz (1972); Mei and Ünlüata (1972) analyzed this phenomenon using shallow water wave theory. Table 3 shows the wave parameters, the number of harmonics, and the nonlinearity parameters calculated for this experiment. We used $N = 5$ harmonics for all cases, but the first four harmonics are compared with that of the experimental data.

Table 3 Wave parameters of Chapalain et al. (1992), and the nonlinearity parameters.

Case	a_0 (m)	T (s)	h (m)	kh	Ur
A	0.042	2.5	0.4	0.530	0.373
C	0.042	3.5	0.4	0.371	0.764
D	0.0355	2.5	0.3	0.454	0.574
H	0.035	3	0.4	0.436	0.460

Figures 6-7 compare the numerical results for each case obtained by the models of Kaihatu and Kirby (1995) (hereinafter KK95 in figures and tables), Freilich and Guza (1984) (hereinafter FG84 in figures and tables), and the present model (both with and without the second-order correction) with the experimental data of Chapalain et al. (1992). For unidirectional wave, the Kadomtsev-Petviashvili (K-P) model of Liu et al. (1985) (hereinafter KP85 in figures and tables) is reduced to that of Freilich and Guza (1984), and the model of Tang and Ouellet (1997) (hereinafter TO97 in figures and tables) is also reduced to that of Kaihatu and Kirby (1995); thus, these other models are implicitly included. The agreement between experimental data and numerical solution of the present model is reasonable. The first-, second-, and third-harmonic wave amplitudes are in good agreement with experimental data, but the numerical model underestimates the fourth-harmonic component. For the first-, second-, and third-harmonic, the present model mostly outperforms the previous models in terms of the amplitudes and the recurrence distances, with the exception that Freilich and Guza (1984) is in closer agreement in Case C, where *kh* is small. For the fourth-harmonic, on the other hand,

Kaihatu and Kirby (1995) agrees more favorably in most of the comparisons. The inclusion of the second-order correction with Equation (2.84) increases the amplitude, leading to better agreement for the fourth harmonic. Since there is no bottom variation in this experiment, $A_x A$ are the only terms of present model that are additional to that of Kaihatu and Kirby (1995). As seen in Section 2.3.3, these added terms contribute to additional nonlinear effect despite the explicit use of the fully-dispersive linear theory.

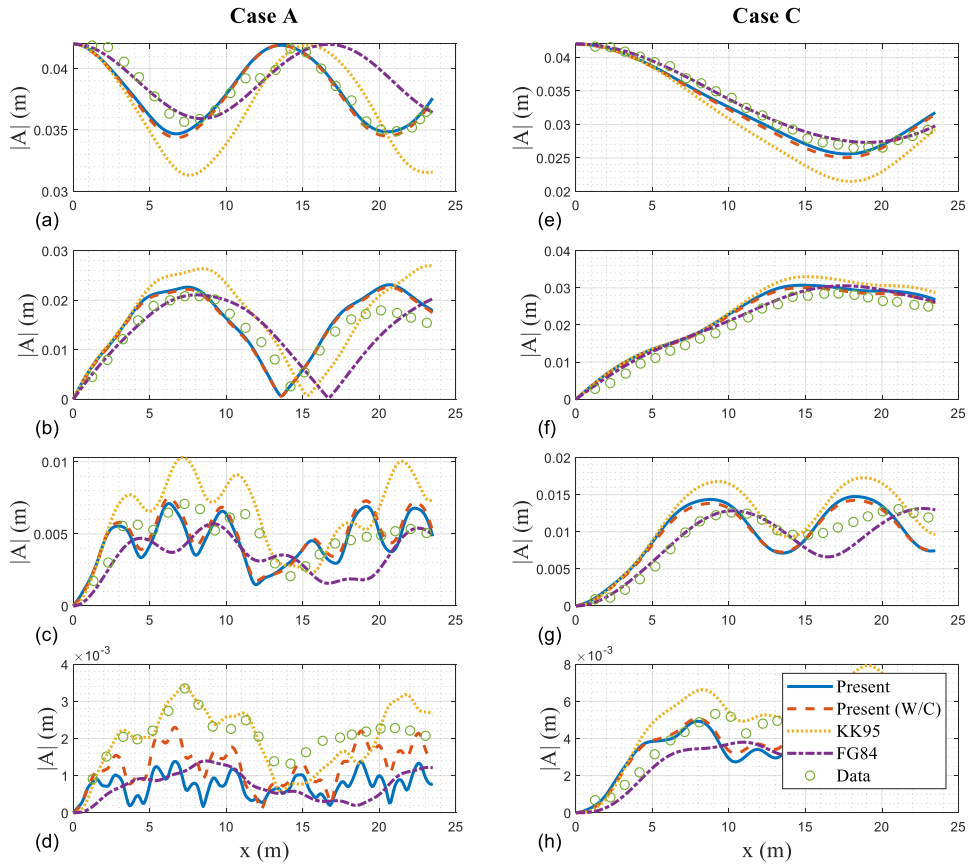

Figure 6 Comparison of wave amplitudes between models and data of Chapalain et al. (1992) for Case A: (a) first harmonic; (b) second harmonic; (c) third harmonic; (d) fourth harmonic; for Case C: (e) first harmonic; (f) second harmonic; (g) third harmonic; (h) fourth harmonic (Solid: present model; Dashed: present model with second-order correction; Dotted: model of Kaihatu and Kirby (1995); Dash-dot: model of Freilich and Guza (1984); Circle: experimental data).

Table 4 Comparison of IOA between models for Case A and C of Chapalain et al. (1992).

Case	Harmonics	Present	Present with correction	KK95	FG84
A	1	0.9475	0.9408	0.7848	0.7563
	2	0.9344	0.9399	0.8466	0.8067
	3	0.6678	0.7081	0.7448	0.6595
	4	0.3286	0.4840	0.8706	0.3804
C	1	0.9900	0.9850	0.9365	0.9980
	2	0.9734	0.9811	0.9529	0.9873
	3	0.8691	0.8856	0.8522	0.9606
	4	0.8505	0.8968	0.8889	0.8230

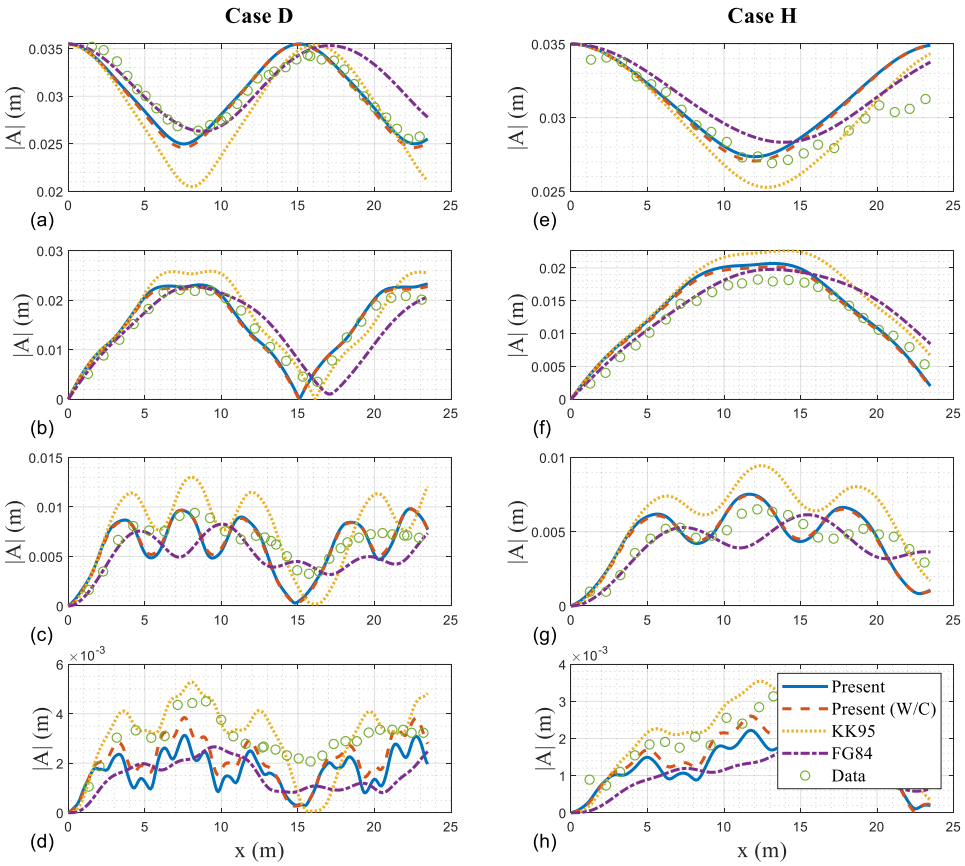

Figure 7 Comparison of wave amplitudes between models and data of Chapalain et al. (1992) for Case D: (a) first harmonic; (b) second harmonic; (c) third harmonic; (d) fourth harmonic; for Case H: (e) first harmonic; (f) second harmonic; (g) third harmonic; (h) fourth harmonic (Solid: present model; Dashed: present model with second-order correction; Dotted: model of Kaihatu and Kirby (1995); Dash-dot: model of Freilich and Guza (1984); Circle: experimental data).

Table 5 Comparison of IOA between models for Case D and H of Chapalain et al. (1992).

Case	Harmonics	Present	Present with correction	KK95	FG84
D	1	0.9667	0.9598	0.8759	0.8761
	2	0.9776	0.9793	0.9536	0.9077
	3	0.7547	0.7704	0.7745	0.7214
	4	0.4679	0.6233	0.7757	0.4787
H	1	0.8711	0.8787	0.9342	0.9228
	2	0.9602	0.9684	0.9026	0.9504
	3	0.8237	0.8387	0.7541	0.8720
	4	0.6101	0.7451	0.9009	0.6120

3.3 Whalin (1971)

Whalin (1971) carried out a laboratory experiment to investigate wave convergence and wave refraction over a varying bottom, shown in Figure 8. The bottom configuration consists of two regions of constant depth connected with a tilted cylinder; the cylinder acts as a refractive focal lens, and the amplified wave amplitude at the focus point expected to lead to energy transfer among wave frequencies. In Table 6, we summarize wave parameters, the number of harmonics, and the nonlinearity parameters calculated for this experiment. The values with subscripts 1 and 2 in Table 6 refer to the deep and shallow portion of the tank, respectively (h_1 = 0.457 m, h_2 = 0.152 m). The reflective lateral boundary conditions are used along the side-wall and the centerline of the wave tank:

$$\frac{\partial a}{\partial y} = 0 \quad \text{at } y = 0 \text{ and } 3.048 \text{ m} \tag{3.4}$$

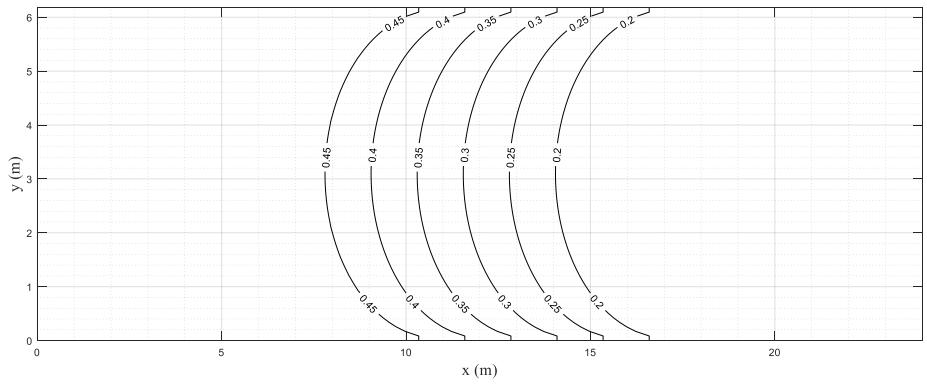

Figure 8 Wave tank bathymetry of Whalin (1971).

Table 6 Wave parameters of Whalin (1971), the number of harmonics, and the nonlinearity parameters.

Case	a_0 (m)	T (s)	N	k_1h_1	k_2h_2	Ur_1	Ur_2
31	0.0068	3	5	0.468	0.264	0.068	0.640
32	0.0098	3	5	0.468	0.264	0.098	0.922
33	0.0146	3	5	0.468	0.264	0.146	1.373
21	0.0075	2	3	0.735	0.402	0.030	0.305
22	0.0106	2	3	0.735	0.402	0.043	0.431
23	0.0149	2	3	0.735	0.402	0.060	0.605
11	0.0097	1	2	1.921	0.873	0.006	0.084
12	0.0195	1	2	1.921	0.873	0.012	0.168

Figures 9-12 show wave amplitudes along the centerline of the wave tank for each case, comparing the values obtained by the models of Kaihatu and Kirby (1995), Tang and Ouellet (1997), the K-P model of Liu et al. (1985), and the present model with the experimental data of Whalin (1971). Since the case of T = 1 s shows obvious differences after incorporation of second-order correction (Equation 2.84) only for the case of T = 1 s, Figure 12 compares results with the second-order correction by model of Kaihatu and Kirby (1995), and the present model. We note that the case of T = 1 s was obviously outside the range of validity for Boussinesq so that we do not compare the K-P model of Liu et al. (1985) for the case of T = 1 s.

For the case of T = 3 s, no model shows a good agreement with first harmonic amplitudes, while the second- and third-harmonic amplitudes are well predicted by all the models. Frictional dissipation of the waves could partially cause this deviation at first

harmonic amplitudes (Liu et al, 1985). None of the models discussed here include the effect of viscous damping in the boundary conditions, while there was a very small amount of wave damping from the viscous boundary layers in wave tank (Whalin, 1971). The present model uniformly overpredicts the first harmonic wave amplitudes, and underpredicts the third harmonic wave amplitudes; this behavior is also seen with the other models in this comparison.

For the case of T = 2 s, the amplitudes predicted by all nonlinear parabolic mild-slope equation models are nearly identical. For the cases of T = 1 s and 2 s, where the shallow water assumption might not be applicable, the results of the K-P model (Liu et al., 1985) show significant discrepancy between theory and experiment. As the initial amplitude a_0 decreases, the performance of the present model improves. In particular, the present model appears to outperform the other models for the cases of the smallest amplitude from T = 1, 2 s (i.e., Case 11 and 21). For example, the value of a_0 in Case 21 is the smallest than that of the other cases of T = 2 s, therefore, Case 21 has the smallest value of Ur, which might support the ordering of present study rather than that of Boussinesq-type model, based on $O(Ur) \sim O(1)$.

Kaihatu and Kirby (1995) argued that case of T = 1 s is a severe test of their model due to the great value of kh (i.e., k_1h_1 = 1.921 at the wave maker corresponds to intermediate depth), causing considerable phase mismatches and severe amplitude change oscillation with increasing grid size. However, the present model shows better accuracy in case of T = 1 s, which could imply that the effect of phase mismatches is alleviated by x-derivative nonlinear terms A_xA. From Figure 12 (T = 1 s), we note that

the present model is generally in agreement with oscillating second harmonic amplitude. These oscillations in amplitude occur with wave propagating in *x*-direction; the amplitudes in nonlinear terms are thus variable in *x* and the cause for the oscillations in *A*. This is in contrast with the situation described in Figure 1, where the oscillation is directly related to the grid size rather than the wave amplitude propagation characteristics. As explained in comparisons with model of Kaihatu and Kirby (1995) of Section 2.3, the exponential function multiplied by A_x on the right-hand side of Equation (2.48), might alleviate the effect of phase mismatch, as it serves as an oscillating coefficient.

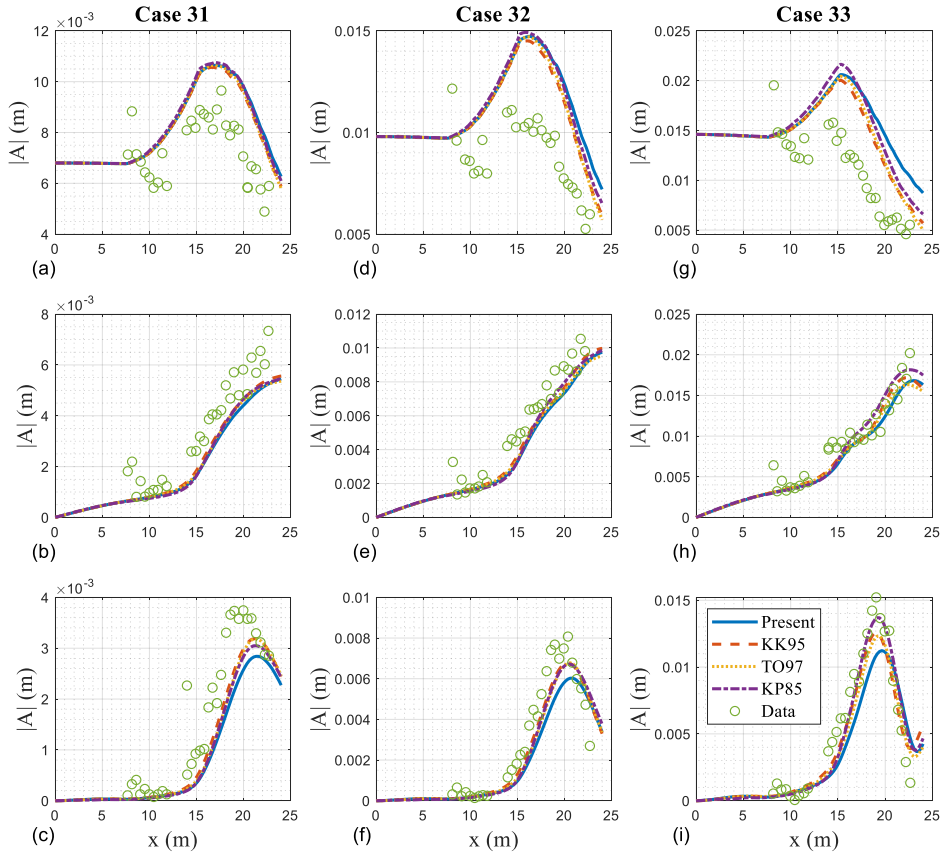

Figure 9 Comparison of wave amplitudes between models and data of Whalin (1971) for Case 31: (a) first harmonic; (b) second harmonic; (c) third harmonic; for Case 32: (d) first harmonic; (e) second harmonic; (f) third harmonic; for Case 33: (g) first harmonic; (h) second harmonic; (i) third harmonic (Solid: present model; Dashed: model of Kaihatu and Kirby (1995); Dotted: model of Tang and Ouellet; Dash-dot: K-P model of Liu et al. (1985); Circle: experimental data).

Table 7 Comparison of IOA between models for T = 3 s of Whalin (1971).

Case	Harmonics	Present	KK95	TO97	KP85
31	1	0.6077	0.6375	0.6330	0.6120
	2	0.9168	0.9389	0.9280	0.9298
	3	0.8905	0.9376	0.9251	0.9179
32	1	0.4944	0.5771	0.5659	0.5213
	2	0.9551	0.9712	0.9629	0.9692
	3	0.9316	0.9727	0.9621	0.9622
33	1	0.5217	0.6917	0.6676	0.5994
	2	0.9633	0.9725	0.9672	0.9664
	3	0.9304	0.9794	0.9718	0.9799

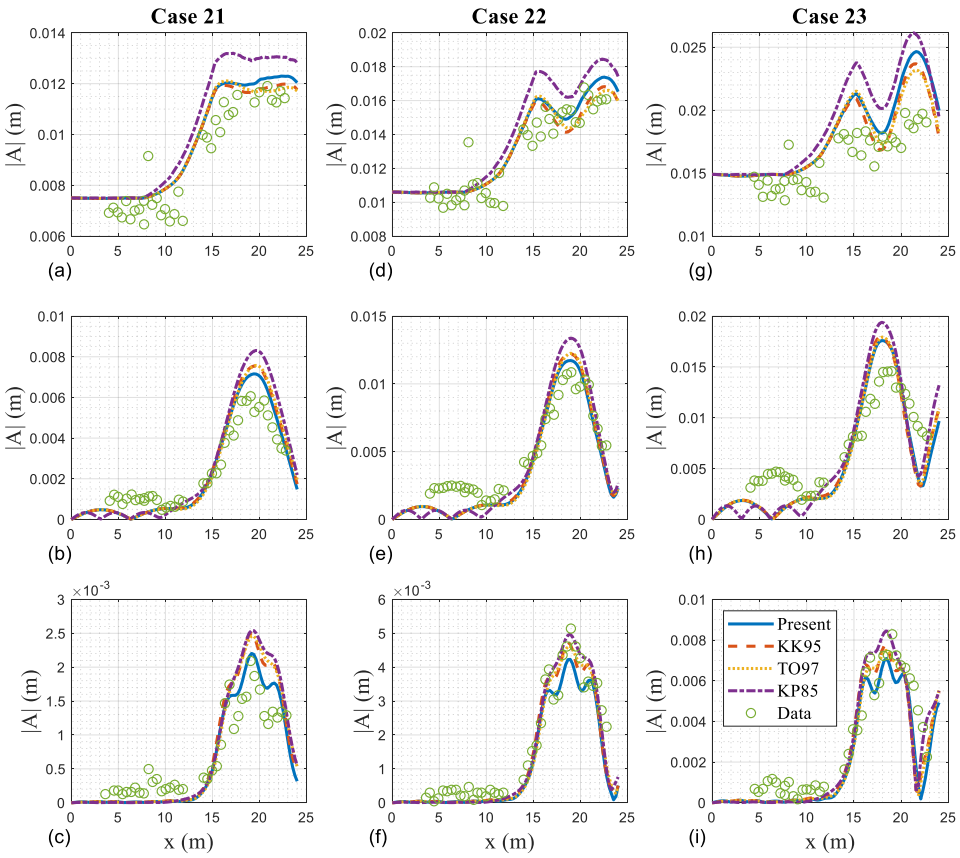

Figure 10 Comparison of wave amplitudes between models and data of Whalin (1971) for Case 21: (a) first harmonic; (b) second harmonic; (c) third harmonic; for Case 22: (d) first harmonic; (e) second harmonic; (f) third harmonic; for Case 23: (g) first harmonic; (h) second harmonic; (i) third harmonic (Solid: present model; Dashed: model of Kaihatu and Kirby (1995); Dotted: model of Tang and Ouellet; Dash-dot: K-P model of Liu et al. (1985); Circle: experimental data).

Table 8 Comparison of IOA between models for T = 2 s of Whalin (1971).

Case	Harmonics	Present	KK95	TO97	KP85
21	1	0.9460	0.9493	0.9461	0.8909
	2	0.9653	0.9534	0.9543	0.9263
	3	0.9639	0.9320	0.9310	0.9189
22	1	0.9519	0.9516	0.9481	0.8932
	2	0.9660	0.9629	0.9656	0.9534
	3	0.9789	0.9845	0.9861	0.9851
23	1	0.7601	0.7976	0.7951	0.6538
	2	0.9168	0.9077	0.9151	0.9034
	3	0.9530	0.9531	0.9566	0.9548

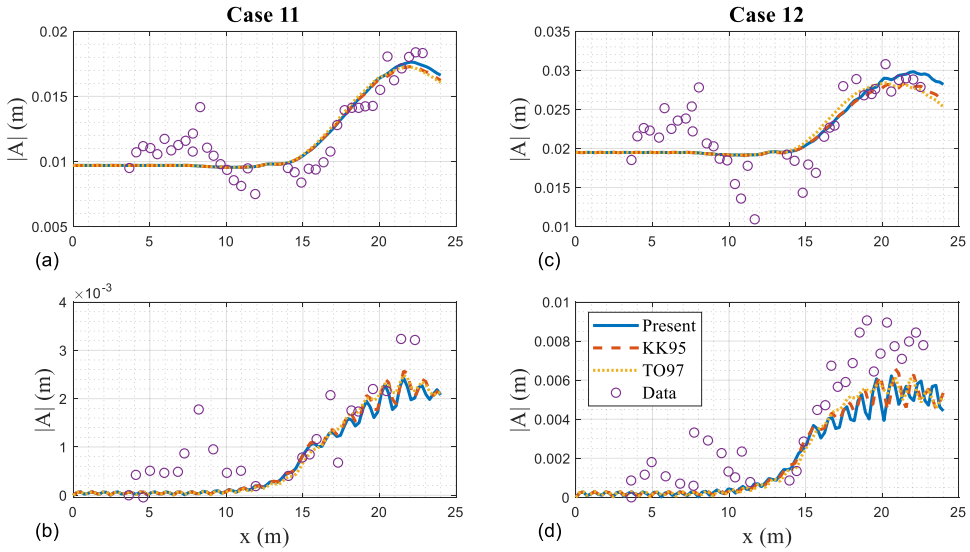

Figure 11 Comparison of wave amplitudes between models and data of Whalin (1971) for Case 11: (a) first harmonic; (b) second harmonic; for Case 12: (c) first harmonic; (d) second harmonic (Solid: present model; Dashed: model of Kaihatu and Kirby (1995); Dotted: model of Tang and Ouellet; Circle: experimental data).

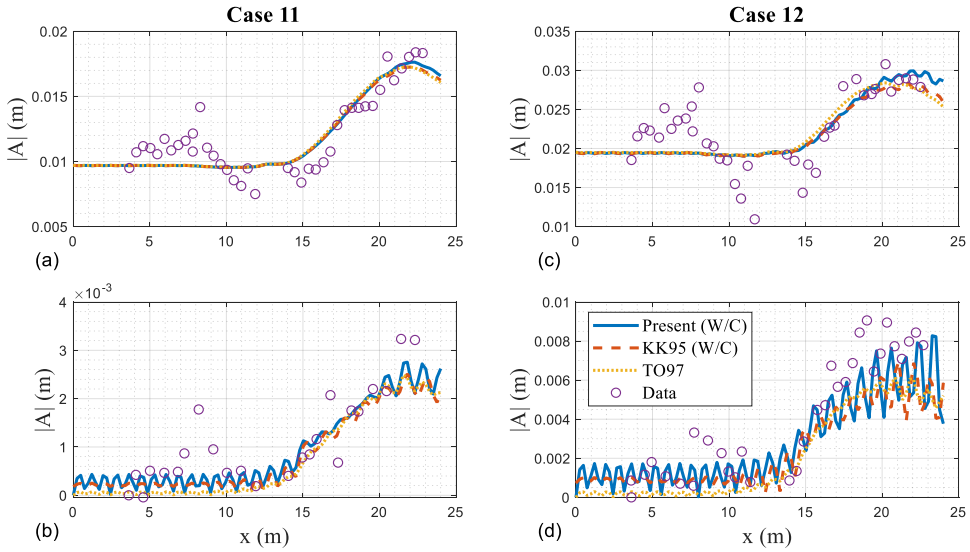

Figure 12 Comparison of wave amplitudes between models and data of Whalin (1971) for Case 11: (a) first harmonic; (b) second harmonic; for Case 12: (c) first harmonic; (d) second harmonic (Solid: present model with second-order correction; Dashed: model of Kaihatu and Kirby (1995) with second-order correction; Dotted: model of Tang and Ouellet; Circle: experimental data).

Table 9 Comparison of IOA between models for T = 1 s of Whalin (1971).

Case	Harmonics	Present	Present (W/C)	KK95	KK95 (W/C)	TO97
11	1	0.9418	0.9417	0.9387	0.9387	0.9360
	2	0.8688	0.8834	0.8768	0.8795	0.8834
12	1	0.8455	0.8458	0.8320	0.8315	0.8316
	2	0.8507	0.9032	0.8751	0.8734	0.8908

3.4 Berkhoff et al. (1982)

Berkhoff et al. (1982) conducted a laboratory experiment over a varying bottom with elliptic shoal situated on a 1:50 slope, shown in Figure 13, to investigate the behavior of wave focusing by a submerged shoal. Unlike the experiment of Whalin (1971), wave propagation in this experiment would be adequately described with a linear wave model (e.g., Berkhoff et al., 1982). However, it has been shown (e.g., Kirby and Dalrymple, 1984; Suh et al., 1990; Wei and Kirby, 1995) that wave propagation processes in this experiment are better replicated by a nonlinear wave model.

We ran parabolic linear mild-slope equation (linearized form of Equation 2.48), Kaihatu and Kirby (1995), Tang and Ouellet (1997), and the present model against the data of Berkhoff et al. (1982). Table 10 shows the wave parameters, the number of harmonics, and the nonlinearity parameters calculated for this experiment. The values with subscripts 1 and 2 are the values corresponding to the initial condition and the values at the shoal crest, respectively (h_1 = 0.45 m, h_2 = 0.128 m). At the wave maker station, a sinusoidal wave was input to the model and the value of kh = 1.895 would likely lead to appreciable phase mismatch. We used N = 2 harmonics, but the first harmonics were used to obtain relative amplitudes and the relative amplitudes are compared with the results of the experimental data. To investigate the effect of phase mismatch in the present model, we used N = 3 as well. For frequency domain mild-slope equations, increasing N results in more nonlinear terms with phase mismatch. Therefore, when N = 3 is used, frequency domain mild-slope equations can be expected to show more obvious discrepancy between numerical and experimental results. The sum of odd

number harmonics was used in calculating relative amplitude (i.e., $a_1 + a_3$) for $N = 3$. We apply reflective lateral boundaries; however, the width of the numerical model grid is wide enough so that sidewall reflections do not affect the wave processes near the shoal. These lateral boundary conditions are:

$$\frac{\partial a}{\partial y} = 0 \quad \text{at } y = 0 \text{ and } 20 \text{ m} \tag{3.5}$$

Table 10 Wave parameters of Berkhoff et al. (1982), the number of harmonics, and the nonlinearity parameters.

a_0 (m)	h_1 (m)	h_2 (m)	T (s)	N	kh_1	kh_2	Ur_1	Ur_2
0.0232	0.45	0.128	1	2, 3	1.895	0.788	0.014	0.292

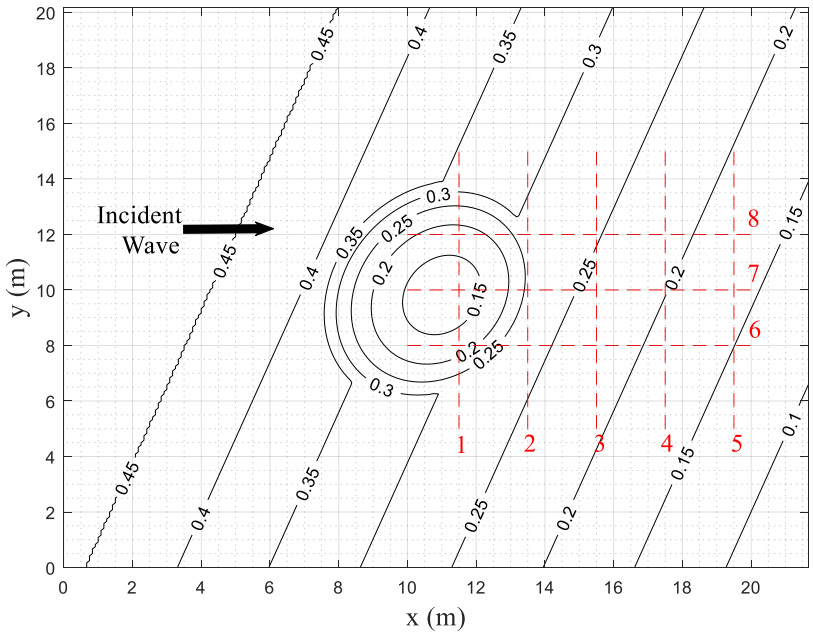

Figure 13 Bathymetry and gauge Layout of Berkhoff et al. (1982) (Dashed: gauge transects).

Figure 14 show the results of the models using $N = 2$ (for nonlinear models) at the gauge locations. Although the high kh value would lead to appreciable mismatch, all mild-slope equations models, including our model, agree favorably with the experimental data. This can be interpreted as a result of few nonlinear terms and the use of fundamental harmonics only, because $N = 2$ was used. Comparison of the IOA values at gauge transect 3-6 (Tables 11 and 12) show that the present model outperforms the other models used. This is likely due to the additional AA_x and A_yA_y terms in Equation (2.48). While the linear model used here shows reasonable results at gauge transect 1, its performance worsens at succeeding gauges. Berkhoff et al. (1982) noted that gauge transect 6 is near an amphidromic point; this is also where the present model performs particularly well, capturing the reduction in amplitude seen in the data far better than other models.

The results using $N = 3$, shown in Figure 15, validates the hypothesis that the predictions of Kaihatu and Kirby (1995) and Tang and Ouellet (1997) become worse than the results of $N = 2$. The results of present model, on the other hand, shows better prediction at several gauges. This result is a manifestation of the ability of the model to alleviate phase mismatches, as discussed earlier. The present model shows notably better prediction skill at several gauges. Additionally, there are no obvious improvements using the second-order correction with Equation (2.84).

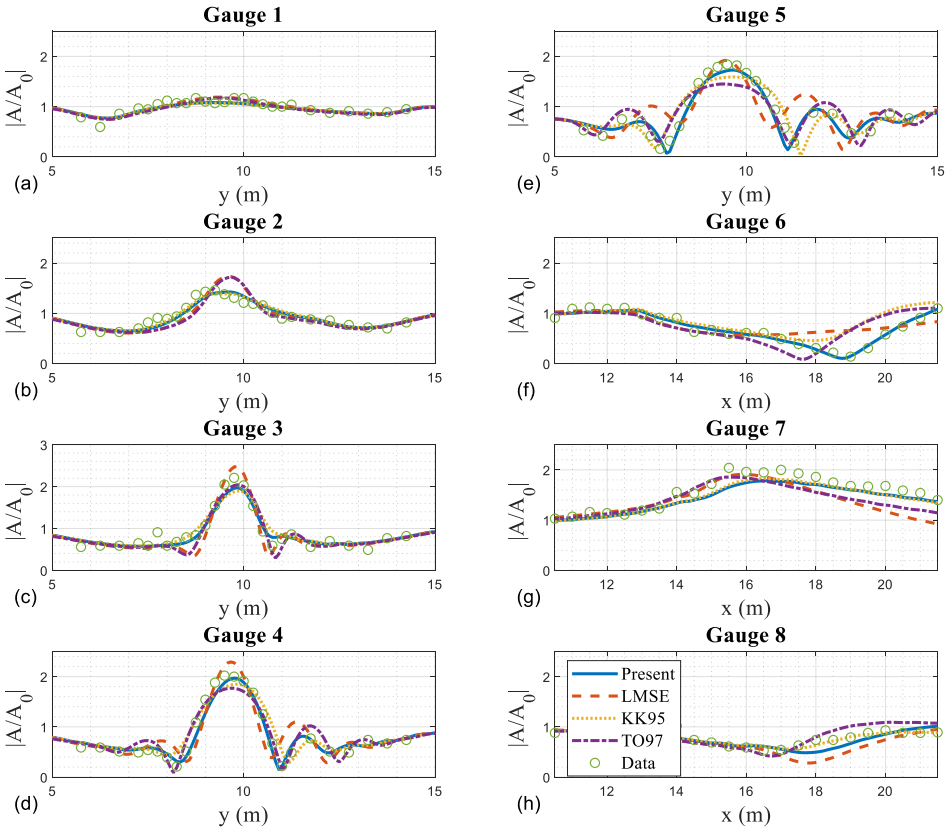

Figure 14 Comparison of normalized wave amplitudes between models and data of Berkhoff et al. (1982) for *N* = 2: (a) gauge 1; (b) gauge 2; (c) gauge 3; (d) gauge 4; (e) gauge 5; (f) gauge 6; (g) gauge 7; (h) gauge 8 (Solid: present model; Dashed: Linearized mild-slope equation; Dotted: model of Kaihatu and Kirby (1995); Dash-dot: model of Tang and Ouellet (1997); Circle: experimental data).

Table 11 Comparison of IOA between models at 1-8 Gauge of Berkhoff et al. (1982) for $N = 2$.

Gauge	Present	LMSE	KK95	TO97
1	0.9127	0.9416	0.9036	0.9312
2	0.9726	0.9200	0.9767	0.9083
3	0.9801	0.9701	0.9665	0.9728
4	0.9877	0.9427	0.9769	0.9833
5	0.9789	0.8476	0.9583	0.9445
6	0.9910	0.8082	0.8151	0.8377
7	0.9304	0.8205	0.9452	0.8703
8	0.8694	0.7353	0.9388	0.8448

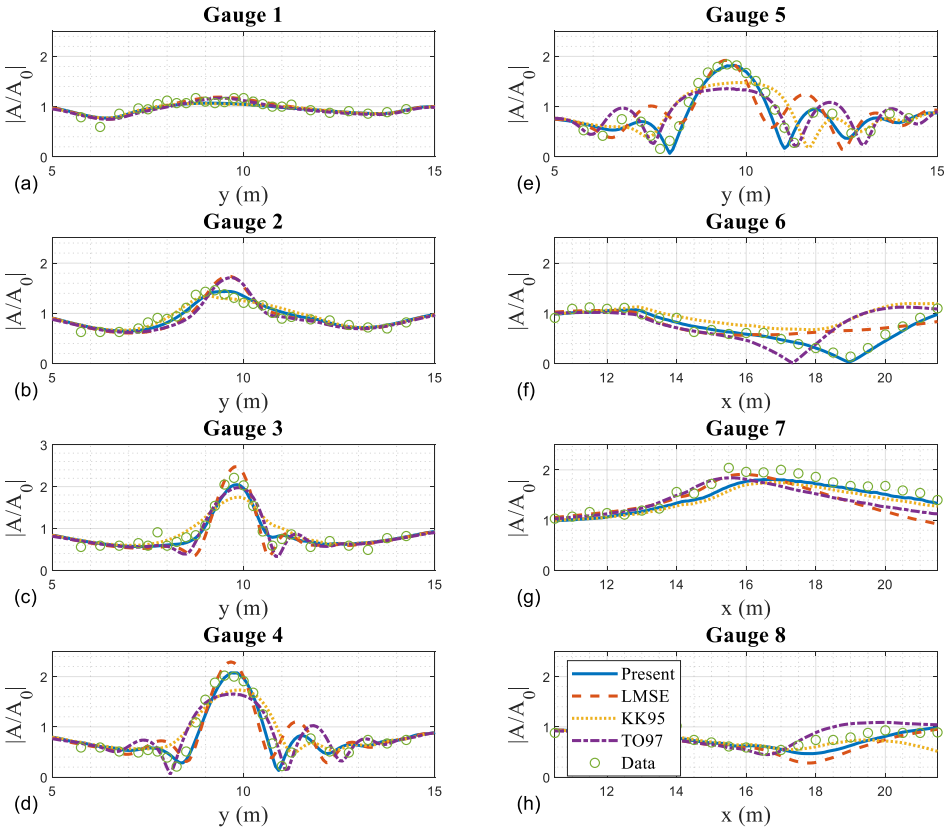

Figure 15 Comparison of normalized wave amplitudes between models and data of Berkhoff et al. (1982) for *N* = 3: (a) gauge 1; (b) gauge 2; (c) gauge 3; (d) gauge 4; (e) gauge 5; (f) gauge 6; (g) gauge 7; (h) gauge 8 (Solid: present model; Dashed: Linearized mild-slope equation; Dotted: model of Kaihatu and Kirby (1995); Dash-dot: model of Tang and Ouellet (1997); Circle: experimental data).

Table 12 Comparison of IOA between models at 1-8 Gauge of Berkhoff et al. (1982) for $N = 3$.

Gauge	Present	LMSE	KK95	TO97
1	0.9043	0.9416	0.9062	0.9332
2	0.9735	0.9200	0.9706	0.9099
3	0.9838	0.9701	0.9348	0.9686
4	0.9838	0.9427	0.9399	0.9623
5	0.9682	0.8476	0.8696	0.8965
6	0.9862	0.8082	0.6498	0.7241
7	0.9397	0.8205	0.8846	0.8405
8	0.8461	0.7353	0.7488	0.8166

CHAPTER IV

HYBRID CONSISTENT NONLINEAR MILD-SLOPE EQUATION MODEL

4.1 Introduction

In a realistic surface wave environment, the wavefield is represented by random waves, a superposition of a number of sinusoidal waves with their own phases and amplitudes. This is distinctly unlike the finite number of waves covered in Chapter 3, which were harmonics of a fundamental wave. The most common representation of random waves is the wave spectrum, a graphical representation of wave energy as a function of wave frequency. Noting the evolution of wave spectra provides a qualitative depiction of transferred energy between frequency components. As waves propagate into the nearshore region, triad wave-wave interactions among wave components dominate the wave evolution process. Due to this nonlinear effect becoming more apparent in shallow water, strong evolutional variability on the spectrum takes place over an extensive range of frequencies.

To predict wave spectra both in deep water and in shoaling region, two classes of models for wave propagation have been developed: as mentioned in Section 1.1, deterministic model (or phase-resolving model) simulates individual waves and the correlation between waves, which should be powerful and appealing aspect especially in shallow water where the assumption of normal distribution for wave phase is not easily able to be justified (e.g., Freilich and Guza, 1984; Madsen and Sørensen, 1993; Kaihatu and Kirby, 1995; Ardani and Kaihatu, 2019 among many others).

As an alternative, many researchers have presented stochastic evolution equations, corresponding to a phase-averaged model, to describe the variation of surface gravity wave spectrum (e.g., Agnon and Sheremet, 1997; Herbers and Burton, 1997; Kofoed-Hansen and Rasmussen, 1998; Eldeberky and Madsen, 1999; Sheremet et al, 2011; Vrecica and Toledo, 2016, 2019). These stochastic models are developed by averaging the nonlinear phase-resolved equations and then specifying a closure to truncate the system. This is different from spectral phase-averaged models such as SWAN (Booij et al. 1999), which are developed using averaged variables (e.g., spectral density) with no phase information. Most of these stochastic models consist of a coupled set of evolution equations: one equation is that of the wave power spectrum and the bispectrum derived by manipulating the deterministic formulations for the complex amplitude; the other equation involves the bispectrum and trispectrum (the next order cumulant of bispectrum). At the heart of derivation of stochastic model, there are two significant schemes as in turbulence problem: (1) a stochastic closure; (2) ensemble average. Although Gaussian Sea state where waves are statistically independent is required to apply the methods, the stochastic closure is also valid for non-Gaussian waves for weakly nonlinear waves (Benney and Saffman, 1966). Since the equations are averaged (and thus ensembles do not need to be run through the model), the stochastic models calculate wave spectrum and bispectrum with computational efficiency, which leads the stochastic model feasible and practical in relatively extensive area in time and space.

4.2 Derivation of equations

To investigate the spectral evolution of unidirectional random waves, we reduce the equations of Kaihatu and Kirby (1995) (Equation 2.63) to one dimension for variable depth:

$$A_{nx}+\frac{\left(kCC_g\right)_{nx}}{2\left(kCC_g\right)_n}A_n=-\frac{i}{8\left(kCC_g\right)_n}\left[\sum_{l=1}^{n-1}R_1A_lA_{n-l}e^{i\theta}+2\sum_{l=1}^{N-n}S_1A_l^{*}A_{n+l}e^{i\psi}\right] \tag{4.1}$$

The corresponding one-dimensional version of the present model for varying depth, equivalent to Equation (2.60), is:

$$\begin{aligned}&A_{nx}+\frac{\left(kCC_g\right)_{nx}}{2\left(kCC_g\right)_n}A_n\\&=-\frac{i}{8\left(kCC_g\right)_n}\left[\begin{array}{l}\displaystyle\sum_{l=1}^{n-1}\left[R_1A_lA_{n-l}+R_2A_{lx}A_{n-l}+R_3A_lA_{n-lx}\right]e^{i\theta}\\+2\displaystyle\sum_{l=1}^{N-n}\left[S_1A_l^{*}A_{n+l}+S_2A_{lx}^{*}A_{n+l}+S_3A_l^{*}A_{n+lx}\right]e^{i\psi}\end{array}\right]\end{aligned} \tag{4.2}$$

Equation (4.2) of the present model retains *x*-derivative of amplitude in the nonlinear terms (on the right-hand side), which the model of Kaihatu and Kirby (1995) (Equation 4.1) does not. Even though Equation (4.2) is solved for *n*th component of wave amplitude we are thus able to get *x*-derivative of amplitude for *n*th component (i.e., A_{nx}), it is also necessary to have *x*-derivative of amplitude of different components from *n*th component (i.e., A_{lx}, A_{n-lx}, A_{lx}^{*}, and A_{n+lx}), which results in higher number of iterations compared to the model of Kaihatu and Kirby (1995; Equation 4.1). Consequently, while inclusion of the term ensures the model is less affected by mismatch shown in Section 2.3.1, it could make the present model computationally

demanding, which becomes especially severe in the case of random waves and might give rise to numerical divergence problem (computational instability). Also, the *x*-derivative nonlinear term A_xA precludes use of the fourth-order Runge-Kutta method because nonlinear terms are required to be obtained to apply the method; while Kaihatu and Kirby (1995) accomplished this using adaptive stepsize schemes, this may be difficult to reliably accomplish with gradients in the nonlinear summations

For these reasons, we simplify the present model to apply for the problem where the surface gravity waves can be represented as a superposition of an arbitrary number of waves. To begin with, the interaction coefficients and the phase mismatches are modified with additional subscripts to indicate frequency modes interacting:

$$\begin{aligned} &A_{nx}+\frac{\left(kCC_g\right)_{nx}}{2\left(kCC_g\right)_n}A_n \\ &=-\frac{i}{8\left(kCC_g\right)_n}\left[\begin{array}{l}\displaystyle\sum_{l=1}^{n-1}\left[R_{1(l,n-l)}A_lA_{n-l}+R_{2(l,n-l)}A_{lx}A_{n-l}+R_{3(l,n-l)}A_lA_{n-lx}\right]e^{i\theta_{(l,n-l)}} \\ \displaystyle+2\sum_{l=1}^{N-n}\left[S_{1(l,n+l)}A_l^{*}A_{n+l}+S_{2(l,n+l)}A_{lx}^{*}A_{n+l}+S_{3(l,n+l)}A_l^{*}A_{n+lx}\right]e^{i\psi_{(l,n+l)}}\end{array}\right] \end{aligned} \tag{4.3}$$

where

$$\begin{aligned} R_{1(l,n-l)}=&\frac{g}{\omega_l\omega_{n-l}}\left[\omega_n^{\,2}k_lk_{n-l}+\left(k_l+k_{n-l}\right)\left(\omega_{n-l}k_l+\omega_lk_{n-l}\right)\omega_n\right] \\ &-\frac{\omega_n^{\,2}}{g}\left(\omega_l^{\,2}+\omega_l\omega_{n-l}+\omega_{n-l}^{\,2}\right)\end{aligned} \tag{4.4}$$

$$R_{2(l,n-l)}=-2i\frac{g\omega_n^{\,2}k_{n-l}}{\omega_l\omega_{n-l}} \tag{4.5}$$

$$R_{3(l,n-l)}=-2i\frac{g\omega_n^{\,2}k_l}{\omega_l\omega_{n-l}} \tag{4.6}$$

$$\theta_{(l,n-l)} = \int k_l + k_{n-l} - k_n dx \tag{4.7}$$

and

$$\begin{aligned} S_{1(l,n+l)} = {} & \frac{g}{\omega_l \omega_{n+l}} \left[{\omega_n}^2 k_l k_{n+l} + \left(k_{n+l} - k_l \right) \left(\omega_{n+l} k_l + \omega_l k_{n+l} \right) \omega_n \right] \\ & - \frac{{\omega_n}^2}{g} \left({\omega_l}^2 - \omega_l \omega_{n+l} + {\omega_{n+l}}^2 \right) \end{aligned} \tag{4.8}$$

$$S_{2(l,n+l)} = 2i \frac{g {\omega_n}^2 k_{n+l}}{\omega_l \omega_{n+l}} \tag{4.9}$$

$$S_{3(l,n+l)} = -2i \frac{g {\omega_n}^2 k_l}{\omega_l \omega_{n+l}} \tag{4.10}$$

$$\psi_{(l,n+l)} = \int k_{n+l} - k_l - k_n dx \tag{4.11}$$

The next step is to express A_{nx} and ${A_{nx}}^*$ up to third order in ε because x-derivative nonlinear terms $A_x A$ consist of A_x and A (where $A \sim O(\varepsilon)$), and we retain terms of $O(\varepsilon^4)$ or lower in parabolic approximation:

$$A_{nx} = -\frac{1}{2\left(kCC_g \right)_n} \left[\left(kCC_g \right)_{nx} A_n + \frac{i}{4} \left(\sum A^2 \right)_n \right] + O\left(\varepsilon^4 \right) \tag{4.12}$$

$${A_{nx}}^* = -\frac{1}{2\left(kCC_g \right)_n} \left[\left(kCC_g \right)_{nx} {A_n}^* + \frac{i}{4} \left(\sum A^2 \right)_n^* \right] + O\left(\varepsilon^4 \right) \tag{4.13}$$

where $(\Sigma A^2)_n$ denotes nonlinear summation in model of Kaihatu and Kirby (1995) shown in right-hand side of Equation (4.1) at second order in ε:

$$\left(\sum A^2 \right)_n = \left[\sum_{l=1}^{n-1} R_{1(l,n-l)} A_l A_{n-l} e^{i\theta_{(l,n-l)}} + 2 \sum_{l=1}^{N-n} S_{1(l,n+l)} {A_l}^* A_{n+l} e^{i\psi_{(l,n+l)}} \right] \tag{4.14}$$

and $(\Sigma A^2)_n{}^*$ is conjugate complex of $(\Sigma A^2)_n$:

$$\left(\sum A^2\right)_n^* = \left[\sum_{l=1}^{n-1} R_{1(l,n-l)} A_l^* A_{n-l}^* e^{-i\theta_{(l,n-l)}} + 2\sum_{l=1}^{N-n} S_{1(l,n+l)} A_l A_{n+l}^* e^{-i\psi_{(l,n+l)}}\right] \tag{4.15}$$

Substituting Equations (4.12) and (4.13) into nonlinear part of Equation (4.3) with adjusting to the frequency modes of A_x in right-hand side of Equation (4.3) (i.e., l, $n-l$, and $n+l$):

$$\begin{aligned}
&A_{nx} + \frac{\left(kCC_g\right)_{nx}}{2\left(kCC_g\right)_n} A_n \\
&= -\frac{i}{8\left(kCC_g\right)_n}\left[\sum_{l=1}^{n-1} R_{1(l,n-l)} A_l A_{n-l} e^{i\theta_{(l,n-l)}} + 2\sum_{l=1}^{N-n} S_{1(l,n+l)} A_l^* A_{n+l} e^{i\psi_{(l,n+l)}}\right] \\
&-\frac{i}{8\left(kCC_g\right)_n}\left\{\begin{array}{l}
\displaystyle\sum_{l=1}^{n-1}\left[\begin{array}{l}
\displaystyle -\frac{R_{2(l,n-l)}}{2\left(kCC_g\right)_l}\left[\left(kCC_g\right)_{lx} A_l + \frac{i}{4}\left(\sum A^2\right)_l\right] A_{n-l} e^{i\theta_{(l,n-l)}} \\
\displaystyle -\frac{R_{3(l,n-l)}}{2\left(kCC_g\right)_{n-l}}\left[\left(kCC_g\right)_{n-lx} A_{n-l} + \frac{i}{4}\left(\sum A^2\right)_{n-l}\right] A_l e^{i\theta_{(l,n-l)}}
\end{array}\right] \\
\displaystyle +2\sum_{l=1}^{N-n}\left[\begin{array}{l}
\displaystyle -\frac{S_{2(l,n+l)}}{2\left(kCC_g\right)_l}\left[\left(kCC_g\right)_{lx} A_l^* - \frac{i}{4}\left(\sum A^2\right)_l^*\right] A_{n+l} e^{i\psi_{(l,n+l)}} \\
\displaystyle -\frac{S_{3(l,n+l)}}{2\left(kCC_g\right)_{n+l}}\left[\left(kCC_g\right)_{n+lx} A_{n+l} + \frac{i}{4}\left(\sum A^2\right)_{n+l}\right] A_l^* e^{i\psi_{(l,n+l)}}
\end{array}\right]
\end{array}\right\}
\end{aligned} \tag{4.16}$$

By applying the closure of Benney and Saffman (1966) to the second nonlinear summation in curly bracket of Equation (4.16), the simplified version of present model is finally derived (further details in Appendix B):

$$
\begin{aligned}
&A_{nx}+\frac{\left(kCC_g\right)_{nx}}{2\left(kCC_g\right)_n}A_n \\
&=-\frac{i}{8\left(kCC_g\right)_n}\left[\begin{array}{l}\displaystyle\sum_{l=1}^{n-1}\left(R_{1(l,n-l)}-R_{2(l,n-l)}\frac{\left(kCC_g\right)_{lx}}{2\left(kCC_g\right)_l}-R_{3(l,n-l)}\frac{\left(kCC_g\right)_{n-lx}}{2\left(kCC_g\right)_{n-l}}\right)A_lA_{n-l}e^{i\theta_{(l,n-l)}} \\ \displaystyle+2\sum_{l=1}^{N-n}\left(S_{1(l,n+l)}-S_{2(l,n+l)}\frac{\left(kCC_g\right)_{lx}}{2\left(kCC_g\right)_l}-S_{3(l,n+l)}\frac{\left(kCC_g\right)_{n+lx}}{2\left(kCC_g\right)_{n+l}}\right)A_l^*A_{n+l}e^{i\psi_{(l,n+l)}}\end{array}\right] \\
&-\frac{i}{8\left(kCC_g\right)_n}\left\{\begin{array}{l}\displaystyle\sum_{l=1}^{n-1}\left(-\frac{iR_{2(l,n-l)}S_{1(n-l,n)}}{4\left(kCC_g\right)_l}\left|A_{n-l}\right|^2A_n-\frac{iR_{3(l,n-l)}S_{1(l,n)}}{4\left(kCC_g\right)_{n-l}}\left|A_l\right|^2A_n\right) \\ \displaystyle+2\sum_{l=1}^{N-n}\left[\frac{iS_{2(l,n+l)}S_{1(n,l+n)}}{4\left(kCC_g\right)_l}\left|A_{l+n}\right|^2A_n-\frac{iS_{3(l,n+l)}R_{1(l,n)}}{4\left(kCC_g\right)_{n+l}}\left|A_l\right|^2A_n\right]\end{array}\right\}
\end{aligned}
\tag{4.17}
$$

4.3 Comparisons with other models

Equation (4.17) has eased the computational demands compared to the original consistent nonlinear mild-slope equation (Equation 4.3) by adopting the closure scheme of Benney and Saffman (1966) used in stochastic models, but is an extension of the deterministic model of Kaihatu and Kirby (1995) in that ensemble average is not implemented and part of nonlinear terms retain the phase-mismatch of all combinations of triads. This combination of approaches is why we refer to this model as a "hybrid" model. The remaining terms in the first nonlinear summation represent the interaction between water depth change (shoaling) and near-resonant quadratic interactions. Furthermore, the second nonlinear summation in curly bracket consists of quasi-cubic terms, which have a form of cubic term but come from one of quadratic terms, which is

the x-derivative nonlinear term A_xA. As we argue in Section 2.3, the effect of phase mismatches is alleviated by x-derivative nonlinear terms A_xA, which is reflected in the equation where one result is that the terms in the second summation have zero mismatch.

Benney and Saffman (1966) mentioned that Gaussian closure hypothesis is valid for weakly nonlinear waves even in the region of non-Gaussian waves such as nearshore region. Nevertheless, the stochastic model is restricted to a certain condition: the model can be applicable for moderately-nonlinear waves in adequately-shallow water (e.g., $Ur < 1.5$ in Agnon and Sheremet, 1997). However, we extend the deterministic evolution equations of Kaihatu and Kirby (1995) to include not only nonlinear terms retaining the phase-mismatch but also additional consistently-ordered term by a means of the closure of Benney and Saffman (1966). Hence, the hybrid model should have a strength of deterministic model and fully considering triad wave-wave interaction over stochastic model and model of Kaihatu and Kirby (1995), respectively.

Before we verify the ability of the model in terms of spectral evolution in random waves, we again conduct a comparison between the results from the simplified version of present model to previous models including the original model of present study and experimental data of Chapalain et al. (1992). According to the conclusions of Kaihatu (2001), second order-correction with Equation (2.84) shows mostly significant improvement in simulation of wavefield in terms of random waves with the exception of little impact on the evolution of wave spectrum for frequency < 1.7 Hz. It is a kind of examination preliminary to verification in random waves, and hence we present second-order corrected results for all the models except for model of Freilich and Guza (1984).

Figures 16 and 17 show the numerical results for each case obtained by the hybrid consistent nonlinear mild-slope equation (Equation 4.17, hereinafter HCNMSE in figures and tables) with second-order correction, the original consistent nonlinear mild-slope equation (Equation 4.3, hereinafter CNMSE in figures and tables) with second-order correction, the models of Kaihatu and Kirby (1995) with second-order correction, and Freilich and Guza (1984), all compared to the experimental data of Chapalain et al. (1992).

In Tables 13 and 14, in addition to the values of IOA for each harmonic, average values of IOA over 1 through 4 harmonics are added for comprehensive comparison of models over the entire harmonics. Overall, the simplified version of the present model (or hybrid consistent nonlinear mild-slope equation) shows the most striking agreement. In particular, the newly developed model has higher values of IOA than the other models (see Tables 13 and 14) for higher order harmonic waves (i.e., third- and fourth-harmonic) which have the greatest value of relative water depth (kh) and the smallest nonlinearity parameter (a/h), which leads to the smallest value of Ursell number ($Ur = \frac{a}{k^2h^3}$). The harmonic waves of higher order are consistent with the Gaussian Sea state in deep water, and have the effect of nonlinearity (the normalized amplitude, e.g., A_nk_n) approaching to zero (Benney and Saffman, 1966), implying a justification for application of the Gaussian closure scheme. Furthermore, it is apparent that the hybrid model better predicts all harmonic wave amplitudes than the deterministic models of Kaihatu and Kirby (1995) for the most of cases. This is primarily due to the inclusion of A_xA as the form of quasi-cubic term with zero mismatch in Equation (4.17). Therefore, despite the

application of a simplifying closure method (Benney and Saffman 1966), one may conclude from the comparison of IOA values (see Tables 13 and 14) that the hybrid model better works and account for the triad wave interaction compared to the previous deterministic models.

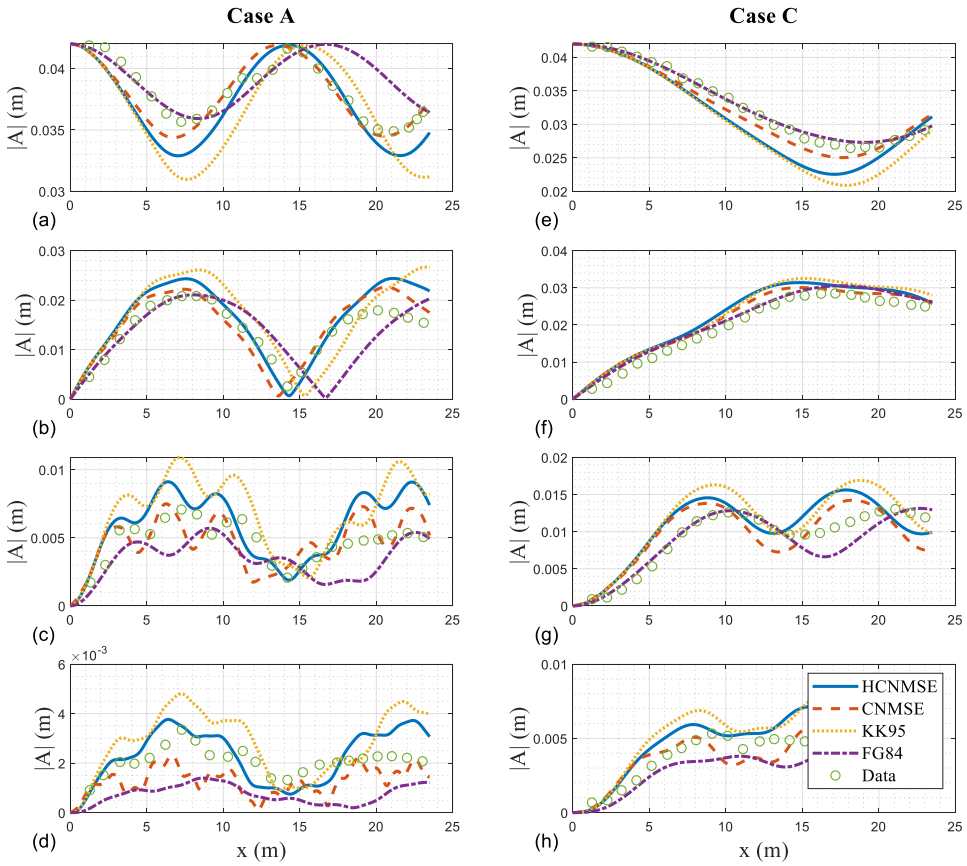

Figure 16 Comparison of wave amplitudes between models and data of Chapalain et al. (1992) for Case A: (a) first harmonic; (b) second harmonic; (c) third harmonic; (d) fourth harmonic; for Case C: (e) first harmonic; (f) second harmonic; (g) third harmonic; (h) fourth harmonic (Solid: hybrid consistent nonlinear mild-slope equation; Dashed: consistent nonlinear mild-slope equation; Dotted: model of Kaihatu and Kirby (1995); Dash-dot: model of Freilich and Guza (1984); Circle: experimental data).

Table 13 Comparison of IOA between models including hybrid consistent nonlinear mild-slope equation for Case A and C of Chapalain et al. (1992).

Case	Harmonics	HCNMSE	CNMSE	KK95	FG84
A	1	0.8911	0.9408	0.7674	0.7563
	2	0.9205	0.9399	0.8519	0.8067
	3	0.7263	0.7081	0.6795	0.6595
	4	0.7369	0.4840	0.6216	0.3804
	Average	0.8187	0.7682	0.7301	0.6507
C	1	0.9465	0.9850	0.9236	0.9980
	2	0.9638	0.9811	0.9607	0.9873
	3	0.8786	0.8856	0.8680	0.9606
	4	0.8908	0.8968	0.8513	0.8230
	Average	0.9199	0.9372	0.9009	0.9422

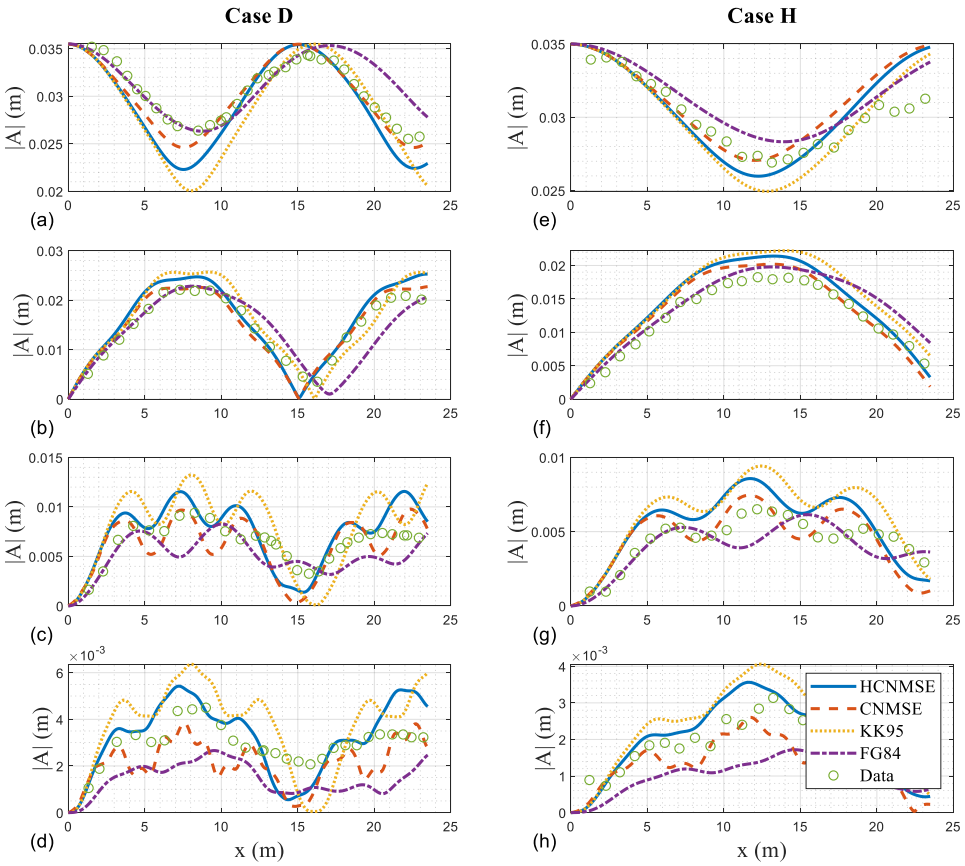

Figure 17 Comparison of wave amplitudes between models and data of Chapalain et al. (1992) for Case D: (a) first harmonic; (b) second harmonic; (c) third harmonic; (d) fourth harmonic; for Case H: (e) first harmonic; (f) second harmonic; (g) third harmonic; (h) fourth harmonic (Solid: hybrid consistent nonlinear mild-slope equation; Dashed: consistent nonlinear mild-slope equation; Dotted: model of Kaihatu and Kirby (1995); Dash-dot: model of Freilich and Guza (1984); Circle: experimental data).

Table 14 Comparison of IOA between models including hybrid consistent nonlinear mild-slope equation for Case D and H of Chapalain et al. (1992).

Case	Harmonics	HCNMSE	CNMSE	KK95	FG84
D	1	0.9088	0.9598	0.8658	0.8761
	2	0.9654	0.9793	0.9571	0.9077
	3	0.7651	0.7704	0.7620	0.7214
	4	0.7623	0.6233	0.6572	0.4787
	Average	0.8504	0.8332	0.8105	0.7460
H	1	0.9106	0.8787	0.9252	0.9228
	2	0.9496	0.9684	0.9164	0.9504
	3	0.8087	0.8387	0.7529	0.872
	4	0.8706	0.7451	0.7961	0.612
	Average	0.8849	0.8577	0.8477	0.8393

CHAPTER V

COMPARISON TO DATA: RANDOM WAVES

5.1 Introduction

While it is possible to treat random wave dissipation on a wave-by-wave basis in the frequency domain (e.g., Bredmose et al. 2004), spectral phase-resolving wave models are more readily served by statistical approaches. The model of Battjes and Janssen (1978), which estimated the spatial decay of energy flux due to the wave breaking in the energy flux balance equation, is widely used for breaking and decay descriptions. Thornton and Guza (1983) extended the model of Battjes and Janssen (1978) to describe more realistic wave height distribution in the surf zone, allowing waves to be temporarily higher than their theoretical limiting height in order to account for the spatial lag between height limit exceedance and actual breaking. Whereas Battjes and Janssen (1978) express non-breaking wave distribution as a Rayleigh distribution with a sharp wave height cutoff to replicate the impact of breaking on the probability distribution, Thornton and Guza (1983) redistributed the truncated probability over the remainder of the distribution in order to replicate the effect of momentary exceedance of wave height above breaking. Recently, several attempts have been made to improve modelling in shallow water on steeper beaches: Baldock et al. (1998) used a Rayleigh distribution with a Heaviside step function for broken waves across the surf zone instead of the delta function at the breaker criterion H_b in the model of Battjes and Janssen (1978), and Janssen and Battjes (2007) extended Baldock et al. (1998) to correct the

shoaling law so that the model of Janssen and Battjes (2007) allows for the vanishing of wave height at the shoreline.

To predict wave spectra or wave shape, phase-resolving frequency domain models have incorporated the dissipation models of Battjes and Janssen (1978) and Thornton and Guza (1983). In incorporating the lumped parameter dissipation model, a frequency distribution function was first introduced by Mase and Kirby (1993) to address the breaking-induced energy decay proportional to the wave frequency squared, and the proposed dissipation term α_n with the squared-frequency distribution is given by

$$\alpha_n = \beta\left[F + (1-F)\frac{f_n^{\,2}\sum|A_n|^2}{\sum f_n^{\,2}|A_n|^2}\right] \tag{5.1}$$

where β is dissipation function, f is frequency, A is complex amplitude, and subscript n is an index indicating the nth frequency component. Furthermore, F is a free parameter that weights frequency dependence for α_n (i.e., $F = 0$: f^2 dependence for the entire dissipation term; $F = 1$: frequency independence for α_n). The frequency dependent dissipation (i.e., $F = 0$) gives better prediction of wave shape than the frequency independent dissipation (Kaihatu and Kirby, 1997; Chen et al., 1997; Kaihatu, 2001), we thus use $F = 0$ in this section. The dissipation term is incorporated in the linear part of frequency-domain models:

$$
\begin{aligned}
&A_{nx}+\frac{\left(kCC_g\right)_{nx}}{2\left(kCC_g\right)_n}A_n+\alpha_n A_n \\
&=-\frac{i}{8\left(kCC_g\right)_n}\times\left[\begin{array}{l}\displaystyle\sum_{l=1}^{n-1}\left(R_{1(l,n-l)}-R_{2(l,n-l)}\frac{\left(kCC_g\right)_{lx}}{2\left(kCC_g\right)_l}-R_{3(l,n-l)}\frac{\left(kCC_g\right)_{n-lx}}{2\left(kCC_g\right)_{n-l}}\right)A_l A_{n-l}e^{i\theta_{(l,n-l)}} \\ \displaystyle+2\sum_{l=1}^{N-n}\left(S_{1(l,n+l)}-S_{2(l,n+l)}\frac{\left(kCC_g\right)_{lx}}{2\left(kCC_g\right)_l}-S_{3(l,n+l)}\frac{\left(kCC_g\right)_{n+lx}}{2\left(kCC_g\right)_{n+l}}\right)A_l^{*}A_{n+l}e^{i\psi_{(l,n+l)}}\end{array}\right] \\
&-\frac{i}{8\left(kCC_g\right)_n}\left\{\begin{array}{l}\displaystyle\sum_{l=1}^{n-1}\left(-\frac{iR_{2(l,n-l)}S_{1(n-l,n)}}{4\left(kCC_g\right)_l}\left|A_{n-l}\right|^2A_n-\frac{iR_{3(l,n-l)}S_{1(l,n)}}{4\left(kCC_g\right)_{n-l}}\left|A_l\right|^2A_n\right) \\ \displaystyle+2\sum_{l=1}^{N-n}\left[\frac{iS_{2(l,n+l)}S_{1(n,l+n)}}{4\left(kCC_g\right)_l}\left|A_{l+n}\right|^2A_n-\frac{iS_{3(l,n+l)}R_{1(l,n)}}{4\left(kCC_g\right)_{n+l}}\left|A_l\right|^2A_n\right]\end{array}\right.
\end{aligned}
\tag{5.2}
$$

The "simple" dissipation function of Thornton and Guza (1983) with shallow water approximation for the group velocity C_g is selected as β in the present study:

$$
\beta=\frac{3\sqrt{\pi}}{4\sqrt{gh}}\frac{B^3f_p}{\gamma^4h^5}H_{rms}{}^5 \tag{5.3}
$$

where B is a breaking coefficient, f_p is a peak frequency of the spectrum, g is the gravitational acceleration, h is a water depth, and γ is a parameter related to the root-mean-square wave height (H_{rms}):

$$
H_{rms}=2\sqrt{\sum_{n=1}^{N}\left|A_n\right|^2} \tag{5.4}
$$

The wave setup is obtained using balance of momentum flux (Longuet-Higgins and Stewart, 1964):

$$\frac{d\bar{\eta}}{dx} = -\frac{1}{\rho g\left(\bar{\eta}+h\right)}\frac{dS_{xx}}{dx} \tag{5.5}$$

where $\bar{\eta}$ is the wave setup and S_{xx} is the onshore component of the wave-driven momentum flux tensor (or wave radiation stress), and shallow water approximation of S_{xx} is given by

$$S_{xx} = \frac{3}{4}\sum_{n=1}^{N}\rho g\left|A_n\right|^2 \tag{5.6}$$

Though wave setup is considered as a prescribed value for dissipation term rather than iterative process in simulation, subsequent simulations have shown that the inclusion of setup has limited effect on model accuracy.

Owing to the demonstrated improvement by the second-order correction (Equation 2.84) for the permanent form solutions in Chapter 2 (as seen in Figures 2 through 5), the finite number of waves in Chapter 3 (i.e., Figures 6, 7, and 12), and the random waves in Kaihatu (2001), we concern ourselves with the second-order corrected results for all the models except for the model of Freilich and Guza (1984), where the shallow-water formulation obviates the advantages imparted by a second-order correction. The complex Fourier amplitudes of free surface elevation A_n at the upwave boundary are obtained from time series for water surface elevation η by a means of Fast Fourier Transform (FFT). The wave models (e.g., Equation 5.2) is then used to predict the complex Fourier amplitudes for shallower gauge locations. The simulated results of wave amplitude are then used to calculate wave energy spectrum:

$$S\left(f_n\right) = \frac{\left|A_n\right|^2}{2\Delta f} \tag{5.7}$$

where $S(f_n)$ is the calculated wave energy spectrum of frequency f_n (n = 1 to N), and $\Delta f = 1/T$ is the frequency resolution (where T is record length of one segment). The resulting spectrum is then averaged across all segments, leading to an ensemble averaged spectrum. Additional smoothing is accomplished by band averaging.

The RMSPE (Root-Mean-Square Percentage-Error) is used to evaluate the performance of the models over the entire frequency component range as the average value of IOA in Tables 13 and 14, and it ranges from 0 to ∞, with 0 corresponding to the ideal model (see Equation 5.8):

$$\mathrm{RMSPE}_j = \sqrt{\frac{1}{N}\sum_{i=1}^{N}\left(\frac{S_j(f_i) - S_{j,obs}(f_i)}{S_{j,obs}(f_i)}\right)^2} \tag{5.8}$$

where RMSPE_j is evaluated at jth gauge (j = 1 to N_{gauge}), $S_j(f_i)$ is the calculated wave energy spectrum of frequency f_i (i = 1 to N) at the jth gauge (j = 1 to N_{gauge}) and $S_{j,obs}(f_i)$ is the observed wave energy spectrum of frequency f_i (i = 1 to N) at the jth gauge (j = 1 to N_{gauge}).

5.2 Mase and Kirby (1993), Bowen and Kirby (1994)

We use two laboratory experimental data sets in this section. First data set considered is the data set of Case 2 of Mase and Kirby (1993) (hereinafter MK93 in figures and tables), in which random waves were generated and allowed to propagate over a sloping bottom, with conditions leading to spilling-type wave breaking. The shapes of the spectra were determined by a Pierson-Moskowitz spectrum with f_p = 1 Hz, and irregular waves were generated for the initial condition at the wave paddle, and the

relative depth is high enough to be in fairly deep water range ($k_p h$ = 1.97). Data were taken at 12 different gauges along the 1:20 slope beach, but we do not consider the shallowest gauge (h = 2.5 cm) because of the anomalous measurement where the choice of F = 0 caused the destroyed tail of power spectrum at h = 2.5 cm (Mase and Kirby, 1993; Kirby and Kaihatu, 1997; Chen et al., 1997). The data were split into 7 segments of 2048 points with the sampling rate of 20 Hz. Following Mase and Kirby (1993), assigned values of B and γ in β (Equation 5.3) are 1.0 and 0.6, respectively. A sketch of experimental setup is shown in Figure 18.

The second data set used to analyze the performance of the hybrid consistent nonlinear mild-slope model is that of the Bowen and Kirby (1994) (hereinafter BK94 in figures and tables). Of the three wave conditions present in the experimental data set, we use Case A in order to investigate the validity of the present model in intermediate water depth range ($k_p h$ = 0.72). Following Bowen and Kirby (1994), the free surface elevation has been measured in the sampling rate of 25 Hz, and is divided into 24 realizations, and each realization has 1024 data points. Bowen and Kirby (1994) found the optimal values of B and γ in β (Equation 5.3) as 1.15 and 0.6, respectively, and thus these are assigned in this study. Figure 19 presents the experimental layout showing 44 gauges along the 1:35 beach slope of total 47 wave gauges, and Table 15 details wave parameters and experiment setups of Mase and Kirby (1993) and Bowen and Kirby (1994).

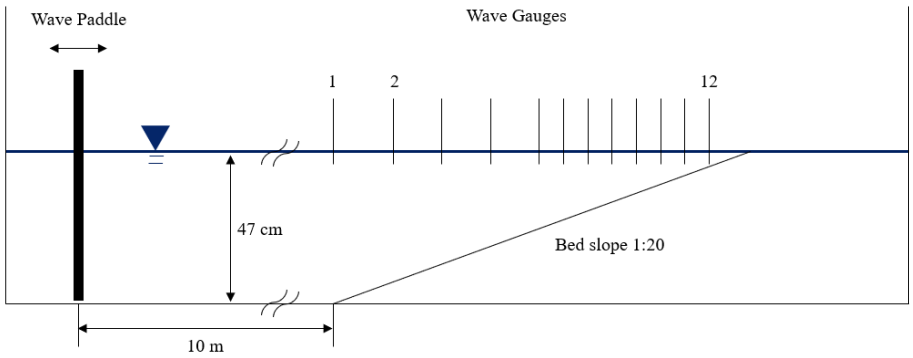

Figure 18 Layout of experiment of Mase and Kirby (1993).

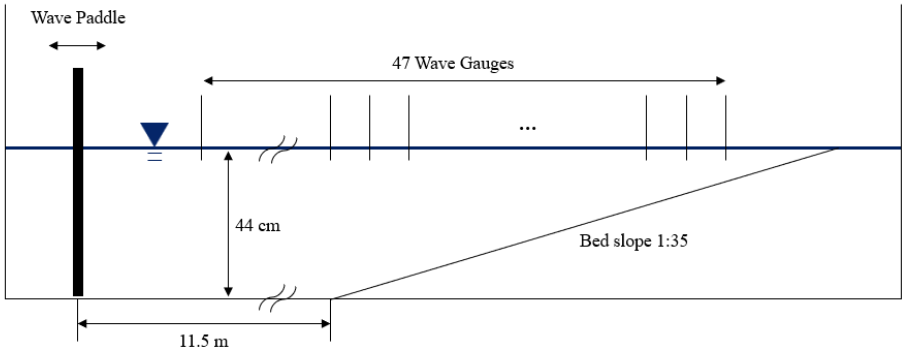

Figure 19 Layout of experiment of Bowen and Kirby (1994).

Table 15 Wave parameters and experiment setups of Mase and Kirby (1993) and Bowen and Kirby (1994).

Experiment	Bed slope	H_{rms} (cm)	f_p (Hz)	N	k_ph	Ur_p
Case 2 of MK93	1:20	4.7	1	400	1.97	0.01
Case A of BK94	1:35	6.6	0.5	150	0.72	0.15

Figures 20-21 and 22-23 show the wave spectra comparison between the data with the hybrid version of present model, models of Kaihatu and Kirby (1995), and Freilich and Guza (1984) for Case 2 of Mase and Kirby (1993) and Case A of Bowen and Kirby (1994), respectively. Tables 16 and 17 provide comparison of RMSPE between models for Case 2 of Mase and Kirby (1993) and Case A of Bowen and Kirby (1994), respectively. Following Kaihatu and Kirby (1995), the present model uses the linear shoaling mechanism while Freilich and Guza (1984) took non-dispersive relation for shoaling (i.e., Green's law shoaling). For Case 2 of Mase and Kirby (1993), owing to the high relative depth at the first gauge ($k_p h$ = 1.97), the predictions of two model with the fully-dispersive linear theory for the dispersive and shoaling characteristics (i.e., the present model and the model of Kaihatu and Kirby (1995)) are in better agreement with the measured data compared to those of Freilich and Guza (1984).

On the other hand, Case A of Bowen and Kirby (1994) corresponds to the shallower water case than Case 2 of Mase and Kirby (1993), and as the water get shallower, the relative depth at a peak become smaller and arrive at the shallow water range for Boussinesq theory (e.g., $k_p h$ = 0.31 at h = 10 cm). Consequently, the model of Freilich and Guza (1984) shows better predictions for the lower frequencies (nearshore part of the spectra) at the shallower gauges. The model of Kaihatu and Kirby (1995) underestimates the energy spectrum of peak frequency at the shallower gauges, and this may be due to the linear dispersive relation, as opposed to the weakly dispersive relation. We note that the linear shoaling term includes more terms at $O(\varepsilon\alpha\mu^2)$ (where $h_x \sim O(\alpha)$) in comparison to the non-dispersive shoaling term ($\frac{h_x}{4h}A$):

$$\frac{\left(kCC_g\right)_x}{2\left(kCC_g\right)}A=\frac{h_x}{4h}\left[1+O\left(\mu^2\right)\right]A \tag{5.9}$$

Although the shoaling mechanism based on fully dispersive linear theory has an asymptote of that based on the non-dispersive relation in shallow water (or the higher-order terms at $O(\varepsilon\alpha\mu^2)$ in the linear shoaling term approaches to zero at the shallower gauge), the integrated effect of the higher-order terms from the initial gauge to the shallower gauge may not be negligible. Therefore, the accumulated effect of the terms at $O(\varepsilon\alpha\mu^2)$ probably attribute to the underestimated predictions (or overestimated shoaling effect) of the model of Kaihatu and Kirby (1995) at peak frequency, which begin to become noticeable from h = 18 cm (Figure 23(b)).

Despite the fact that the present study also takes into consideration the identical linear dispersive relation, we notice that, comparing to the model of Kaihatu and Kirby (1995), the present model shows improvement in prediction of the peak wave energy spectra probably due to the inclusion of additional quasi-cubic terms (see Figure 23). This advancement is valid for Case 2 of Mase and Kirby (1993) as well shown in Figure 21. Additionally, the present formulations give the best performances for the higher frequencies (deep water part of spectra) at most of shallow gauges in the both cases. In the higher frequency range of spectra, the value of mismatch becomes larger, which gives the present model an advantage since it is less affected by large mismatch due to the presence of additional nonlinear terms with zero-mismatch, which is the most obvious at $f > 2$ Hz in Case A of Bowen and Kirby (1994) as seen in Figure 23. Also, the value of Ursell number Ur_n ($\frac{H_{rms}}{2{k_n}^2h^3}$) approaches to zero in the deep water range of

wave power spectra, which might validate the ordering of present study instead of that of Boussinesq type model with $O(Ur) \sim O(1)$. Moreover, when applying to the laboratory and field data where the total number of frequency components are larger and the offshore part of spectra is more dominant, the present model may be even more feasible alternative to the previous models.

The low frequency wave range ($f < 0.5f_p$) is likely influenced by strong reflected effects from shorelines which is not simulated by all the models. Therefore, the lack of considering the reflected waves in frequency-domain model may lead to a strong deviation for the measurement at the low frequency range. The predictions of the wave spectrum at the low frequency wave range ($f < 0.5\ f_p$) in the case of Mase and Kirby (1993) are worse than those in the case of Bowen and Kirby (1994), which may be ascribed to the steeper slope of Mase and Kirby (1993) (bed slope = 1/20) causing more obvious reflected waves due to the more rapid shoaling compared to Bowen and Kirby (1994) (bed slope = 1/35).

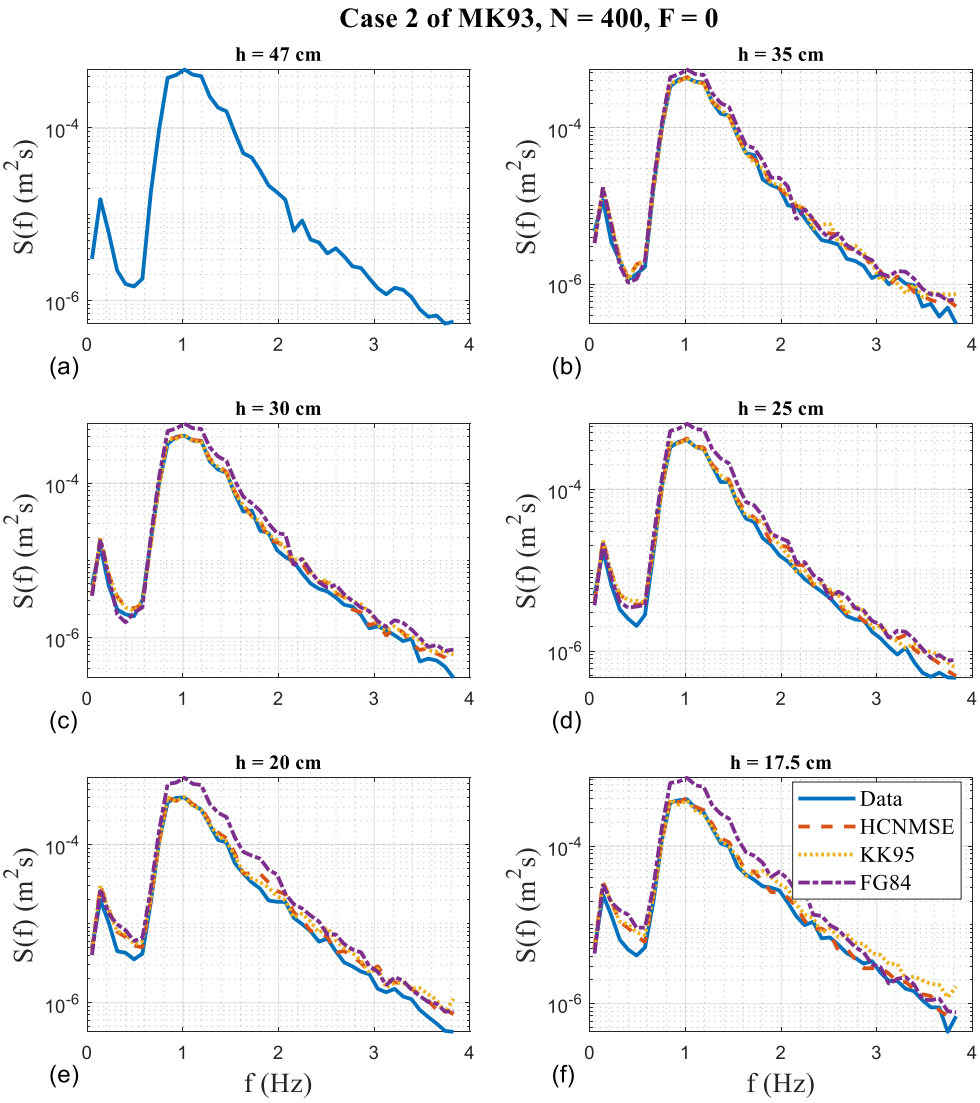

Figure 20 Comparison of wave spectra density using *N* = 400 for Case 2 of MK93: (a) *h* = 47 cm; (b) *h* = 35 cm; (c) *h* = 30 cm; (d) *h* = 25 cm; (e) *h* = 20 cm; (f) *h* = 17.5 cm (Solid: experimental data; Dashed: hybrid consistent nonlinear mild-slope equation; Dotted: model of Kaihatu and Kirby (1995); Dash-dot: model of Freilich and Guza (1984)).

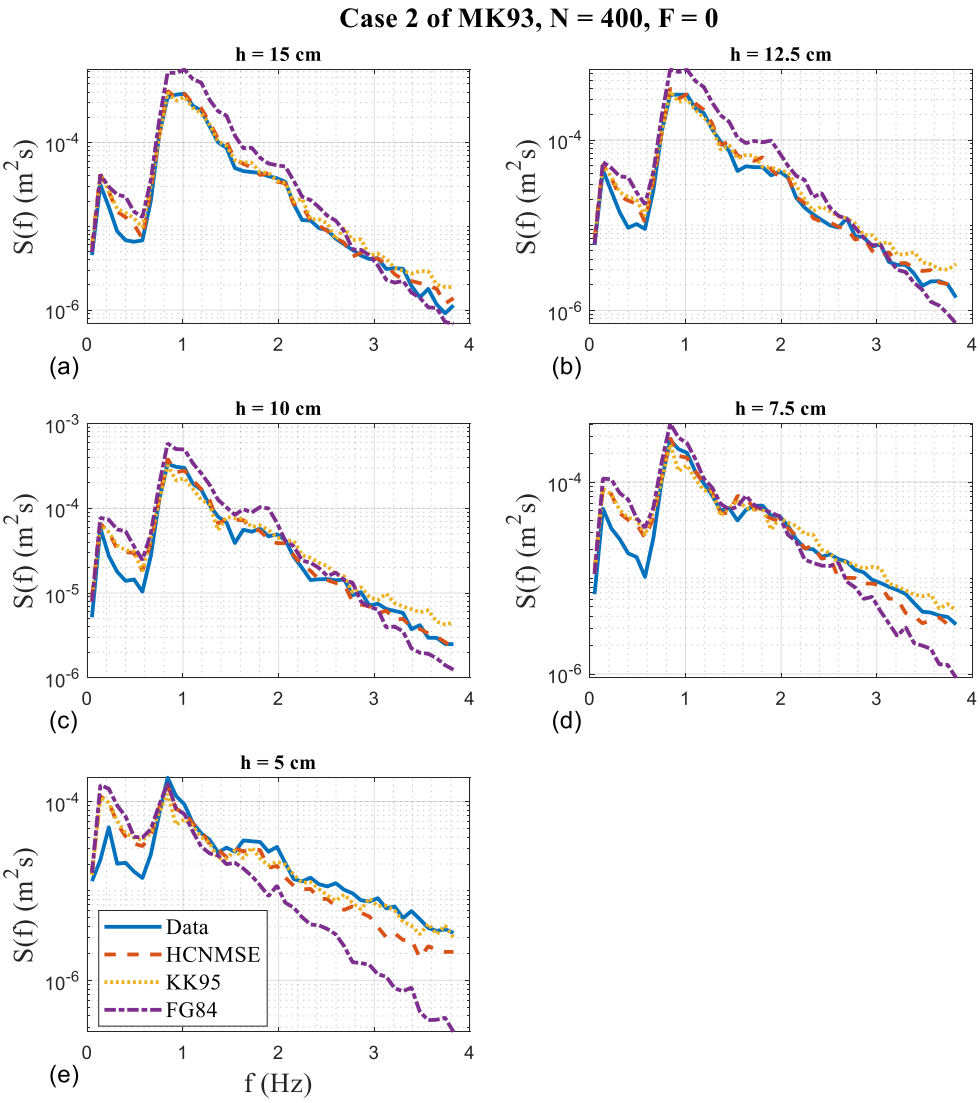

Figure 21 Comparison of wave spectra density using N = 400 for Case 2 of MK93: (a) h = 15 cm; (b) h = 12.5 cm; (c) h = 10 cm; (d) h = 7.5 cm; (e) h = 5 cm (Solid: experimental data; Dashed: hybrid consistent nonlinear mild-slope equation; Dotted: model of Kaihatu and Kirby (1995); Dash-dot: model of Freilich and Guza (1984)).

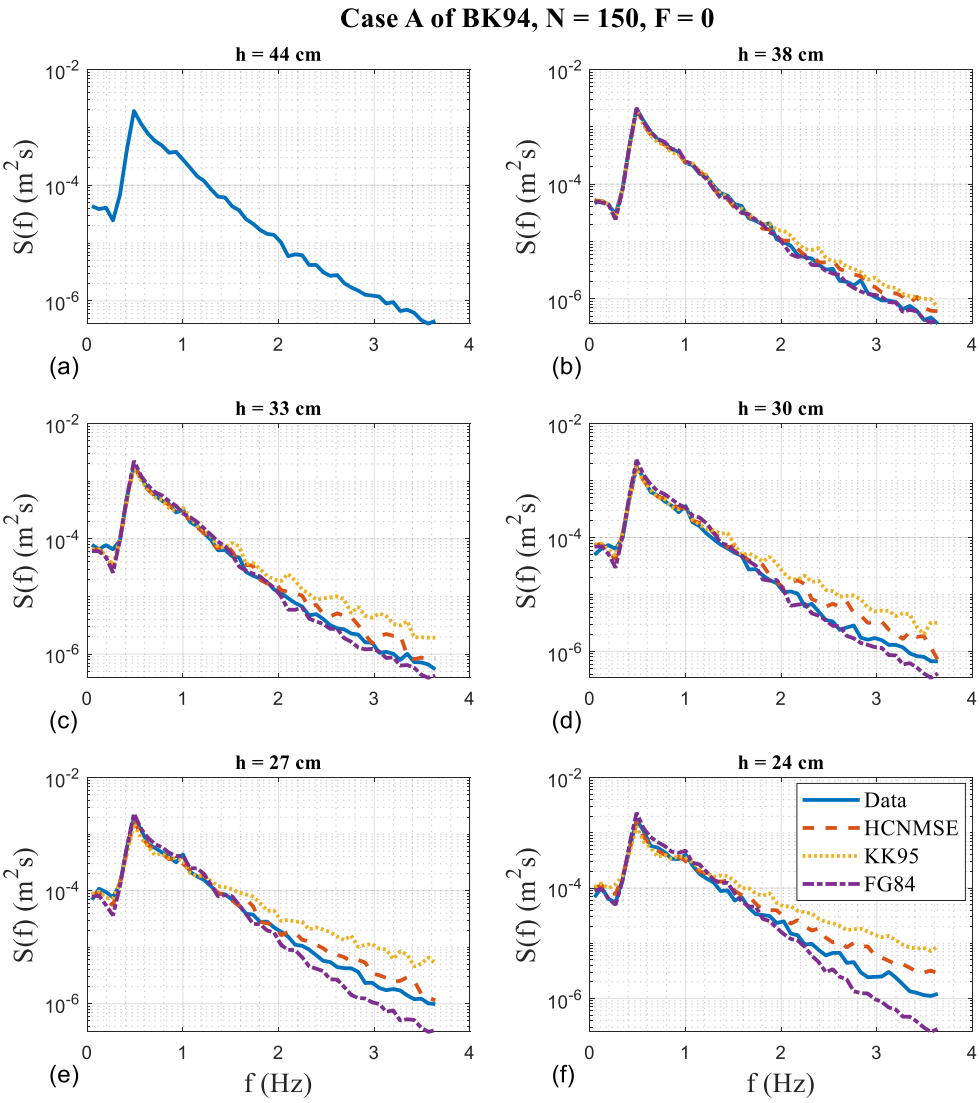

Figure 22 Comparison of wave spectra density using *N* = 150 for Case A of BK93: (a) *h* = 44 cm; (b) *h* = 38 cm; (c) *h* = 33 cm; (d) *h* = 30 cm; (e) *h* = 27 cm; (f) *h* = 24 cm (Solid: experimental data; Dashed: hybrid consistent nonlinear mild-slope equation; Dotted: model of Kaihatu and Kirby (1995); Dash-dot: model of Freilich and Guza (1984)).

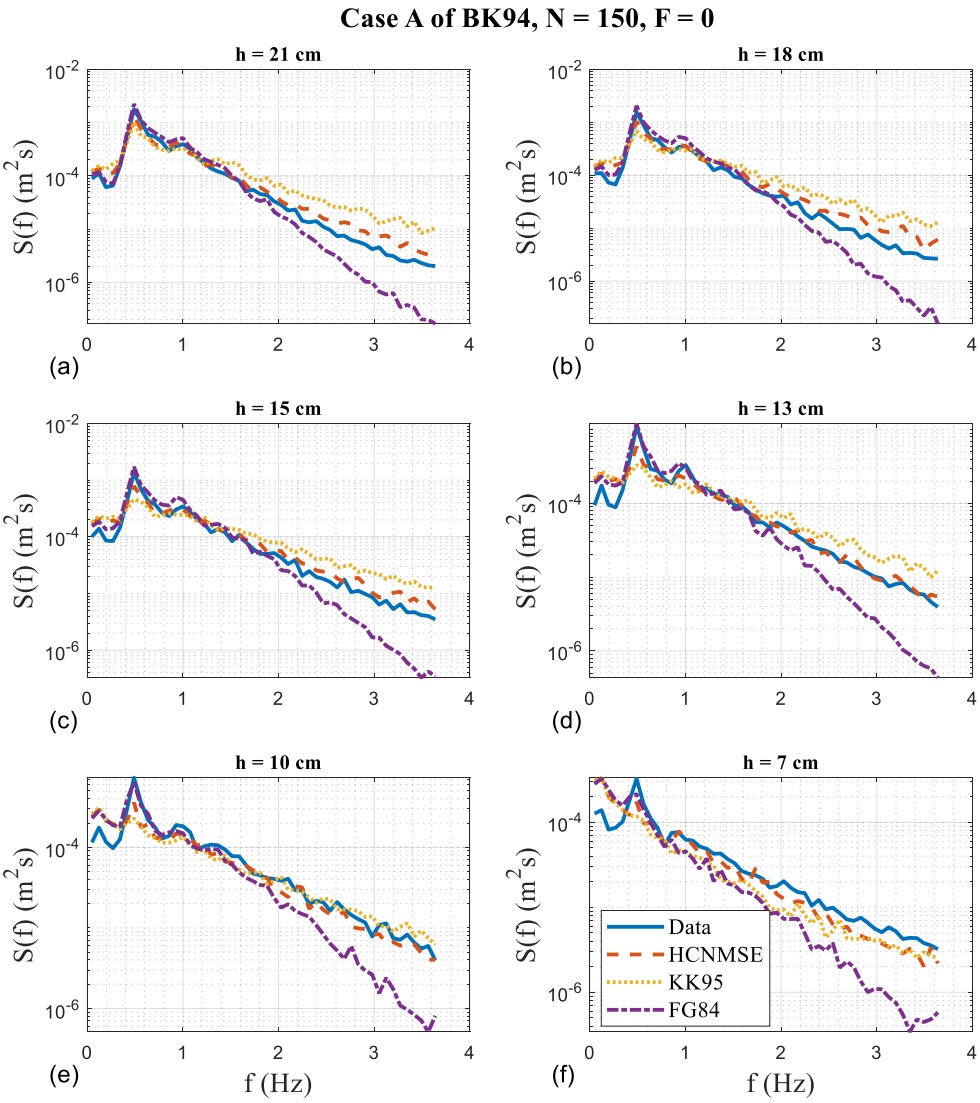

Figure 23 Comparison of wave spectra density using *N* = 150 for Case A of BK93: (a) *h* = 21 cm; (b) *h* = 18 cm; (c) *h* = 15 cm; (d) *h* = 13 cm; (e) *h* = 10 cm; (f) *h* = 7 cm (Solid: experimental data; Dashed: hybrid consistent nonlinear mild-slope equation; Dotted: model of Kaihatu and Kirby (1995); Dash-dot: model of Freilich and Guza (1984)).

Table 16 Comparison of RMSPE between models for Case 2 of Mase and Kirby (1993).

Case	Depth (cm)	HCNMSE	KK95	FG84
Case 2 of MK93	47	-	-	-
	35	1.650	1.741	2.242
	30	0.957	1.070	1.236
	25	1.329	1.378	1.330
	20	1.037	1.175	1.444
	17.5	1.650	1.741	2.242
	15	0.957	1.070	1.236
	12.5	1.329	1.378	1.330
	10	0.816	1.118	1.362
	7.5	0.933	1.134	1.339
	5	3.638	3.648	4.778
	Average	1.295	1.449	1.802

Table 17 Comparison of RMSPE between models for Case A of Bowen and Kirby (1994).

Case	Depth (cm)	HCNMSE	KK95	FG84
Case A of BK94	44	-	-	-
	41	0.319	0.557	0.216
	38	0.408	0.679	0.240
	35	0.518	1.205	0.309
	33	0.594	1.615	0.305
	30	0.817	1.947	0.370
	27	0.571	2.294	0.427
	24	1.037	2.926	0.495
	21	0.665	2.262	0.545
	18	0.835	2.039	0.571
	15	0.593	1.437	0.590
	13	0.471	0.957	0.600
	10	0.417	0.482	0.595
	7	0.553	0.584	0.763
	Average	0.600	1.461	0.464

5.3 Smith and Vincent (1992)

Smith and Vincent (1992) investigated a laboratory examination where random waves having bimodal spectra were transformed through the bottom rising at a slope of 1:30. In order to generate the double-peaked spectra, they superimposed two TMA (Texel, MARSEN, and ARSLOE, Bouws et al., 1985) spectra at a piston-type wave paddle. Data were taken at 9 different gauges along the 1:30 slope beach and sampled at 10 Hz, and then divided into 11 realizations of 1024 points each. B and γ in β (Equation 5.3) are valued at 0.8 and 0.6, respectively, and we used a mean frequency for the peak frequency in β (Equation 5.3) for the cases of Smith and Vincent (1992). Figure 24 displays the experimental flume with 9 gauges along the 1:30 beach slope. They used two sets of two double-peak wave period: one combination shows that the second peak was at a harmonic of the first peak (T_p = 2.5 s/1.25 s); other does not (T_p = 2.5 s/1.75 s). They argued that regardless of the fact that the second peak is a multiple of the first peak, all the cases had similar trends in spectral evolutions. To examine the energy transfer between the frequency modes, in particular, two primary peaks, we select Cases 2, 5, 8, and 11 where the-low frequency peak is almost equal in energy to that of the high-frequency. Table 18 represents wave parameters including the total number of frequency component taken for the simulation and experiment setup of Smith and Vincent (1992).

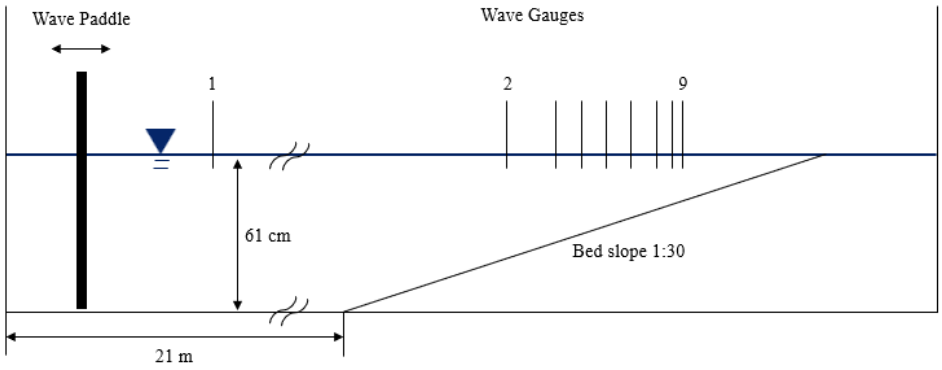

Figure 24 Layout of experiment of Smith and Vincent (1992).

Table 18 Wave parameters and experiment setup of Smith and Vincent (1992).

Experiments	Bed slope	H_{rms} (cm)	f_p (Hz)	N	k_ph	Ur_p
Case 2 of SV92	1:30	9.8	0.4/0.8	250	0.67/1.68	0.18/0.03
Case 5 of SV92	1:30	5.9	0.4/0.8	250	0.67/1.68	0.11/0.02
Case 8 of SV92	1:30	10.3	0.4/0.57	250	0.67/1.03	0.19/0.08
Case 11 of SV92	1:30	6.1	0.4/0.57	250	0.67/1.03	0.11/0.05

Figures 25 through 28 compare the energy spectra of the surface elevation computed by the models with the laboratory measurements at the selected gauges. As in the experiments of Mase and Kirby (1993) and Bowen and Kirby (1994), the impact of the improvements of the present model relative to earlier models in two metrics are also observed in the experimental dataset of Smith and Vincent (1992): (1) the improved computations of power wave spectra at two peaks; (2) the better predictions over the higher frequency range of the spectra. In addition, comparison of the average RMSPE

values from Tables 19 and 20 shows that the present model provides much better agreement with the measurements over all frequency ranges of the spectra than the other models. The second point is likely to be a clear indication that the inclusion of additional nonlinear terms having zero-mismatch relives the phase mismatches effect. Although the interaction between wave numbers (e.g., $k_l + k_{n-l} - k_n$) becomes the smallest at the shallowest gauge, the phase mismatches have the largest value at the shallowest measurement location. This is because the phase mismatch describes the accumulation of the interaction between wave numbers from offshore to the shallow gauge location. It probably explains the much better agreement of present model compared to that of Kaihatu and Kirby (1995) at the shallowest location of the shallower cases (Cases 2 and 8 where Ur_p = 0.18 and 0.19 at the first peak, respectively) as seen in Figures 25 (f) and 27 (f) where nonlinear terms with zero-mismatch may be desirable as in Boussinesq-type equations.

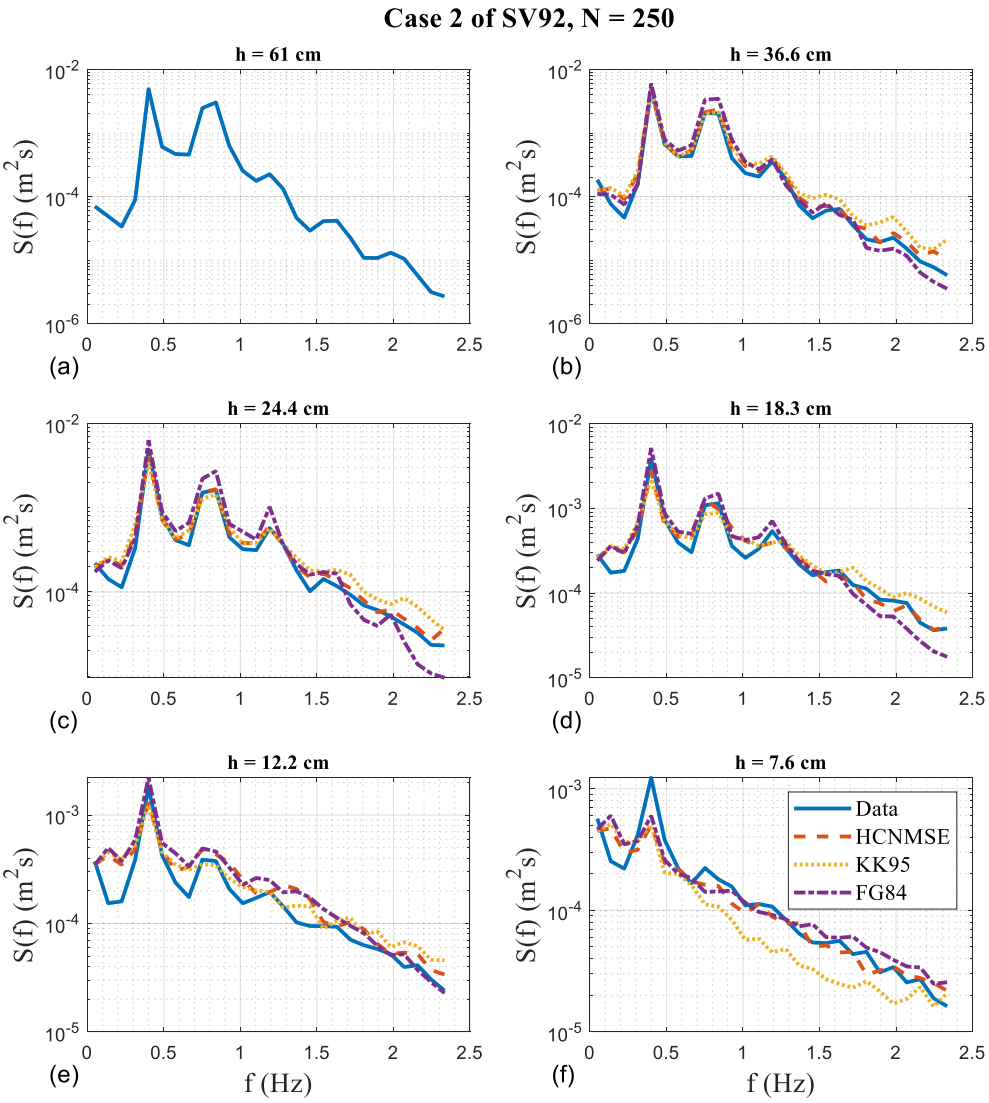

Figure 25 Comparison of wave spectra density using *N* = 250 for Case 2 of SV92: (a) *h* = 61 cm; (b) *h* = 36.6 cm; (c) *h* = 24.4 cm; (d) *h* = 18.3 cm; (e) *h* = 12.2 cm; (f) *h* = 7.6 cm (Solid: experimental data; Dashed: hybrid consistent nonlinear mild-slope equation; Dotted: model of Kaihatu and Kirby (1995); Dash-dot: model of Freilich and Guza (1984)).

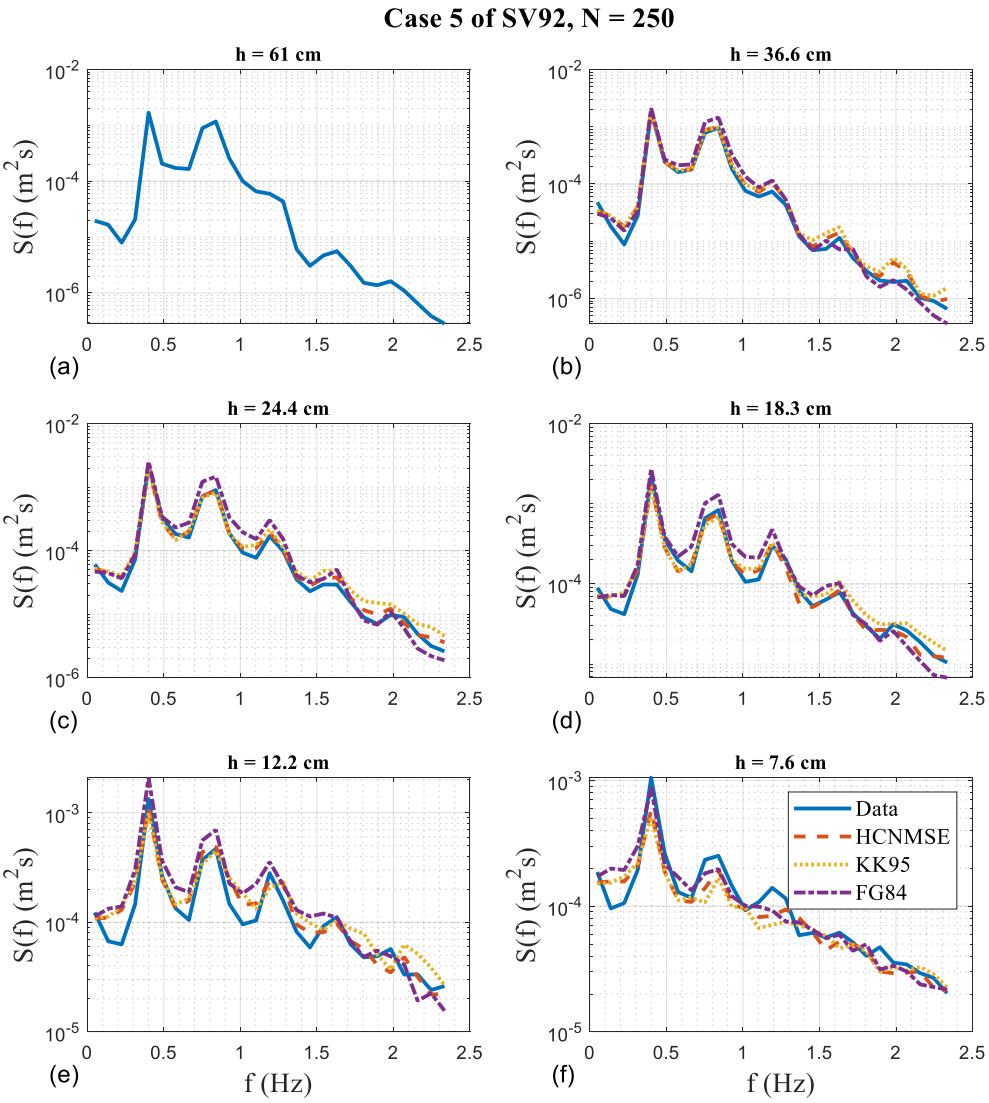

Figure 26 Comparison of wave spectra density using *N* = 250 for Case 5 of SV92: (a) *h* = 61 cm; (b) *h* = 36.6 cm; (c) *h* = 24.4 cm; (d) *h* = 18.3 cm; (e) *h* = 12.2 cm; (f) *h* = 7.6 cm (Solid: experimental data; Dashed: hybrid consistent nonlinear mild-slope equation; Dotted: model of Kaihatu and Kirby (1995); Dash-dot: model of Freilich and Guza (1984)).

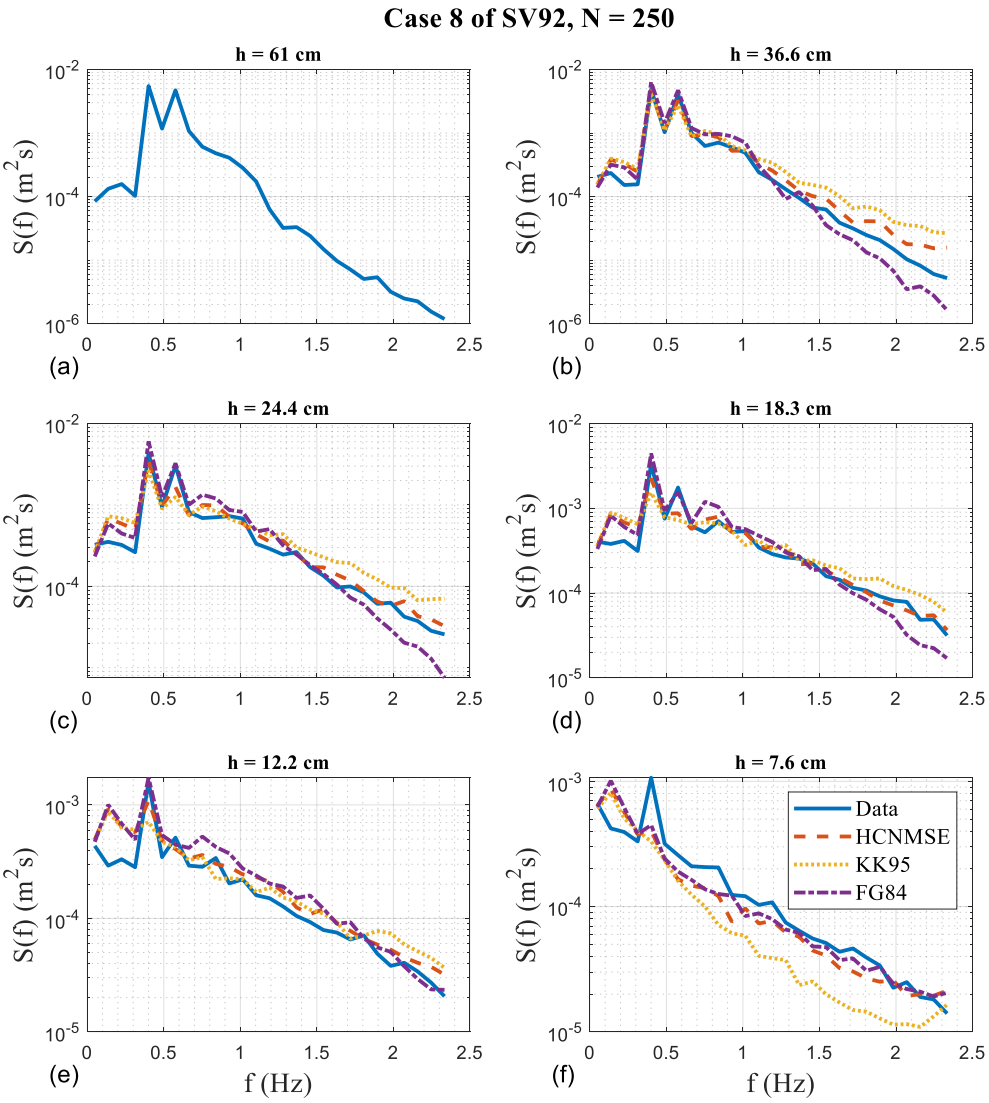

Figure 27 Comparison of wave spectra density using *N* = 250 for Case 8 of SV92: (a) *h* = 61 cm; (b) *h* = 36.6 cm; (c) *h* = 24.4 cm; (d) *h* = 18.3 cm; (e) *h* = 12.2 cm; (f) *h* = 7.6 cm (Solid: experimental data; Dashed: hybrid consistent nonlinear mild-slope equation; Dotted: model of Kaihatu and Kirby (1995); Dash-dot: model of Freilich and Guza (1984)).

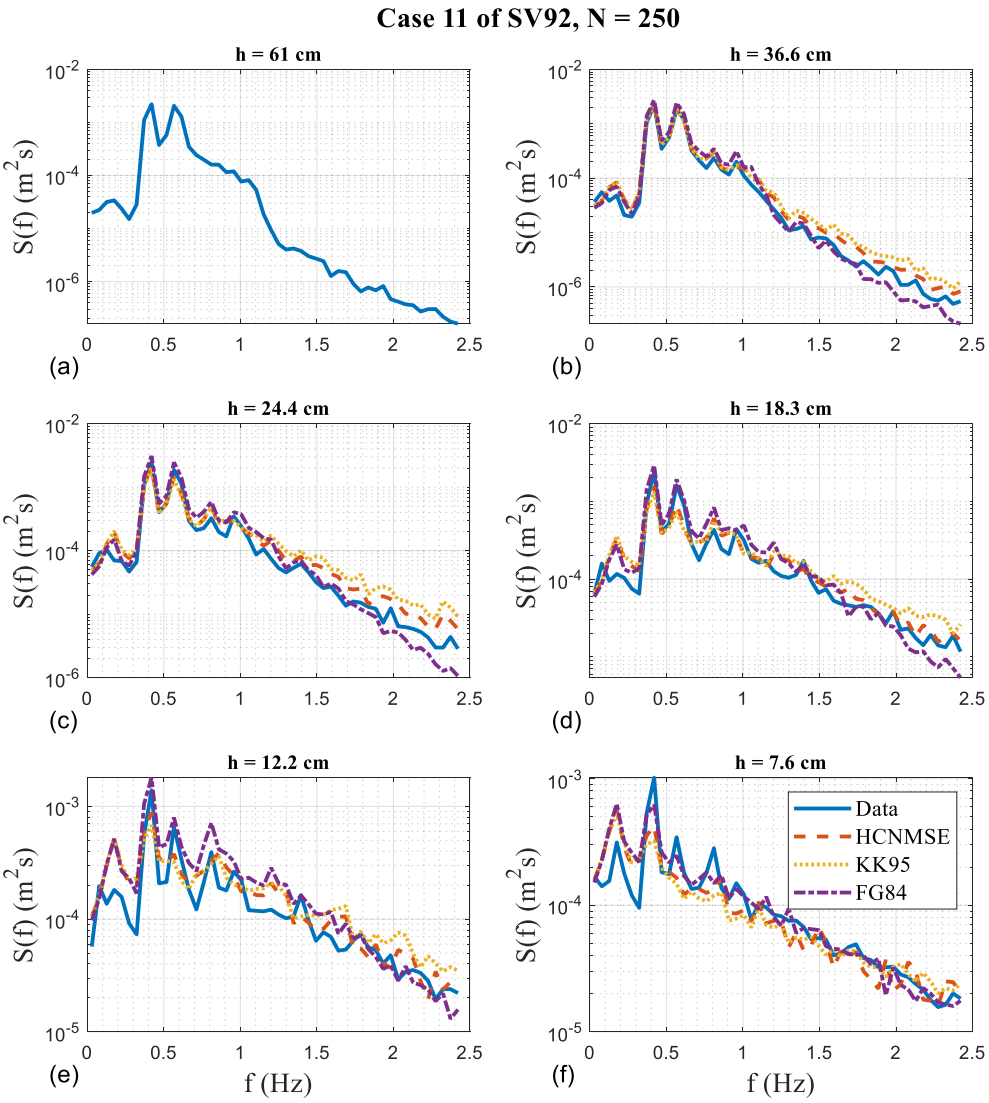

Figure 28 Comparison of wave spectra density using *N* = 250 for Case 11 of SV92: (a) *h* = 61 cm; (b) *h* = 36.6 cm; (c) *h* = 24.4 cm; (d) *h* = 18.3 cm; (e) *h* = 12.2 cm; (f) *h* = 7.6 cm (Solid: experimental data; Dashed: hybrid consistent nonlinear mild-slope equation; Dotted: model of Kaihatu and Kirby (1995); Dash-dot: model of Freilich and Guza (1984)).

Table 19 Comparison of RMSPE between models for Case 2 and 5 of Smith and Vincent (1992).

Case	Depth (cm)	HCNMSE	KK95	FG84
Case 2 of SV92	61	-	-	-
	36.6	0.896	1.281	0.726
	24.4	0.668	1.008	0.767
	18.3	0.764	0.923	0.702
	15.3	0.822	0.855	0.755
	12.2	0.985	1.027	1.015
	9.2	0.995	0.906	1.067
	7.6	0.816	0.852	0.943
	6.1	1.001	1.049	1.186
	Average	0.868	0.988	0.895
Case 5 of SV92	61	-	-	-
	36.6	0.897	1.112	0.812
	24.4	0.712	0.997	0.850
	18.3	0.729	0.837	0.961
	15.3	0.626	0.733	0.917
	12.2	0.804	0.938	1.075
	9.2	0.779	0.794	0.915
	7.6	0.586	0.597	0.688
	6.1	0.874	0.855	0.979
	Average	0.751	0.858	0.900

Table 20 Comparison of RMSPE between models for Case 8 and 11 of Smith and Vincent (1992).

Case	Depth (cm)	HCNMSE	KK95	FG84
Case 8 of SV92	61	-	-	-
	36.6	1.179	2.226	0.704
	24.4	0.806	1.296	0.783
	18.3	0.628	0.864	0.711
	15.3	0.696	0.901	0.747
	12.2	0.896	1.020	0.995
	9.2	0.720	0.704	0.885
	7.6	0.605	0.664	0.697
	6.1	0.657	0.843	0.723
	Average	0.773	1.065	0.781
Case 11 of SV92	61	-	-	-
	36.6	0.984	1.450	0.685
	24.4	1.130	1.764	0.782
	18.3	0.833	1.124	0.827
	15.3	0.778	1.017	0.879
	12.2	0.967	1.197	1.060
	9.2	0.802	0.862	0.925
	7.6	0.742	0.768	0.810
	6.1	0.761	0.745	0.794
	Average	0.874	1.116	0.845

CHAPTER VI

MODELS FOR WIDE-ANGLE WATER WAVES

6.1 Introduction

While they have severe disadvantages in other aspects, elliptic equation models (e.g., Berkhoff, 1973) have no limit to the application of wide-angle propagation (Dalrymple et al., 1989). However, the application of the parabolic equation implies the major limitation in terms of a principal propagation direction, the equation therefore may be applied to the problems where the wave propagates at or close to a given direction or the refraction effect is not significant over the entire area (Kirby, 1986a, 1986b; Dalrymple and Kirby, 1988). In contrast, parabolic wave models are numerically convenient to apply (particularly over an open coastline), but suffer in accuracy when the wave approach direction is at an oblique angle to the cross-shore (typically x) axis of the numerical grid (Kirby, 1986a, 1986b; Dalrymple and Kirby, 1988; Dalrymple et al., 1989; Suh et al., 1990).

Several higher-order parabolic models have emerged since then, based on the original parabolic equation (Radder, 1979; Lozano and Liu, 1980), to increase the range of wave directions over two-dimensional topography (Booij, 1981; Kirby, 1986a, 1986b). Booij (1981) provided a wave-current parabolic model for wider wave angles by applying splitting method for forward and backward scattered components to the wave field. Kirby (1986a) made use of the derivation of the wide-angle parabolic model of Booij (1981) to formulate a higher-order parabolic model to improve the range of

applicability into wider-angle propagation. Kirby (1986b) developed approximations based on minimax principle which minimizes maximum error over a prespecified range of wave direction, and confirmed that the parabolic approximation of Kirby (1986a) is related to (1,1) Padé approximant and the asymptote of minimax approximant when the prespecified aperture approaches to 0°.

Alternatively, considerable effort has been expended in attempts to derive a model valid for angles of propagation up to 90° by using the concept of the angular spectrum. The angular spectrum model is essentially based on the assumption that the wave field and the underlying bathymetry is periodic in the alongshore direction. By taking the Fourier transform of the wave field in the direction parallel to the longshore direction (typically *y*), the Fourier components called the angular spectrum express the wave field along a straight line, propagating independently in a specific direction. First, Dalrymple and Kirby (1988) and Dalrymple et al. (1989) developed solutions of the mild-slope equation (Berkhoff, 1973) in terms of the spectrum in longshore wavenumber for parallel bathymetry and irregular bathymetry, respectively. Next, Suh et al. (1990) developed extended the angular spectrum model to the case of the propagation of Stokes waves over water of slowly varying depths, involving the cubic nonlinearity and interaction between wave and lateral bottom variation. Kirby (1991) formulated a Boussinesq-type angular spectrum model to account for triadic nonlinear interaction between angular modes as well as frequency modes over alongshore-uniform topography. For the past several years, the angular spectrum approach has been extensively applied. For example, Agnon and Sheremet (1997), Eldeberky and Madsen

(1999), and Herbers et al. (2003) used the longshore periodic formulation as a means to develop a stochastic (phase-averaged) model for directional wave propagation. Bredmose et al. (2005) and Vrecica and Toledo (2016, 2019) used a "dispersion operator" (essentially a series expansion of trigonometric functions) to further improve deep water accuracy. Janssen et al. (2006) derived a set of unified evolution equations valid for both Stokes and Boussinesq regimes with longshore periodicity. Toledo (2013) introduced nonlinear alongshore wave number by using a perturbation method for the wave number field for the extension of mild-slope equation model to the oblique incident wave; Davis et al. (2014) and Sheremet et al. (2016) applied the phase-resolved model to the offshore directional wave spectrum (e.g., JONSWAP spectrum, Hasselmann et al., 1973).

6.2 Higher-order parabolic model

Kirby (1984) proposed a lowest-order wave-current parabolic approximation by correcting the dynamic free surface boundary condition in Booij (1981). Based on the splitting approach of Booij (1981), Kirby (1986a) revisited the linear wave-current mild-slope equation of Kirby (1984) to develop nonlinear version of the equation. The higher-order parabolic model of Kirby (1986a) appears to be reduced to (1,1) Padé approximant in the absence of ambient current and varying depth. Kirby (1986a) showed that the higher-order model is superior to the lowest-order parabolic approximation (Kirby and Dalrymple, 1983; Kirby, 1984) in describing the behavior of wave focusing by a submerged shoal (Berkhoff et al., 1982), in particular the diffraction fringe away from

the focal region. Kaihatu (2001) extended the higher-order parabolic approximation of Kirby (1986a) by adding the nonlinear terms of Kaihatu and Kirby (1995) to the linear model of Kirby (1986a), and Kaihatu (2001) shows that the model agrees very well with the experimental data for wide-angle propagation (Chawla, 1995).

One feature that is apparent with the Padé approximant is that it returns the exact solution (i.e., $\cos\theta_p$ in Equation 6.1) at a principle prescribed direction ($\theta_p = 0°$; where θ_p is propagation direction) and the accuracy of the approximation decreases with increasing θ_p. It is therefore not surprising that the models based on the Padé approximant (i.e., Kirby, 1986a; Kaihatu, 2001) gives poor performance for large angles of propagation, though still improved over the classical small-angle parabolic approximation. To address this shortcoming, an alternative approach – the minimax approximation – can also be used. The minimax approximation is intended to minimize the global maximum error within a prescribed interval ($0 \leq \theta_p \leq \theta_a$; where θ_a denotes aperture angle, a pre-set parameter within the approximation) by tolerating a minor deviation from optimal accuracy at small grazing angles. Realizing that the (1,1) Padé approximation is identical to the minimax approximation as $\theta_a \rightarrow 0$, Kirby (1986b) modified the parabolic approximation of Kirby (1986a) in the absence of current by replacing the Padé approximation coefficients with the coefficients of the minimax approach. Kirby (1986b) concluded that the minimax model with $\theta_a = 60°$ is the best model because the model shows similar and better performances than the (1,1) Padé model in the case of small-angle and wide-angle propagations, respectively (see

Equation 6.1 and Figure 29).

$$\cos\theta_p = \left(1-\sin^2\theta_p\right)^{1/2} : \text{exact solution}$$

$$\text{APRX}\left(\cos\theta_p\right) = \begin{cases} 1-\dfrac{1}{2}\sin^2\theta_p : \text{lowest-order approximation} \\ \dfrac{1-\dfrac{3}{4}\sin^2\theta_p}{1-\dfrac{1}{4}\sin^2\theta_p} ; (1,1)\,\text{padé approximation} \\ \dfrac{a_0 + a_1\sin^2\theta_p}{1+b_1\sin^2\theta_p} ; \text{minimax approximation} \end{cases} \tag{6.1}$$

where the coefficients of the minimax approximation with $\theta_a = 60°$ are given:

$$a_0 = 0.998213736;\ a_1 = -0.854229482;\ b_1 = -0.383283081 \tag{6.2}$$

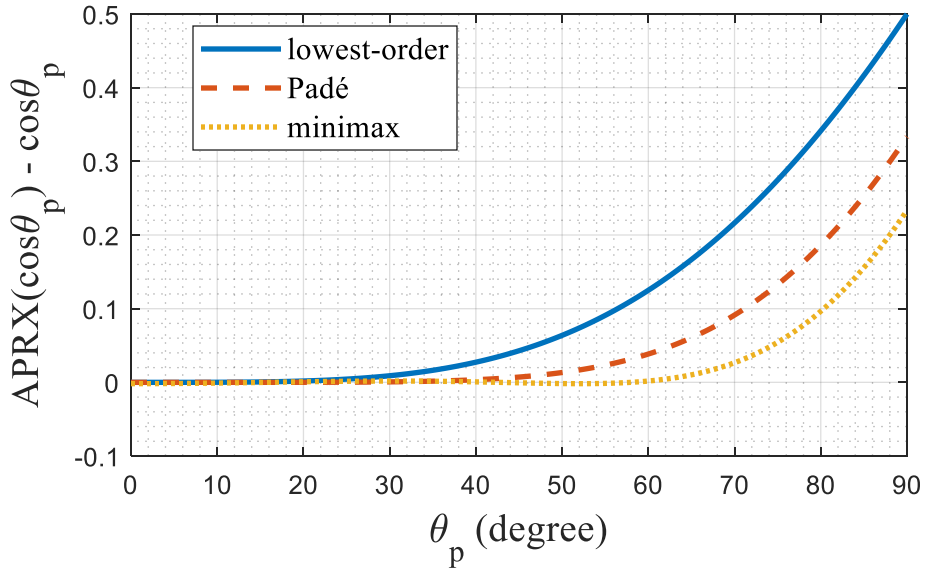

Figure 29 Comparison of absolute errors for various approximations (Solid: lowest-order approximation; Dashed: (1,1) Padé approximation; Dotted: minimax approximation with θ_a = 60°).

In order to allow for large-angle propagation, we thus select the minimax model with θ_a = 60° for the higher-order linear terms of the present model:

$$\begin{aligned} & 2i\left(kCC_g\right)_n A_{nx} - 2\left(kCC_g\right)_n \left(\bar{k}_n - a_0 k_n\right) A_n + i\left(kCC_g\right)_{nx} A_n \\ & +2\left\{-a_1 + b_1 \frac{\bar{k}_n}{k_n} + ib_1 \frac{k_{nx}}{k_n^2} + b_1 \frac{i\left(kCC_g\right)_{nx}}{2\left(k^2 CC_g\right)_n}\right\}\left[\left(CC_g\right)_n A_{ny}\right]_y \\ & -b_1 \frac{2i}{k_n}\left[\left(CC_g\right)_n A_{ny}\right]_{yx} = 0 \end{aligned} \tag{6.3}$$

where A_n is the complex amplitude of free surface elevation of nth frequency component, $\bar{k}_n$ is the y-averaged wave number, and subscribes x and y refer to derivatives with respect to x and y, respectively.

Kirby (1986a) chose a different ordering system from classic Stokes-type mild-slope equation models (Yue and Mei, 1980; Kirby and Dalrymple, 1983), which is the relation between the wave steepness ε (= ka where a is the wave amplitude), the modulation scale δ (where A_n is function of δx and $\delta^{1/2}y$), and the scale for bottom slope α. Kirby (1986a) chose the following ordering:

$$A_n \sim O(\varepsilon),\ O(\delta^2) \sim O(\varepsilon) \sim O(\alpha^{1/2}) \tag{6.4}$$

The present study obtained an elliptic mild-slope equation which is slightly different from that of previous studies (e.g., Agnon et al., 1993; Kaihatu and Kirby, 1995; Tang and Ouellet, 1997; Eldeberky and Madsen, 1999 among many others), as it was derived by using the combined free surface boundary condition with fewer horizontal derivative terms. In addition, the revised scaling relating bathymetric variations to amplitude modulations ($O(\delta) \sim O(\varepsilon^2)$) was employed, allowing consideration of additional triad wave-wave interaction terms. In the present study, we make use of the nonlinear terms in the present elliptic equation (nonlinear part of Equation 2.37):

$$\begin{aligned}(N.L) = &-\frac{i}{4}\left[\sum_{l=1}^{n-1} 2\omega_n \nabla_h \hat{\phi}_l \cdot \nabla_h \hat{\phi}_{n-l} - \left(\omega_l {k_{n-l}}^2 + \omega_{n-l} {k_l}^2\right)\hat{\phi}_l \hat{\phi}_{n-l} + \left\{\frac{\omega_l \omega_{n-l} \omega_n}{g^2}\left({\omega_l}^2 + {\omega_{n-l}}^2 + \omega_l \omega_{n-l}\right)\hat{\phi}_l \hat{\phi}_{n-l}\right\}\right] \\ &-\frac{i}{2}\left[\sum_{l=1}^{N-n} 2\omega_n \nabla_h \hat{\phi}_l^* \cdot \nabla_h \hat{\phi}_{n+l} - \left(\omega_{n+l} {k_l}^2 - \omega_l {k_l}^2\right)\hat{\phi}_l^* \hat{\phi}_{n+l} - \left\{\frac{\omega_l \omega_{n+l} \omega_n}{g^2}\left({\omega_l}^2 + {\omega_{n+l}}^2 - \omega_l \omega_{n+l}\right)\hat{\phi}_l^* \hat{\phi}_{n+l}\right\}\right]\end{aligned} \tag{6.5}$$

where ω_n is the wave angular frequency, g is the gravitational acceleration, two sets of two arbitrary frequency components, (l, $n - l$) and (l, $n + l$) interact with the nth frequency mode through triad nonlinear interaction.

Following the ordering approach of Kirby (1986a), the following terms have the highest order in the linear higher-order parabolic model:

$$2ib_1 \frac{k_{nx}}{k_n^{\ 2}} \left(CC_g\right)_{ny} A_{ny}, b_1 \frac{2i}{k_n} \left(CC_g\right)_{nyx} A_{ny} = O\left(\varepsilon\alpha^2\delta\right) \sim O\left(\varepsilon^{5.5}\right) \tag{6.6}$$

Of the nonlinear terms in Equation (6.5), we have the following term at the highest order:

$$A_{lx} A_{n-lx} = O\left(\varepsilon^2\delta^4\right) \sim O\left(\varepsilon^4\right) \tag{6.7}$$

Hence, the choice of ordering system of Kirby (1986a) allows the model to include all the nonlinear terms without any terms eliminated from Equation (6.5):

$$\begin{aligned}
&2i\left(kCC_g\right)_n A_{nx} - 2\left(kCC_g\right)_n \left(\bar{k}_n - a_0 k_n\right) A_n + i\left(kCC_g\right)_{nx} A_n \\
&+2\left\{-a_1 + b_1 \frac{\bar{k}_n}{k_n} + ib_1 \frac{k_{nx}}{k_n^2} + b_1 \frac{i\left(kCC_g\right)_{nx}}{2\left(k^2 CC_g\right)_n}\right\}\left[\left(CC_g\right)_n A_{ny}\right]_y - b_1 \frac{2i}{k_n}\left[\left(CC_g\right)_n A_{ny}\right]_{yx} \\
&= \frac{1}{4}\sum_{l=1}^{n-1} \begin{bmatrix} R_1 A_l A_{n-l} + R_2\left(i\left\{\bar{k}_l - k_l\right\} A_l A_{n-l} + A_{lx} A_{n-l}\right) \\ +R_3\left(i\left\{\bar{k}_{n-l} - k_{n-l}\right\} A_l A_{n-l} + A_l A_{n-lx}\right) + R_4 A_{ly} A_{n-ly} \\ +R_4\left(i\left\{\bar{k}_l - k_l\right\} A_l + A_{lx}\right)\left(i\left\{\bar{k}_{n-l} - k_{n-l}\right\} A_{n-l} + A_{n-lx}\right) \end{bmatrix} e^{i\int\left(\bar{k}_l + \bar{k}_{n-l} - \bar{k}_n\right)dx} \\
&+\frac{1}{2}\sum_{l=1}^{N-n} \begin{bmatrix} S_1 A_l^{\ *} A_{n+l} + S_2\left(-i\left\{\bar{k}_l - k_l\right\} A_l^{\ *} A_{n+l} + A_{lx}^{\ *} A_{n+l}\right) \\ +S_3\left(i\left\{\bar{k}_{n+l} - k_{n+l}\right\} A_l^{\ *} A_{n+l} + A_l^{\ *} A_{n+lx}\right) + S_4 A_{ly}^{\ *} A_{n+ly} \\ +S_4\left(-i\left\{\bar{k}_l - k_l\right\} A_l^{\ *} + A_{lx}^{\ *}\right)\left(i\left\{\bar{k}_{n+l} - k_{n+l}\right\} A_{n+l} + A_{n+lx}\right) \end{bmatrix} e^{i\int\left(\bar{k}_{n+l} - \bar{k}_l - \bar{k}_n\right)dx}
\end{aligned} \tag{6.8}$$

where the interaction coefficients (R and S) are the same as Equation (2.48). We note that A_xA_x is added to the nonlinear terms of Equation (2.59) where a_n in Equation (2.59) is equivalent to A_n in Equation (6.8).

6.3 Angular spectrum model

6.3.1 Lateral depth variation

Higher-order approximations require more terms for higher accuracy at very wide-angle propagation (Dalrymple and Kirby, 1988). These terms may not be accommodated by the parabolic formulation, destroying a key advantage over elliptic models. Therefore, in order to develop the models which is available for the large wave angles up to 90°, many researchers have used the angular spectrum formulation for multi-directional wave propagation. The angular spectrum model requires the use of a Fourier transform in the alongshore direction (i.e., y-direction, where x is positive when pointed in the onshore direction), by which the wave train is decomposed into discrete Fourier components in longshore wavenumber. This may also require that the environmental conditions present (bathymetry, currents, etc.) satisfy longshore periodicity. Several attempts have been made in this regard: (1) alongshore-uniform topography is assumed (Dalrymple and Kirby, 1988; Kirby, 1991; Agnon and Sheremet, 1997; Eldeberky and Madsen, 1999; Herbers et al., 2003; Vrecica and Toledo, 2016, 2019); (2) the lateral bottom variation is expressed in terms of an x-varying laterally averaged wave number (Dalrymple et al., 1989; Bredmose et al., 2005); (3) ordered

lateral depth variation represents the interaction between bottom change in the transverse y-direction and surface wave (Suh et al., 1990; Janssen et al., 2006).

In the present study, we follow the same kind of manipulation by way of laterally averaged water depth $\bar{h}$ (Suh et al., 1990; Janssen et al., 2006) in order to formulate a consistently-ordered model with the consistent nonlinear mild-slope equation model. The bathymetry is defined by a one-dimensional reference depth (or $\bar{h}$) and the lateral depth variations $\bar{h}$:

$$h(x,y) = \bar{h}(x) - \tilde{h}(x,y) \tag{6.9}$$

where the lateral average of water depth is defined by:

$$\bar{h} = \frac{1}{y}\int_0^y h(x,\xi)\,d\xi \tag{6.10}$$

We define that the lateral depth variation is of order of the small parameter γ_h, and we assume $O(\gamma_h) \sim O(\varepsilon)$ in order to use perturbation scheme:

$$O\left(\frac{\tilde{h}_0}{\bar{h}_0}\right) = O(\gamma_h) \sim O(\varepsilon) << 1 \tag{6.11}$$

where subscript 0 denotes the references values. For later convenience, $v \sim O(1)$ is introduced to obviously express the order of lateral depth variation:

$$\tilde{h}(x,y) = \varepsilon \bar{h}(x) v(x,y) \tag{6.12}$$

6.3.2 Derivation of elliptic equation

Using Taylor series about still water level and laterally-averaged water depth (i.e., $z = 0$ and $z = -\bar{h}$ where z is positive vertically upward from the still water level) for free surface boundary conditions and bottom boundary condition, respectively, the truncated boundary value problem is formulated with the leading order nonlinearity of $O(\varepsilon^2)$ as:

$$\nabla_h{}^2\phi + \phi_{zz} = 0 \; ; \; -\bar{h} \le z \le 0 \tag{6.13}$$

$$\phi_z = -\tilde{h}\phi_{zz} - \partial_x\bar{h}\partial_x\phi - \tilde{h}\partial_x\bar{h}\partial_x\phi_z + \nabla_h\tilde{h}\cdot\nabla_h\phi + O\left(\varepsilon^3\right) \; ; \; z = -\bar{h} \tag{6.14}$$

$$g\eta = -\phi_t - \frac{1}{2}\left(\nabla_h\phi\right)^2 - \frac{1}{2}\phi_z{}^2 - \eta\phi_{tz} + O\left(\varepsilon^3\right) \; ; \; z = 0 \tag{6.15}$$

$$\eta_t = \phi_z - \nabla_h\eta\cdot\nabla_h\phi + \eta\phi_{zz} + O\left(\varepsilon^3\right) \; ; \; z = 0 \tag{6.16}$$

Combined free surface elevation is obtained by manipulating Equations (6.15) and (6.16):

$$\phi_z = -\frac{1}{g}\left[\phi_{tt} + \frac{1}{2}\left(\nabla_h\phi\right)^2{}_t + \frac{1}{2}\left(\phi_z\right)^2{}_t - \frac{1}{2g}\left(\phi_t\right)^2{}_{zt} + \nabla_h\phi_t\cdot\nabla_h\phi - \phi_t\phi_{zz}\right]; \; z = 0 \tag{6.17}$$

Wave potential function is given as a superposition of solutions from fully dispersive linear theory:

$$\phi\left(x,y,z,t\right) = \sum_{n=1}^{N} f_n\left(z,\bar{h}\right)\tilde{\phi}_n\left(x,y,t\right) \tag{6.18}$$

Further, the depth dependence function is independent of y-direction:

$$f_n\left(z,\bar{h}\right) = \frac{\cosh\bar{k}_n\left(\bar{h}+z\right)}{\cosh k_n\bar{h}} \tag{6.19}$$

The wave frequency and the y-averaged wave number are related by the linear dispersion relation:

$$\omega_n^{\,2} = g\bar{k}_n \tanh \bar{k}_n \bar{h} \tag{6.20}$$

Following Smith and Sprinks (1975), we apply Green's second identity:

$$\int_{-\bar{h}}^{0} \left(f\phi_{zz} - \phi f_{zz} \right) dz = \left[f\phi_z - \phi f_z \right]_{-\bar{h}}^{0} \tag{6.21}$$

Using features of depth dependence function f and Equations (6.13), (6.14), and (6.17) gives:

$$\begin{aligned} &-\int_{-\bar{h}}^{0} \left(f_n \nabla_h^{\,2} \phi_n + \bar{k}_n^{\,2} \phi_n f_n \right) dz \\ &= \left(N.L. \right) - \left[\frac{1}{g} \phi_{ntt} f_n + \frac{\omega_n^{\,2}}{g} \phi_n f_n \right]_{z=0} \\ &+ \left[f_n \tilde{h} \phi_{nzz} + f_n \partial_x \bar{h} \partial_x \phi_n + f_n \tilde{h} \partial_x \bar{h} \partial_x \phi_{nz} - f_n \nabla_h \tilde{h} \cdot \nabla_h \phi_n \right]_{z=-\bar{h}} \end{aligned} \tag{6.22}$$

where nonlinear term is:

$$\left(N.L. \right) = \left[-\frac{f_n}{g} \left\{ \left(\nabla_h \phi_n \right)_t^{\,2} + \frac{1}{2} \left(\phi_{nz} \right)_t^{\,2} - \frac{1}{2g} \left(\phi_{nt} \right)_{zt}^{\,2} - \phi_{nt} \phi_{nzz} \right\} \right]_{z=0} \tag{6.23}$$

We use $\tilde{\phi}$ and f to represent horizontal derivatives of potential function ϕ:

$$\nabla_h \phi = \nabla_h \left(\tilde{\phi}(x,y)\, f\left(z, \bar{h}\right) \right) = \left(f \partial_x \tilde{\phi} + \tilde{\phi} \frac{\partial f}{\partial \bar{h}} \partial_x \bar{h},\, f \partial_y \tilde{\phi} \right) \tag{6.24}$$

$$\begin{aligned} \nabla_h^{\,2} \phi &= \left(\nabla_h^{\,2} \tilde{\phi} \right) f + 2 \partial_x \tilde{\phi} \frac{\partial f}{\partial \bar{h}} \partial_x \bar{h} + \tilde{\phi} \frac{\partial^2 f}{\partial \bar{h}^2} \left(\partial_x \bar{h} \right)^2 + \tilde{\phi} \frac{\partial f}{\partial \bar{h}} \partial_x^{\,2} \bar{h} \\ &= \frac{1}{f} \nabla_h \left[\left(\nabla_h \tilde{\phi} \right) f^2 \right] + \tilde{\phi} \frac{\partial^2 f}{\partial \bar{h}^2} \left(\partial_x \bar{h} \right)^2 + \tilde{\phi} \frac{\partial f}{\partial \bar{h}} \partial_x^{\,2} \bar{h} \end{aligned} \tag{6.25}$$

Plugging Equations (6.24) and (6.25) into Equation (6.22):

$$
\begin{aligned}
&-\int_{-\bar{h}}^{0}\left(\nabla_h\left[\left(\nabla_h\tilde{\phi}_n\right)f_n{}^2\right]+\tilde{\phi}_n f_n\frac{\partial^2 f_n}{\partial\bar{h}^2}\left(\partial_x\bar{h}\right)^2+\tilde{\phi}_n f_n\frac{\partial f_n}{\partial\bar{h}}\partial_x{}^2\bar{h}+\bar{k}_n{}^2\tilde{\phi}_n f_n{}^2\right)dz\\
&=\left(N.L.\right)-\left[\frac{1}{g}\tilde{\phi}_{ntt}f_n{}^2+\frac{\omega_n{}^2}{g}\tilde{\phi}_n f_n{}^2\right]_{z=0}\\
&+\left[\begin{array}{l}
f_n f_{nzz}\tilde{\phi}_n\tilde{h}+f_n{}^2\partial_x\tilde{\phi}_n\partial_x\bar{h}+f_n\frac{\partial f_n}{\partial\bar{h}}\tilde{\phi}_n\left(\partial_x\bar{h}\right)^2\\
+f_n f_{nz}\partial_x\tilde{\phi}_n\tilde{h}\partial_x\bar{h}+f_n\frac{\partial f_{nz}}{\partial\bar{h}}\tilde{\phi}_n\tilde{h}\left(\partial_x\bar{h}\right)^2\\
-f_n{}^2\nabla_h\tilde{\phi}\cdot\nabla_h\tilde{h}-f_n\frac{\partial f_n}{\partial\bar{h}}\tilde{\phi}\partial_x\bar{h}\partial_x\tilde{h}
\end{array}\right]_{z=-\bar{h}}
\end{aligned}
\tag{6.26}
$$

Applying Leibnitz' rule, we obtain:

$$
\begin{aligned}
&-\nabla_h\left(\left[\int_{-\bar{h}}^{0}f_n{}^2dz\right]\nabla_h\tilde{\phi}_n\right)+\left[f_n{}^2\partial_x\tilde{\phi}_n\partial_x\bar{h}\right]_{z=-\bar{h}}\\
&-\bar{k}_n{}^2\left(\int_{-\bar{h}}^{0}f_n{}^2dz\right)\tilde{\phi}_n-\int_{-h}^{0}\left(f_n\frac{\partial^2 f_n}{\partial\bar{h}^2}\tilde{\phi}_n\left(\partial_x\bar{h}\right)^2+f_n\frac{\partial f_n}{\partial h}\tilde{\phi}_n\partial_x{}^2h\right)dz\\
&=(N.L.)-\left[\frac{1}{g}f_n{}^2\tilde{\phi}_{ntt}+\frac{\omega_n{}^2}{g}f_n{}^2\tilde{\phi}_n\right]_{z=0}+\left[f_n f_{nzz}\tilde{\phi}_n\tilde{h}+f_n{}^2\partial_x\tilde{\phi}_n\partial_x\bar{h}\right]_{z=-\bar{h}}\\
&+\left[\begin{array}{l}
f_n\frac{\partial f_n}{\partial\bar{h}}\tilde{\phi}_n\left(\partial_x\bar{h}\right)^2+f_n f_{nz}\partial_x\tilde{\phi}_n\tilde{h}\partial_x\bar{h}\\
+f_n\frac{\partial f_{nz}}{\partial\bar{h}}\tilde{\phi}_n\tilde{h}\left(\partial_x\bar{h}\right)^2-f_n{}^2\nabla_h\tilde{\phi}\cdot\nabla_h\tilde{h}-f_n\frac{\partial f_n}{\partial\bar{h}}\partial_x\bar{h}\partial_x\tilde{h}\tilde{\phi}_n
\end{array}\right]_{z=-h}
\end{aligned}
\tag{6.27}
$$

Following Kirby and Dalrymple (1983), we assumed $O(a) \sim O(\varepsilon^2)$ for the slowly varying water depth (i.e., $|\nabla_h h| = O(\alpha) << 1$) to properly balance nonlinear effect with bathymetric variations. In order to maintain the consistency with the present ordering system, we assume the sales for the horizontal derivatives of *h* and *v*:

$$
O\left(\partial_x\bar{h}\right)=O(\alpha)\sim O\left(\varepsilon^2\right),O\left(\nabla_h v\right)\sim O(\varepsilon)
\tag{6.28}
$$

and the order of the bottom slope then becomes equivalent to $O(a) \sim O(\varepsilon^2)$:

$$\begin{bmatrix} O\left(\partial_x h\right) = O\left(\partial_x \bar{h}\right) \\ = O\left(\alpha\right) \sim O\left(\varepsilon^2\right) \end{bmatrix} = \begin{bmatrix} O\left(\partial_y h\right) = O\left(\partial_y \tilde{h}\right) \\ = O\left(\varepsilon \bar{h} \partial_y v\right) \sim O\left(\varepsilon^2\right) \end{bmatrix} \tag{6.29}$$

We note that this scaling approach is identical to that of Janssen et al. (2006) in the case of intermediate water depth (i.e., $O\left(k_0 \bar{h}\right) \sim O(1)$ in Equation (2.3) of that publication). Then, we simplify the equation by eliminating the terms which are at higher order than the leading order nonlinearity $O(\varepsilon^2)$:

$$\begin{aligned} &-\nabla_h \left(\left[\int_{-\bar{h}}^{0} {f_n}^2 dz \right] \nabla_h \tilde{\phi}_n \right) - \bar{k}_n^{\,2} \left(\int_{-\bar{h}}^{0} {f_n}^2 dz \right) \tilde{\phi}_n - \left[f_n f_{nzz} \tilde{\phi}_n \tilde{h} \right]_{z=-\bar{h}} \\ &= (N.L.) - \left[\frac{1}{g} {f_n}^2 \tilde{\phi}_{ntt} + \frac{{\omega_n}^2}{g} {f_n}^2 \tilde{\phi}_n \right]_{z=0} \end{aligned} \tag{6.30}$$

where nonlinear terms are also simplified:

$$\left(N.L.\right) = -\frac{1}{g} \left[\begin{aligned} &\left\{ \sum_l \sum_m \left[f_l f_m \left(\nabla_h \tilde{\phi}_l \right) \cdot \left(\nabla_h \tilde{\phi}_m \right) \right] \right\}_t \\ &+ \frac{1}{2} \left\{ \sum_l \sum_m f_{lz} f_{mz} \tilde{\phi}_l \tilde{\phi}_m \right\}_t \\ &- \frac{1}{2g} \left\{ \sum_l \sum_m \left(f_{lz} f_m + f_l f_{mz} \right) \tilde{\phi}_{lt} \tilde{\phi}_{mt} \right\}_t \\ &- \frac{1}{2} \left\{ \sum_l \sum_m f_l f_{mzz} \tilde{\phi}_{lt} \tilde{\phi}_m + f_{lzz} f_m \tilde{\phi}_l \tilde{\phi}_{mt} \right\} \end{aligned} \right]_{z=0} \tag{6.31}$$

The frequency-domain model is derived under the assumption of periodicity in time:

$$\tilde{\phi}_n \left(x, y, t \right) = \frac{\hat{\phi}_n}{2} e^{-i\omega_n t} + \frac{\hat{\phi}_n^{\,*}}{2} e^{i\omega_n t} \tag{6.32}$$

With the values of expressions with depth dependence function *f* at the surface and bottom boundaries, we obtain:

$$\nabla_h \cdot \left[\left(\overline{CC_g} \right)_n \nabla_h \hat{\phi}_n \right] + \bar{k}_n^{\,2} \left(\overline{CC_g} \right)_n \hat{\phi}_n + \frac{g \bar{k}_n^{\,2}}{\cosh^2 \bar{k}_n \bar{h}} \tilde{h} \hat{\phi}_n$$

$$= \begin{pmatrix} -\frac{i}{4} \left[\sum_{l=1}^{n-1} \begin{matrix} 2\omega_n \left(\nabla_h \hat{\phi}_l \cdot \nabla_h \hat{\phi}_{n-l} \right) - \left(\omega_l \bar{k}_{n-l}^{\,2} + \omega_{n-l} \bar{k}_l^{\,2} \right) \hat{\phi}_l \hat{\phi}_{n-l} \\ + \left\{ \frac{\omega_l \omega_{n-l} \omega_n}{g^2} \left(\omega_l^{\,2} + \omega_{n-l}^{\,2} + \omega_l \omega_{n-l} \right) \hat{\phi}_l \hat{\phi}_{n-l} \right\} \end{matrix} \right] \\ -\frac{i}{2} \left[\sum_{l=1}^{N-n} \begin{matrix} 2\omega_n \left(\nabla_h \hat{\phi}_l^{\,*} \cdot \nabla_h \hat{\phi}_{n+l} \right) - \left(\omega_{n+l} \bar{k}_l^{\,2} - \omega_l \bar{k}_l^{\,2} \right) \hat{\phi}_l^{\,*} \hat{\phi}_{n+l} \\ - \left\{ \frac{\omega_l \omega_{n+l} \omega_n}{g^2} \left(\omega_l^{\,2} + \omega_{n+l}^{\,2} - \omega_l \omega_{n+l} \right) \hat{\phi}_l^{\,*} \hat{\phi}_{n+l} \right\} \end{matrix} \right] \end{pmatrix} \tag{6.33}$$

where

$$\left(\overline{CC_g} \right)_n = \frac{g}{\cosh^2 \bar{k}_n \bar{h}} \left(\frac{\sinh 2\bar{k}_n \bar{h}}{4\bar{k}_n} + \frac{\bar{h}}{2} \right) \tag{6.34}$$

There are two differences between Equation (6.33) and the elliptic equation of CNMSE (Equation 2.37): (1) all the wave characteristics (i.e., $\bar{h}$, $\overline{k_n}$, $\overline{(CC_g)_n}$) are of *y*-averaged value in Equation (6.33) except for the third term on its left-hand side; (2) the third term is added and it represents the interaction between $\hat{\phi}_n$ and $\tilde{h}$, thereby involving the effect of lateral depth variation effects in Equation (6.33).

6.3.3 Derivation of Angular spectrum model

The wave potential function Equation (6.18) is (via the depth-dependence function) based on the premise of fully dispersive linear theory applied to a surface wave field propagating over straight and parallel bathymetric contours (Suh et al. 1990). Due to this longshore-periodic assumption, we can then decompose the *y*-dependent wave

potential function into a superposition of the discrete alongshore component wavenumbers by Fourier transform:

$$F_m\left[\hat{\phi}_n(x,y)\right] = -\frac{ig}{\omega_n} A_{n,m}(x) \exp\left[i\int k_{n,m}dx\right] \tag{6.35}$$

where F_m denote the mth component of the discrete Fourier transform in y-direction, we thus have:

$$\hat{\phi}_n(x,y) = -\frac{ig}{\omega_n} \sum_{m=-M}^{M} A_{n,m}(x) e^{i\left[\int k_{n,m}dx + m\lambda y\right]} \tag{6.36}$$

and

$$\hat{\phi}_n^{\,*}(x,y) = \frac{ig}{\omega_n} \sum_{m=-M}^{M} A_{n,m}^{\,*}(x) e^{-i\left[\int k_{n,m}dx + m\lambda y\right]} \tag{6.37}$$

where $A_{n,m}$ is the complex amplitude of nth frequency component and mth alongshore component, which propagates independently in the direction:

$$\theta_p = \tan^{-1}\left(\frac{m\lambda}{k_{n,m}}\right) \tag{6.38}$$

where alongshore wavenumber increment is given by:

$$\lambda = \frac{2\pi}{(2M+1)\Delta y} \tag{6.39}$$

Here the width of domain is $L_y = (2M)\cdot\Delta y$, and the Pythagoras theorem is satisfied between wavenumbers:

$$\left(\bar{k}_n\right)^2 = \left(k_{n,m}\right)^2 + \left(m\lambda\right)^2 \tag{6.40}$$

The evanescent modes (or non-progressive modes) m where $(k_{n,m})^2 < 0$ decline exponentially. Following Suh et al. (1990), we neglect the evanescent modes at the offshore boundary under the assumption that the evanescent modes are negligible compared to the progressive modes. Since y-averaged wave number $\overline{k_n}$ increases with both decreasing water depth $\bar{h}$, and wave frequency ω_n, the number of alongshore components varies with the frequency component n. Thus, we introduce a notation M_n to indicate the number of active modes in alongshore-domain (i.e., $2M_n + 1$).

As mentioned earlier, the application of the elliptic version to the open-ocean conditions results in several problems (computational inefficiency, inability to specify downwave boundary condition). Based on the parabolic approximation of the consistent nonlinear mild-slope equation (see Chapter 2), we thus eliminate terms of $O(\varepsilon\delta\alpha, \varepsilon\delta^2) \sim O(\varepsilon^5)$ or higher in Equation (6.33) in order to derive parabolic form:

$$
\begin{aligned}
&2i\left(k_{n,m}\left[\overline{CC_g}\right]_n\right)A_{n,mx} + i\left(k_{n,m}\left[\overline{CC_g}\right]_n\right)_x A_{n,m} \\
&+\frac{g\overline{k}_n^{\,2}}{\cosh^2 k_n\bar{h}} F_m\left[\tilde{h}(x,y)\,F^{-1}\left(A_{n,m}e^{i\int k_{n,m}dx}\right)\right]e^{-i\left[\int k_{n,m}dx\right]} \\
&=\frac{1}{4}\sum_{p=\max\{-M_{n-l}+m,-M_l\}}^{\min\{M_{n-l}+m,M_l\}}\sum_{l=1}^{n-1}\left[\begin{array}{l}\overline{R}_1 A_{l,p}A_{n-l,m-p} \\ +\overline{R}_2 A_{l,px}A_{n-l,m-p} + \overline{R}_3 A_{l,p}A_{n-l,m-px}\end{array}\right]e^{\left(i\int k_{l,p}+k_{n-l,m-p}-k_{n,m}dx\right)} \\
&+\frac{1}{2}\sum_{p=\max\{-M_{n+l}-m,-M_l\}}^{\min\{M_{n+l}-m,M_l\}}\sum_{l=1}^{N-n}\left[\begin{array}{l}\overline{S}_1 A_{l,p}{}^{*}A_{n+l,m+p} \\ +\overline{S}_2 A_{l,px}{}^{*}A_{n+l,m+p} + \overline{S}_3 A_{l,p}{}^{*}A_{n+l,m+px}\end{array}\right]e^{\left(i\int -k_{l,p}+k_{n+l,m+p}-k_{n,m}dx\right)}
\end{aligned}
\tag{6.41}
$$

where F^{-1} denotes the inverse Fourier transform, and the overbarred interaction coefficients are:

$$\bar{R}_1 = \frac{g}{\omega_l \omega_{n-l}}\left[2\omega_n{}^2\left(k_{l,p}k_{n-l,m-p} + p(m-p)\lambda^2\right) + \omega_n\left(\omega_{n-l}\bar{k}_l{}^2 + \omega_l\bar{k}_{n-l}{}^2\right)\right] - \frac{\omega_n{}^2}{g}\left(\omega_l{}^2 + \omega_l\omega_{n-l} + \omega_{n-l}{}^2\right) \tag{6.42}$$

$$\bar{R}_2 = -2i\frac{g\omega_n{}^2 k_{n-l,m-p}}{\omega_l\omega_{n-l}} \tag{6.43}$$

$$\bar{R}_3 = -2i\frac{g\omega_n{}^2 k_{l,p}}{\omega_l\omega_{n-l}} \tag{6.44}$$

and

$$\bar{S}_1 = \frac{g}{\omega_l \omega_{n+l}}\left[2\omega_n{}^2\left(k_{l,p}k_{n+l,m+p} + p(m+p)\lambda^2\right) + \omega_n\left(\omega_l\bar{k}_{n+l}{}^2 - \omega_{n+l}\bar{k}_l{}^2\right)\right] - \frac{\omega_n{}^2}{g}\left(\omega_l{}^2 - \omega_l\omega_{n+l} + \omega_{n+l}{}^2\right) \tag{6.45}$$

$$\bar{S}_2 = 2i\frac{g\omega_n{}^2 k_{n+l,m+p}}{\omega_l\omega_{n+l}} \tag{6.46}$$

$$\bar{S}_3 = -2i\frac{g\omega_n{}^2 k_{l,p}}{\omega_l\omega_{n+l}} \tag{6.47}$$

The last term on the left-hand side of Equation (6.41) represents the interaction between surface wave modes and lateral bottom variation, which is a subset of the forcing terms in Janssen et al. (2006). The premise of the leading order nonlinearity of $O(\varepsilon^2)$ leads us to discard the higher-order terms accounting for the interaction between wave and lateral bottom variation. In this study, we however correct the forcing term for a case with a significant lateral depth variation by fully consideration of the terms in Janssen et al. (2006):

$$
\begin{aligned}
&2i\left(k_{n,m}\left[\overline{CC_g}\right]_n\right)A_{n,mx}+i\left(k_{n,m}\left[\overline{CC_g}\right]_n\right)_x A_{n,m}\\
&+\frac{g}{\cosh^2\bar{k}_n\bar{h}}\left[\begin{array}{l}
\bar{k}_n{}^2F_m\left\{\tilde{h}(x,y)F^{-1}\left(A_{n,p}e^{i\int k_{n,p}dx}\right)\right\}\\
-ik_{n,m}P_{n,m}F_m\left\{\tilde{h}_x(x,y)F^{-1}\left(A_{n,p}e^{i\int k_{n,p}dx}\right)\right\}\\
-im\lambda\left(\bar{k}_n\bar{h}T_1-1\right)F_m\left\{\tilde{h}_y(x,y)F^{-1}\left(A_{n,p}e^{i\int k_{n,p}dx}\right)\right\}\\
+\bar{k}_n{}^3\dfrac{\bar{C}_n}{2\bar{C}_{gn}}\dfrac{\left(1-T_n{}^2\right)}{T_n}\left[\dfrac{1}{1-T_n{}^2}-P_{n,m}\right]F_m\left\{\tilde{h}^2(x,y)F^{-1}\left(A_{n,p}e^{i\int k_{n,p}dx}\right)\right\}
\end{array}\right]e^{-i\int k_{n,m}dx}\\
&=\frac{1}{4}\sum_{p=\max\{-M_{n-l}+m,-M_l\}}^{\min\{M_{n-l}+m,M_l\}}\sum_{l=1}^{n-1}\left[\begin{array}{l}
\overline{R_1}A_{l,p}A_{n-l,m-p}\\
+\overline{R_2}A_{l,px}A_{n-l,m-p}+\overline{R_3}A_{l,p}A_{n-l,m-px}
\end{array}\right]e^{\left(i\int k_{l,p}+k_{n-l,m-p}-k_{n,m}dx\right)}\\
&+\frac{1}{2}\sum_{p=\max\{-M_{n+l}-m,-M_l\}}^{\min\{M_{n+l}-m,M_l\}}\sum_{l=1}^{N-n}\left[\begin{array}{l}
\overline{S_1}A_{l,p}{}^*A_{n+l,m+p}\\
+\overline{S_2}A_{l,px}{}^*A_{n+l,m+p}+\overline{S_3}A_{l,p}{}^*A_{n+l,m+px}
\end{array}\right]e^{\left(i\int -k_{l,p}+k_{n+l,m+p}-k_{n,m}dx\right)}
\end{aligned}
\tag{6.48}
$$

where

$$
P_{n,m}=\left\{\frac{1}{2}\left[\left(\frac{\bar{k}_n}{k_{n,m}}\right)^2-1\right]-\frac{\bar{C}_n}{2\bar{C}_{gn}}\left(1-\bar{k}_n\bar{h}T_n\right)\right\}
\tag{6.49}
$$

and

$$
T_n=\tanh\bar{k}_n\bar{h}
\tag{6.50}
$$

Despite the fact that the effects of lateral depth variation are further taken into consideration in an *a posteriori* sense, it is noteworthy that the additional forcing terms are at lower order than the neglected terms in the parabolic approach, that is, the terms are at equal to or lower than $O(\varepsilon^4)$:

$$\tilde{h}_x(x,y)F^{-1}\left(A_{n,p}e^{i\int k_{n,p}dx}\right),\tilde{h}_y(x,y)F^{-1}\left(A_{n,p}e^{i\int k_{n,p}dx}\right)=O\left(\varepsilon^2\alpha\right)\sim O\left(\varepsilon^4\right) \quad (6.51)$$

$$\tilde{h}^2(x,y)F^{-1}\left(A_{n,p}e^{i\int k_{n,p}dx}\right)\sim O\left(\varepsilon^3\right) \quad (6.52)$$

6.4 Model validation

In order to address whether the Fourier spectrum in the longshore direction results in any loss of accuracy and test the capability of models for wide-angle propagation, we now conduct several comparisons between the higher-order parabolic equation model (Equation 6.8; hereinafter HPM: CNMSE in figures and tables) and the angular spectrum model (Equation 6.48; hereinafter ASM: CNMSE in figures and tables) and experimental data. Furthermore, in order to study the nonlinear amplitude gradient terms (e.g., A_xA, A_yA_y) that we added to the consistent nonlinear mild-slope equation model, we also compare the reduced equations of Equations (6.8) and (6.48) retaining only the nonlinear terms of Kaihatu and Kirby (1995) (i.e., AA), which are referred to as HPM: KK95 and ASM: KK95 in figures and tables, respectively. The higher-order parabolic model with the nonlinear terms of Kaihatu and Kirby (1995) is:

$$\begin{aligned}
&2i\left(kCC_g\right)_n A_{nx}-2\left(kCC_g\right)_n\left(\bar{k}_n-a_0k_n\right)A_n+i\left(kCC_g\right)_{nx}A_n\\
&+2\left\{-a_1+b_1\frac{\bar{k}_n}{k_n}+ib_1\frac{k_{nx}}{k_n^2}+b_1\frac{i\left(kCC_g\right)_{nx}}{2\left(k^2CC_g\right)_n}\right\}\left[\left(CC_g\right)_n A_{ny}\right]_y\\
&-b_1\frac{2i}{k_n}\left[\left(CC_g\right)_n A_{ny}\right]_{yx}\\
&=\frac{1}{4}\sum_{l=1}^{n-1}R_1A_lA_{n-l}e^{i\int\left(\bar{k}_l+\bar{k}_{n-l}-\bar{k}_n\right)dx}+\frac{1}{2}\sum_{l=1}^{N-n}S_1A_l^*A_{n+l}e^{i\int\left(\bar{k}_{n+l}-\bar{k}_l-\bar{k}_n\right)dx}
\end{aligned} \quad (6.53)$$

For the angular spectrum model with the nonlinear terms of Kaihatu and Kirby (1995), Equation (6.48) is reduced to Equation (6.54):

$$
\begin{aligned}
&2i\left(k_{n,m}\left[\overline{CC_g}\right]_n\right)A_{n,mx}+i\left(k_{n,m}\left[\overline{CC_g}\right]_n\right)_x A_{n,m}\\
&+\frac{g}{\cosh^2\bar{k}_n\bar{h}}\left[\begin{array}{l}
\bar{k}_n{}^2F_m\left\{\tilde{h}(x,y)F^{-1}\left(A_{n,p}e^{i\int k_{n,p}dx}\right)\right\}\\
-ik_{n,m}P_{n,m}F_m\left\{\tilde{h}_x(x,y)F^{-1}\left(A_{n,p}e^{i\int k_{n,p}dx}\right)\right\}\\
-im\lambda\left(\bar{k}_n\bar{h}T_1-1\right)F_m\left\{\tilde{h}_y(x,y)F^{-1}\left(A_{n,p}e^{i\int k_{n,p}dx}\right)\right\}\\
+\bar{k}_n{}^3\dfrac{\bar{C}_n}{2\bar{C}_{gn}}\dfrac{\left(1-T_n{}^2\right)}{T_n}\left[\dfrac{1}{1-T_n{}^2}-P_{n,m}\right]F_m\left\{\tilde{h}^2(x,y)F^{-1}\left(A_{n,p}e^{i\int k_{n,p}dx}\right)\right\}
\end{array}\right]e^{-i\int k_{n,m}dx}\\
&=\frac{1}{4}\sum_{p=\max\{m-M_{n-l},-M_l\}}^{\min\{M_l,M_{n-l}+m\}}\sum_{l=1}^{n-1}\overline{R}_1A_{l,p}A_{n-l,m-p}e^{\left(i\int k_{l,p}+k_{n-l,m-p}-k_{n,m}dx\right)}\\
&+\frac{1}{2}\sum_{p=\max\{-m-M_{n+l},-M_l\}}^{\min\{M_{n+l}-m,M_l\}}\sum_{l=1}^{N-n}\overline{S}_1A_{l,p}{}^*A_{n+l,m+p}e^{\left(i\int -k_{l,p}+k_{n+l,m+p}-k_{n,m}dx\right)}
\end{aligned}
\tag{6.54}
$$

The numerical integration is done by schemes of the Crank-Nicolson (Crank and Nicolson, 1947), and the iteration procedure (where relative tolerance 10^{-3}) is necessary to obtain the solutions of the parabolic equations. Since the second-order accuracy in the surface elevation was confirmed for the case of the finite number of waves in Chapter 3, we compare the corrected results by a second-order correction (Equation 2.84). For the angular spectrum model, we also derive the second-order relationships by substituting the decomposed angular spectrum of wave potential $A_{n,m}$ and that of free surface elevation $B_{n,m}$ into the dynamic free surface boundary condition (6.17):

$$B_{n,m} = A_{n,m} + \frac{1}{4g} \sum_{p=\max\{-M_l,-M_{n-l}+m\}}^{\min\{M_l,M_{n-l}+m\}} \left[\sum_{l=1}^{n-1} \bar{I} A_{l,p} A_{n-l,m-p} e^{\left(i\int k_{l,p}+k_{n-l,m-p}-k_{n,m}dx \right)} \right] + \frac{1}{2g} \sum_{p=\max\{-M_l,-M_{n+l}-m\}}^{\min\{M_l,M_{n+l}-m\}} \left[\sum_{l=1}^{N-n} \bar{J} A_{l,p}^{\ *} A_{n+l,m+p} e^{\left(i\int -k_{l,p}+k_{n+l,m+p}-k_{n,m}dx \right)} \right] \tag{6.55}$$

where the *y*-averaged interaction coefficients are:

$$\bar{I} = \omega_l^{\,2} + \omega_l \omega_{n-l} + \omega_{n-l}^{\,2} - g^2 \left(\frac{k_{l,p} k_{n-l,m-p} + p(m-p)\lambda^2}{\omega_l \omega_{n-l}} \right) \tag{6.56}$$

$$\bar{J} = \omega_l^{\,2} - \omega_l \omega_{n+l} + \omega_{n+l}^{\,2} - g^2 \left(\frac{k_{l,p} k_{n+l,m+p} + p(m+p)\lambda^2}{\omega_l \omega_{n+l}} \right) \tag{6.57}$$

We determined the optimal grid size by conducting a grid convergence procedure, in which the grid size was systematically reduced until no further improvements were possible. Table 21 details the grid sizes and the number of grids used for the final numerical calculations of each test. For each of the cases considered, we initialized the amplitude for the first harmonic with the given input values at the deeper array while the higher harmonic waves were set to be zero-amplitude. We note that the lateral boundaries are taken to be reflective for all the experiments. To give a more quantitative evaluation of the model accuracy, we compare the value of index of agreement (IOA; Willmott, 1982) ranging from 0 to 1 where 1 indicates a perfect match:

$$I_a = 1 - \frac{\sum_{j=1}^{N_y} \sum_{i=1}^{N_x} \left(A_{n,j}^i - A_{n.j,obs}^i \right)^2}{\sum_{j=1}^{N_y} \sum_{i=1}^{N_x} \left[\left| A_{n,j}^i - \bar{A}_{n.j,obs}^i \right| + \left| A_{n,j,obs}^i - \bar{A}_{n.j,obs}^i \right| \right]^2} \tag{6.58}$$

where $A_{n,j}^{i}$ is the computed *n*th amplitude from models at *x* (= $i\Delta x$, i = 1 to N_x) and *y* (= $j\Delta y$, j = 1 to N_y), and $A_{n,j,obs}^{i}$ is the observed *n*th harmonic function from experimental data at *x* (= $i\Delta x$, i = 1 to N_x) and *y* (= $j\Delta y$, j = 1 to N_y), and over bar indicates an average.

Table 21 Grid sizes and the total number of grids for computation of each experiment.

Data	Whalin (1971)	Berkhoff et al. (1982)	Circular shoal
Δx (m)	0.242	0.083	0.083
Δy (m)	0.056	0.083	0.333
Grids	100×109	261×243	300×297

6.4.1 Whalin et al. (1971)

As a first step, we compare numerical results from the models described in this chapter, as well as previously-developed models, with the experimental data of Whalin (1971), who conducted a laboratory experiment to study wave focusing and wave refraction over two-dimensional bathymetry. Table 22 details wave parameter including the number of harmonics used in the numerical implementation, and the nonlinearity parameters for the experiment of Whalin (1971).

Table 22 Wave parameters and dimensionless parameters of Whalin (1971).

Case	a_0 (m)	T (s)	N	M
31	0.0068	3	5	54
32	0.0098	3	5	54
33	0.0146	3	5	54
21	0.0075	2	3	54
22	0.0106	2	3	54
23	0.0149	2	3	54
11	0.0097	1	2	54
12	0.0195	1	2	54

Comparison with the measurements along the centerline of the wave tank for all the cases is shown in Figures 30-32. Tables 23-25 compare the statistical parameters for model accuracy between models. The numerical results are obtained by the present higher-order parabolic model (Equation 6.8; HPM: CNMSE), the higher-order parabolic model with the nonlinear terms of Kaihatu and Kirby (1995) (Equation 6.53; HPM: KK95), the present angular spectrum model (Equation 6.48; ASM: CNMSE), and the angular spectrum model with the nonlinear terms of Kaihatu and Kirby (Equation 6.54; ASM: KK95).

For the case of T = 3 s, although the higher-order parabolic models predict the first harmonic amplitude in a better way than the angular spectrum models, all the models exhibit significant deviation from the measurement. This disagreement is probably ascribed to the frictional dissipation of the waves (Liu et al. 1985), which is consistent to the report by Whalin (1971) that there is a very small amount to wave

damping owing to the viscous boundary layers along the wave tank. However, the viscous damping mechanisms were not considered in none of the models compared here. For the second and third-harmonic amplitudes, the agreements between the observations and predictions by all the models are satisfactorily good.

At near the beginning of the slope (x = 8 m), the focusing occurred more rapidly due to the wave convergence and wave refraction caused by the sudden change from the flat bottom to the sloping bottom. It is remarkable that the sudden increases of the first harmonic amplitudes in the case of T = 3 s are captured satisfactorily well by the angular spectrum models. Although many previous studies have compared to the T = 3 s case of Whalin's experiment (Tang and Ouellet, 1997; Engsig-Karup et al., 2009; Raoult et al. 2019; Kim and Kaihatu, 2021; Lin et al., 2021 among many others), none of them predicted the abrupt rises in the amplitudes of the first harmonic. The predictions of the rises by the angular spectrum models are probably due to the analysis of wave train via the superposition of a wavefield propagating in a specific direction, which renders the angular spectrum models to account for the simultaneous diffraction and refraction of waves as well as simulate the wave ray crossing with great accuracy.

As can be seen in Figure 31 and Table 24 for the case of T = 2 s, the agreement between experimental data and numerical solution of all the present models is reasonable with the exception that angular spectrum models overpredicts the amplitudes of first harmonics. For the case of T = 1 s, all the mild-slope equation models agree favorably with the experimental data: the oscillating second harmonic amplitudes are well modeled by all the models, which is consistent with the improvements obtained in Kim and

Kaihatu (2021). While we demonstrate the ability of the angular spectrum models to address the focused wave at the entrance of slope in the case of T = 3 s, neither of models account for the generation of the sudden increases of the first harmonic amplitudes in the case of T = 1 and 2 s.

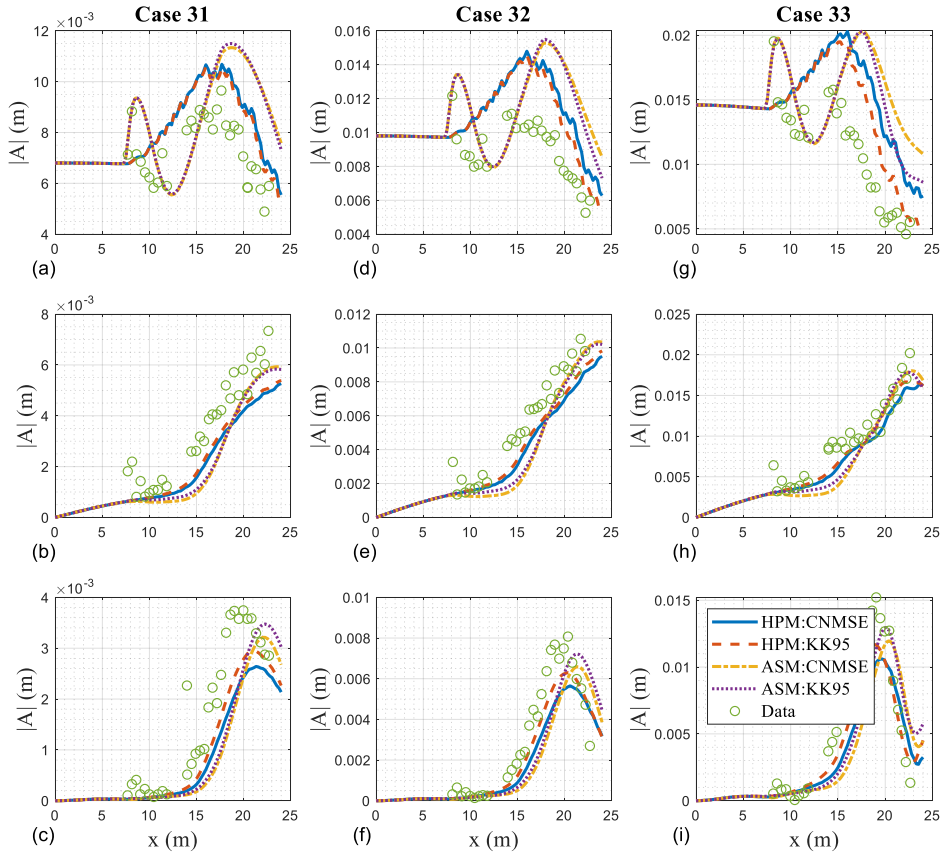

Figure 30 Comparison of wave amplitudes between models and data of Whalin (1971) for Case 31: (a) first harmonic; (b) second harmonic; (c) third harmonic; for Case 32: (d) first harmonic; (e) second harmonic; (f) third harmonic; for Case 33: (g) first harmonic; (h) second harmonic; (i) third harmonic (Solid: HPM: CNMSE; Dashed: HPM: KK95; Dotted: ASM: CNMSE; Dash-dot: ASM: CNMSE; Circle: experimental data).

Table 23 Comparison of IOA between models for T = 3 s of Whalin (1971).

Case	N	HPM: CNMSE	HPM: KK95	ASM: CNMSE	ASM: KK95
31	1	0.6685	0.7025	0.4393	0.4415
	2	0.8898	0.9153	0.8983	0.9012
	3	0.8696	0.9219	0.8455	0.8669
32	1	0.5717	0.6587	0.3717	0.3922
	2	0.9305	0.9525	0.9202	0.9275
	3	0.9159	0.9637	0.8724	0.8978
33	1	0.6134	0.7750	0.4598	0.5429
	2	0.9435	0.9648	0.9242	0.9394
	3	0.9181	0.9668	0.8532	0.9091

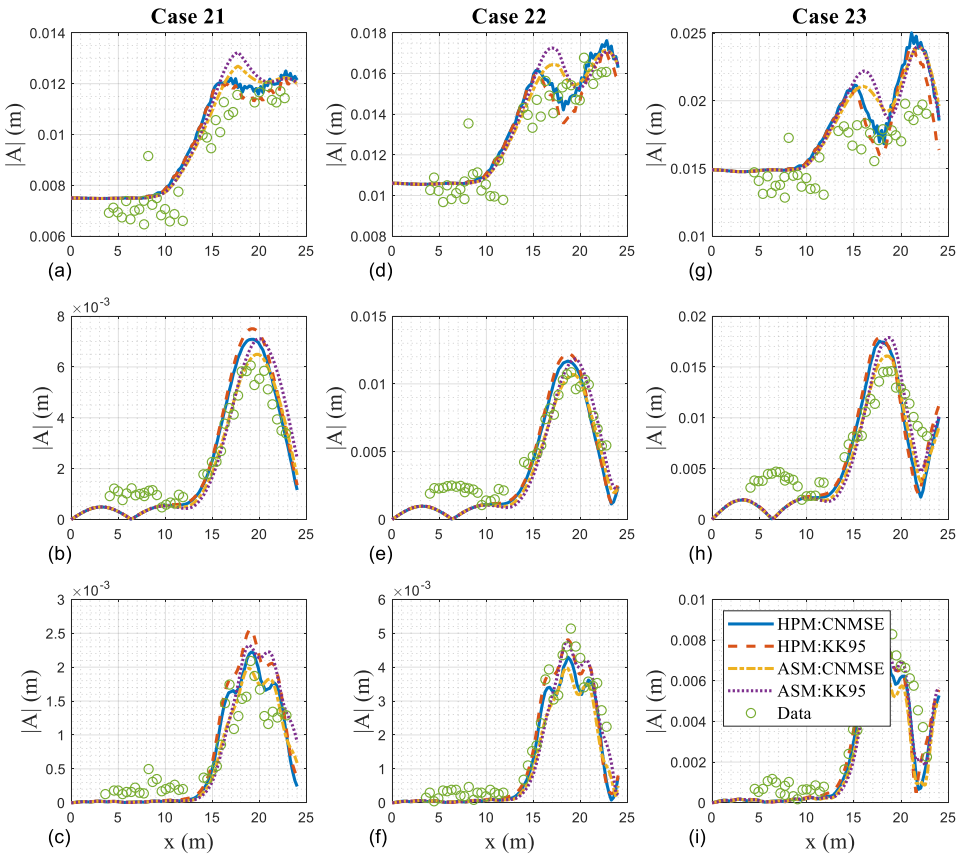

Figure 31 Comparison of wave amplitudes between models and data of Whalin (1971) for Case 21: (a) first harmonic; (b) second harmonic; (c) third harmonic; for Case 22: (d) first harmonic; (e) second harmonic; (f) third harmonic; for Case 23: (g) first harmonic; (h) second harmonic; (i) third harmonic (Solid: HPM: CNMSE; Dashed: HPM: KK95; Dotted: ASM: CNMSE; Dash-dot: ASM: CNMSE; Circle: experimental data).

Table 24 Comparison of IOA between models for T = 2 s of Whalin (1971).

Case	N	HPM: CNMSE	HPM: KK95	ASM: CNMSE	ASM: KK95
21	1	0.9407	0.9425	0.9499	0.9365
	2	0.9666	0.9548	0.9776	0.9595
	3	0.9623	0.9281	0.9603	0.9294
22	1	0.9467	0.9407	0.9531	0.9361
	2	0.9615	0.9579	0.9668	0.9670
	3	0.9769	0.9797	0.9605	0.9801
23	1	0.7678	0.7907	0.7722	0.7497
	2	0.9040	0.8952	0.9296	0.9326
	3	0.9521	0.9494	0.9269	0.9623

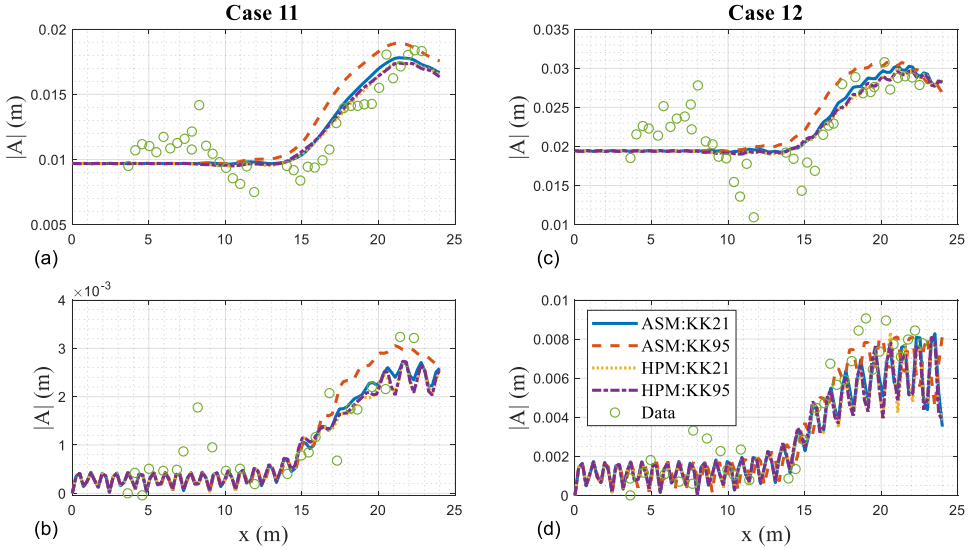

Figure 32 Comparison of wave amplitudes between models and data of Whalin (1971) for Case 11: (a) first harmonic; (b) second harmonic; for Case 12: (c) first harmonic; (d) second harmonic (Solid: HPM: CNMSE; Dashed: HPM: KK95; Dotted: ASM: CNMSE; Dash-dot: ASM: CNMSE; Circle: experimental data).

Table 25 Comparison of IOA between models for T = 1 s of Whalin (1971).

Case	*N*	HPM: CNMSE	HPM: KK95	ASM: CNMSE	ASM: KK95
11	1	0.9392	0.9358	0.9365	0.8954
	2	0.8833	0.8982	0.8975	0.9057
12	1	0.8452	0.8271	0.8474	0.8110
	2	0.9091	0.9198	0.9268	0.9667

6.4.2 Berkhoff et al. (1982)

According to Janssen et al. (2006), the experimental topography of Whalin (1971) corresponds to a mildly two-dimensional bathymetry, where the premise of lateral depth variation is thus adequately acceptable This mild degree of lateral variation may not be generally descriptive of coastal bathymetry; it is thus necessary to test whether the models are applicable to one with severe lateral bottom changes. For this purpose of the verification of the models for the wave forecast over a pronounced two-dimensional bottom, we conduct a comparison of numerical results and data from the experiment of Berkhoff et al. (1982). The experiment was conducted by Berkhoff et al. (1982) to study the wave evolution over the topography consisting of an elliptic shoal situating on a plane sloping beach with a slope of 1:50 (see Figure 13).

We compare model simulations by a linear model of the higher-order approximation (linearized from of Equation 6.8; hereinafter HPM: LMSE in figures and tables) and a linear version of the angular spectrum model (linearized from of Equation 6.48; hereinafter ASM: LMSE in figures and tables) as well as the present higher-order parabolic model (Equation 6.8), the higher-order parabolic model with the nonlinear terms of Kaihatu and Kirby (1995) (Equation 6.53), the present angular spectrum model (Equation 6.48), and the angular spectrum model with the nonlinear terms of Kaihatu and Kirby (Equation 6.53) to the observations. Table 26 presents the wave parameters and the nonlinearity parameters of Berkhoff et al. (1982), where the subscripts 1 and 2 indicate the initial condition and the shoal crest, respectively (h_1 = 0.45 m, h_2 = 0.128 m). The relatively large value of kh = 1.895 (or the relatively small value of Ur = 0.014)

would likely result in an appreciable phase mismatch (Equations 2.66 and 2.67), indicating that the Stokes-type model, for example, Kirby and Dalrymple (1983) and Suh et al. (1990) should be a suitable predictor of the experimental condition (Kirby and Dalrymple, 1984).

Table 26 Wave parameters and the dimensionless parameters of Berkhoff et al. (1982).

a_0 (m)	h_1 (m)	h_2 (m)	T (s)	N	M	kh_1	kh_2	Ur_1	Ur_2
0.0232	0.45	0.128	1	2	121	1.895	0.788	0.014	0.292

Figures 33 and 34 show comparison between the higher-order parabolic models and the angular spectrum models, respectively, and Table 27 presents the comparison of index of agreement between models. At Gauge 1, the wave focusing starts to occur along this section, and both linear and nonlinear models predict reasonably well. After the waves pass by the elliptic shoal, the lateral variation of the diffraction fringes becomes obvious and the region of wave focusing is expanded.

In the cross sections, two aspects are commonly found both in the comparisons between the higher-order models and the angular spectrum models: (1) on Gauges 2 and 3 between where the cusped caustic is developed (at about x = 16 m and y = 10 in Figure 13, Berkhoff et al., 1982), the nonlinear models compare significantly better to the data for the height of the central focused region than the linear models; (2) on Gauges 4 and 5, the present models outperform the previously-developed models in terms of the shape

of side lobes in the diffraction pattern. Also, on the transects 6, 7, and 8 along the propagating direction, the present models overall even better captures increase and decrease in amplitude in comparison to the other models of each type, with the exception that the linear angular model is in closer agreement in the gauge 6 than the nonlinear angular models. The inclusion of nonlinear amplitude gradient and diffraction effects (from A_xA and A_yA_y, respectively) contributes to the improvement which is very similar to that of Stokes-type models (e.g., Kirby, 1986a, Kirby, 1986b, Dalrymple et al., 1989, Suh et al., 1990), where nonlinear dispersion relation is considered via the inclusion of a cubic nonlinearity or the use of an empirical nonlinear dispersion relation.

Since the overall results show that the two present model predictions are in best agreement with the observations in each group, it is worth here to discuss the difference between the present higher-order model (Equation 6.8) and the present angular spectrum model (Equation 6.48). It is clear that the higher-order model and the angular spectrum model give more accurate predictions in the alongshore direction (y-direction) and the cross-shore direction (x-direction, except for the gauge 6), respectively (see Table 27). This is primarily due to the assumption of the weak lateral bottom variation in the angular spectrum approach, whereas the higher-order parabolic model does not have this restriction on the lateral change in bathymetry. Therefore, one would likely conclude that the topography of Berkhoff et al. (1982) comprises a challenging test of the angular spectrum model.

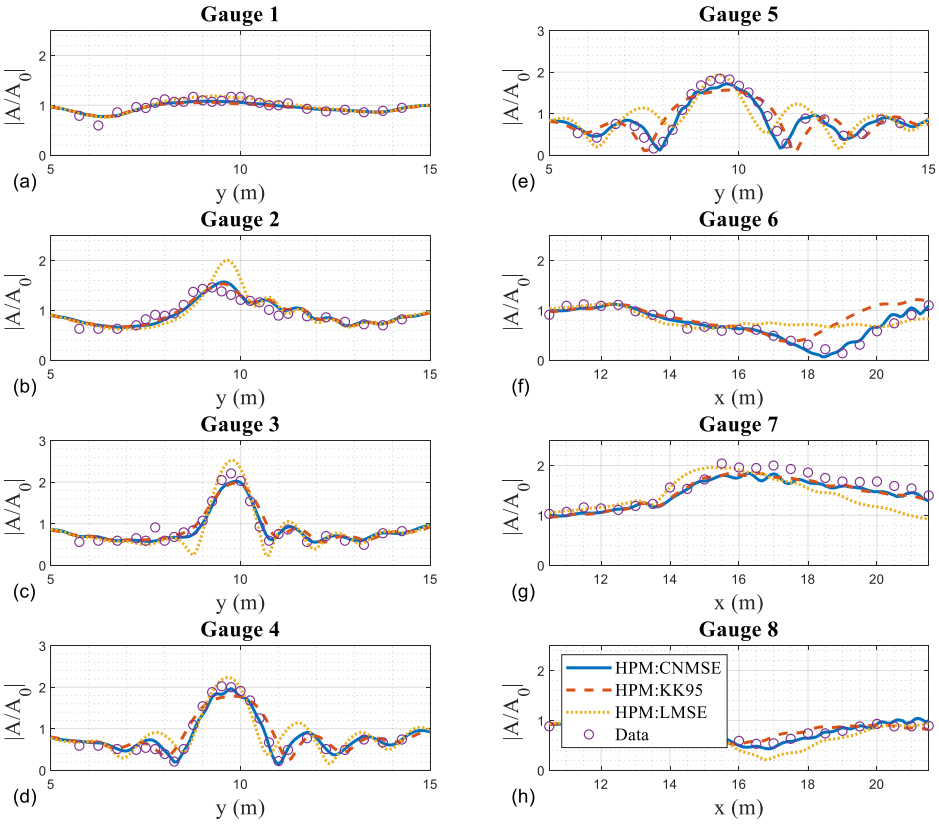

Figure 33 Comparison of normalized wave amplitudes between higher-order parabolic models and data of Berkhoff et al. (1982): (a) gauge 1; (b) gauge 2; (c) gauge 3; (d) gauge 4; (e) gauge 5; (f) gauge 6; (g) gauge 7; (h) gauge 8 (Solid: HPM: CNMSE; Dashed: HPM: KK95; Dotted: HPM: LMSE; Circle: experimental data).

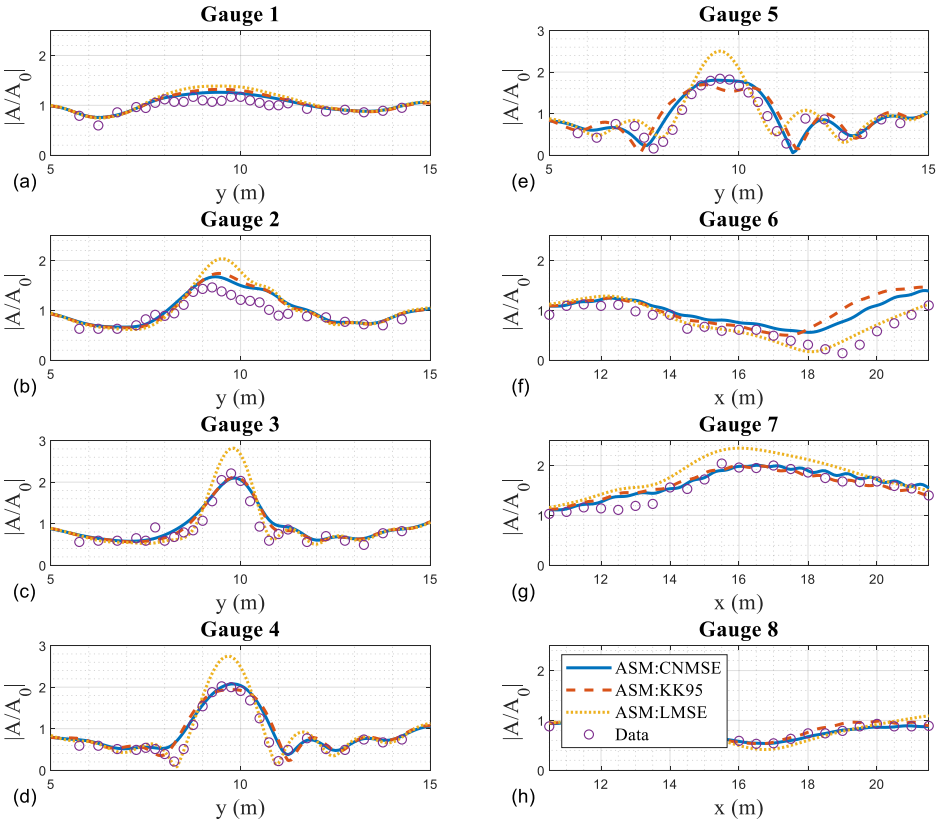

Figure 34 Comparison of normalized wave amplitudes between angular spectrum models and data of Berkhoff et al. (1982): (a) gauge 1; (b) gauge 2; (c) gauge 3; (d) gauge 4; (e) gauge 5; (f) gauge 6; (g) gauge 7; (h) gauge 8 (Solid: ASM: CNMSE; Dashed: ASM: KK95; Dotted: ASM: LMSE; Circle: experimental data).

Table 27 Comparison of IOA between models for Berkhoff et al. (1982)

Gauge	HPM: CNMSE	HPM: KK95	HPM: LMSE	ASM: CNMSE	ASM: KK95	ASM: LMSE
1	0.9213	0.8880	0.9419	0.8811	0.8371	0.7657
2	0.9574	0.9639	0.8644	0.9085	0.8986	0.8323
3	0.9850	0.9703	0.9625	0.9550	0.9637	0.9469
4	0.9901	0.9678	0.9384	0.9697	0.9553	0.9625
5	0.9844	0.9325	0.8390	0.9519	0.8791	0.9366
6	0.9789	0.7728	0.7427	0.7445	0.6454	0.9580
7	0.9379	0.9486	0.8082	0.9606	0.9448	0.8500
8	0.9150	0.8910	0.8191	0.9497	0.9237	0.9055

6.4.3 Circular shoal

As in the previous studies for very large-angle water waves (Kirby, 1986b; Dalrymple et al., 1989; Suh et al., 1990), in order to examine the large-angle capabilities of the models, the last example is that of wave propagation over a bathymetry with a circular shoal resting on a flat bottom which is quite similar in dimension to that of Berkhoff et al. (1982). Because the circular shoal situated on a flat beach satisfies axisymmetry, it is desirable to have no distortion to the resulting focusing pattern behind the wave shoal due to changes in the incident angle θ_p. Following Dalrymple et al. (1989), the case of a circular shoal with higher shoal height (0.12 m) is taken to consider the severe bottom variation, and the depth is given with the origin corresponding to the center of the shoal:

$$h = \begin{cases} h_0 = 0.336 \text{ m} & ; r > R \\ h_0 + 0.18 - 0.3\left\{1 - \left(x/5\right)^2 - \left(y/5\right)^2\right\}^{1/2} & ; r \le R \end{cases} \tag{6.59}$$

where the radius of the shoal R = 4 m and $r = (x^2 + y^2)^{1/2}$ with the coordinates (x, y).

A monochromatic wavetrain propagates over the circular shoal for three different incident angles: θ_p = 0°, 22.5°, and 45°, with the same wave information as those of Berkhoff et al. (1982), shown in Table 28 where the subscripts 1 and 2 indicate the flat bottom depth and the shoal crest, respectively (h_1 = 0.336 m, h_2 = 0.216 m). The primary goal of this section is to investigate wave propagation at wide propagation angles to the pre-specified numerical grid, as simulated by the two approaches outlined in this chapter (higher-order parabolic model and angular spectrum model), therefore, we consider the numerical results by the two present models (Equations 6.8 and 6.48).

Table 28 Wave parameters and the dimensionless parameters of circular shoal.

a_0 (m)	h_1 (m)	h_2 (m)	T (s)	N	M	kh_1	kh_2	Ur_1	Ur_2
0.0232	0.336	0.216	1	2	148	1.496	1.091	0.031	0.090

Figure 35 shows wave focusing pattern behind a circular shoal resting on a flat bottom. For $\theta_p = 0°$, both of the higher-order parabolic and angular spectrum models give similar results, however, the higher-order parabolic approach results in a more distorted wave focusing pattern at larger angle compared to that of normal incidence ($\theta_p = 0°$). In contrast, the present angular spectrum model displays less distortion to the resulting focusing pattern caused by the changes of θ_p. To quantitatively assess the distortion, the normalized amplitudes at transects 10 m away from the center of the circular shoal are shown in Figure 36, in which we obtain the results along the transect for $\theta_p = 22.5$ and 45° by digitization from Figure 35. The results of the present higher-order model show the obvious shift to the right, which all worsen with the increasing angle of incidence θ_p. On the other hand, the present angular spectrum model shows equivalent wave patterns for $\theta_p = 22.5$ and 45° in comparison to those of normal incidence, indicating that the model is suitable for wave propagating at large angles. This advantageous feature of the angular spectrum model is most likely due to the approach where the wave field is decomposed into an angular spectrum propagating independently into the shallower regions (or half-plane, $x > 0$). The wiggles in the results of the angular spectrum model may be due to the discontinuities from the use of a finite Fourier

transform in the *y*-direction; several approaches are available to smooth the oscillations in the solution (Suh et al., 1990).

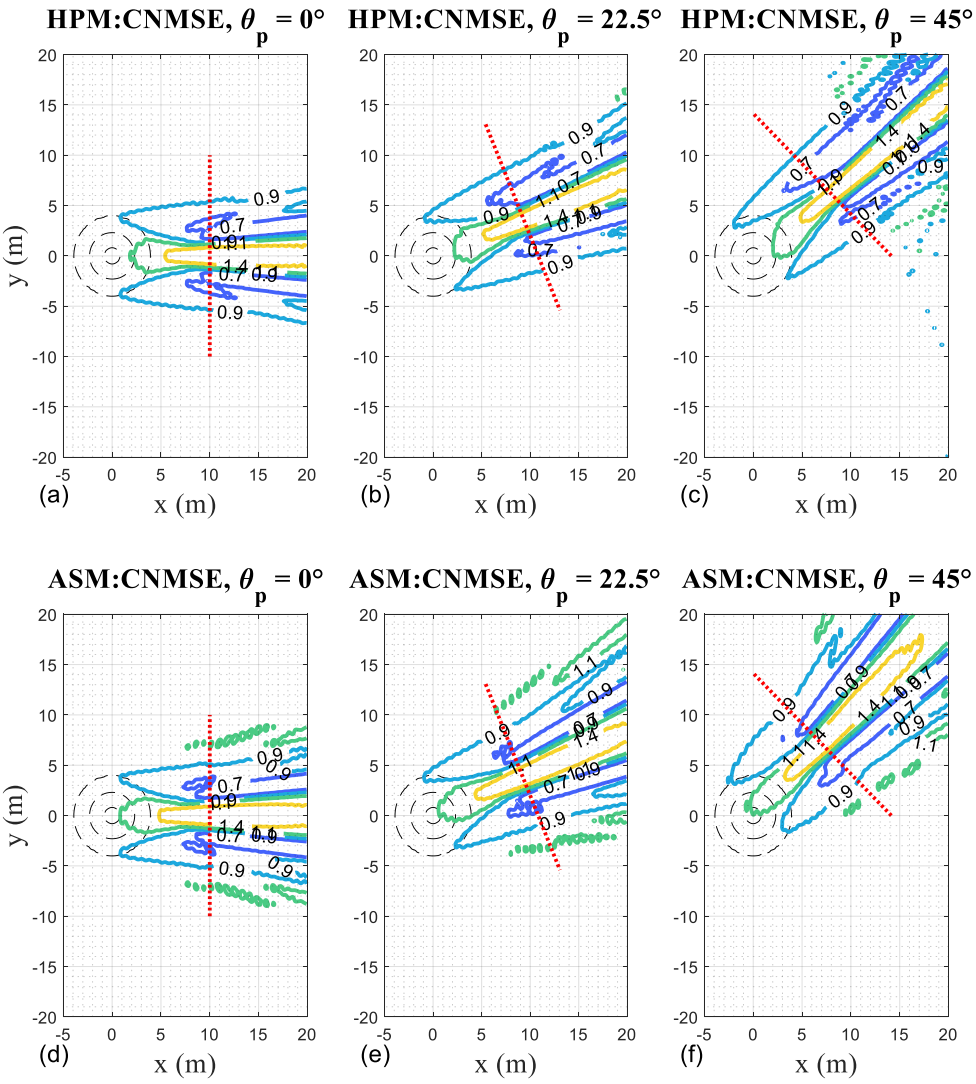

Figure 35 Contour of normalized wave amplitudes and topography for circular shoal: (a) HPM: CNMSE with θ_p = 0°; (b) HPM: CNMSE with θ_p = 22.5°; (c) HPM: CNMSE with θ_p = 45°; (d) ASM: CNMSE with θ_p = 0°; (e) ASM: CNMSE with θ_p = 22.5°; (f) ASM: CNMSE with θ_p = 45° (Dashed: depth contours; Dotted: transect at 10 m from shoal crest).

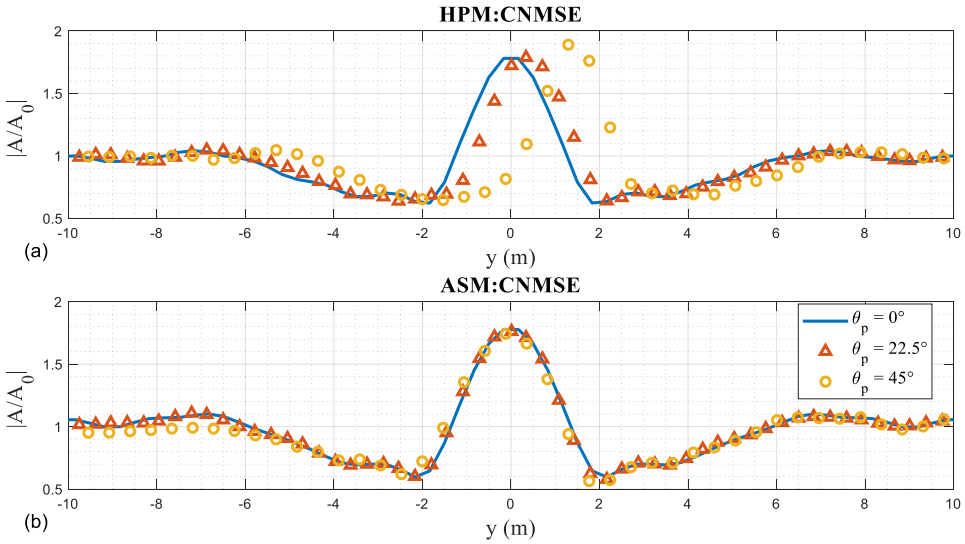

Figure 36 Comparison of normalized wave amplitudes at 10 m from circular shoal depending on angle of incidence θ_p: (a) HPM: CNMSE; (b) ASM: CNMSE (Solid: θ_p = 0°; Triangle: θ_p = 22.5°; Circle: θ_p = 45°).

Considering the performances of the two present models for the experimental data of Berkhoff et al. (1982) and the circular shoal, the opposite tendency is found: the present higher-order model shows better performance for the experiment of Berkhoff et al. (1982), and vice versa for the case of circular shoal. We calculate the curvature of the bathymetry in the *y*-direction, with expectation that the poor level of agreement of the present angular spectrum model can be attributed to the severe lateral depth variation in the bathymetry of Berkhoff et al. (1982):

$$\kappa_c\left(x,y\right)=\frac{\left|\frac{d^2h\left(x,y\right)}{dy^2}\right|}{\left[1+\left(\frac{dh\left(x,y\right)}{dy}\right)^2\right]^{\frac{3}{2}}} \tag{6.60}$$

As anticipated, the comparison of bottom curvature around the shoals, shown in Figure 37, validates the hypothesis that large value of alongshore bottom curvature (or strong lateral depth variation) in the bottom bathymetry of Berkhoff et al. (1982) may violate the assumption of small longshore depth variation inherent in the model development. This renders the angular spectrum model to be relatively unable to replicate the properties of the wave field evolution in detail (e.g., the diffraction fringe away from the focal region). In contrast, the higher-order parabolic model (not subject to this assumption on longshore depth variability) demonstrates better performance in this case. In conclusion, the angular spectrum therefore seems to be a better choice for situations where the initial propagation is at large angle to the computational grid but also where longshore bathymetric variability is mild. On the other hand, the higher-order

parabolic model is preferable when the diffraction and refraction effects are significantly caused by a comparatively severe lateral depth variation unless the initial approach angle is quite large. It is noteworthy that Tsay et al. (1989) overcame the limitation in the parabolic equation model regarding the initial approach angle through the introduction of coordinate system based on refraction rays fitted for a boundary condition.

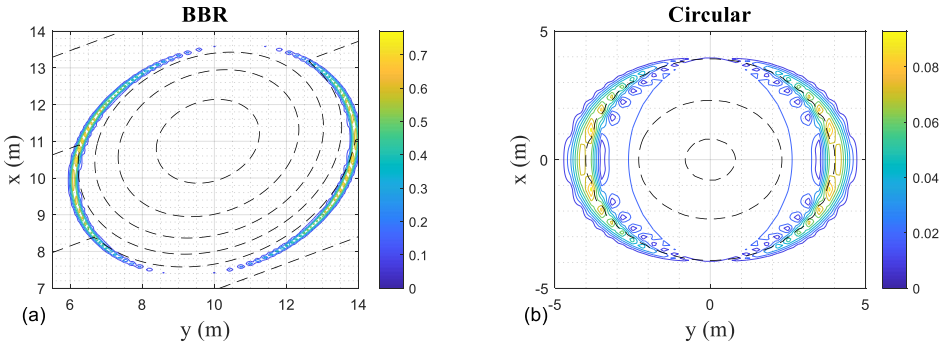

Figure 37 Comparison of bottom curvature: (a) elliptic shoal of Berkhoff et al. (1982); (b) circular shoal (Dashed: depth contours).

CHAPTER VII

COMPARISON TO FIELD OBSERVATIONS

7.1 Introduction

In time-domain model simulations, painstaking effort on data analysis is needed to deal with uncertainties and details in boundary conditions are often not available (Herbers et al. 2003, Sheremet et al. 2016). Also, it can be argued that the time-domain model is numerically expensive for large domains coupling the coastal wave field with a sediment transport module and morphological evolution since the dependent variable is modeled as an arbitrary function of space and time. In contrast, the frequency-domain models are numerically straightforward due to *apriori* assumption of temporal periodicity.

In general, the distinctive features of deep water waves can be explained in terms of the fundamental dynamics: strong dispersion, random phases (quasi-Gaussian Sea state), and four wave exact-resonant (quartet) interactions, while shallow-water wave dynamics are characterized by weak dispersion, strong phase correlations, and three-wave (triad) near-resonant interactions. Triad interactions inherent to shallow water (and predictable by CNMSE models) are responsible for nearshore infragravity waves, which have a critical influence on morphological evolution of coastlines such as erosion, inundation, and accretion. In shallow water, the suitability of the parameterized triad interaction source term and phase-decoupled diffractive term in operational forecasting models such as SWAN is suspect due to the inability of these terms to account for a two-

dimensional wave field (responsible for redistributing the energy over a wide range of directions), as well as the lack of history of phase correlations in the wave train. In contrast, the phase-resolved model has the advantage of fully describing subharmonic and superharmonic interactions so that important process such as infragravity wave generation, spectrum widening, and the broadening of the directional range can be realistically simulated.

We can use the consistent nonlinear mild-slope equation model as a useful transition model between phase-averaged operational offshore models (e.g., SWAN, Booij et al., 1999) and phase-resolved time-domain nearshore models (e.g., FUNWAVE, Wei et al., 1999). Frequency domain phase-resolving models strike the right balance between over-approximated phase-averaged models (which contain linear wave dynamics for the nearshore zone) and computationally-intensive time-domain models in areas still somewhat spatially removed from breaking wave impact in the surf.

7.2 DUCK94

For the purpose of testing the present models in field situations, we use data from the field campaign DUCK94 (Fall 1994) where the U.S. Army Field Research Facility collected measurements of shoaling and breaking waves across an ocean beach at Duck, North Carolina, USA (Birkemeier and Thronton, 1994; Birkemeier et al., 1997). As shown in Figure 38 where x and y are the cross- and along-shore coordinates, respectively, collocated pressure gauges and current meters deployed at cross-shore locations between the shoreline and about 5-m depth were used to record pressure at a

sampling rate of 2 Hz. Also, wave frequency-directional spectra were obtained from alongshore array of pressure sensors (9 elements, 255 m aperture) located in 8-m depth (FRF 8-m array at x = 900 m). A downward-looking sonar altimeter collocated with pressure gauges and current meters estimated depth contours through linear interpolation. The spatial domain is discretized as Δx = 1 m and Δy = 9.4828 m until further reduction does not make any difference in results.

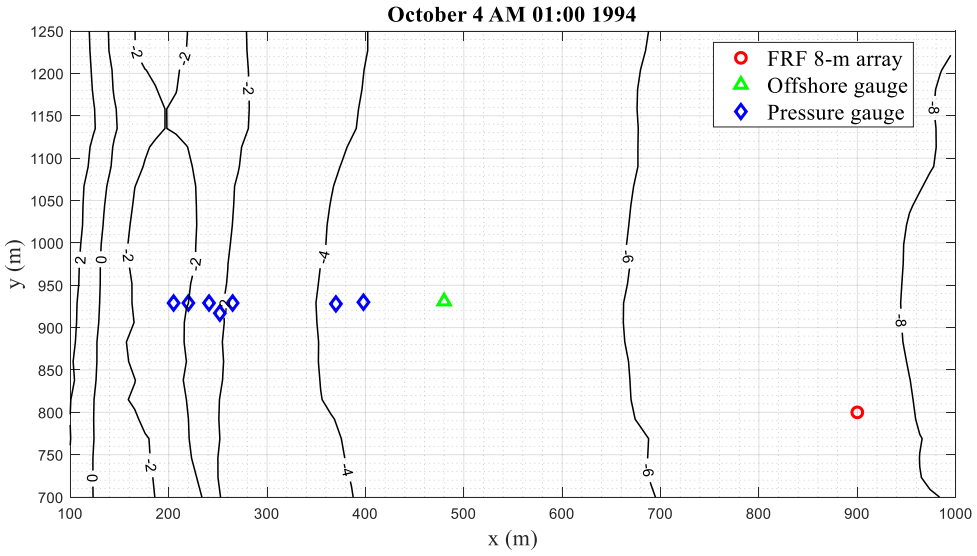

Figure 38 Instrument array locations during DUCK94 on October 4 1994 AM 01:00 (Solid: depth contours; Circle: FRF 8-m array; Triangle: most offshore pressure gauge at x = 480 m; Diamond: pressure gauges at shallower locations).

7.3 Numerical implementation

7.3.1 Wave models

To study refraction, shoaling, nonlinear interactions, and breaking characteristics of random waves in comparison to field measurement, we modify the consistent nonlinear mild-slope equation model (Equation 7.1; PEM: CNMSE hereafter) and the angular spectrum version of consistent nonlinear mild-slope equation model (Equation 7.5; ASM: CNMSE) with the breaking-induced energy dissipation formulation. For CNMSE, we obtain:

$$\begin{aligned} &2i\left(kCC_g\right)_n A_{nx} + i\left(kCC_g\right)_{nx} A_n + \left[\left(CC_g\right)_n \left(A_n\right)_y\right]_y + 2i\left(kCC_g\right)_n \alpha_n A_n \\ &= \frac{1}{4}\sum_{l=1}^{n-1}\left[R_1 A_l A_{n-l} + R_2 A_{lx} A_{n-l} + R_3 A_l A_{n-lx} + R_4 A_{ly} A_{n-ly}\right] e^{i\int (k_l + k_{n-l} - k_n)dx} \\ &+ \frac{1}{2}\sum_{l=1}^{N-n}\left[S_1 A_l^* A_{n+l} + S_2 A_{lx}^* A_{n+l} + S_3 A_l^* A_{n+lx} + S_4 A_{ly}^* A_{n+ly}\right] e^{i\int (k_{n+l} - k_l - k_n)dx} \end{aligned} \tag{7.1}$$

where the interaction coefficients (R and S) are the same as Equation (2.48). Further, the dissipation term α_n is a function dependent on frequency (Mase and Kirby, 1993):

$$\alpha_n\left(x,y\right) = \beta\left(x,y\right)\left[F + \left(1-F\right)\frac{f_n{}^2 \sum \left|A_n\left(x,y\right)\right|^2}{\sum f_n{}^2 \left|A_n\left(x,y\right)\right|^2}\right] \tag{7.2}$$

while the lumped dissipation β is approximated for shallow water case (Thornton and Guza, 1983).:

$$\beta = \frac{3\sqrt{\pi}}{4\sqrt{gh}}\frac{B^3 f_p}{\gamma^4 h^5} H_{rms}{}^5 \tag{7.3}$$

and

$$H_{rms} = 2\sqrt{\sum_{n=1}^{N} \left|A_n\right|^2} \tag{7.4}$$

The angular spectrum version of consistent nonlinear mild-slope equation model (ASM: CNMSE) incorporates the simplified breaking function of Thronton and Guza (1983):

$$\begin{aligned}
&2i\left(k_{n,m}\left[\overline{CC_g}\right]_n\right)A_{n,mx} + i\left(k_{n,m}\left[\overline{CC_g}\right]_n\right)_x A_{n,m} + \left[\xi^{wb}\right]_{n,m} + 2i\left(k_{n,m}\left[\overline{CC_g}\right]_n\right)\bar{\alpha}_n A_{n,m} \\
&= \frac{1}{4}\sum_{p=\max\{-M_{n-l}+m,-M_l\}}^{\min\{M_{n-l}+m,M_l\}} \sum_{l=1}^{n-1} \left[\begin{array}{l} \overline{R_1} A_{l,p} A_{n-l,m-p} \\ +\overline{R_2} A_{l,px} A_{n-l,m-p} + \overline{R_3} A_{l,p} A_{n-l,m-px} \end{array}\right] e^{\left(i\int k_{l,p}+k_{n-l,m-p}-k_{n,m}dx\right)} \\
&+ \frac{1}{2}\sum_{p=\max\{-M_{n+l}-m,-M_l\}}^{\min\{M_{n+l}-m,M_l\}} \sum_{l=1}^{N-n} \left[\begin{array}{l} \overline{S_1} A_{l,p}{}^{*} A_{n+l,m+p} \\ +\overline{S_2} A_{l,px}{}^{*} A_{n+l,m+p} + \overline{S_3} A_{l,p}{}^{*} A_{n+l,m+px} \end{array}\right] e^{\left(i\int -k_{l,p}+k_{n+l,m+p}-k_{n,m}dx\right)}
\end{aligned} \tag{7.5}$$

where $[\xi^{wb}]_{n,m}$ represents the forcing due to the interaction between surface wave modes and lateral bottom variation (see Equation 6.48), and the *y*-averaged interaction coefficients ($\bar{R}$ and $\bar{S}$) are the same as Equation (6.41).

The dissipation term $\bar{\alpha}_n$ is a *y*-averaged dissipation term with the squared-frequency distribution (Mase and Kirby, 1993):

$$\bar{\alpha}_n(x) = \bar{\beta}(x)\left[F + (1-F)\frac{f_n{}^2 \sum_m \sum_n \left|A_{n,m}(x)\right|^2}{\sum_m \sum_n f_n{}^2 \left|A_{n,m}(x)\right|^2}\right] \tag{7.6}$$

and

$$\bar{\beta} = \frac{3\sqrt{\pi}}{4\sqrt{g\bar{h}}}\frac{B^3 f_p}{\gamma^4 \bar{h}^5}\left[\overline{H_{rms}}\right]^5 \tag{7.7}$$

with

$$\overline{H_{rms}} = \left[2\sqrt{\sum_{n=1}^{N} \sum_{m=-M_n}^{M_n} \left| A_{n,m} \right|^2} \right] \tag{7.8}$$

Following Sheremet et al. (2016), who studied directional spectral evolution in the same location at Duck, North Carolina, USA, the free parameters in dissipation functions (Equations 7.2, 7.3, 7.6, and 7.7) are assigned as $F = 0.5$, $B = 1$, and $\gamma = 0.7$.

Table 29 Wave parameters and for numerical implementation of DUCK94.

T (s)	N	M	λ (1/m)
1024	300	29	0.0112

7.3.2 Preprocessing for simulation

The models should be initialized with directional wave spectra obtained from alongshore array of pressure sensors or results of operational phase-averaging wave models (e.g., SWAN), which are given as a form in (f, θ) (where θ is propagation direction in this chapter) and thus mapping the directional wave spectra is required between (f, θ) and (f, λ) grids for a numerical implementation of both parabolic equation and angular spectrum models in frequency-domain. The working of transforming the directional wave spectra in (f, θ) ($S(f, \theta)$) to complex amplitudes in (f, λ) (i.e., $A_{n,m}$) can be done in a few steps: (1) one should pair each alongshore wave component to a

propagation direction θ by using (Equation 6.38 or $\theta = \tan^{-1}(\frac{m\lambda}{k_{n,m}})$); (2) lower and upper limits of θ (θ_l and θ_u) are determined by median values between the consecutive values of paired θ; (3) the sum of angular spectrum between θ_l and θ_u is assigned to the value at each alongshore component; (4) with random phase approximation based on the uniform distribution, the complex amplitudes is obtained.

Since the directional wave spectrum (e.g., JONSWAP spectrum) does not include any information for infragravity wave ($f < 0.5f_p$), the missing values over infragravity wave range are necessarily approximated by using two different approaches: (1) second-order bound wave correction (Davis et al., 2014; Sheremet et al., 2016); (2) simple linear interpolation. Additionally, high frequency motions are hardly recorded by a pressure transducer located at the bottom in deep water because of confusion between real signal and noise of the gauge. For these reasons, it is suggested that the spectral density over high-frequency range is approximated with the high-frequency tail of the input spectra (e.g., Kaihatu et al., 2007b) to use wave information measured in deep water.

To circumvent these limitations related with directional wave spectrum such as for missing and inaccurate values in low- and high-frequency bands, respectively and to minimize the physical effects not addressed here, we initialize the present models at the most offshore pressure gauge (x = 480 m), which is relatively shallower than the location of FRF 8-m array, where we can obtain time series of surface elevation from pressure records collected by collocated pressure gauges and current meters. To generate the directional wave spectrum (or 2D spectral density), the frequency surface spectrum (or 1D spectral density) from pressure records needs to be combined with the information of

directional spreading. Therefore, we initialize linear angular spectrum model (linearized form of Equation 7.5) with an incident wave directional spectrum observed at FRF 8-m array (x = 900 m), and then the directional spreading at x = 480 m is obtained by the normalized wave density:

$$D(f_n, m\lambda) = \frac{S(f_n, m\lambda)}{\sum_m S(f_n, m\lambda)} \tag{7.9}$$

At x = 480 m, the free surface elevation obtained from pressure record at a sampling rate of 2 Hz is divided into 10 realizations of 2048 data points apiece. By using Fast Fourier Transform (FFT), 10 sets of amplitudes A_n and frequency power spectra $S(f_n)$ are calculated, and directional wave spectrum can be given by:

$$S(f_n, m\lambda) = S(f_n) D(f_n, m\lambda) / \lambda \tag{7.10}$$

The magnitude of amplitudes in (f, λ) coordinate is calculated by:

$$\left|A_{n,m}\right| = \sqrt{2S(f_n, m\lambda)\Delta f\,\lambda} \tag{7.11}$$

With random phase approximation based on the uniform distribution, the complex amplitude for the angular spectrum model is obtained:

$$A_{n,m} = \left|A_{n,m}\right| \exp[i \times RN] \tag{7.12}$$

Inverse Fourier transform gives the input for parabolic model equation:

$$A_n(x, y) \exp\left[i \int k_n dx\right] = \sum_{m=-M}^{M} A_{n,m}(x) \exp\left[i \int k_{n,m} dx + m\lambda y\right] \tag{7.13}$$

Figure 39 describes an overview of the numerical simulations.

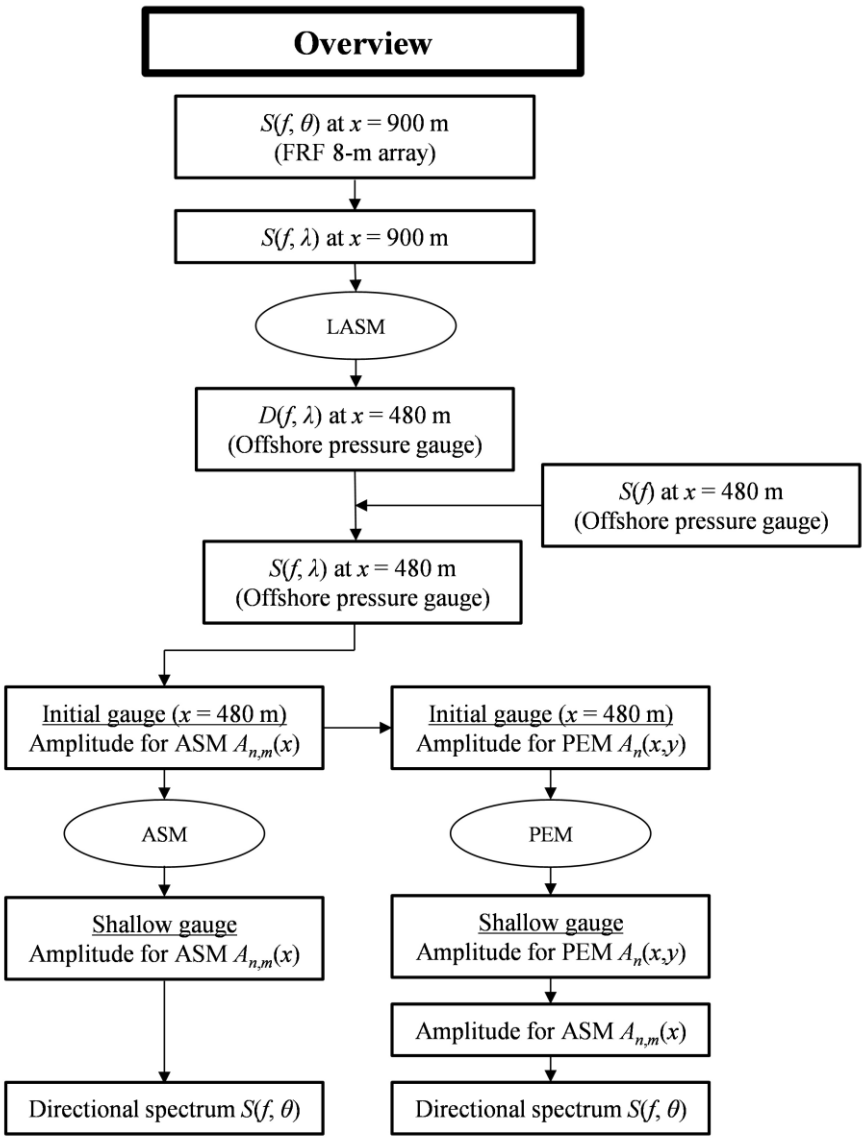

Figure 39 Overview of numerical simulation for DUCK94.

Sheremet et al. (2016) included triad interactions close enough to resonance by using detuning parameter to decreases errors and computational efforts resulted from the highly oscillating nonlinear terms. They implicitly set a cutoff detuning value based on the domain size, a cross-sectional trace of the beach, and the spectral distribution. A modified detuning parameter by replacing k_n with non-dispersive wave number κ in the denominator is used to evaluate the magnitude of interactions between wave number. For the parabolic equation model, the numerical implementation is restricted by:

$$\frac{k_l + k_{n-l} - k_n}{\kappa} \le \frac{{\mu_{cr}}^2}{6}; \frac{-k_l + k_{n+l} - k_n}{\kappa} \le \frac{{\mu_{cr}}^2}{6} \tag{7.14}$$

For the angular spectrum model, we only consider the triads determined by:

$$\frac{k_{l,p} + k_{n-l,m-p} - k_{n,m}}{\kappa} \le \frac{{\mu_{cr}}^2}{6}; \frac{-k_{l,p} + k_{n+l,m+p} - k_{n,m}}{-k_l} \le \frac{{\mu_{cr}}^2}{6} \tag{7.15}$$

where $\mu_{cr} = 3$ is arbitrarily chosen as a basis to exclude the triad interaction in deep water.

It is notable that the maximum effective wave number (M_n) increases with decreasing water depth, resulting in the alongshore discretization in space needs to be finer as waves propagate. However, finer grid size in shallower area for wide-angle propagations is not required since waves usually approach the shore with their crests oriented somewhat parallel to the coast, primarily owing to refraction effect. This has the effect of narrowing the spread of the spectral density in direction so that the equivalent grid spacing is fine enough to take into consideration near-resonant interactions, which is of primary importance to address nonlinearity (Vrecica and Toledo, 2019).

7.3.3 Results

We compare model simulations to measurements for three representative case studies during October 1994 (see Figures 40, 41, and 42). On October 4 AM 01:00, a narrow band swell is incident at x = 480 m with root-mean-square wave height $H_{rms} = 0.71$ m, peak frequency f_p = 0.15 Hz, and a mean direction (at f_p) $\theta_m = 10°$ (from slightly northerly direction). On October 5 AM 01:00, an incident trimodal wave field ($H_{rms} = 0.44$ m) at x = 480 m consists of a dominant wave ($f_p = 0.12$ Hz and $\theta_m = -26°$) arriving from a southerly direction, lower-frequency swell ($f_p = 0.08$ Hz and $\theta_m = -14°$) from south and higher-frequency swells ($f_p = 0.17$ Hz and $\theta_m = 22°$) from north. On October 12 AM 01:00, the wave field at x = 480 m ($H_{rms} = 0.7$ m) consisting of two nearly-equivalently dominant swells ($f_p = 0.13$ Hz and $\theta_m = 10°$; $f_p = 0.16$ Hz and $\theta_m = 10°$) arriving from collinearly northerly direction and much less energetic infragravity $f_p = 0.07$ Hz and $\theta_m = -14°$) arriving from southerly direction is incident.

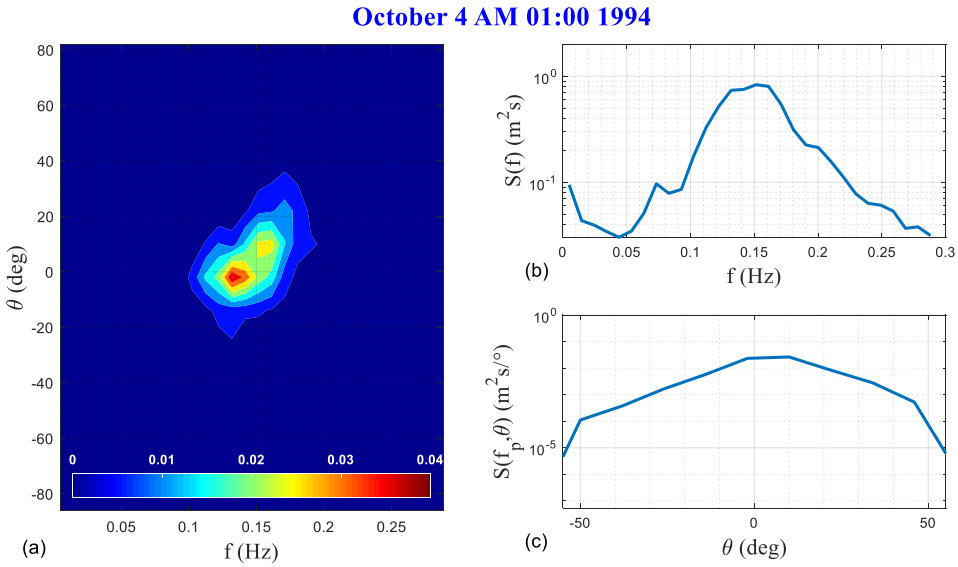

Figure 40 Measurement on October 4 1994 AM 01:00 (a) directional spectrum; (b) frequency spectrum; (c) spectrum at peak frequency.

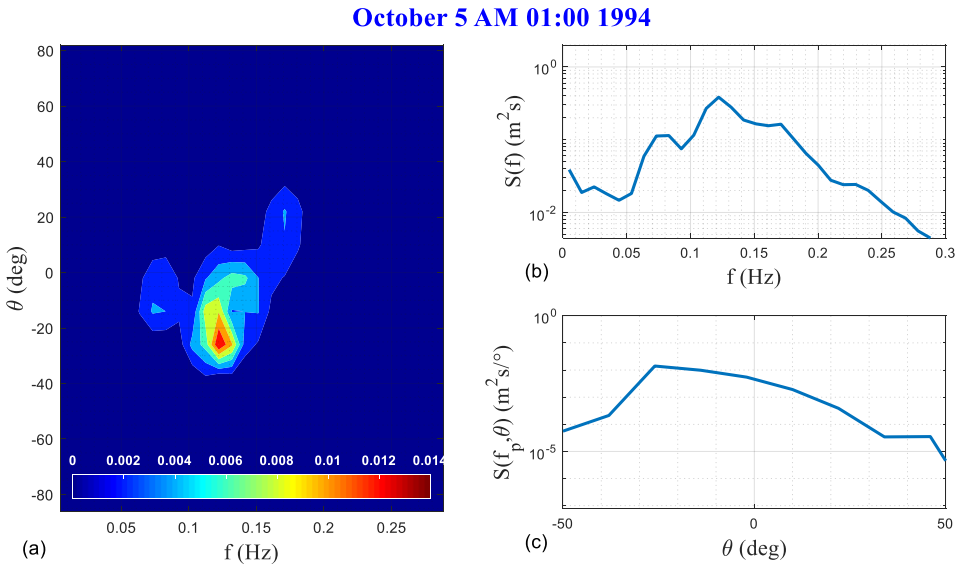

Figure 41 Measurement on October 5 1994 AM 01:00 (a) directional spectrum; (b) frequency spectrum; (c) spectrum at peak frequency.

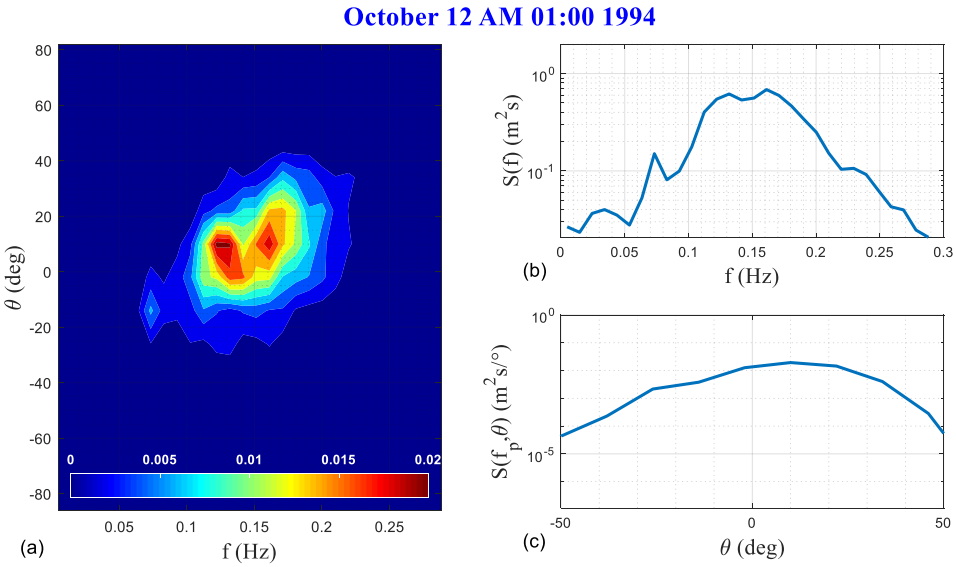

Figure 42 Measurement on October 12 1994 AM 01:00: (a) directional spectrum; (b) frequency spectrum; (c) spectrum at peak frequency.

In Figures 43-48, predictions of the spectral evolution at a few locations outside and over the surf zone from the parabolic equation and angular spectrum models based on CNMSE are compared with field measurements. In Figures of directional wave spectrum, the infragravity band ($f < 0.05$ Hz) is not visualized because the infragravity range is likely influenced by strong reflected effects from shorelines which is not simulated by the model (Herbers et al., 2003). Overall, one may conclude from the comparison of observed with predicted frequency spectrum (i.e., 1D spectral density) that the angular spectrum model compares better to the data for much of the frequency range throughout most cases than the parabolic model. This is not a surprise because the angular spectrum model treats the wave propagating with the separate consideration of wave field in a particular direction by use of the alongshore Fourier component of the wave field while the parabolic equation model is limited to the case of waves propagating nearly in a prespecified direction.

It is expected that the growth of the second and higher harmonics of the peak and the energy transfers to low-frequency infragravity modes causing amplification of the infragravity range (Herbers et al., 2003; Janssen, 2006; Sheremet et al., 2016). However, in both model predictions and observations, it appears that self- and cross-interactions between wave components are very negligible or weak for the present case studies, which is attributed to the fact that the nonlinearity in the surface boundary conditions is much weaker than dispersive effect ($Ur_p = 0.1$ at $x = 480$ m for the three test cases). Nevertheless, the angular spectrum model predictions are in overall good agreement with the measurement where initially-narrow spectrum in frequency space was

broadened with attenuated swell conditions, with the exception in lower- and higher-frequency ranges in the surf zone. The inability of the model to account for the infragravity band may be due to the reflection effects not considered in the model. Additionally, the long wavelength of very-low-frequency may violate the assumption of slow horizontal variation of water depth (Janssen, 2006). The strong deviation from data over the higher-frequency band at the shallow gauges may result from the upper frequency cutoff (i.e., the limited number of frequency mode) because triad wave-wave interaction with any frequency modes above the cutoff could induce the amplification of energy levels at the high frequencies (Sheremet et al., 2016). The discrepancies over high-frequency range are possibly attributed to the trade-off between the energies of low- and high-frequency bands to conserve energy flux.

The modeled inshore spectra are either uniformly wide in directional space or the energy is distributed at large oblique angles. Although we do not compare with the observed directional wave spectral density in this study, the directional broadening appears to be common in the observed cross-shore evolution of directional wave spectrum (e.g., Herbers et al., 2003; Janssen, 2006; Sheremet et al., 2016). Whereas the phenomenon was not simulated in the previous models (Herbers et al., 2003; Janssen, 2006; Sheremet et al., 2016) where lateral depth variations were neglected, the present angular spectrum model better describes the wide directional spread at high frequency range and refraction shifts toward normal incidence to the shoreline at lower frequencies primarily due to the consideration of the lateral depth variation.

Figures 49-51 compare bulk wave parameters, namely root-mean-square wave height H_{rms} (Equations 7.4 and 7.8) and maximum bottom wave orbital velocity $|U_b|$ between the data, the parabolic equation and angular spectrum models based on CNMSE. The accurate prediction of bottom wave orbital velocity may lead to better estimation of the sediment transport and nearshore morphological evolution in coastal regions and linear wave theory calculate the value at bottom layer:

$$|U_b| = \frac{H_{rms}\pi}{T\sinh(kh)} \tag{7.16}$$

As seen in Figures 49 through 51, the angular spectrum model shows much better agreement with the measurements in comparison to the parabolic equation model, a result consistent with those of the frequency spectrum comparisons (i.e., 1D spectral density). It supports the conclusion that the angular spectrum seems to be a better choice for situations where the initial propagation is at large angle to the shoreline but alongshore homogeneity is satisfied in bathymetry.

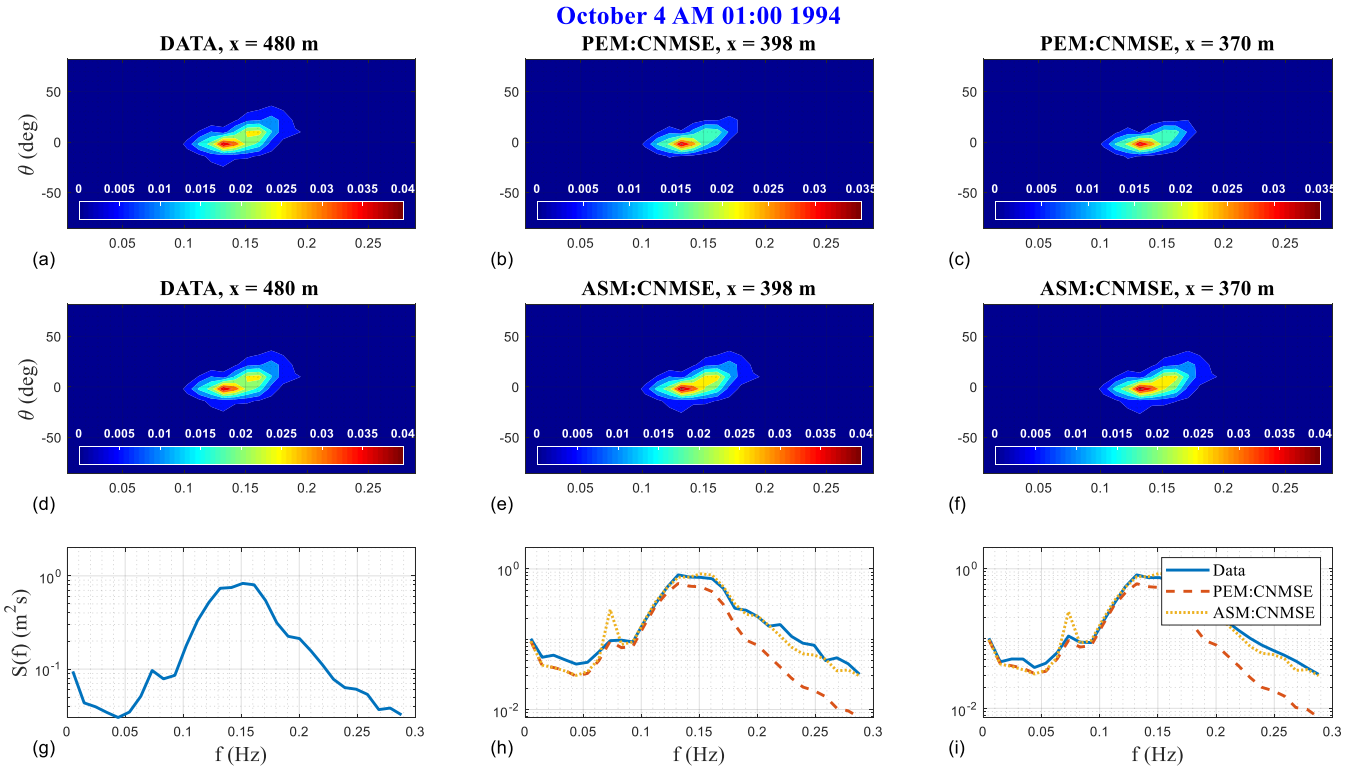

Figure 43 Comparison of directional wave between models and comparison of observed with predicted frequency spectrum on October 4 1994 AM 01:00: (a) Data at *x* = 480 m; (b) PEM: CNMSE at *x* = 398 m; (c) PEM: CNMSE at *x* = 370 m; (d) Data at *x* = 480 m; (e) ASM: CNMSE at *x* = 398 m; (f) ASM: CNMSE at *x* = 370 m; (g) frequency spectrum at *x* = 480 m; (h) frequency spectrum at *x* = 398 m; (i) frequency spectrum at *x* = 370 m (Solid: field data; Dashed: PEM: CNMSE; Dotted: ASM: CNSME).

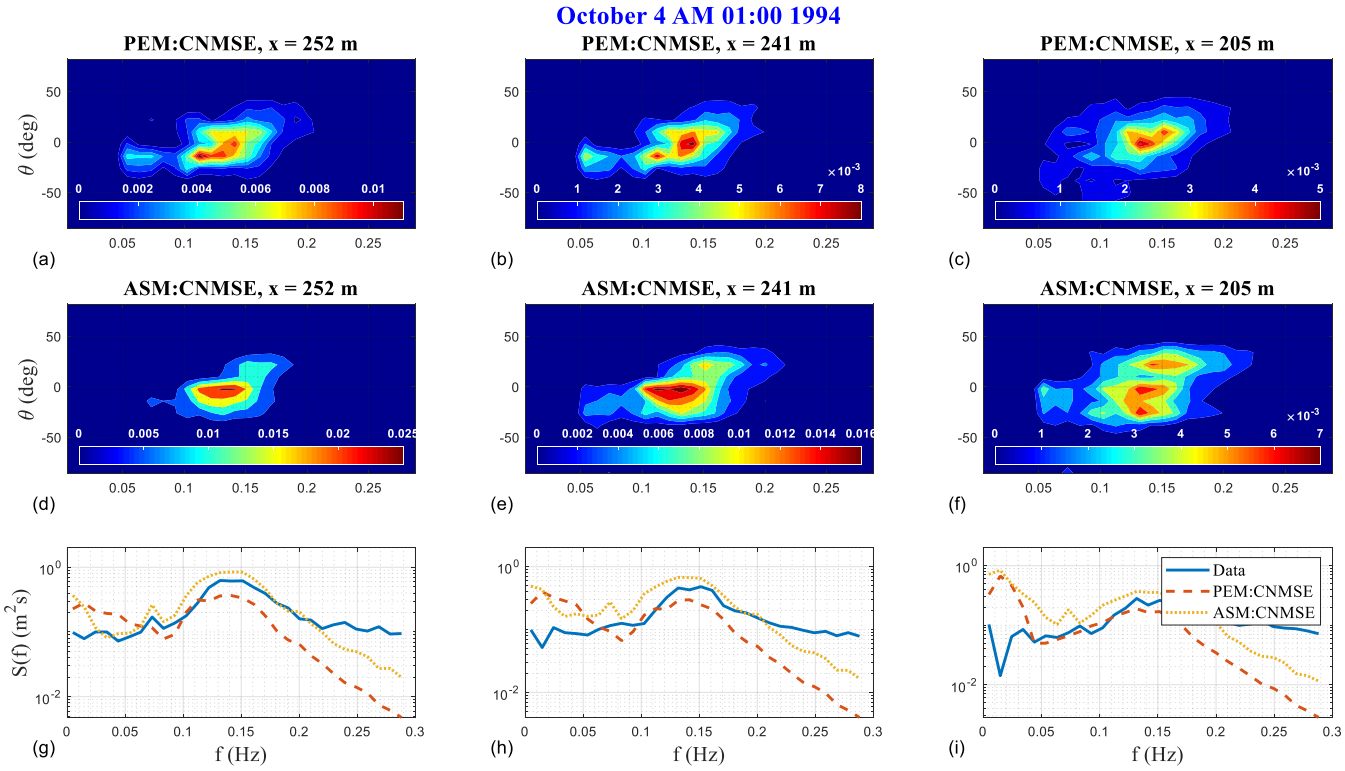

Figure 44 Comparison of directional wave between models and comparison of observed with predicted frequency spectrum on October 4 1994 AM 01:00: (a) PEM: CNMSE at *x* = 252 m; (b) PEM: CNMSE at *x* = 241 m; (c) PEM: CNMSE at *x* = 205 m; (d) Data at *x* = 252 m; (e) ASM: CNMSE at *x* = 241 m; (f) ASM: CNMSE at *x* = 205 m; (g) frequency spectrum at *x* = 480 m; (h) frequency spectrum at *x* = 398 m; (i) frequency spectrum at *x* = 370 m (Solid: field data; Dashed: PEM: CNMSE; Dotted: ASM: CNSME).

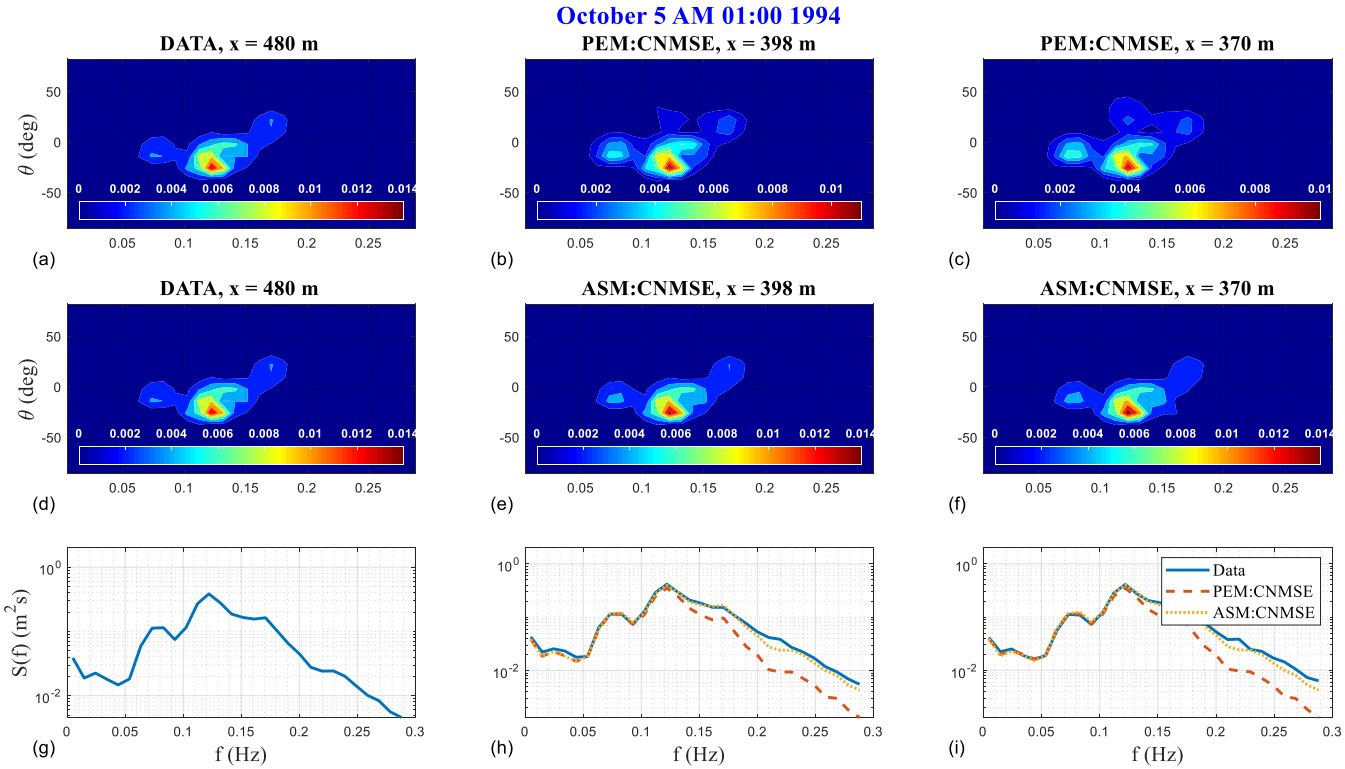

Figure 45 Comparison of directional wave between models and comparison of observed with predicted frequency spectrum on October 5 1994 AM 01:00: (a) Data at *x* = 480 m; (b) PEM: CNMSE at *x* = 398 m; (c) PEM: CNMSE at *x* = 370 m; (d) Data at *x* = 480 m; (e) ASM: CNMSE at *x* = 398 m; (f) ASM: CNMSE at *x* = 370 m; (g) frequency spectrum at *x* = 480 m; (h) frequency spectrum at *x* = 398 m; (i) frequency spectrum at *x* = 370 m (Solid: field data; Dashed: PEM: CNMSE; Dotted: ASM: CNSME).

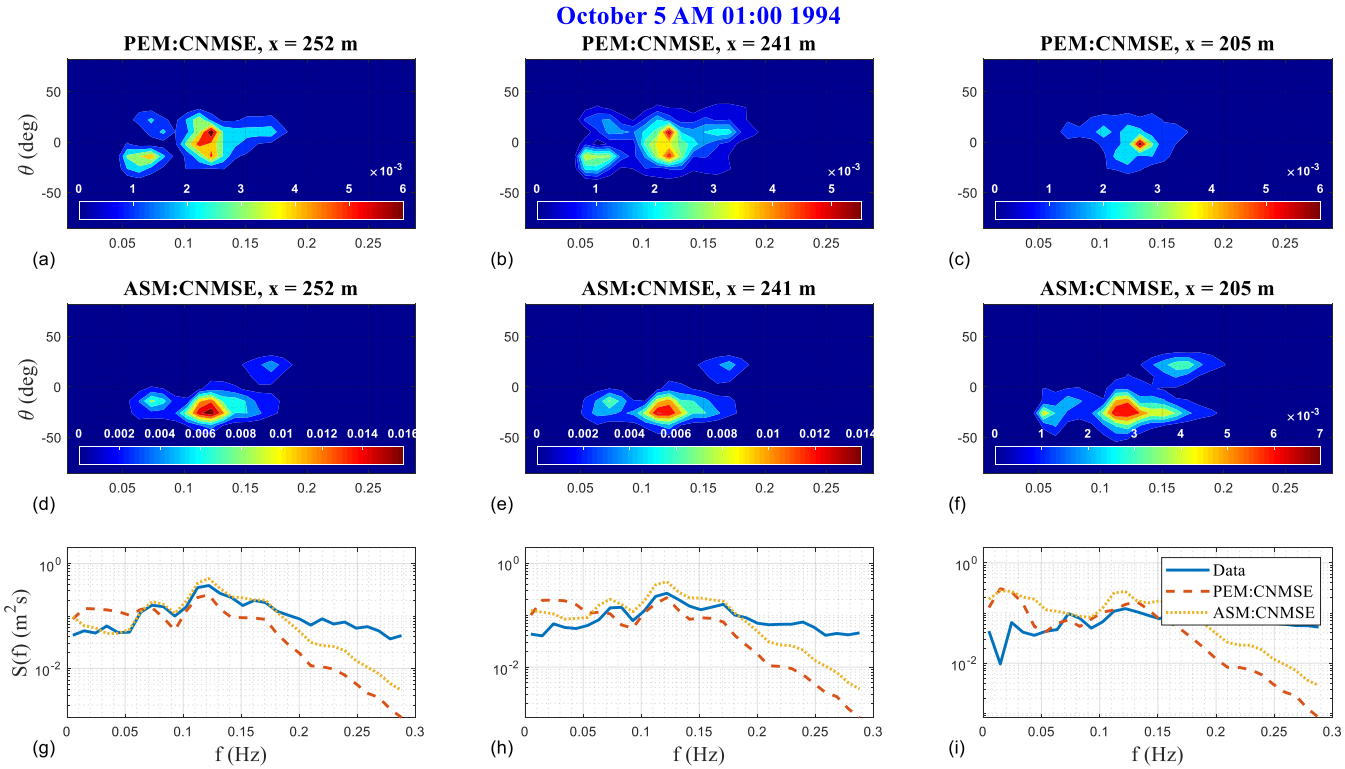

Figure 46 Comparison of directional wave between models and comparison of observed with predicted frequency spectrum on October 5 1994 AM 01:00: (a) PEM: CNMSE at *x* = 252 m; (b) PEM: CNMSE at *x* = 241 m; (c) PEM: CNMSE at *x* = 205 m; (d) Data at *x* = 252 m; (e) ASM: CNMSE at *x* = 241 m; (f) ASM: CNMSE at *x* = 205 m; (g) frequency spectrum at *x* = 480 m; (h) frequency spectrum at *x* = 398 m; (i) frequency spectrum at *x* = 370 m (Solid: field data; Dashed: PEM: CNMSE; Dotted: ASM: CNSME).

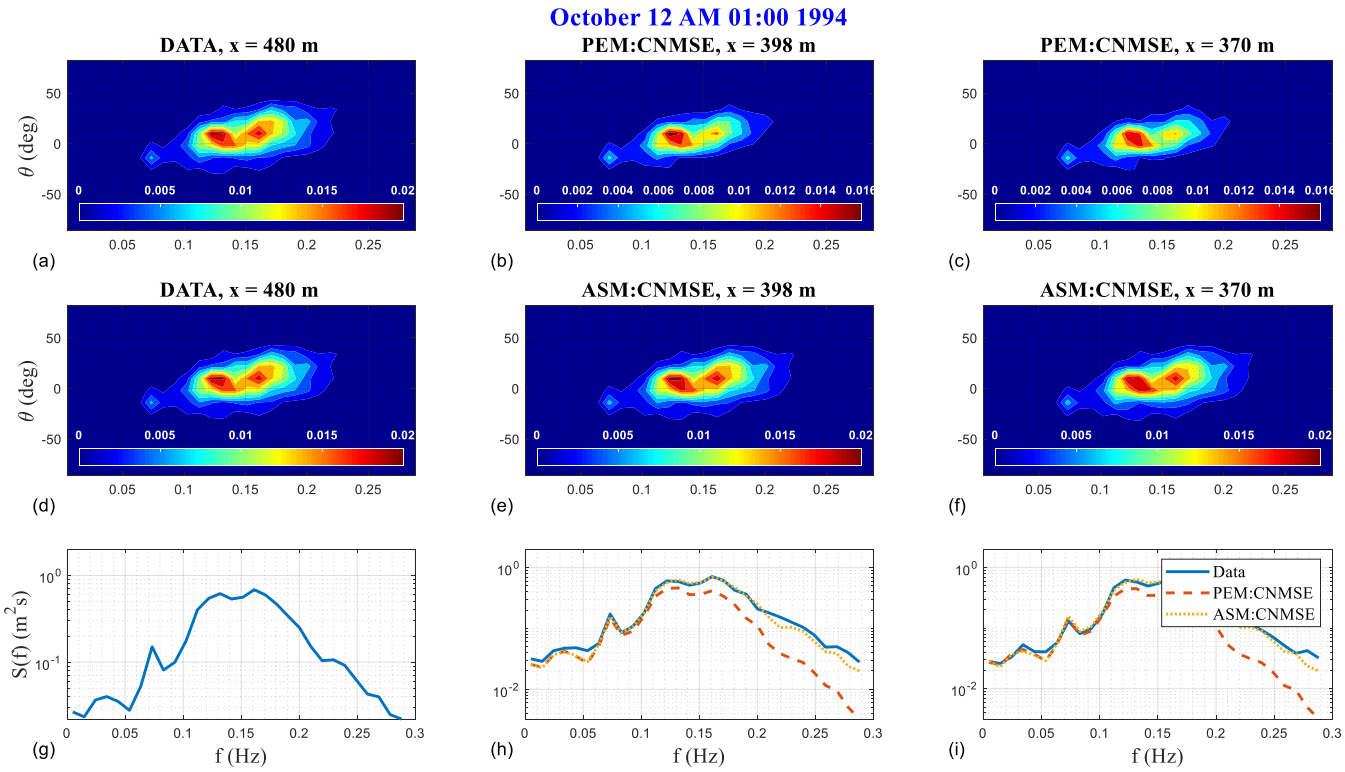

Figure 47 Comparison of directional wave between models and comparison of observed with predicted frequency spectrum on October 12 1994 AM 01:00: (a) Data at *x* = 480 m; (b) PEM: CNMSE at *x* = 398 m; (c) PEM: CNMSE at *x* = 370 m; (d) Data at *x* = 480 m; (e) ASM: CNMSE at *x* = 398 m; (f) ASM: CNMSE at *x* = 370 m; (g) frequency spectrum at *x* = 480 m; (h) frequency spectrum at *x* = 398 m; (i) frequency spectrum at *x* = 370 m (Solid: field data; Dashed: PEM: CNMSE; Dotted: ASM: CNSME).

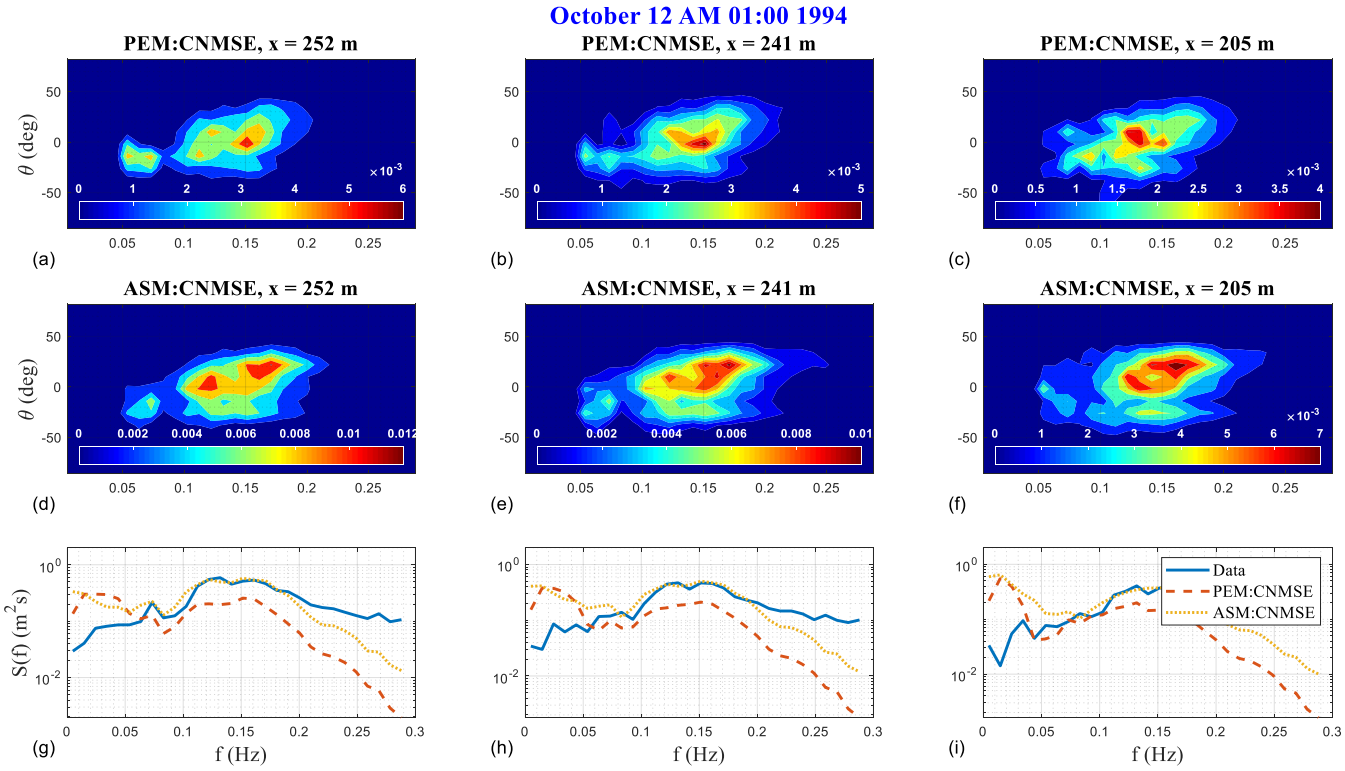

Figure 48 Comparison of directional wave between models and comparison of observed with predicted frequency spectrum on October 12 1994 AM 01:00: (a) PEM: CNMSE at *x* = 252 m; (b) PEM: CNMSE at *x* = 241 m; (c) PEM: CNMSE at *x* = 205 m; (d) Data at *x* = 252 m; (e) ASM: CNMSE at *x* = 241 m; (f) ASM: CNMSE at *x* = 205 m; (g) frequency spectrum at *x* = 480 m; (h) frequency spectrum at *x* = 398 m; (i) frequency spectrum at *x* = 370 m (Solid: field data; Dashed: PEM: CNMSE; Dotted: ASM: CNSME).

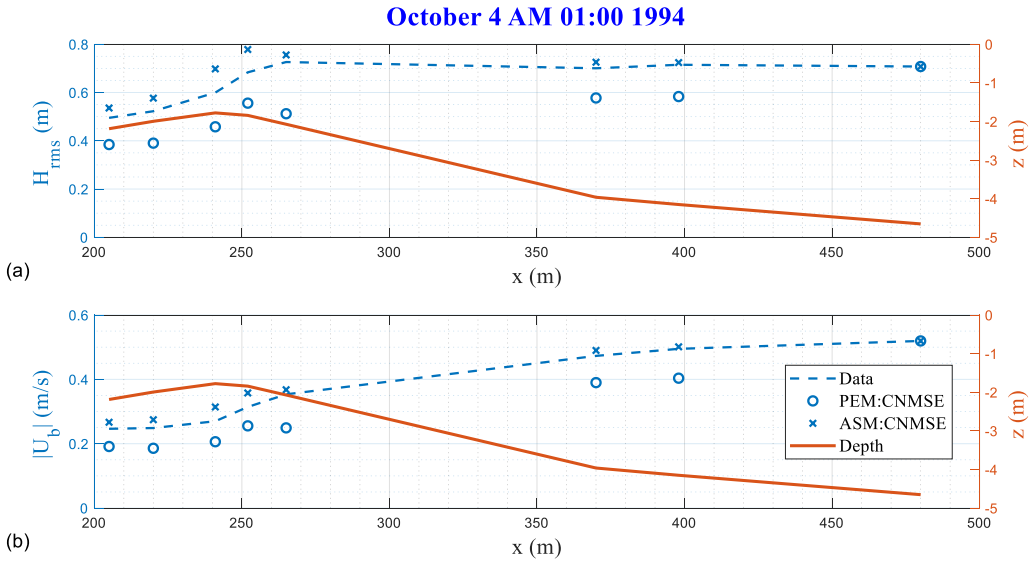

Figure 49 Comparison of bulk parameters on October 4 1994 AM 01:00: (a) H_{rms}; (b) $|U_b|$ (Dashed: field data; Circle: PEM: CNMSE; Ex: ASM: CNSME; Solid: depth).

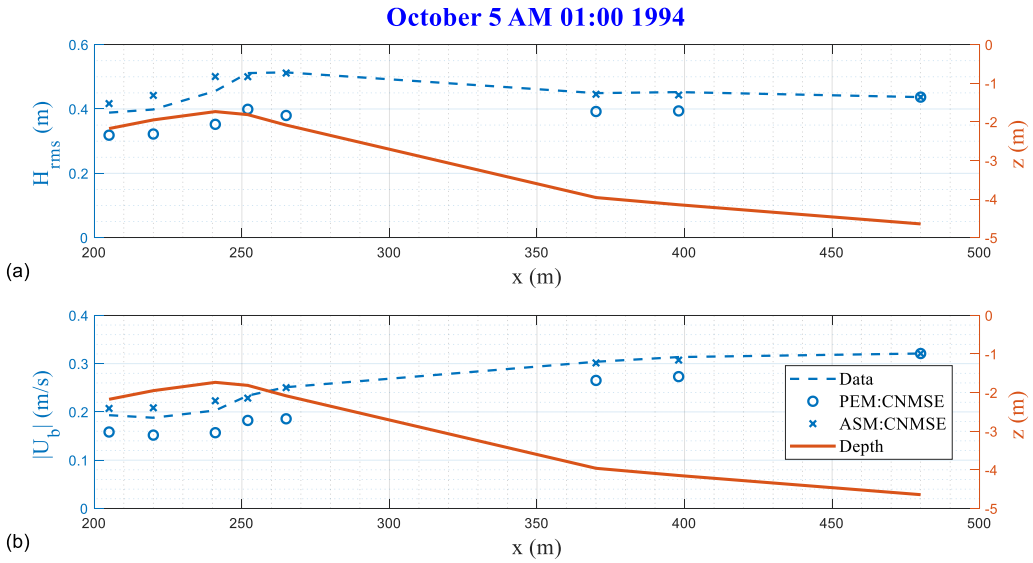

Figure 50 Comparison of bulk parameters on October 5 1994 AM 01:00: (a) H_{rms}; (b) $|U_b|$ (Dashed: field data; Circle: PEM: CNMSE; Ex: ASM: CNSME; Solid: depth).

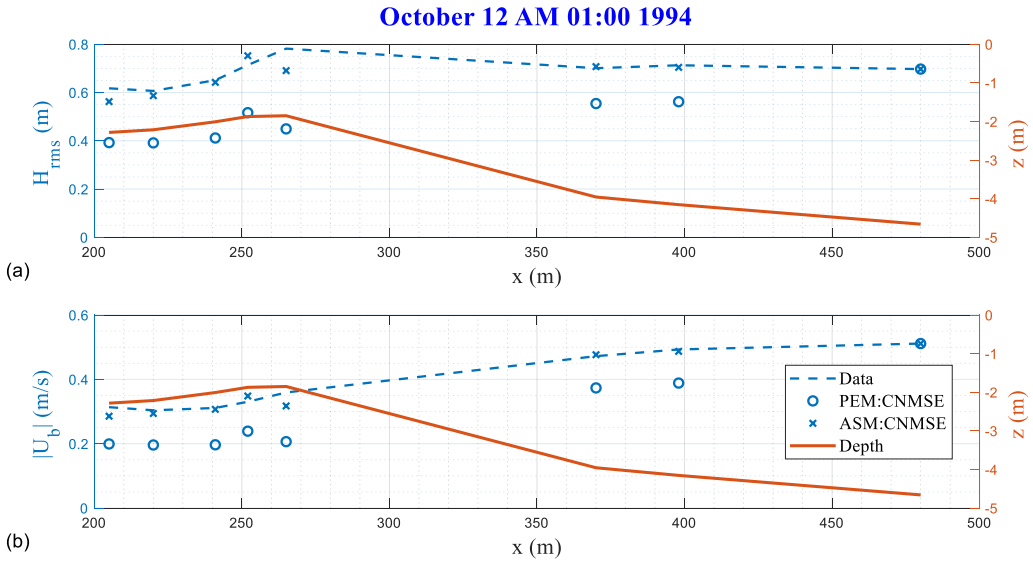

Figure 51 Comparison of bulk parameters on October 12 1994 AM 01:00: (a) H_{rms}; (b) $|U_b|$ (Dashed: field data; Circle: PEM: CNMSE; Ex: ASM: CNSME; Solid: depth).

It is confirmed from the comparison of frequency spectral density and bulk wave statistics with the measurements that the angular spectrum model better predicts wave evolution processes measured during the DUCK94 experiment in comparison to the parabolic equation models. To examine the effect of nonlinearity as well as the added nonlinear amplitude gradient terms (i.e., $A_x A$), the predicted bulk statistics of the present nonlinear angular spectrum model (Equation 7.5; ASM: CNMSE), angular spectrum model based on Kaihatu and Kirby (1995) (retaining only the nonlinear terms of which the interaction coefficients are R_1 and S_1; ASM: KK95), and its linearized counterpart (ASM: LMSE) are shown in comparison to the observed results in Figures 52-54. It is shown that linear theory overpredicts wave heights and the magnitude of bottom velocity in the surf zone and the nonlinear models give better agreement with the field measurement than the linearized model. Comparing the angular spectrum models based on the consistent nonlinear mild-slope equation and the equation of Kaihatu and Kirby (1995), the nonlinear amplitude gradient terms contribute to the additional nonlinear effect and the present model shows improvement in prediction of wave height evolution and maximum bottom wave orbital velocity. Therefore, comparisons to the data of field study over a two-dimensional beach confirms the robustness of the present model in more accurately describing bulk quantities, which are potentially useful for an instantaneous sediment transport (Hoefel and Elgar, 2003; Kaihatu et al., 2007b).

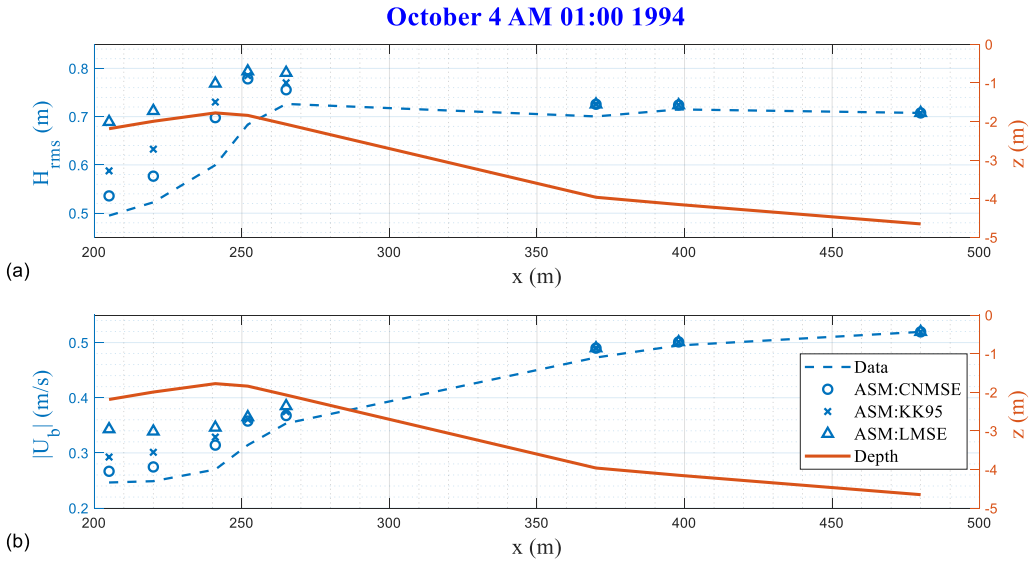

Figure 52 Comparison of bulk parameters on October 4 1994 AM 01:00: (a) H_{rms}; (b) $|U_b|$ (Dashed: field data; Circle: ASM: CNMSE; Ex: ASM: KK95; Triangle: ASM: LMSE; Solid: depth).

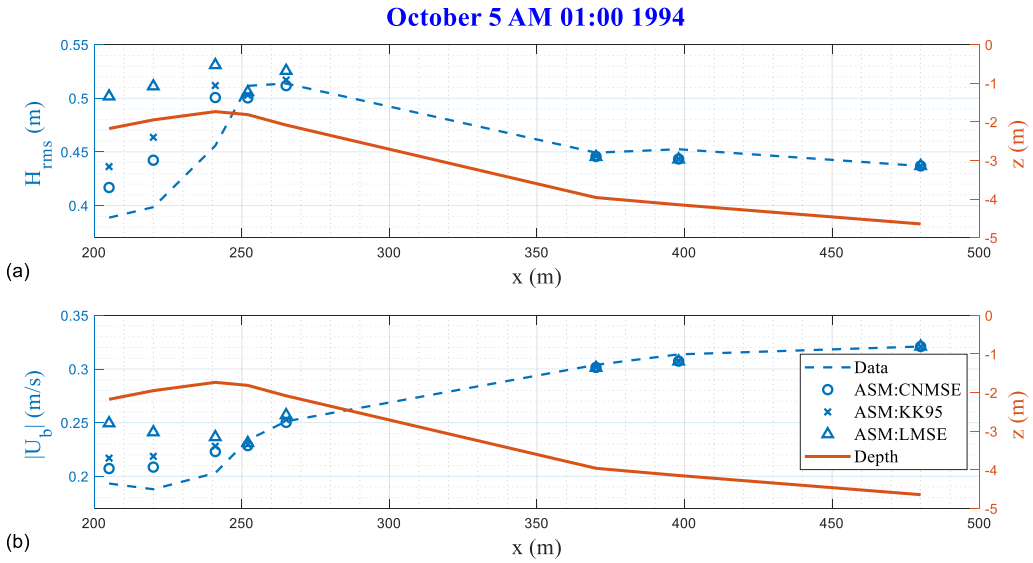

Figure 53 Comparison of bulk parameters on October 5 1994 AM 01:00: (a) H_{rms}; (b) $|U_b|$ (Dashed: field data; Circle: ASM: CNMSE; Ex: ASM: KK95; Triangle: ASM: LMSE; Solid: depth).

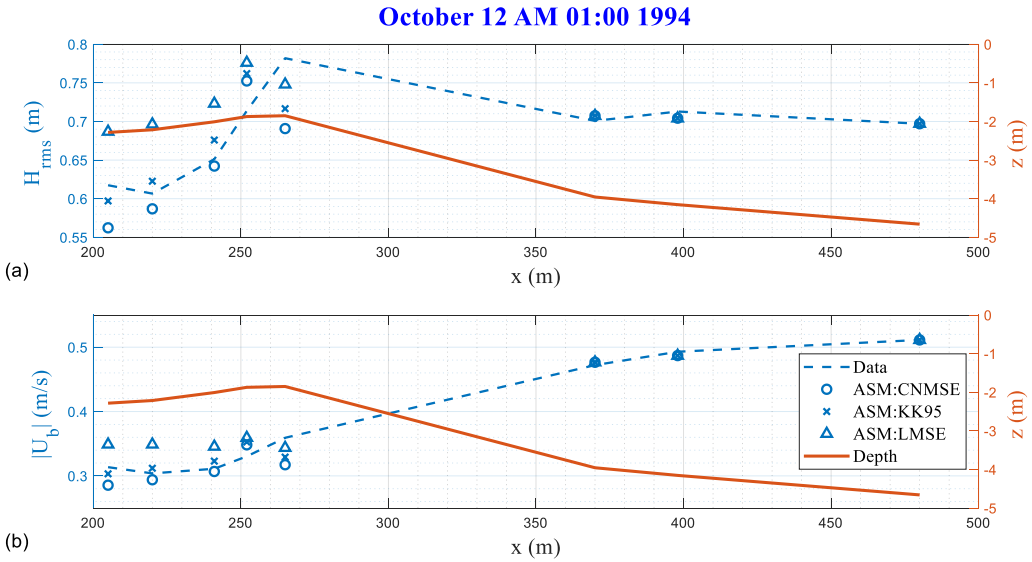

Figure 54 Comparison of bulk parameters on October 12 1994 AM 01:00: (a) H_{rms}; (b) $|U_b|$ (Dashed: field data; Circle: ASM: CNMSE; Ex: ASM: KK95; Triangle: ASM: LMSE; Solid: depth).

7.4 Triad interactions source term

In the phase-averaged operational wave models (e.g., SWAN) based on the spectral action balance equation, several attempts have been made to account for triad wave-wave interactions: the first attempt for the nonlinear evolution of a directional spectrum of Abreu et al. (1992); the lumped-triad approximation (LTA) of Eldeberky (1996); the original collinear approximation (OCA) of Booij et al. (1999); the stochastic parametric model based on Boussinesq equations (SPB) of Becq-Girard et al. (1999); the consistent collinear triad approximation (CCA) of Salmon et al. (2016); and the full two-dimensional source term of Vrecica and Toledo (2019). In this section, we include the development of the CNMSE model as a triad source term formulation suitable for implementation into the SWAN model to account for the advanced nonlinear interaction effect. The parametrized energy term for triad interactions is derived by manipulating the stochastic evolution equation (Eldeberky, 1996). The derivation is fully outlined in Appendix C.

For energy flux $C_g E(f)$ (where energy density is $E(f) = |A_n|^2/\Delta f$), the final form of triad interactions source term is developed from the CNMSE model:

$$S_{nl3}(f_n) = S^{+}_{nl3}(f_n) + S^{-}_{nl3}(f_n) \tag{7.17}$$

where

$$S^{+}_{nl3}(f_n) = \alpha_{EB} C_n C_{gn} \begin{Bmatrix} \left(W1_{n,n/2,n/2}\right)^2 E(f_{n/2}) E(f_{n/2}) \\ +W1_{n,n/2,n/2} W1_{n/2,(-n/2),n} E(f_n) E(f_{n/2}) \\ +W1_{n,n/2,n/2} W1_{n/2,(-n/2),n} E(f_{n/2}) E(f_n) \end{Bmatrix} \sin\left(\Delta_{n,n/2,n/2}\right)$$
$$-\frac{\alpha_{EB}}{4} f_n C_{gn} \begin{bmatrix} W2_{n,n/2,n/2} \begin{Bmatrix} W2_{n/2,(-n/2),n} E(f_{n/2})_x E(f_n) \\ +W3_{n/2,(-n/2),n} E(f_n)_x E(f_{n/2}) \end{Bmatrix} \\ +W3_{n,n/2,n/2} \begin{Bmatrix} W2_{n/2,(-n/2),n} E(f_{n/2})_x E(f_n) \\ +W3_{n/2,(-n/2),n} E(f_n)_x E(f_{n/2}) \end{Bmatrix} \end{bmatrix} \tag{7.18}$$

and

$$S^{-}_{nl3}(f_n) = -2\alpha_{EB} C_{2n} C_{gn} \begin{Bmatrix} \left(W_{n,(-n),2n}\right)^2 E(f_n) E(f_{2n}) \\ +W_{n,(-n),2n} W_{n,(-n),2n} E(f_n) E(f_{2n}) \\ +W_{n,(-n),2n} W_{2n,n,n} E(f_n) E(f_n) \end{Bmatrix} \sin\left(\Delta_{n,(-n),2n}\right)$$
$$+\frac{\alpha_{EB}}{2} f_{2n} C_{gn} \begin{bmatrix} W2_{n,(-n),2n} \begin{Bmatrix} W2_{n,(-n),2n} E(f_n)_x E(f_{2n}) \\ +W3_{n,(-n),2n} E(f_{2n})_x E(f_n) \end{Bmatrix} \\ +W3_{n,(-n),2n} \begin{Bmatrix} -W2_{2n,n,n} E(f_n)_x E(f_n) \\ -W3_{2n,n,n} E(fn)_x E(f_n) \end{Bmatrix} \end{bmatrix} \tag{7.19}$$

where the new interaction coefficients:

$$W1_{n,l,n-l} = \frac{g\omega_n}{8C_{gn}\omega_l\omega_{n-l}} \left[2k_l k_{n-l} + \frac{\omega_{n-l} k_l^{\,2}}{\omega_n} + \frac{\omega_l k_{n-l}^{\,2}}{\omega_n} - \frac{\omega_n^{\,2}\omega_l\omega_{n-l}}{g^2} + \frac{\omega_l^{\,2}\omega_{n-l}^{\,2}}{g^2} \right] \tag{7.20}$$

$$W2_{n,l,n-l} = \frac{g\omega_n k_{n-l}}{4C_{gn}\omega_l\omega_{n-l}} \tag{7.21}$$

$$W3_{n,l,n-l} = \frac{g\omega_n k_l}{4C_{gn}\omega_l\omega_{n-l}} \tag{7.22}$$

and

$$W1_{n,(-l),n+l} = \frac{g\omega_n}{8C_{gn}\omega_l\omega_{n+l}}\left[-2k_l k_{n+l} + \frac{\omega_{n+l}k_l^{\,2}}{\omega_n} - \frac{\omega_l k_{n+l}^{\,2}}{\omega_n} + \frac{\omega_n^{\,2}\omega_l\omega_{n+l}}{g^2} + \frac{\omega_l^{\,2}\omega_{n+l}^{\,2}}{g^2}\right] \quad (7.23)$$

$$W2_{n,(-l),n+l} = \frac{g\omega_n k_{n+l}}{4C_{gn}\omega_l\omega_{n+l}} \quad (7.24)$$

$$W3_{n,(-l),n+l} = -\frac{g\omega_n k_l}{4C_{gn}\omega_l\omega_{n+l}} \quad (7.25)$$

and phase mismatches are newly denoted as:

$$\Delta_{n,l,n-l} = \int -k_n + k_l + k_{n-l}dx \quad (7.26)$$

$$\Delta_{n,(-l),n+l} = \int -k_n - k_l + k_{n+l}dx \quad (7.27)$$

with α_{EB} is a tunning parameter in Eldeberky (1996) ($\alpha_{EB} = 1$ in SWAN, Holthuijsen, 2010).

Finally, the source term based on the consistent nonlinear mild-slope equation model is developed to modify the existing parameterized formulation (e.g., Eldeberky, 1996) to include the additional nonlinear effect from the *x*-derivative nonlinear term A_xA.

CHAPTER VIII

SUMMARY AND FURTHER RESEARCH[*]

8.1 Consistent nonlinear mild-slope equation model

Kaihatu and Kirby (1995) and Tang and Ouellet (1997) extended the model of Agnon et al. (1993) from one-dimensional frequency domain model to the two-dimensional frequency domain models, including quadratic nonlinear terms which represent triad wave-wave interaction between frequency components. One major limitation of previous models from the boundary value problem are the possibility of severe phase mismatches between wave frequencies in high relative water depth, which violates the assumption of slow variation in the horizontal direction.

In this study, we further extended the model of Kaihatu and Kirby (1995) by following the scaling approach of Yue and Mei (1980) and Kirby and Dalrymple (1983). Since the order of amplitude used is lower than the orders of both depth change and modulation scale δ (where A_n is function of δx and $\delta^{1/2} y$), the x-derivative nonlinear term $A_x A$ is retained in the model equation. In addition, horizontal derivative was replaced by vertical derivative in the combined free surface boundary condition, therefore, more triad wave-wave interaction between frequency components is taken into consideration in the model than previous models.

[*] Part of this chapter is reprinted with permission from Kim, I. C. and Kaihatu, J. M., 2021. A consistent nonlinear mild-slope equation model. Coastal Engineering, 170: 104006. Copyright [2021] by Elsevier. DOI: https://doi.org/10.1016/j.coastaleng.2021.104006.

In the region of shallow water, it was shown that the results of present model are in closer agreement with that of experiment compared to frequency domain Boussinesq models. In the region of intermediate or deep water, it is shown that the present model outperforms the previous models from the boundary value problem. Experiment of Chaplain et al. (1992) is one-dimensional case for constant depth, therefore, the only differences between the present and the previous models (Kaihatu and Kirby, 1995 and Tang and Ouellet, 1997) are x-derivative nonlinear term A_xA. As a result, this is probably the effect of x-derivative nonlinear term A_xA, alleviating the effect of phase mismatch.

8.2 Hybrid consistent nonlinear mild-slope equation model

The consistent nonlinear mild-slope equation model was developed in the form of a parabolic equation in the frequency-domain, and takes into consideration a consistent ordering combining the order of bottom change scales in Kirby and Dalrymple (1983) and the modulation scale of Yue and Mei (1980). Despite the fact that the added nonlinear terms (e.g., $A_{lx}A_{n-l}$) allows the consistent model to better describes the triad wave-wave interaction including more nonlinear effect than earlier models (e.g., Kaihatu and Kirby 1995), the addition of new nonlinear terms may increase the iterations required in numerical integration and thus can lead to a more computationally demanding model.

To simulate irregular wave processes in a computationally convenient format, the closure of Benney and Saffman (1966) is introduced within the derivation of simplified formulations from the original consistent nonlinear mild-slope equation, and thus

neglected terms have near-resonant interactions between four waves. Therefore, the final form of nonlinear terms in the equation consists of one part that is proportional to mismatches, and another part with zero mismatch. As expected, the gradient amplitude nonlinear terms A_xA give rise to the nonlinear terms independent of mismatches, mitigating the effect of these mismatches potentially imparting artificially high variability to the wavefield.

Numerical investigations are conducted to test the ability of the new formulations to simulate random waves. The observed spatial evolution of wave spectra is predicted qualitatively well by the present model mainly due to the additional nonlinear terms (independent of phase mismatches) serving as the x-derivative nonlinear term A_xA in the original consistent nonlinear mild-slope equation. The improved performance for the deep water portion of the wave spectra can be explained by the reduced vulnerability of the new model to the impact of strong mismatches in deep water. Besides, the additional nonlinear effect contributed by the quasi-cubic terms lead that the observed spectral evolution at a single- and double-peaks is modeled more precisely in the majority of cases of deep water as well as shallow water by the present model than by the previous model.

8.3 Models for wide-angle water waves

The parabolic equation model has been extensively used for studying the wave transformation due to refraction, diffraction, shoaling, and nonlinear wave interactions, however, the prescribed principal propagation direction inherent in the parabolic

approaches results in the restriction that the wave field must be confined to the propagation at small angles with a preferred direction so that accuracy is optimized. In this study, we suggest two approaches based on the consistent nonlinear mild-slope equation in order to permit wave field propagating into broad band of directions. First model uses the minimax approximation of Kirby (1986b) for the linear terms and nonlinear summation is developed under the ordering system of Kirby (1986a). Secondly, we extend the parabolic equation model of Kim and Kaihatu (2021) by means of alongshore wavenumber components by Fourier decomposition. The inverse Fourier transform terms are further modified with the forcing terms of Janssen et al. (2006) for the interaction between the lateral bottom variation and the wave field.

Two comparisons are provided to demonstrate the ability of the present models to account for the wave focusing by (1) a topographical lens; (2) an elliptic shoal; (3) a circular shoal. Numerical examples show that the first model, based on the higher-order parabolic approximation, accurately describe the simultaneous diffraction and refraction of waves in a realistic topography characterized by strong lateral bottom variation; however, it is also shown that the first model exhibits large distortion of wave pattern resulting from changes in the angle of incidence. This distortion can be interpreted as a result of appreciable error in the minimax approximations as the propagation direction approaches to 90° although the error is minimized over a prespecified range of wave directions in the minimax approximations relative to the previous lower-order equations.

On the other hand, the application of the second (angular spectrum) model to the wave propagation problems confirms that there is little restriction on the range of wave

angles and this model therefore is especially useful in applications to the wide-angle propagation. This is because the summation of angularly spreading waves only affected by refraction and shoaling described the wave field. In accordance with the conclusion of Dalrymple et al. (1989) as to the application to a realistic problem, the second approach has an obvious limitation in that it requires minor bottom variation in alongshore direction. However, the present appears to offer improvement over the other previous angular spectrum models due to the additional nonlinear amplitude gradient terms (i.e., $A_x A$) to that of previous model (e.g., Kaihatu and Kirby, 1995).

8.4 Comparison to field observations

In order to ensure the models' capability in simulating irregular wave processes, the newly developed models are examined with field data from field campaign DUCK94 (Fall 1994) where the U.S. Army Field Research Facility collected measurements of shoaling and breaking waves across an ocean beach at Duck, North Carolina, USA. The parabolic equation model and angular spectrum model based on the consistent nonlinear mild-slope equation incorporate energy dissipation by breaking, using a realistic wave breaking function of Thronton and Guza (1983) modified by Mase and Kirby (1993) to consider the distribution of the dissipation over the frequency range. To minimize the deviation caused by missing values of spectrum in the infragravity band ($f < 0.5f_p$), inaccuracy in the sea band ($f > 1.5f_p$), and the physical mechanisms not included in the present models (e.g., wind input, white-capping, bottom friction, and four-wave interactions), we initialize the present models with the observed measurement at the

most offshore pressure gauge (at x = 480 m) and simulate wave propagation for about 300 m across the beach to the shoreline.

To the best knowledge of the author, this study presents the first comparison between a parabolic equation model and a corresponding angular spectrum model against field experiments. The overall results in the directional wave spectrum and bulk statistics show that the angular spectrum model predicts more accurately the process of dispersion, refraction, shoaling, and nonlinear energy transfer. Additionally, compared to the previous model with less nonlinear summations (i.e., Kaihatu and Kirby, 1995), due to the additional nonlinear amplitude gradient term (i.e., A_xA), the present model does evidence improvement in the prediction of wave height and bottom velocity, which may be required for nearshore applications such as sediment transport.

Lastly, to increase the utility of phase-averaged models (e.g., SWAN) in the nearshore (and thus more effectively link it to larger scale ocean wave modeling), a nonlinear source term based on the consistent nonlinear mild-slope equation model is developed to replace the existing parameterized formulation (e.g., Eldeberky, 1996) to include the added nonlinear effect from the x-derivative nonlinear term A_xA.

8.5 Future research

Future work will focus on using the model to include other effects and consider other situations. With respect to larger scales of operation, it should be desirable to take into account additional physical characteristics such as the ambient current (e.g., Kirby, 1986a; Kirby and Chen, 1989). To study the effect of ambient currents on nearshore

nonlinear cross-spectral energy exchange, we should derive a frequency-domain phase-resolving model for wave propagation that combines motion of waves and current.

As a suggestion for extension of the present model, the dissipation term can be formulated for nearshore sediment transport (e.g., Kaihatu et al., 2007a; Tahvildari and Kaihatu, 2011). Wave energy dissipation over mud is an important mechanism so that accurate prediction of a mud-induced damping is important for understanding nearshore circulation and accounting for costal processes in muddy coastal areas. Most analytical formulations of bed-induced wave dissipation typically, concentrating on a single physical process in terms of the bed state and composition and providing the characteristics of the mud for energy damping, are based on linear theory. Therefore, in order to take into incorporating more realistic scenarios, phase-resolving frequency-domain models have incorporated these analytical functions to investigate the effect of sediment on nearshore wave evolution.

Furthermore, we can potentially extend the consistent nonlinear mild-slope equation model to the case of steep slope such as fringing coral reefs, where the total rate of breaking-induced energy dissipation becomes larger than over a gentle sloping beach. The model can be modified by keeping higher-order bottom change terms neglected in the original form in an *a posteriori* sense. The reefs feature steep slope and complex structures that can potentially protect shorelines from the impact of waves and strong currents, which further impact morphological evolution. The steep face induces an intense wave breaking which is as large as the nonlinear interactions, leading to a reduction in wave action on the areas of coral reef. One often observes high water-level

events and high infragravity wave runup events on the regions, which consequently cause quarrying of blocks from the cliff top (Sheremet et al., 2014).

The present model, in its phase-resolved form, rigorously describes subharmonic and superharmonic interactions (to its order of truncation) so that important process such as infragravity wave generation and frequency-directional spectral widening can be realistically simulated. Therefore, the model can provide insight on the complex physics of triad interactions to phase-averaged spectral operational models (e.g., SWAN) and nearshore numerical models for nearshore and coastal areas (e.g., XBeach, Roelvink et al., 2009). Moreover, the present angular spectrum model based on the consistent nonlinear mild-slope equation model will be extended to the development of triad interactions source term to account for not only the additional nonlinear effect but also a two-dimensional wave field which is responsible for redistributing the energy over a wide range of directions (Vrecica and Toledo, 2019).

Lastly, by coupling numerical wave models, namely, phase-averaged operational wave model (e.g., SWAN) and phase-resolving model in frequency-domain (e.g., CNMSE model) with machine learning methods (e.g., artificial neural network (ANN) model), we can propose a new system for wave parameter prediction. While the ANN model reduces numerical complexity inherent in the numerical wave models (e.g., CNMSE model), the numerical wave models provide wave data which retains phase information for training, thus providing the relevant nearshore physics to the training set. For example, an operational spectral wave model can be used with wind data to calculate directional wave spectrum, which is in turn used to obtain the higher-order statistics as

well as spectral density in shallow water by using the CNMSE model. Then, the ANN model can output the significant wave height through using not only wind velocities but also the skewness and asymmetry as input values to get significant improvements in the prediction of wave heights. Through this work, we can construct an accurate and economical approach for short-term wave forecasts for coastal protection.

REFERENCES

Abreu, M., Larraza, A. and Thornton, E., 1992. Nonlinear transformation of directional wave spectra in shallow water. Journal of Geophysical Research: Oceans, 97(C10): 15579-15589.

Agnon, Y., Madsen, P.A. and Schäffer, H., 1999. A new approach to high-order boussinesq models. J Fluid Mech, 399: 319-333.

Agnon, Y. and Sheremet, A., 1997. Stochastic nonlinear shoaling of directional spectra. J Fluid Mech, 345: 79-99.

Agnon, Y., Sheremet, A., Gonsalves, J. and Stiassnie, M., 1993. Nonlinear evolution of a unidirectional shoaling wave field. Coastal Engineering, 20(1-2): 29-58.

Ardani, S. and Kaihatu, J.M., 2019. Evolution of high frequency waves in shoaling and breaking wave spectra. Physics of Fluids, 31(8): 087102.

Baldock, T., Holmes, P., Bunker, S. and Van Weert, P., 1998. Cross-shore hydrodynamics within an unsaturated surf zone. Coastal Engineering, 34(3-4): 173-196.

Battjes, J.A. and Janssen, J., 1978. Energy loss and set-up due to breaking of random waves, Coastal engineering 1978, pp. 569-587.

Becq-Girard, F., Forget, P. and Benoit, M., 1999. Non-linear propagation of unidirectional wave fields over varying topography. Coastal Engineering, 38(2): 91-113.

Benney, D. and Saffman, P.G., 1966. Nonlinear interactions of random waves in a dispersive medium. Proceedings of the Royal Society of London. Series A. Mathematical and Physical Sciences, 289(1418): 301-320.

Berkhoff, J., 1973. Computation of combined refraction—diffraction, Coastal engineering 1972, pp. 471-490.

Berkhoff, J., Booy, N. and Radder, A.C., 1982. Verification of numerical wave propagation models for simple harmonic linear water waves. Coastal Engineering, 6(3): 255-279.

Birkemeier, W.A., Long, C.E. and Hathaway, K.K., 1997. Delilah, duck94 & sandyduck: Three nearshore field experiments, Coastal engineering 1996, pp. 4052-4065.

Birkemeier, W.A. and Thornton, E.B., 1994. The duck94 nearshore field experiment. Coastal Dynamics94, pp. 815-821.

Boczar-Karakiewicz, B., 1972. Transformation of wave profile in shallow water—a fourier analysis. Arch. Hydrotechnik, 19: 197-210.

Booij, N., 1981. Gravity waves on water with non-uniform depth and current.

Booij, N., Ris, R.C. and Holthuijsen, L.H., 1999. A third-generation wave model for coastal regions: 1. Model description and validation. Journal of geophysical research: Oceans, 104(C4): 7649-7666.

Bouws, E., Günther, H., Rosenthal, W. and Vincent, C., 1985. Similarity of the wind wave spectrum in finite depth water: 1. Spectral form. Journal of Geophysical Research: Oceans, 90(C1): 975-986.

Bowen, G.D. and Kirby, J.T., 1994. Shoaling and breaking random waves on a 1: 35 laboratory beach. University of Delaware, Department of Civil Engineering, Center for Applied Coastal Res.

Bredmose, H., Agnon, Y., Madsen, P.A. and Schäffer, H.A., 2005. Wave transformation models with exact second-order transfer. European Journal of Mechanics-B/Fluids, 24(6): 659-682.

Bredmose, H., Schäffer, H. and Madsen, P.A., 2004. Boussinesq evolution equations: Numerical efficiency, breaking and amplitude dispersion. Coastal Engineering, 51(11-12): 1117-1142.

Bryant, P., 1973. Periodic waves in shallow water. J Fluid Mech, 59(4): 625-644.

Bryant, P., 1974. Stability of periodic waves in shallow water. J Fluid Mech, 66(1): 81-96.

Chapalain, G., Cointe, R. and Temperville, A., 1992. Observed and modeled resonantly interacting progressive water-waves. Coastal engineering, 16(3): 267-300.

Chawla, A., 1995. Wave transformation over a submerged shoal. MS thesis, Department of Civil Engineering, University of Delaware.

Chen, Y., Guza, R. and Elgar, S., 1997. Modeling spectra of breaking surface waves in shallow water. Journal of Geophysical Research: Oceans, 102(C11): 25035-25046.

Chen, Y. and Liu, P.L.F., 1995. Modified boussinesq equations and associated parabolic models for water wave propagation. J Fluid Mech, 288: 351-381.

Crank, J. and Nicolson, P., 1947. A practical method for numerical evaluation of solutions of partial differential equations of the heat-conduction type. Mathematical Proceedings of the Cambridge Philosophical Society, pp. 50-67.

Dalrymple, R.A. and Kirby, J.T., 1988. Models for very wide-angle water waves and wave diffraction. J Fluid Mech, 192: 33-50.

Dalrymple, R.A., Kirby, J.T. and Hwang, P.A., 1984. Wave diffraction due to areas of energy-dissipation. J Waterw Port C-Asce, 110(1): 67-79.

Dalrymple, R.A., Suh, K.D., Kirby, J.T. and Chae, J.W., 1989. Models for very wide-angle water waves and wave diffraction. Part 2. Irregular bathymetry. J Fluid Mech, 201: 299-322.

Davis, J.R., Sheremet, A., Tian, M. and Saxena, S., 2014. A numerical implementation of a nonlinear mild slope model for shoaling directional waves. Journal of Marine Science and Engineering, 2(1): 140-158.

Dean, R.G., 1965. Stream function representation of nonlinear ocean waves. Journal of Geophysical Research, 70(18): 4561-4572.

Dean, R.G. and Dalrymple, R.A., 1991. Water wave mechanics for engineers and scientists, 2. world scientific publishing company.

Eldeberky, Y., 1996. Nonlinear transformation of wave spectra in the nearshore zone. PhD thesis. Delft University of Technology, Netherlands.

Eldeberky, Y. and Battjes, J.A., 1996. Spectral modeling of wave breaking: Application to boussinesq equations. Journal of Geophysical Research: Oceans, 101(C1): 1253-1264.

Eldeberky, Y. and Madsen, P.A., 1999. Deterministic and stochastic evolution equations for fully dispersive and weakly nonlinear waves. Coastal Engineering, 38(1): 1-24.

Engsig-Karup, A.P., Bingham, H.B. and Lindberg, O., 2009. An efficient flexible-order model for 3d nonlinear water waves. Journal of computational physics, 228(6): 2100-2118.

Freilich, M. and Guza, R., 1984. Nonlinear effects on shoaling surface gravity waves. Philosophical Transactions of the Royal Society of London. Series A, Mathematical and Physical Sciences, 311(1515): 1-41.

Fuhrman, D.R. and Madsen, P.A., 2009. Tsunami generation, propagation, and run-up with a high-order boussinesq model. Coastal Engineering, 56(7): 747-758.

Gobbi, M.F., Kirby, J.T. and Wei, G., 2000. A fully nonlinear boussinesq model for surface waves. Part 2. Extension to o (kh) 4. J Fluid Mech, 405: 181-210.

Hasselmann, K. et al., 1973. Measurements of wind-wave growth and swell decay during the joint north sea wave project (JONSWAP). Ergaenzungsheft zur Deutschen Hydrographischen Zeitschrift, Reihe A.

Herbers, T. and Burton, M., 1997. Nonlinear shoaling of directionally spread waves on a beach. Journal of Geophysical Research: Oceans, 102(C9): 21101-21114.

Herbers, T., Orzech, M., Elgar, S. and Guza, R., 2003. Shoaling transformation of wave frequency-directional spectra. Journal of Geophysical Research: Oceans, 108(C1).

Hoefel, F. and Elgar, S., 2003. Wave-induced sediment transport and sandbar migration. Science, 299(5614): 1885-1887.

Holthuijsen, L.H., 2010. Waves in oceanic and coastal waters. Cambridge university press.

Janssen, T.T., 2006. Nonlinear surface waves over topography. PhD thesis. Delft University of Technology, Netherlands.

Janssen, T.T. and Battjes, J., 2007. A note on wave energy dissipation over steep beaches. Coastal Engineering, 54(9): 711-716.

Janssen, T.T., Herbers, T. and Battjes, J., 2006. Generalized evolution equations for nonlinear surface gravity waves over two-dimensional topography. J Fluid Mech, 552: 393.

Kaihatu, J.M., 2001. Improvement of parabolic nonlinear dispersive wave model. Journal of waterway, port, coastal, and ocean engineering, 127(2): 113-121.

Kaihatu, J.M. and Kirby, J.T., 1995. Nonlinear transformation of waves in finite water depth. Physics of Fluids, 7(8): 1903-1914.

Kaihatu, J.M. and Kirby, J.T., 1997. Effects of mode truncation and dissipation on predictions of higher order statistics, Coastal engineering 1996, pp. 123-136.

Kaihatu, J.M. and Kirby, J.T., 1998. Two-dimensional parabolic modeling of extended boussinesq equations. Journal of waterway, port, coastal, and ocean engineering, 124(2): 57-67.

Kaihatu, J.M., Sheremet, A. and Holland, K.T., 2007a. A model for the propagation of nonlinear surface waves over viscous muds. Coastal Engineering, 54(10): 752-764.

Kaihatu, J.M., Veeramony, J., Edwards, K.L. and Kirby, J.T., 2007b. Asymptotic behavior of frequency and wave number spectra of nearshore shoaling and breaking waves. Journal of geophysical research: Oceans, 112(C6).

Keller, J.B., 1958. Surface waves on water of non-uniform depth. J Fluid Mech, 4(6): 607-614.

Kim, I.-C. and Kaihatu, J.M., 2021. A consistent nonlinear mild-slope equation model. Coastal Engineering, 170: 104006.

Kirby, J.T., 1984. A note on linear surface wave-current interaction over slowly varying topography. Journal of Geophysical Research: Oceans, 89(C1): 745-747.

Kirby, J.T., 1986a. Higher-order approximations in the parabolic equation method for water waves. Journal of Geophysical Research: Oceans, 91(C1): 933-952.

Kirby, J.T., 1986b. Rational approximations in the parabolic equation method for water waves. Coastal Engineering, 10(4): 355-378.

Kirby, J.T., 1991. Modelling shoaling directional wave spectra in shallow water, Coastal engineering 1990, pp. 109-122.

Kirby, J.T. and Chen, T.M., 1989. Surface waves on vertically sheared flows: Approximate dispersion relations. Journal of Geophysical Research: Oceans, 94(C1): 1013-1027.

Kirby, J.T. and Dalrymple, R.A., 1983. A parabolic equation for the combined refraction–diffraction of stokes waves by mildly varying topography. J Fluid Mech, 136: 453-466.

Kirby, J.T. and Dalrymple, R.A., 1984. Verification of a parabolic equation for propagation of weakly-nonlinear waves. Coastal Engineering, 8(3): 219-232.

Kirby, J.T. and Kaihatu, J.M., 1997. Structure of frequency domain models for random wave breaking, Coastal engineering 1996, pp. 1144-1155.

Kofoed-Hansen, H. and Rasmussen, J.H., 1998. Modelling of nonlinear shoaling based on stochastic evolution equations. Coastal engineering, 33(2-3): 203-232.

Lin, Z. et al., 2021. A finite volume based fully nonlinear potential flow model for water wave problems. Applied Ocean Research, 106: 102445.

Liu, P.L.F., 1983. Wave-current interactions on a slowly varying topography. Journal of Geophysical Research: Oceans, 88(C7): 4421-4426.

Liu, P.L.F., 1986. Parabolic wave equation for surface water waves, COASTAL ENGINEERING RESEARCH CENTER VICKSBURG MS.

Liu, P.L.F. and Tsay, T.-K., 1984. Refraction-diffraction model for weakly nonlinear water waves. J Fluid Mech, 141: 265-274.

Liu, P.L.F., Yoon, S.B. and Kirby, J.T., 1985. Nonlinear refraction–diffraction of waves in shallow water. J Fluid Mech, 153: 185-201.

Liu, Z. and Fang, K., 2016. A new two-layer boussinesq model for coastal waves from deep to shallow water: Derivation and analysis. Wave Motion, 67: 1-14.

Liu, Z., Fang, K. and Cheng, Y., 2018. A new multi-layer irrotational boussinesq-type model for highly nonlinear and dispersive surface waves over a mildly sloping seabed. J Fluid Mech, 842: 323.

Longuet-Higgins, M.S. and Stewart, R., 1964. Radiation stresses in water waves; a physical discussion, with applications. Deep-Sea Res, 11(4): 529-562.

Lozano, C. and Liu, P.L.F., 1980. Refraction-diffraction model for linear surface-water waves. J Fluid Mech, 101(Dec): 705-720.

Luke, J.C., 1967. A variational principle for a fluid with a free surface. J Fluid Mech, 27(2): 395-397.

Lynett, P. and Liu, P.L.F., 2004. A two-layer approach to wave modelling. Proceedings of the Royal Society of London. Series A: Mathematical, Physical and Engineering Sciences, 460(2049): 2637-2669.

Madsen, P.A., Bingham, H. and Schäffer, H., 2003. Boussinesq-type formulations for fully nonlinear and extremely dispersive water waves: Derivation and analysis. Proceedings of the Royal Society of London. Series A: Mathematical, Physical and Engineering Sciences, 459(2033): 1075-1104.

Madsen, P.A., Murray, R. and Sørensen, O.R., 1991. A new form of the boussinesq equations with improved linear dispersion characteristics. Coastal engineering, 15(4): 371-388.

Madsen, P.A. and Schäffer, H., 1998. Higher–order boussinesq–type equations for surface gravity waves: Derivation and analysis. Philosophical Transactions of the

Royal Society of London. Series A: Mathematical, Physical and Engineering Sciences, 356(1749): 3123-3181.

Madsen, P.A. and Sørensen, O., 1993. Bound waves and triad interactions in shallow water. Ocean Engineering, 20(4): 359-388.

Mase, H. and Kirby, J.T., 1993. Hybrid frequency-domain kdv equation for random wave transformation, Coastal engineering 1992, pp. 474-487.

Mei, C.C., 1983. The applied dynamics of ocean surface waves. Wiley.

Mei, C.C. and Ünlüata, U., 1972. Harmonic generation in shallow water waves. Waves on beaches, re meyer, ed. Academic Press.

Memos, C., 1980. Water waves diffracted by two breakwaters. Journal of Hydraulic Research, 18(4): 343-357.

Nwogu, O., 1993. Alternative form of boussinesq equations for nearshore wave propagation. Journal of waterway, port, coastal, and ocean engineering, 119(6): 618-638.

O'Brien, M.P. and Mason, M.A., 1942. A summary of the theory of oscillatory waves. Columbia University Libraries.

Penney, W.G. et al., 1952. Part i. The diffraction theory of sea waves and the shelter afforded by breakwaters. Philosophical Transactions of the Royal Society of London. Series A, Mathematical and Physical Sciences, 244(882): 236-253.

Peregrine, D.H., 1967. Long waves on a beach. J Fluid Mech, 27(4): 815-827.

Radder, A., 1979. On the parabolic equation method for water-wave propagation. J Fluid Mech, 95(1): 159-176.

Raoult, C., Benoit, M. and Yates, M.L., 2019. Development and validation of a 3d rbf-spectral model for coastal wave simulation. Journal of Computational Physics, 378: 278-302.

Roelvink, D. et al., 2009. Modelling storm impacts on beaches, dunes and barrier islands. Coastal Engineering, 56(11-12): 1133-1152.

Rygg, O.B., 1988. Nonlinear refraction-diffraction of surface waves in intermediate and shallow water. Coastal Engineering, 12(3): 191-211.

Salmon, J., Smit, P., Janssen, T.T. and Holthuijsen, L., 2016. A consistent collinear triad approximation for operational wave models. Ocean Modelling, 104: 203-212.

Sharma, A., Panchang, V.G. and Kaihatu, J.M., 2014. Modeling nonlinear wave–wave interactions with the elliptic mild slope equation. Applied Ocean Research, 48: 114-125.

Sheremet, A., Davis, J.R., Tian, M., Hanson, J.L. and Hathaway, K.K., 2016. Triads: A phase-resolving model for nonlinear shoaling of directional wave spectra. Ocean Modelling, 99: 60-74.

Sheremet, A., Kaihatu, J., Su, S.-F., Smith, E. and Smith, J., 2011. Modeling of nonlinear wave propagation over fringing reefs. Coastal Engineering, 58(12): 1125-1137.

Sheremet, A., Staples, T., Ardhuin, F., Suanez, S. and Fichaut, B., 2014. Observations of large infragravity wave runup at banneg island, france. Geophysical Research Letters, 41(3): 976-982.

Smith, J.M. and Vincent, C.L., 1992. Shoaling and decay of two wave trains on beach. Journal of waterway, port, coastal, and ocean engineering, 118(5): 517-533.

Smith, R. and Sprinks, T., 1975. Scattering of surface waves by a conical island. J Fluid Mech, 72(2): 373-384.

Suh, K.D., Dalrymple, R.A. and Kirby, J.T., 1990. An angular spectrum model for propagation of stokes waves. J Fluid Mech, 221: 205-232.

Tahvildari, N. and Kaihatu, J.M., 2011. Optimized determination of viscous mud properties using a nonlinear wave–mud interaction model. Journal of Atmospheric and Oceanic Technology, 28(11): 1486-1503.

Tang, Y. and Ouellet, Y., 1997. A new kind of nonlinear mild-slope equation for combined refraction-diffraction of multifrequency waves. Coastal Engineering, 31(1-4): 3-36.

Thornton, E.B. and Guza, R., 1983. Transformation of wave height distribution. Journal of Geophysical Research: Oceans, 88(C10): 5925-5938.

Toledo, Y., 2013. The oblique parabolic equation model for linear and nonlinear wave shoaling. J Fluid Mech, 715: 103.

Tsay, T.K., Ebersole, B.A. and Liu, P.L.F., 1989. Numerical modelling of wave propagation using parabolic approximation with a boundary-fitted co-ordinate system. International journal for numerical methods in engineering, 27(1): 37-55.

Tsay, T.K. and Liu, P.L.F., 1982. Numerical solution of water-wave refraction and diffraction problems in the parabolic approximation. Journal of Geophysical Research: Oceans, 87(C10): 7932-7940.

Vrecica, T. and Toledo, Y., 2016. Consistent nonlinear stochastic evolution equations for deep to shallow water wave shoaling. J Fluid Mech, 794: 310.

Vrecica, T. and Toledo, Y., 2019. Consistent nonlinear deterministic and stochastic wave evolution equations from deep water to the breaking region. J Fluid Mech, 877: 373-404.

Wei, G. and Kirby, J.T., 1995. Time-dependent numerical code for extended boussinesq equations. Journal of waterway, port, coastal, and ocean engineering, 121(5): 251-261.

Wei, G., Kirby, J.T., Grilli, S.T. and Subramanya, R., 1995. A fully nonlinear boussinesq model for surface waves. Part 1. Highly nonlinear unsteady waves. J Fluid Mech, 294: 71-92.

Wei, G., Kirby, J.T. and Sinha, A., 1999. Generation of waves in boussinesq models using a source function method. Coastal Engineering, 36(4): 271-299.

Whalin, R.W., 1971. The limit of applicability of linear wave refraction theory in a convergence zone. Waterways Experiment Station.

Willmott, C.J., 1982. Some comments on the evaluation of model performance. Bulletin of the American Meteorological Society, 63(11): 1309-1313.

Witting, J.M., 1984. A unified model for the evolution nonlinear water waves. Journal of computational physics, 56(2): 203-236.

Yue, D.K. and Mei, C.C., 1980. Forward diffraction of stokes waves by a thin wedge. J Fluid Mech, 99(1): 33-52.

APPENDIX A*

In Section 2.3, we illustrated the impact of the additional terms developed by the consistent ordering on the phase mismatch, which was often mentioned (e.g., Kaihatu and Kirby, 1995) as a drawback of their nonlinear mild-slope equation. In this appendix we illustrate the impact of these additional terms on the phase mismatch for the case of $N = 2$, or two frequency components. At the wave maker station ($x = 0$), the equations can be simplified since all values are given, with the x-derivatives of amplitude the only unknown.

(1) Kaihatu and Kirby (1995) (Equation 2.64)

When $N = 2$ and a grid step size of Δx, the one-dimensional equations of Kaihatu and Kirby (1995) can be written for a constant depth:

$$A_{1x} = -i\frac{2S_1}{8\left(kCC_g\right)_1}A_1^* A_2 \exp\left[i\left(k_2 - 2k_1\right)\Delta x\right] \tag{A.1}$$

$$A_{2x} = -i\frac{R_1}{8\left(kCC_g\right)_2}A_1^2 \exp\left[i\left(2k_1 - k_2\right)\Delta x\right] \tag{A.2}$$

The phase mismatches can be simplified up to second order in μ, similarly to what was done in Section 2.3:

$$k_2 - 2k_1 = \mu^2\kappa + O\left(\mu^4\right) \tag{A.3}$$

* This chapter is reprinted with permission from Kim, I. C. and Kaihatu, J. M., 2021. A consistent nonlinear mild-slope equation model. Coastal Engineering, 170: 104006. Copyright [2021] by Elsevier. DOI: https://doi.org/10.1016/j.coastaleng.2021.104006.

Except for *x*-derivatives of amplitude and phase mismatches, all the variables are given values, so the equations can be written with complex number constant *K* combining all given values (these are distinguished by subscripts and primes):

$$A_{1x} = K_1 \exp\left[i\mu^2 \kappa \Delta x \right] \tag{A.4}$$

$$A_{2x} = K_1' \exp\left[-i\mu^2 \kappa \Delta x \right] \tag{A.5}$$

(2) Present model (Equation 2.65)

When $N = 2$, the one-dimensional form of the present model can be written for a constant depth as follows:

$$A_{1x} = -\frac{i}{8\left(kCC_g\right)_1}\left\{2S_1 A_1^* A_2 + 2S_2 A_{1x}^* A_2 + 2S_3 A_1^* A_{2x}\right\} \exp\left[i\left(k_2 - 2k_1\right)\Delta x \right] \tag{A.6}$$

$$A_{2x} = -\frac{i}{8\left(kCC_g\right)_2}\left\{R_1 A_1^{\,2} + R_2 A_{1x} A_1 + R_3 A_1 A_{1x}\right\} \exp\left[i\left(2k_1 - k_2\right)\Delta x \right] \tag{A.7}$$

and again, combining all known values into a complex constant *K*:

$$A_{1x} = \left(K_1 + K_2 A_{1x}^* + K_3 A_{2x}\right) \exp\left[i\mu^2 \kappa \Delta x \right] \tag{A.8}$$

$$A_{2x} = \left(K_1' + K_2' A_{1x}\right) \exp\left[-i\mu^2 \kappa \Delta x \right] \tag{A.9}$$

where K_2' includes both terms with R_2 and R_3.

Substituting Equation (A.9) into (A.8) to eliminate A_{2x}:

$$\left(1 - K_3 K_2'\right) A_{1x} = K_1 \exp\left[i\mu^2 \kappa \Delta x \right] + K_2 A_{1x}^* \exp\left[i\mu^2 \kappa \Delta x \right] + K_3 K_1' \tag{A.10}$$

If A_{1x} has terms with $\exp[ia\mu^2\kappa\Delta x]$, then a can take the values 1, – *a* +1, or 0. Therefore, A_{1x} can be set as follows with the complex number coefficients *C*:

$$A_{1x} = C_1 \exp\left[i\mu^2 \kappa \Delta x \right] + C_2 \exp\left[i \frac{\mu^2}{2} \kappa \Delta x \right] + C_3 \tag{A.11}$$

Finally, A_{2x} can be also obtained:

$$A_{2x} = \left(K_1' + C_3 K_2' \right) \exp\left[-i\mu^2 \kappa \Delta x \right] + C_2 K_2' \exp\left[-i \frac{\mu^2}{2} \kappa \Delta x \right] + C_1 K_2' \tag{A.12}$$

Substituting Equations (A.11) and (A.12) into Equation (A.8), the coefficients C can be obtained from the given amplitude:

$$\left(1 - K_3 K_2' \right) C_2 = K_2 C_2^* \tag{A.13}$$

$$\left(1 - K_3 K_2' \right) C_1 = K_1 + K_2 C_3^* \tag{A.14}$$

$$\left(1 - K_3 K_2' \right) C_3 = K_3 K_1' + K_2 C_1^* \tag{A.15}$$

Finally, unlike model of Kaihatu and Kirby (1995) (i.e., Equation A.4), present model contains the term C_3 which has the effect of a buffer against high degrees of oscillation. Additionally, terms proportional to $\exp[(i\mu^2 \kappa \Delta x)/2]$ appear; these terms have longer cycle than $\exp[i\mu^2 \kappa \Delta x]$, and can thus also alleviate the impact of phase mismatch. This appendix therefore shows that the present model is less sensitive to the grid size $\kappa \Delta x$ in this artificial case than the model of Kaihatu and Kirby (1995) for the case of two distinct frequencies, thus extending the related discussion in Section 2.3.

APPENDIX B

In Section 4.2, the hybrid consistent nonlinear mild-slope equation is derived, and we provide the derivation in detail in this appendix. We take a careful look at second nonlinear summation in curly bracket of the right-hand side of Equation (4.16):

$$\sum_{l=1}^{n-1}\left[\begin{array}{l} -\dfrac{R_{2(l,n-l)}}{2\left(kCC_g\right)_l}\left[\left(kCC_g\right)_{lx}A_l+\dfrac{i}{4}\left(\sum A^2\right)_l\right]A_{n-l}e^{i\theta_{(l,n-l)}} \\ -\dfrac{R_{3(l,n-l)}}{2\left(kCC_g\right)_{n-l}}\left[\left(kCC_g\right)_{n-lx}A_{n-l}+\dfrac{i}{4}\left(\sum A^2\right)_{n-l}\right]A_l e^{i\theta_{(l,n-l)}} \end{array}\right] \\ +2\sum_{l=1}^{N-n}\left[\begin{array}{l} -\dfrac{S_{2(l,n+l)}}{2\left(kCC_g\right)_l}\left[\left(kCC_g\right)_{lx}A_l^{*}-\dfrac{i}{4}\left(\sum A^2\right)_l^{*}\right]A_{n+l}e^{i\psi_{(l,n+l)}} \\ -\dfrac{S_{3(l,n+l)}}{2\left(kCC_g\right)_{n+l}}\left[\left(kCC_g\right)_{n+lx}A_{n+l}+\dfrac{i}{4}\left(\sum A^2\right)_{n+l}\right]A_l^{*}e^{i\psi_{(l,n+l)}} \end{array}\right] \tag{B.1}$$

where index *m* is used instead of *l* for the internal summations:

$$\left(\sum A^2\right)_l=\left[\sum_{m=1}^{l-1}R_{1(m,l-m)}A_mA_{l-m}e^{i\theta_{(m,l-m)}}+2\sum_{m=1}^{N-l}S_{1(m,l+m)}A_m{}^{*}A_{l+m}e^{i\psi_{(m,l+m)}}\right] \tag{B.2}$$

$$\left(\sum A^2\right)_{n-l}=\left[\sum_{m=1}^{n-l-1}R_{1(m,n-l-m)}A_mA_{n-l-m}e^{i\theta_{(m,n-l-m)}}+2\sum_{m=1}^{N-(n-l)}S_{1(m,n-l+m)}A_m{}^{*}A_{n-l+m}e^{i\psi_{(m,n-l+m)}}\right] \tag{B.3}$$

$$\left(\sum A^2\right)_l^{*}=\left[\sum_{m=1}^{l-1}R_{1(m,l-m)}A_m{}^{*}A_{l-m}{}^{*}e^{-i\theta_{(m,l-m)}}+2\sum_{m=1}^{N-l}S_{1(m,l+m)}A_mA_{l+m}{}^{*}e^{-i\psi_{(m,l+m)}}\right] \tag{B.4}$$

$$\left(\sum A^2\right)_{n+l}=\left[\sum_{m=1}^{n+l-1}R_{1(m,n+l-m)}A_mA_{n+l-m}e^{i\theta_{(m,n+l-m)}}+2\sum_{m=1}^{N-(n+l)}S_{1(m,n+l+m)}A_m{}^{*}A_{n+l+m}e^{i\psi_{(m,n+l+m)}}\right] \tag{B.5}$$

The internal summations of Equations (B.2) through (B.5), containing mismatch of trial wave-wave interaction, are multiplied by another mismatch between three waves but one component of each mismatch is canceled out, and hence final form of mismatch can show wave-wave interaction between four waves. Following the closure method of Benney and Saffman (1966), except for four-wave interactions only with the matching indices (i.e., exact resonant interactions), we neglect the terms involving other interactions (i.e., near resonant interactions). Each internal summation has two summations, and hence there are totally eight summations, to focus on the frequency modes of wave-wave interaction, we rewrite the mismatches of summations only:

(1) First summation

$$\begin{aligned}\theta_{(m,l-m)}\theta_{(l,n-l)} &= \int \left(k_m + k_{l-m} - k_l\right) + \left(k_l + k_{n-l} - k_n\right) dx \\ &= \int k_m + k_{l-m} + k_{n-l} - k_n dx\end{aligned} \tag{B.6}$$

The case of exact resonance does not exist.

(2) Second summation

$$\begin{aligned}\psi_{(m,l+m)}\theta_{(l,n-l)} &= \int \left(k_{l+m} - k_m - k_l\right) + \left(k_l + k_{n-l} - k_n\right) dx \\ &= \int k_{l+m} - k_m + k_{n-l} - k_n dx\end{aligned} \tag{B.7}$$

When $m = n - l$, exact resonance is satisfied.

(3) Third summation

$$\begin{aligned}\theta_{(m,n-l-m)}\theta_{(l,n-l)} &= \int \left(k_m + k_{n-l-m} - k_{n-l}\right) + \left(k_l + k_{n-l} - k_n\right) dx \\ &= \int k_m + k_{n-l-m} + k_l - k_n dx\end{aligned} \tag{B.8}$$

The case of exact resonance does not exist.

(4) Fourth summation

$$\begin{aligned}\psi_{(m,n-l+m)}\theta_{(l,n-l)} &= \int \left(k_{n-l+m} - k_m - k_{n-l}\right) + \left(k_l + k_{n-l} - k_n\right) dx \\ &= \int k_{n-l+m} - k_m + k_l - k_n dx\end{aligned} \tag{B.9}$$

When $m = n$, exact resonance is satisfied.

(5) Fifth summation

$$\begin{aligned}-\theta_{(m,l-m)}\psi_{(l,n+l)} &= \int -\left(k_m + k_{l-m} - k_l\right) + \left(k_{n+l} - k_l - k_n\right) dx \\ &= \int -k_m - k_{l-m} + k_{n+l} - k_n dx\end{aligned} \tag{B.10}$$

The case of exact resonance does not exist.

(6) Sixth summation

$$\begin{aligned}-\psi_{(m,l+m)}\psi_{(l,n+l)} &= \int -\left(k_{l+m} - k_m - k_l\right) + \left(k_{n+l} - k_l - k_n\right) dx \\ &= \int -k_{l+m} + k_m + k_{n+l} - k_n dx\end{aligned} \tag{B.11}$$

When $m = n$, exact resonance is satisfied.

(7) Seventh summation

$$\begin{aligned}\theta_{(m,n+l-m)}\psi_{(l,n+l)} &= \int \left(k_m + k_{n+l-m} - k_{n+l}\right) + \left(k_{n+l} - k_l - k_n\right) dx \\ &= \int k_m + k_{n+l-m} - k_l - k_n dx\end{aligned} \tag{B.12}$$

When $m = l$ and $m = n$, exact resonance is satisfied.

(8) Eighth summation

$$\begin{aligned}\psi_{(m,n+l+m)}\psi_{(l,n+l)} &= \int \left(k_{n+l+m} - k_m - k_{n+l}\right) + \left(k_{n+l} - k_l - k_n\right) dx \\ &= \int k_{n+l+m} - k_m - k_l - k_n dx\end{aligned} \tag{B.13}$$

The case of exact resonance does not exist.

Considering all the case of exact resonance, Equation (B.1) becomes:

$$\sum_{l=1}^{n-1}\left(-R_{2(l,n-l)}\frac{\left(kCC_g\right)_{lx}}{2\left(kCC_g\right)_l}-R_{3(l,n-l)}\frac{\left(kCC_g\right)_{n-lx}}{2\left(kCC_g\right)_{n-l}}\right)A_lA_{n-l}e^{i\theta_{(l,n-l)}}$$

$$+2\sum_{l=1}^{N-n}\left(-S_{2(l,n+l)}\frac{\left(kCC_g\right)_{lx}}{2\left(kCC_g\right)_l}-S_{3(l,n+l)}\frac{\left(kCC_g\right)_{n+lx}}{2\left(kCC_g\right)_{n+l}}\right)A_l^*A_{n+l}e^{i\psi_{(l,n+l)}} \qquad \text{(B.14)}$$

$$+\left\{\begin{array}{l}\displaystyle\sum_{l=1}^{n-1}\left(-\frac{iR_{2(l,n-l)}S_{1(n-l,n)}}{4\left(kCC_g\right)_l}\left|A_{n-l}\right|^2A_n-\frac{iR_{3(l,n-l)}S_{1(l,n)}}{4\left(kCC_g\right)_{n-l}}\left|A_l\right|^2A_n\right)\\ \displaystyle+2\sum_{l=1}^{N-n}\left[\frac{iS_{2(l,n+l)}S_{1(n,l+n)}}{4\left(kCC_g\right)_l}\left|A_{l+n}\right|^2A_n-\frac{iS_{3(l,n+l)}R_{1(l,n)}}{4\left(kCC_g\right)_{n+l}}\left|A_l\right|^2A_n\right]\end{array}\right\}$$

which is reflected in Equation (4.17).

APPENDIX C

In Section 7.4, by manipulating the one-dimensional CNMSE model (Equation 2.60), the parametrized energy term for triad interactions which is suitable for implementation into the SWAN model is derived and we provide the derivation in detail in this appendix. First, we provide the derivation of stochastic version of consistent mild-slope equation model in detail in this appendix. Based on the assumption in the Gaussian Sea state (or using Gaussian closure hypothesis), nonlinear phase-resolved models have been extended to develop stochastic evolution equations for wave physics in deep and intermediate water depths (Agnon and Sheremet, 1997; Herbers and Burton, 1997; Kofoed-Hansen and Rasmussen, 1998; Eldeberky and Madsen, 1999; Sheremet et al., 2011; Vrecica and Toledo, 2016 among many others).

Following Eldeberky and Battjes (1999), we neglect the shoaling term for brevity and present the one-dimensional consistent mild-slope equation model with the new complicated interaction coefficients:

$$A_{nx} = -\left[\sum_{l=1}^{n-1}\left(iW1_{n,l,n-l}A_lA_{n-l} + W2_{n,l,n-l}A_{lx}A_{n-l} + W3_{n,l,n-l}A_lA_{n-lx}\right)e^{i\int k_l + k_{n-l} - k_n dx}\right] + \left[2\sum_{l=1}^{N-n}\left(iW1_{n,(-l),n+l}A_l^*A_{n+l} + W2_{n,(-l),n+l}A_{lx}{}^*A_{n+l} + W3_{n,(-l),n+l}A_l^*A_{n+lx}\right)e^{i\int -k_l + k_{n+l} - k_n dx}\right] \quad \text{(C.1)}$$

where

$$W1_{n,l,n-l} = \frac{g\omega_n}{8C_{gn}\omega_l\omega_{n-l}}\left[2k_lk_{n-l} + \frac{\omega_{n-l}k_l^{\,2}}{\omega_n} + \frac{\omega_lk_{n-l}{}^2}{\omega_n} - \frac{\omega_n{}^2\omega_l\omega_{n-l}}{g^2} + \frac{\omega_l{}^2\omega_{n-l}{}^2}{g^2}\right] \quad \text{(C.2)}$$

$$W2_{n,l,n-l} = \frac{g\omega_n k_{n-l}}{4C_{gn}\omega_l\omega_{n-l}} \tag{C.3}$$

$$W3_{n,l,n-l} = \frac{g\omega_n k_l}{4C_{gn}\omega_l\omega_{n-l}} \tag{C.4}$$

and

$$W1_{n,(-l),n+l} = \frac{g\omega_n}{8C_{gn}\omega_l\omega_{n+l}}\left[-2k_l k_{n+l} + \frac{\omega_{n+l}k_l^{\,2}}{\omega_n} - \frac{\omega_l k_{n+l}^{\,2}}{\omega_n} + \frac{\omega_n^{\,2}\omega_l\omega_{n+l}}{g^2} + \frac{\omega_l^{\,2}\omega_{n+l}^{\,2}}{g^2}\right] \tag{C.5}$$

$$W2_{n,(-l),n+l} = \frac{g\omega_n k_{n+l}}{4C_{gn}\omega_l\omega_{n+l}} \tag{C.6}$$

$$W3_{n,(-l),n+l} = -\frac{g\omega_n k_l}{4C_{gn}\omega_l\omega_{n+l}} \tag{C.7}$$

(1) Evolution equation for energy spectrum

Adding Equation (C.1) multiplied by A_n^* and the conjugate of Equation (C.1) multiplied by A_n gives the equation for energy spectrum $E_n = |A_n|^2$:

$$\begin{aligned} E_{nx} = &-2\sum_{l=1}^{n-1}\Re\left(iW1_{n,l,n-l}B_{n,l,n-l} + W2_{n,l,n-l}B_{n,\mathbf{l},n-l} + W3_{n,l,n-l}B_{n,l,\mathbf{n-l}}\right) \\ &+4\sum_{l=1}^{N-n}\Re\left(iW1_{n,(-l),n+l}B_{n,(-l),n+l} + W2_{n,(-l),n+l}B_{n,(\mathbf{-l}),n+l} + W3_{n,(-l),n+l}B_{n,(-l),\mathbf{n+l}}\right) \end{aligned} \tag{C.8}$$

where

$$B_{n,l,n-l} = A_n^{\,*}A_l A_{n-l}\exp\left[i\Delta_{n,l,n-l}\right] \tag{C.9}$$

$$B_{n,(-l),n+l} = A_n^{\,*}A_l^{\,*}A_{n+l}\exp\left[i\Delta_{n,(-l),n+l}\right] \tag{C.10}$$

and

$$\Delta_{n,l,n-l} = \int -k_n + k_l + k_{n-l}dx \tag{C.11}$$

$$\Delta_{n,(-l),n+l} = \int -k_n - k_l + k_{n+l} dx \tag{C.12}$$

and $\Re$ denotes the real part and the *x*-derivative of bispectrum is expressed by bold (e.g., $B_{n,\mathbf{l},n-l} = A_n{}^* A_{lx} A_{n-l} \exp[i\Delta_{n,l,n-l}]$).

Applying a statistical closure hypothesis (Benney and Saffman, 1966) which neglect the effects of nonlinearity between four wave components except for opposite-signed phases yields evolution equations for the *x*-derivatives of bispectra $B_{n,l,n-l}$:

$$\begin{aligned} B_{\mathbf{n},l,n-l} &= 2iW1_{n,l,n-l} \left|A_l\right|^2 \left|A_{n-l}\right|^2 \\ &\quad -2W2_{n,n-l,l} A_{n-lx}{}^* A_{n-l} \left|A_l\right|^2 - 2W3_{n,n-l,l} A_{lx}{}^* A_l \left|A_{n-l}\right|^2 \end{aligned} \tag{C.13}$$

$$\begin{aligned} B_{n,\mathbf{l},n-l} &= 2iW1_{l,-(n-l),n} \left|A_n\right|^2 \left|A_{n-l}\right|^2 \\ &\quad +2W2_{l,-(n-l),n} A_{n-lx}{}^* A_{n-l} \left|A_n\right|^2 + 2W3_{l,-(n-l),n} A_{nx} A_n{}^* \left|A_{n-l}\right|^2 \end{aligned} \tag{C.14}$$

$$\begin{aligned} B_{n,l,\mathbf{n-l}} &= 2iW1_{n-l,-l,n} \left|A_l\right|^2 \left|A_n\right|^2 \\ &\quad +2W2_{n-l,(-l),n} A_{lx}{}^* A_l \left|A_n\right|^2 + 2W3_{n-l,(-l),n} A_{nx} A_n{}^* \left|A_l\right|^2 \end{aligned} \tag{C.15}$$

and for the *x*-derivatives of bispectra $B_{n,(-l),n+l}$:

$$\begin{aligned} B_{\mathbf{n},(-l),n+l} &= -2iW1_{n,-l,n+l} \left|A_l\right|^2 \left|A_{n+l}\right|^2 \\ &\quad +2W2_{n,-l,n+l} A_{lx} A_l{}^* \left|A_{n+l}\right|^2 + 2W3_{n,-l,n+l} A_{n+lx}{}^* A_{n+l} \left|A_l\right|^2 \end{aligned} \tag{C.16}$$

$$\begin{aligned} B_{n,(\mathbf{-l}),n+l} &= -2iW1_{l,-n,n+l} \left|A_n\right|^2 \left|A_{n+l}\right|^2 \\ &\quad +2W2_{l,-n,n+l} A_{nx} A_n{}^* \left|A_{n+l}\right|^2 + 2W3_{l,-n,n+l} A_{n+lx}{}^* A_{n+l} \left|A_n\right|^2 \end{aligned} \tag{C.17}$$

$$\begin{aligned} B_{n,(-l),\mathbf{n+l}} &= -2iW_{n+l,l,n} \left|A_l\right|^2 \left|A_n\right|^2 \\ &\quad -2W2_{n+l,n,l} A_{nx} A_n{}^* \left|A_l\right|^2 - 2W3_{n+l,n,l} A_{lx} A_l{}^* \left|A_n\right|^2 \end{aligned} \tag{C.18}$$

The real part $\Re$ gives the following features:

$$\Re\left(2iW2_{n,l,n-l}W1_{l,-(n-l),n}\left|A_n\right|^2\left|A_{n-l}\right|^2\right)=0 \tag{C.19}$$

$$\begin{aligned}&\Re\left(2W2_{n,l,n-l}W2_{l,-(n-l),n}A_{n-lx}{}^{*}A_{n-l}\left|A_n\right|^2\right)\\&=W2_{n,l,n-l}W2_{l,-(n-l),n}\left(A_{n-lx}{}^{*}A_{n-l}\left|A_n\right|^2+A_{n-lx}A_{n-l}{}^{*}\left|A_n\right|^2\right)\\&=W2_{n,l,n-l}W2_{l,-(n-l),n}\frac{d\left|A_{n-l}\right|^2}{dx}\left|A_n\right|^2\end{aligned} \tag{C.20}$$

Plugging Equations (C.14), (C.15), (C.17), and (C.18) into Equation (C.8) and using features (C.19) and (C.20) leads to final form for spectrum:

$$\begin{aligned}E_{nx}&=2\sum_{l=1}^{n-1}W_{n,l,n-l}\left|B_{n,l,n-l}\right|\sin\left(\Delta_{n,l,n-l}\right)\\&-\sum_{l=1}^{n-1}\left[\begin{array}{l}W2_{n,l,n-l}\left\{W2_{l,-(n-l),n}E_{n-lx}E_n+W3_{l,-(n-l),n}E_{nx}E_{n-l}\right\}\\+W3_{n,l,n-l}\left\{W2_{n-l,(-l),n}E_{lx}E_n+W3_{n-l,(-l),n}E_{nx}E_l\right\}\end{array}\right]\\&-4\sum_{l=1}^{N-n}W_{n,-l,n+l}\left|B_{n,-l,n+l}\right|\sin\left(\Delta_{n,(-l),n+l}\right)\\&+2\sum_{l=1}^{N-n}\left[\begin{array}{l}W2_{n,(-l),n+l}\left\{W2_{l,-n,n+l}E_{nx}E_{n+l}+W3_{l,-n,n+l}E_{n+lx}E_n\right\}\\+W3_{n,(-l),n+l}\left\{-W2_{n+l,n,l}E_{nx}E_l-W3_{n+l,n,l}E_{lx}E_n\right\}\end{array}\right]\end{aligned} \tag{C.21}$$

(2) Evolution equation for bispectrum

Combining Equations (C.13) through (C.15), and substituting Equation (C.1) into nonlinear part with adjusting to the frequency component of *x*-derivatives in right-hand side of Equations (C.13) through (C.15). Neglecting quintic polynomial which is consistent with the statistical closure hypothesis (Benney and Saffman, 1966) yields the evolution equation for bispectrum $B_{n,l,n-l}$:

$$\begin{aligned}&\left[\frac{d}{dx}\left(B_{n,l,n-l}\right)\right]+i\left(k_n-k_l-k_{n-l}\right)B_{n,l,n-l}\\&=2iW1_{n,l,n-l}E_lE_{n-l}+2iW1_{l,-(n-l),n}E_nE_{n-l}+2iW1_{n-l,-l,n}E_lE_n\end{aligned} \tag{C.22}$$

In a similar manner, the evolution equation for bispectrum $B_{n,(-l),n+l}$ is obtained:

$$\begin{aligned}&\left[\frac{d}{dx}\left(B_{n,(-l),n+l}\right)\right]+i\left(k_n+k_l-k_{n+l}\right)B_{n,(-l),n+l}\\&=-2iW1_{n,(-l),n+l}E_lE_{n+l}-2iW1_{l,(-n),n+l}E_nE_{n+l}-2iW1_{n+l,l,n}E_nE_l\end{aligned} \tag{C.23}$$

(3) Triad interactions source term

With the assumption that the terms on the right-hand side of Equations (C.22) and (C.23) are constant and bispectrum is initially zero, integrating from 0 to *x* leads to:

$$B_{n,l,n-l}=\begin{bmatrix}2iW1_{n,l,n-l}E_lE_{n-l}\\+2iW1_{l,-(n-l),n}E_nE_{n-l}+2iW1_{n-l,(-l),n}E_lE_n\end{bmatrix}\left\{\frac{1-\exp\left[-i\Delta_{n,l,n-l}\right]}{i\left(-k_n+k_l+k_{n-l}\right)}\right\} \tag{C.24}$$

$$B_{n,(-l),n+l}=\begin{bmatrix}-2iW1_{n,(-l),n+l}E_lE_{n+l}\\-2iW1_{l,(-n),n+l}E_nE_{n+l}-2iW1_{n+l,l,n}E_nE_l\end{bmatrix}\left\{\frac{1-\exp\left[-i\Delta_{n,(-l),n+l}\right]}{i\left(-k_n-k_l+k_{n+l}\right)}\right\} \tag{C.25}$$

Neglecting the contribution of the fast-oscillating function:

$$B_{n,l,n-l}=\frac{2W1_{n,l,n-l}E_lE_{n-l}+2W1_{l,-(n-l),n}E_nE_{n-l}+2W1_{n-l,(-l),n}E_lE_n}{-k_n+k_l+k_{n-l}} \tag{C.26}$$

$$B_{n,(-l),n+l}=\frac{2W1_{n,(-l),n+l}E_lE_{n+l}+2W1_{l,(-n),n+l}E_nE_{n+l}+2W1_{n+l,l,n}E_nE_l}{k_n+k_l-k_{n+l}} \tag{C.27}$$

Substituting Equations (C.26) and (C.27) into Equations (C.21):

$$
\begin{aligned}
E_{nx} = {} & 4\sum_{l=1}^{n-1}\left[\begin{array}{l}\left(W1_{n,l,n-l}\right)^2 E_l E_{n-l} \\ +W1_{n,l,n-l}W1_{l,-(n-l),n}E_n E_{n-l} + W1_{n,l,n-l}W1_{n-l,-l,n}E_l E_n\end{array}\right]\frac{\sin\left(\Delta_{n,l,n-l}\right)}{-k_n + k_l + k_{n-l}} \\
& -\sum_{l=1}^{n-1}\left[\begin{array}{l}W2_{n,l,n-l}\left\{W2_{l,-(n-l),n}E_{n-lx}E_n + W3_{l,-(n-l),n}E_{nx}E_{n-l}\right\} \\ +W3_{n,l,n-l}\left\{W2_{n-l,(-l),n}E_{lx}E_n + W3_{n-l,(-l),n}E_{nx}E_l\right\}\end{array}\right] \\
& -8\sum_{l=1}^{N-n}\left[\begin{array}{l}\left(W1_{n,-l,n+l}\right)^2 E_l E_{n+l} \\ +W1_{n,-l,n+l}W1_{l,-n,n+l}E_n E_{n+l} + W1_{n,-l,n+l}W1_{n+l,l,n}E_n E_l\end{array}\right]\frac{\sin\left(\Delta_{n,(-l),n+l}\right)}{k_n + k_l - k_{n+l}} \\
& +2\sum_{l=1}^{N-n}\left[\begin{array}{l}W2_{n,(-l),n+l}\left\{W2_{l,-n,n+l}E_{nx}E_{n+l} + W3_{l,-n,n+l}E_{n+lx}E_n\right\} \\ +W3_{n,(-l),n+l}\left\{-W2_{n+l,n,l}E_{nx}E_l - W3_{n+l,n,l}E_{lx}E_n\right\}\end{array}\right]
\end{aligned}
\tag{C.28}
$$

Rewriting discrete energy as $E_n = E(f_n)\Delta f$:

$$
\begin{aligned}
\frac{dE(f_n)}{dx} = {} & 4\sum_{l=1}^{n-1}\Delta f\left[\begin{array}{l}\left(W1_{n,l,n-l}\right)^2 E(f_l)E(f_{n-l}) \\ +W1_{n,l,n-l}W1_{l,-(n-l),n}E(f_n)E(f_{n-l}) \\ +W1_{n,l,n-l}W1_{n-l,(-l),n}E(f_l)E(f_n)\end{array}\right]\frac{\sin\left(\Delta_{n,l,n-l}\right)}{-k_n + k_l + k_{n-l}} \\
& -\sum_{l=1}^{n-1}\Delta f\left[\begin{array}{l}W2_{n,l,n-l}\left\{W2_{l,-(n-l),n}E(f_{n-l})_x E(f_n) + W3_{l,-(n-l),n}E(f_n)_x E(f_{n-l})\right\} \\ +W3_{n,l,n-l}\left\{W2_{n-l,(-l),n}E(f_l)_x E(f_n) + W3_{n-l,(-l),n}E(f_n)_x E(f_l)\right\}\end{array}\right] \\
& -8\sum_{l=1}^{N-n}\Delta f\left[\begin{array}{l}\left(W1_{n,(-l),n+l}\right)^2 E(f_l)E(f_{n+l}) \\ +W1_{n,(-l),n+l}W1_{l,(-n),n+l}E(f_n)E(f_{n+l}) \\ +W1_{n,(-l),n+l}W1_{n+l,l,n}E(f_n)E(f_l)\end{array}\right]\frac{\sin\left(\Delta_{n,(-l),n+l}\right)}{k_n + k_l - k_{n+l}} \\
& +2\sum_{l=1}^{N-n}\Delta f\left[\begin{array}{l}W2_{n,(-l),n+l}\left\{W2_{l,-n,n+l}E(f_n)_x E(f_{n+l}) + W3_{l,-n,n+l}E(f_{n+l})_x E(f_n)\right\} \\ +W3_{n,(-l),n+l}\left\{-W2_{n+l,n,l}E(f_n)_x E(f_l) - W3_{n+l,n,l}E(f_l)_x E(f_n)\right\}\end{array}\right]
\end{aligned}
\tag{C.29}
$$

The effective interaction bandwidth $\Delta f = \delta f_p$ is introduced and the interactions between wavenumber is replaced with k_p, and replacing the summation of triad interactions with self-self-interactions ($\frac{n}{2} + \frac{n}{2} = n$ and $n + n = 2n$) which are dominant among all the triad interactions between two wave components:

$$\frac{dE(f_n)}{dx} = 4\delta C_n \begin{Bmatrix} \left(W1_{n,n/2,n/2}\right)^2 E(f_{n/2}) E(f_{n/2}) \\ +W1_{n,n/2,n/2} W1_{n/2,(-n/2),n} E(f_n) E(f_{n/2}) \\ +W1_{n,n/2,n/2} W1_{n/2,(-n/2),n} E(f_{n/2}) E(f_n) \end{Bmatrix} \sin\left(\Delta_{n,n/2,n/2}\right)$$

$$-\delta f_n \begin{bmatrix} W2_{n,n/2,n/2} \begin{Bmatrix} W2_{n/2,(-n/2),n} E(f_{n/2})_x E(f_n) \\ +W3_{n/2,(-n/2),n} E(f_n)_x E(f_{n/2}) \end{Bmatrix} \\ +W3_{n,n/2,n/2} \begin{Bmatrix} W2_{n/2,(-n/2),n} E(f_{n/2})_x E(f_n) \\ +W3_{n/2,(-n/2),n} E(f_n)_x E(f_{n/2}) \end{Bmatrix} \end{bmatrix}$$

$$-8\delta C_{2n} \begin{Bmatrix} \left(W_{n,(-n),2n}\right)^2 E(f_n) E(f_{2n}) \\ +W_{n,(-n),2n} W_{n,(-n),2n} E(f_n) E(f_{2n}) \\ +W_{n,(-n),2n} W_{2n,n,n} E(f_n) E(f_n) \end{Bmatrix} \sin\left(\Delta_{n,(-n),2n}\right)$$

$$+2\delta f_{2n} \begin{bmatrix} W2_{n,(-n),2n} \begin{Bmatrix} W2_{n,(-n),2n} E(f_n)_x E(f_{2n}) \\ +W3_{n,(-n),2n} E(f_{2n})_x E(f_n) \end{Bmatrix} \\ +W3_{n,(-n),2n} \begin{Bmatrix} -W2_{2n,n,n} E(f_n)_x E(f_n) \\ -W3_{2n,n,n} E(fn)_x E(f_n) \end{Bmatrix} \end{bmatrix} \quad \text{(C.30)}$$

For energy flux $C_g E(f)$:

$$S_{nl3}(f_n) = S^+_{nl3}(f_n) + S^-_{nl3}(f_n) \quad \text{(C.31)}$$

where

$$S^+_{nl3}(f_n) = \alpha_{EB} C_n C_{gn} \begin{Bmatrix} \left(W1_{n,n/2,n/2}\right)^2 E(f_{n/2}) E(f_{n/2}) \\ +W1_{n,n/2,n/2} W1_{n/2,(-n/2),n} E(f_n) E(f_{n/2}) \\ +W1_{n,n/2,n/2} W1_{n/2,(-n/2),n} E(f_{n/2}) E(f_n) \end{Bmatrix} \sin\left(\Delta_{n,n/2,n/2}\right)$$

$$-\frac{\alpha_{EB}}{4} f_n C_{gn} \begin{bmatrix} W2_{n,n/2,n/2} \begin{Bmatrix} W2_{n/2,(-n/2),n} E(f_{n/2})_x E(f_n) \\ +W3_{n/2,(-n/2),n} E(f_n)_x E(f_{n/2}) \end{Bmatrix} \\ +W3_{n,n/2,n/2} \begin{Bmatrix} W2_{n/2,(-n/2),n} E(f_{n/2})_x E(f_n) \\ +W3_{n/2,(-n/2),n} E(f_n)_x E(f_{n/2}) \end{Bmatrix} \end{bmatrix} \quad \text{(C.32)}$$

and

$$S_{nl3}^{-}\left(f_n\right)=-2\alpha C_{2n}C_{gn}\begin{Bmatrix}\left(W_{n,(-n),2n}\right)^2 E\left(f_n\right)E\left(f_{2n}\right)\\ +W_{n,(-n),2n}W_{n,(-n),2n}E\left(f_n\right)E\left(f_{2n}\right)\\ +W_{n,(-n),2n}W_{2n,n,n}E\left(f_n\right)E\left(f_n\right)\end{Bmatrix}\sin\left(\Delta_{n,(-n),2n}\right)$$
$$+\frac{\alpha}{2}f_{2n}C_{gn}\begin{bmatrix}W2_{n,(-n),2n}\begin{Bmatrix}W2_{n,(-n),2n}E\left(f_n\right)_x E\left(f_{2n}\right)\\ +W3_{n,(-n),2n}E\left(f_{2n}\right)_x E\left(f_n\right)\end{Bmatrix}\\ +W3_{n,(-n),2n}\begin{Bmatrix}-W2_{2n,n,n}E\left(f_n\right)_x E\left(f_n\right)\\ -W3_{2n,n,n}E\left(fn\right)_x E\left(f_n\right)\end{Bmatrix}\end{bmatrix} \quad \text{(C.33)}$$

with α_{EB} is a tunning parameter in Eldeberky (1996) ($\alpha_{EB}=1$ in SWAN, Holthuijsen, 2010). Eventually, the source term based on the consistent nonlinear mild-slope equation model is developed to modify the existing parameterized formulation (e.g., Eldeberky, 1996) to include the additional nonlinear effect from the *x*-derivative nonlinear term A_xA.